THE HYDROXYL RADICAL INITIATED OXIDATION OF UNSATURATED HYDROCARBONS IN THE TROPOSPHERE:

A THEORETICAL AND EXPERIMENTAL APPROACH

A Dissertation

by

ERIN ELIZABETH TULLOS

Submitted to the Office of Graduate Studies of
Texas A&M University
in partial fulfillment of the requirements for the degree of

DOCTOR OF PHILOSOPHY

May 2007

Major Subject: Chemistry

THE HYDROXYL RADICAL INITIATED OXIDATION OF UNSATURATED HYDROCARBONS IN THE TROPOSPHERE: A THEORETICAL AND EXPERIMENTAL APPROACH

A Dissertation

by

ERIN ELIZABETH TULLOS

Submitted to the Office of Graduate Studies of
Texas A&M University
in partial fulfillment of the requirements for the degree of

DOCTOR OF PHILOSOPHY

Approved by:

Char of Committee,	Simon W. North
Committee Members,	Daniel A. Singleton
	Robert R. Lucchese
	Yi Qin Gao
	Robert A. Kenefick
Head of Department,	David H. Russell

May 2007

Major Subject: Chemistry

ABSTRACT[*]

The Hydroxyl Radical Initiated Oxidation of Unsaturated Hydrocarbons
in the Troposphere: A Theoretical and Experimental Approach. (May 2007)
Erin Elizabeth Tullos, B.A., Texas A&M University
Chair of Advisory Committee: Dr. Simon W. North

Isoprene is the dominant non-methane organic compound emitted by vegetation into the atmosphere, with a global emission rate of ~ 500 Tg yr^{-1}. Its oxidation serves as a major source of ground level ozone in North America during the summer months. Despite the significant impact on tropospheric chemistry, questions remain concerning the detailed oxidation mechanism. The initial step in the mechanism is the addition of OH to form four distinct isomers. The relative branching between these isomers influences the distribution of the final products. I present a comprehensive investigation into the mechanistic details of early steps in the oxidation mechanism of unsaturated hydrocarbons in the troposphere and employ theoretical and experimental techniques.

To understand the detailed kinetics of the initial OH addition to unsaturated hydrocarbons, I first present a model developed for the ethylene-OH system. I present the details of a robust two-transition state model. I extend the developed two-transition

---

[*] Parts of this abstract are preprinted with permission from "A Two Transition State Model for Radical-Molecule Reactions: Application to Isomeric Branching in the OH-Isoprene Reaction" Greenwald, E. E.; North, S. W.; Georgievskii, Y.; Klippenstein, S. J. *J. Phys. Chem. A* **2007**, submitted and "The OH Initiated Oxidation of Isoprene in the Presence of O_2 and NO: A Photolytic Route to Study Isomeric Selective Reactivity" Greenwald, E. E.; Ghosh, B.; Anderson, K. A.; Dooley, K. S.; North, S. W. *J. Phys. Chem. A.* **2007**, in preparation. Additional parts of this abstract are reprinted with permission from "A Two Transition State Model for Radical-Molecule Reactions: A Case Study of the Addition of OH to C_2H_4" Greenwald, E. E.; North, S. W.; Georgievskii, Y.; Klippenstein, S. J. *J. Phys. Chem. A.* **2005**, *109*, 6031 and "The OH Initiated Oxidation of 1,3-Butadiene in the Presence of O2 and NO: A Photolytic Route to Study Isomeric Selective Reactivity" Greenwald, E. E.; Anderson, K. C.; Park, J.; Kim, H.; Reich, B. J. E.; Miller, S. A.; North, S. W. *J. Phys. Chem.. A* **2005**, *109*, 7915.

state model to the case of OH addition to isoprene. Excellent agreement with observed temperature and pressure dependent rate constants affords a high confidence level in understanding of the kinetics and in the calculated branching ratio of the initial OH addition step.

I then focus attention on the subsequent reactivity of the OH-isoprene adducts. Until recently, all four of the OH-isoprene adducts were supposed to have reacted with O_2 via addition to form alkylperoxy radicals. Previous computational results suggest that two of the OH-isoprene adducts undergo an intramolecular cyclic isomerization followed by hydrogen abstraction by O_2 to form stable carbonyl compounds. I have synthesized photolytic precursors, presenting a novel approach to probe the subsequent reactivity of individual hydroxyalkyl radicals.

Initial verification of the cyclic isomerization pathway involved synthesis of the photolytic precursor corresponding to the 1,3-butadiene-OH adduct. A culmination of theoretical and experimental techniques allowed verification of the cyclic isomerization pathway. I synthesized the photolytic precursor, which provided a single isoprene-OH adduct. Employing laser photolysis/laser induced fluorescence, time-dependent multiplexed mass spectrometry, velocity map ion imaging, and theoretical techniques, we present the full characterization of the reactivity of the single isoprene-OH adduct in the presence of O_2.

To my grandmother

ACKNOWLEDGEMENTS

Immeasurable gratitude permeates my thoughts now, and will, I expect, throughout my career for my advisor, Dr. Simon W. North. Not only did he teach me science, he taught me to love science. His endless enthusiasm and belief in me gave me the motivation to keep going, even when I saw no light at the end of the tunnel. I also owe many thanks to many others: to my committee members Dr. Robert R. Lucchese, Dr. Yi Qin Gao, and Dr. Robert A. Kenefick for serving as mentors and offering helpful suggestions and guidance and to Dr. Daniel A. Singleton (Doc), especially, my undergraduate research advisor, who first introduced me to physical and computational chemistry and for serving on my committee and offering helpful suggestions.

To those I cherish as friends, as well as co-workers, Kate, Kristin, Justine, Andrea, and Buddhadeb, I will always be grateful. In particular, I thank Kate Perkins, who spent long hours and time in the basement lab figuring out the experiment with me. I also thank my previous group members, Dr. Jiho Park, Dr. Hahkjoon Kim, and especially Dr. Peng Zou, with whom I had the great pleasure of continual collaboration at Sandia National Laboratory.

My graduate work would have not been possible in its present form without the help of Dr. Stephen Klippenstein, who collaborated with and taught me a large portion of the theoretical chemistry that comprises the first half of this dissertation. I thank Sandia and Argonne National Laboratories for support and resources. I also thank Dr. David Osborn and Dr. Craig Taatjes of Sandia for collaboration and support. The opportunity to further my experimental knowledge while working at the Advanced Light Source with David and Craig was invaluable. I additionally thank the postdocs and professor who also worked at the ALS, Dr. Peng Zou, Dr. Giovanni Meloni, Dr. Fabien Goulay, Dr. Talitha Selby, and Dr. Askar Fahr. I thank Dr. Musa Ahmed, Dr. Kevin Wilson, and Dr. Steve Leone, as well, for making that experiment possible.

Last, but certainly not least, I thank my loving and supportive husband, Mike and my beloved children Sam and Jack. I also thank a couple of friends, Charles Greenwald

and Amy Thompson. I thank and appreciate all my parents, my brothers, my sisters, and my cousin, who offered endless emotional support, faith, and belief in me. I especially thank my grandparents, who put me through college, for their love and generosity; not pursuing an education was never an easy option.

TABLE OF CONTENTS

Page

CHAPTER

LIST OF FIGURES

FIGURE Page

FIGURE Page

LIST OF TABLES

TABLE Page

CHAPTER I

INTRODUCTION*

Earth's atmosphere is composed of several layers, or spheres, which are characterized by changes in temperature with increasing altitude. The troposphere, so-called after the Greek "tropos" meaning "mixing", is the layer of the atmosphere, which extends from the Earth's surface up to altitudes as high as nearly 15 km. It is characterized by decreasing temperature with increasing altitude. Average temperatures in the troposphere range from about 220-340 K, with the highest surface temperatures in the tropics and the lowest at the poles. As with the atmosphere in general, the density of the air decreases with pressure, which decreases with altitude. At mid-latitudes, more than 75% of all gasses comprising the atmosphere are contained in the troposphere, and in the tropics, up to 90% of the atmospheric mass is contained in the troposphere. The dry atmosphere is composed of approximately 78% N_2, 21% O_2, 0.9% Ar, 0.03% CO_2, and other trace gasses by volume.[1] Additionally, the majority of Earth's water vapor and precipitation is found in the troposphere, creating a rich medium to support a variety of photochemical reactions.[2]

Air quality in the troposphere has been a documented central issue for nearly 2000 years due to its impact on human health and the environment. Sulfurous and photochemical smog are among the foremost concerns in air quality. Sulfurous smog is

---

This dissertation follows the format of the *Journal of Physical Chemistry A.*

* Parts of this chapter are preprinted with permission from "A Two Transition State Model for Radical-Molecule Reactions: Application to Isomeric Branching in the OH-Isoprene Reaction" Greenwald, E. E.; North, S. W.; Georgievskii, Y.; Klippenstein, S. J. *J. Phys. Chem. A* **2007**, submitted and "The OH Initiated Oxidation of Isoprene in the Presence of O_2 and NO: A Photolytic Route to Study Isomeric Selective Reactivity" Greenwald, E. E.; Ghosh, B.; Anderson, K. A.; Dooley, K. S.; North, S. W. *J. Phys. Chem. A.* **2007**, in preparation. Additional parts of this chapter are reprinted with permission from "A Two Transition State Model for Radical-Molecule Reactions: A Case Study of the Addition of OH to C_2H_4" Greenwald, E. E.; North, S. W.; Georgievskii, Y.; Klippenstein, S. J. *J. Phys. Chem. A.* **2005**, *109*, 6031 and "The OH Initiated Oxidation of 1,3-Butadiene in the Presence of O2 and NO: A Photolytic Route to Study Isomeric Selective Reactivity" Greenwald, E. E.; Anderson, K. C.; Park, J.; Kim, H.; Reich, B. J. E.; Miller, S. A.; North, S. W. *J. Phys. Chem.. A* **2005**, *109*, 7915.

mainly comprised of SO_2 (a combustion product of high-sulfur coal) and particulate matter from smoke. A sulfurous smog event occurs when sulfurous pollutants become trapped by a surface level thermal inversion and are concentrated into a small region, suspended in dense fog. These types of smog episodes lead to secondary pollutants such as sulfuric acid, sulfate, and aerosols and have been linked to excessive deaths and grave impacts on human health along with extreme reduction in visibility in the region of the smog. Photochemical smog is largely initiated by volatile organic compounds (VOCs) and nitrous oxides (NO_x). These pollutants become trapped under thermal inversions and, upon sunlight irradiation, lead to secondary pollutants. These pollutants, such as ozone, peroxyacetyl nitrate (PAN), nitric acid, aldehydes, particulate nitrate and sulfate, are strong oxidizers and severe irritants to the membranes of both animals and plants and result in reduced visibility, i.e. haze. Table I-I summarizes some of the characteristics of sulfurous and photochemical smog as have been historically determined in the areas of London and Los Angeles.[3]

Table I-I: The characteristics of sulfurous and photochemical smog

Characteristics	**Sulfurous (London)**	**Photochemical (Los Angeles)**
First recognized	Centuries ago	Mid-1940s
Primary pollutants	SO_2, soot particles	VOC, NO_x
Secondary pollutants	H_2SO_4, sulfate, aerosols, etc.	O_3, PAN, HNO_3, aldehydes, particulate nitrate and sulfate, etc.
Temperature	Cool (< 35°C)	Hot (< 75°F)
Relative humidity	High, usually foggy	Low, usually hot and dry
Type of inversion	Radiation (ground)	Subsidence (overhead)
Time air pollution peaks	Early Morning	Noon to evening

Adopted from Table 1.2 in Ref. 3.

In present times, photochemical smog constitutes the majority of incidences of urban air pollution. To address the impact of photochemical smog, broad research goals must address the following questions: a) Can one derive a global mechanism that explains observed products in smog incidences and offers forecasting capabilities for future smog events? and b) What policies can be implemented to curb the production of photochemical smog and reduce the impact on health and the environment? While environmental scientists have made substantial headway on addressing the first question, detailed chemical kinetics information is requisite to the accuracy of these box models. As such, the remainder of this text is dedicated to unraveling detailed mechanistic and rate information related to photochemical smog.

The overall photochemical smog mechanism is given by,

$$VOC + NOx + h\nu \rightarrow O_3 + other\ photochemical\ smog\ constituents\ , \qquad (1\text{-}1)$$

where $h\nu$ is a photon. VOCs are emitted into the atmosphere by both anthropogenic (man-made) and biogenic sources. Anthropogenic sources include incomplete fossil fuel combustion, direct release, industrial processing, and waste. Anthropogenic sources contribute less than 10% to the annual global flux of VOC emissions with a rate of approximately 1 x 10^{14} gC yr^{-1}. While this contribution does not seem significant on a global scale as compared to biogenic sources, these emissions drive ground level ozone formation in highly industrial and urban areas. Biogenic sources include biological sources (both marine and terrestrial) and vegetation. The annual flux of emissions from vegetation alone is approximately 1.2 x 10^{15} gC yr^{-1}. NO_x ($NO_x = NO + NO_2$) emissions are primarily the result of automobile exhaust and peak concentration times roughly correspond to peak automotive traffic times, i.e. rush hour.[4,5]

VOCs can be removed from the atmosphere by wet or dry deposition, by photolysis, or by reaction with chemical oxidants such as OH, O_3, NO_3, or in some cases Cl atoms. The fate of a particular VOC is largely based on its chemical composition. Non methane organic compounds (NMOCs) are primarily removed via chemical reactions in the atmosphere. Wet and dry deposition is considered to be very minor removal processes. Photolytic processes are only relevant to the troposphere for wavelengths greater than 290 nm as shorter wavelengths are absorbed by molecular oxygen and O_3 in the stratosphere. The radiation of $\lambda > 290$nm (actinic radiation) plays an important role in tropospheric photochemistry, but rarely by photolysis of NMOCs.[5]

Ozone is generally formed in situ in the troposphere, although some ozone is carried down from the stratosphere by eddy diffusion. Tropospheric ozone can be photolyzed at wavelengths greater than 290 nm to produce electronically excited oxygen atoms, $O(^1D)$, which are either collisionally relaxed to form ground state oxygen atoms, $O(^3P)$, or react with water vapor to produce hydroxyl radicals.

$$\begin{aligned} &O_3 + h\nu \rightarrow O_2 + O(^1D) && (290 < \lambda < 330) \\ &O(^1D) + M \rightarrow O(^3P) + M && (M = N_2, O_2)\ , \\ &O(^1D) + H_2O \rightarrow 2OH && \end{aligned} \qquad (1\text{-}2)$$

where $h\nu$ is a photon of light of wavelength λ, and M is a collisional partner. Hydroxyl radical concentrations exhibit a strong diurnal pattern due to generation initiated by photolysis. Typical peak OH radical concentrations measured during the middle of the day are on the order of (2-10) x 10^6 molecule cm^{-3}. Additional sources of hydroxyl radical include photolysis of nitrous acid (HONO) and indirectly from the photolysis of HCHO during the day, and by O_3 reaction with alkenes around the clock.[5]

Isoprene, 2-methyl-1,3-butadiene, contributes 44% to annual vegetation emissions. It is the largest single source biogenic VOC emitted worldwide with an emission rate in excess of ~500 Tg C yr^{-1}. Isoprene is emitted in the daytime by deciduous trees and is likely the result of a natural defense mechanism.[4] Its lifetime in the atmosphere is approximately 1 hour and is dominated by reaction with hydroxyl radical.[3,4,5] Hydroxyl radical initiated photooxidation of isoprene directs much of the ground level ozone production in North America during summer months. The reaction with hydroxyl radical proceeds by electrophilic addition to one of the two double bonds, rather than hydrogen abstraction. Isoprene oxidation is also thought to contribute to secondary organic aerosol (SOA) formation via further reactions of first-generation end products in both high- and low-NO_x conditions[6,7,8,9,10] and to contribute to hygroscopic SOA formation through cloud processing.[11,12,13,14] The detailed mechanism of the OH initiated oxidation of isoprene has been the focus of numerous recent studies. Despite the importance, questions remain.

The general photooxidation mechanism of unsaturated hydrocarbons in the troposphere is illustrated in Figure I-I, where a general unsaturated hydrocarbon, such as isoprene, undergoes electrophilic addition by a hydroxyl radical to produce a hydroxyalkyl radical. The hydroxyalkyl radical then undergoes O_2 addition to form a hydroxyalkylperoxy radical. The peroxy radical is primarily reduced by NO to form an alkoxy radical. Additionally, the peroxy radicals can be terminated by NO to form organic nitrates or react with NO_2 or HO_2. The alkoxy radical, then, either reacts with another peroxy radical to form a variety of carbonyls and alcohols or goes on to form first generation end products.

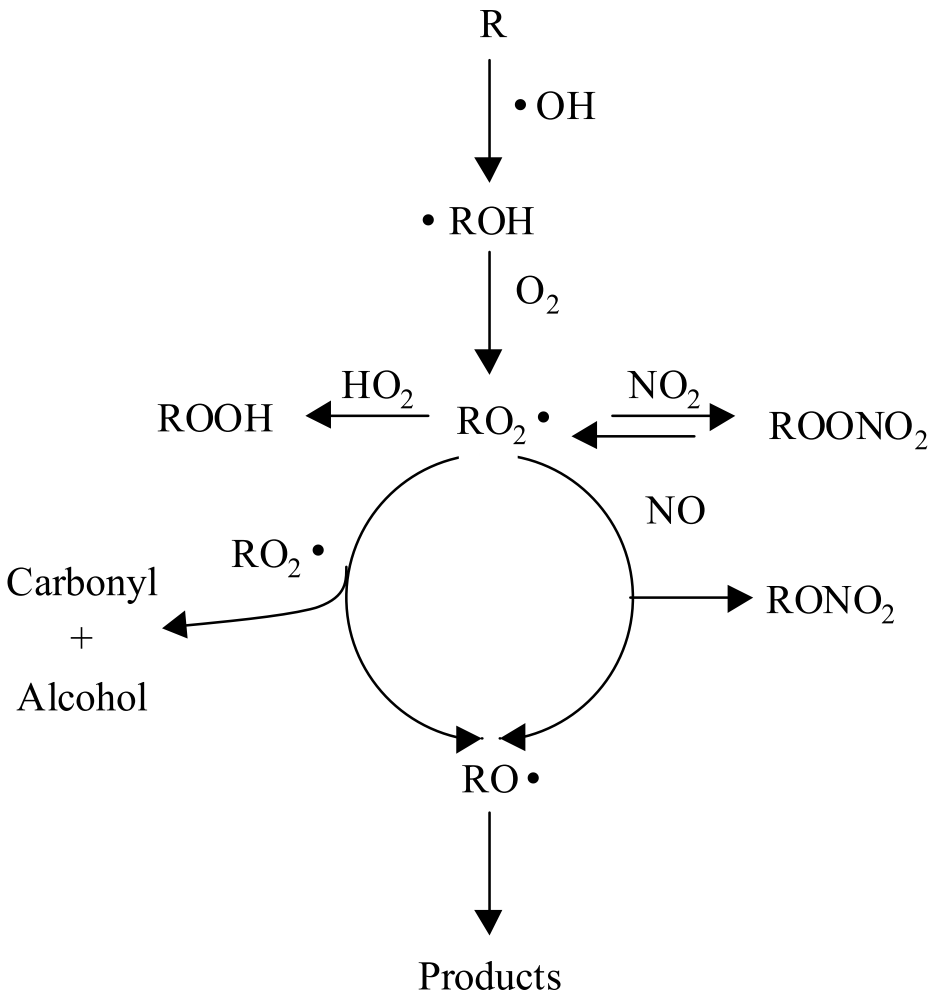

Figure I-I. The general photooxidation mechanism of unsaturated hydrocarbons in the troposphere. Adapted from Reaction Scheme 1 of Ref. 5.

It is noteworthy that a measure of the environmental impact of a particular VOC is based on the number of NO to NO_2 conversions, which take place during its oxidation cycle, such as in the reduction of a peroxy radical to an alkoxy radical. Every NO to NO_2 conversion leads to the formation of an ozone molecule with the following ground level ozone formation mechanism,

$$\begin{gathered} NO_2 + h\nu\,(\lambda < 430\,nm) \rightarrow NO + O, \\ O + O_2 + M \longrightarrow O_3 + M \end{gathered}, \tag{1-3}$$

where $h\nu$ is a photon, λ is the wavelength of light, and M is a collisional partner.[5]

The focus of our research has been on the development of a detailed oxidation mechanism of the early steps in the hydroxyl radical (OH) initiated of unsaturated hydrocarbons in the troposphere, employing both theoretical and experimental techniques. We have primarily been interested in the first few steps of the mechanism as these steps are deterministic when considering subsequent reactivity. In particular, the initial OH addition step strongly influences first generation end products. We have developed a robust model, from first principles, to predict reaction rates as a function of temperature and pressure for the addition rates of OH to unsaturated hydrocarbons and the branching for hydrocarbons with multiple unsaturated sites as discussed in Chapters II-IV. Additionally, we offer explanations of previously unexplained observed products in both remote measurements and smog chamber studies through elucidation of mechanistic details in the case of OH addition to conjugated unsaturated hydrocarbons as presented in Chapters V-VII. Chapters II-IV will present detailed documentation on the addition model and its development from inception to completion. Chapters V-VII are comprised of a variety of experimental techniques, complimented with theoretical applications, outlining the mechanistic details uncovered, which ultimately lead to the verification of the origins of the aforementioned observed products. Chapter VIII offers some concluding remarks as well as the future directions of this research.

CHAPTER II

INTRODUCTION TO THEORETICAL TREATMENTS[*]

A. Background

Electrophilic addition of OH to isoprene is the dominant mechanism under tropospheric conditions. Isotopomeric kinetics experiments (OD + C_5H_8 and OH + C_5D_8) performed by Campuzano-Jost et al.[15] determined that there are no kinetic isotope effects in the temperature regime relevant to the troposphere, (250-340 K) for the addition of OH to isoprene, confirming the dominant addition mechanism. OH addition to isoprene results in 4 distinct hydroxyalkyl radicals (**1-4**) as seen in Figure II-I, with an overall second order reaction rate constant of approximately $1x10^{-10}$ cm^3 $molecule^{-1}$ s^{-1} at 298 K.[3,15,16,17,18,19,20,21,22,23,24,25,26,27,28,29,30,31,32,33] Temperature dependent studies reveal a modest inverse temperature dependence for temperatures of tropospheric relevance.[3,15,20,23,25,29,33]

The atmospheric importance of this reaction has generated abundant experimental data as a function of both temperature and pressure. The advent of Pulsed Laval Nozzle measurements, including those of Spangenberg and co-workers,[30] allow an extension of ambient measurements to very low temperatures. The majority of the experiments performed focus on the high-pressure limit[15,17,18,19,21,22,23,24,25,27,29,30,32] with a few experiments performed in the 1-10 Torr range to examine fall-off behavior.[26,27,31,33] The branching ratio of isoprene-OH adducts (**1-4**) influences the distribution of first-generation end products. The generally accepted mechanism describing the subsequent reactivity of the hydroxyalkyl radicals in the presence of O_2 includes O_2 addition to all

---

[*] Parts of this chapter are preprinted with permission from "A Two Transition State Model for Radical-Molecule Reactions: Application to Isomeric Branching in the OH-Isoprene Reaction" Greenwald, E. E.; North, S. W.; Georgievskii, Y.; Klippenstein, S. J. *J. Phys. Chem. A* **2007**, submitted. Additional parts of this chapter are reprinted with permission from "A Two Transition State Model for Radical-Molecule Reactions: A Case Study of the Addition of OH to C_2H_4" Greenwald, E. E.; North, S. W.; Georgievskii, Y.; Klippenstein, S. J. *J. Phys. Chem. A.* **2005**, *109*, 6031.

four OH-isoprene adducts to form the corresponding peroxy radicals.[3,5,22,34,35,36] Recently, computational studies by Park et al. demonstrated that OH-isoprene adducts 2 and 3 react primarily via a prompt cyclic isomerization to produce α-hydroxyalkyl radicals which subsequently undergo hydrogen abstraction by O_2.[37]

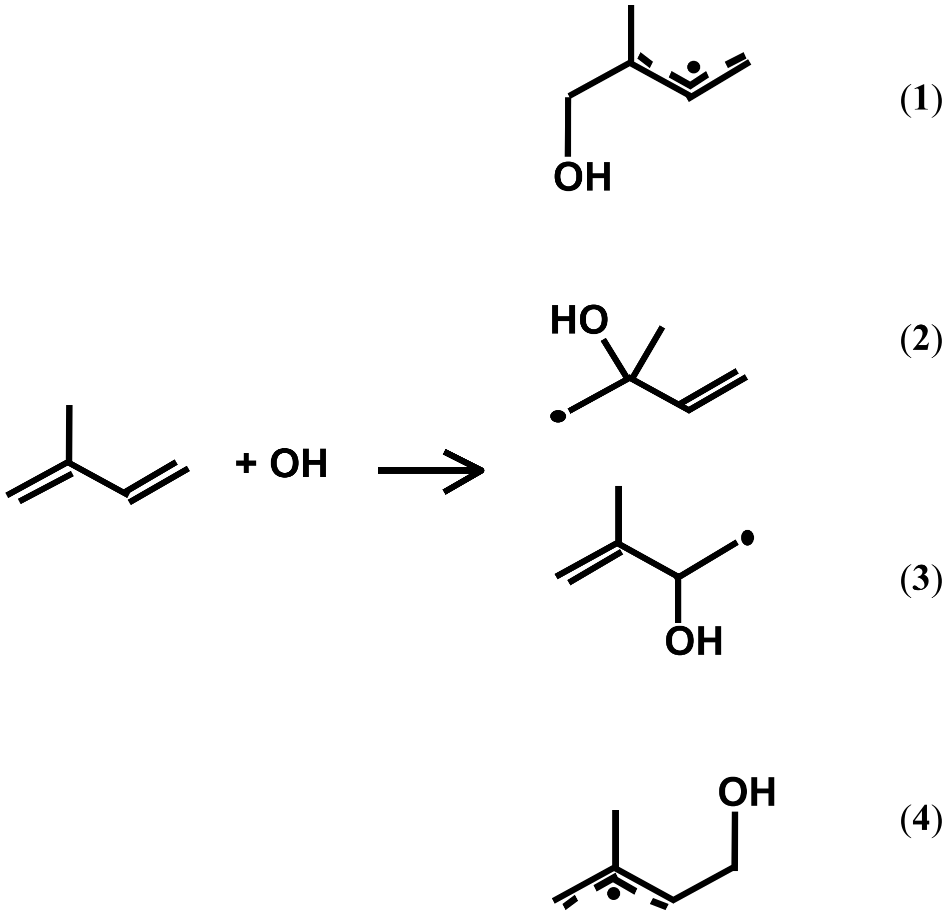

Figure II-I. Isomeric branching in the OH addition to isoprene. Adopted from first schematic of Ref. 38.

In order to explore this new chemistry, Greenwald et al. performed an isomeric-selective study for the case of OH addition to the inner position of butadiene (Chapter VI).[39] Isomeric selectivity was achieved by the preparation of a photolytic precursor, which, upon photolysis, formed the primary radical resulting from the OH addition to butadiene. The study supported the cyclic isomerization pathway and the computational predictions of Park et al. Subsequent work by Greenwald et al. to produce the isoprene-OH hydroxyalkyl radicals provides a more direct confirmation of this pathway in the case of isoprene oxidation (Chapter VII)[40] The addition of OH to one of the inner positions of isoprene will lead to primarily C5-carbonyl products and HO_2, both of which have been observed in the end product analysis of Lee et al.[35] and Paulson et al.[41] Therefore, verification of this pathway provides additional insight into the origins of observed products. Furthermore, these isomeric experiments provide a stringent test for theory.

Experimental determination of the branching ratio, however, has proven to be challenging. Almost all the analysis and interpretation of accurate experimental results is based on a branching ratio determined using structure additivity relationships (SAR) developed by Peeters et al.,[42] slightly adjusted to provide a fit to the data. SARs have been used to determine relative branching for the addition of hydroxyl radicals to a number of alkenes.[42,43] Several experimental studies have attempted to ascertain the branching ratio using OH cycling[28] or end-product distributions.[31,35] Theoretical studies also have been performed.[26,31,44,45]

Previous theoretical investigations of XC_2H_4 (X=O, F, Cl) performed by Peyerimhoff and coworkers[46] showed that multi-configurational treatments in electronic structure calculations greatly reduced the barrier to dissociation. In the case of FC_2H_4, the barrier to dissociation completely disappeared. This is contrary to the analysis employing the single-configurational SCF method, where a marked barrier of 65 kJ/mol is determined. Additional work performed by Espinosa-Garcia[47] on the association of OH and C_2H_4 showed that employing a PMP4sdtq/6-311+G(d,p)//MP4sdq/6-311+G(d,p)[MP2(full)/6-311+G(d,p)] level of theory locates a barrierless minimum energy path for the association. Variational canonical transition state theory rate calculations, performed in that work, reproduced reaction rates and the observed negative temperature dependence observed in experimental temperature dependent rate determinations.

Based on these findings, North and coworkers[26,45] modeled the association of OH and isoprene, employing variational canonical transition state theory on a barrierless Morse potential energy surface with excellent agreement with the high pressure limit experimental temperature dependent rate observations. This approach was later challenged by Vivier-Bunge and coworkers[44,48] when a historic pre-reactive complex model, developed by Singleton and Cvetanovic[49] for the association of oxygen atoms and ethylene, was adopted and applied to the association of OH with a variety of unsaturated hydrocarbons, including ethylene and isoprene. This model involves a van der Waals pre-reactive complex found in a shallow well between separated products and the transition state to adduct formation, as seen in Figure II-II.

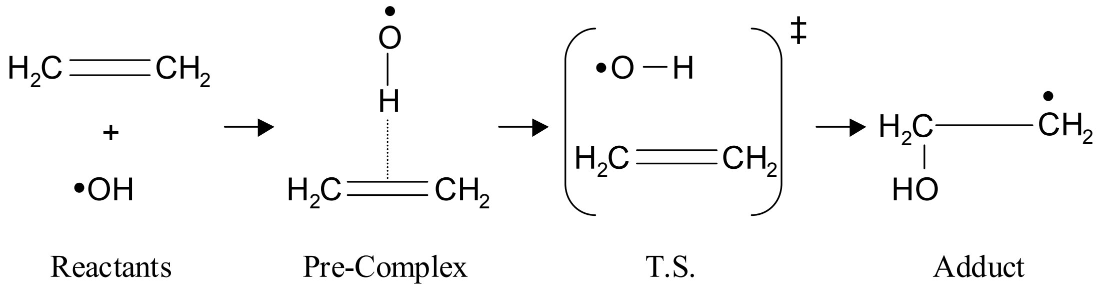

Figure II-II. Pre-reactive complex model for the association of OH to ethylene.

Comparisons to this model will be highlighted throughout Chapters III and IV. The implications for invoking this model, especially at the level of theory employed in the treatments by Vivier-Bunge and coworkers, are great. Firstly, the model relies on the applicability of canonical transition state theory. The shortcomings of this approach will be discussed in detail as applied to the association of OH to ethylene in Chapter III. Additionally, at the level of theory employed in that work, barriers are located above the reaction asymptote to formation of two of the four isoprene-OH adducts. This precludes formation of those adducts entirely at room temperature, which is contrary to experimental observations, as discussed in Chapter IV.

Discrepancies between the theoretical treatments led us to our own investigation of the kinetics. In order to probe the sensitivity of various aspects of treatment, we completed a comprehensive theoretical investigation of the hydroxyl radical initiated oxidation of ethylene. The addition of OH to ethylene represents the simplest example of this class of reactions and is, therefore, a benchmark system for understanding the underlying nature of these reactions. As a consequence, there have been numerous experimental[18,21,33,50,51,52,53,54,55,56,57,58,59,60,61,62,63,64,65,66,,67,68,69,70,71,72,73,74,75,76,77,78,79,80,81,82,83] and theoretical[47,48,84,85,86,87,88,89,90] studies of this reaction.

In the range of low to moderate temperatures, the mechanism is dominated by electrophilic addition of the hydroxyl radical to ethylene. At higher temperatures, the mechanism changes as first redissociation of the stabilized adduct becomes significant at about 450 K,[67] and then either abstraction and/or isomerization of the adduct to ethoxy radical, followed by further reaction, becomes significant at about 600 K.[74,75] Most of the experimental studies have focused on the observation of the thermal rate constants at room temperature or higher. Near room temperature the high-pressure limit is approached at pressures of about 1 atm.[67,68,82] The high pressure addition rate constant for C_2H_4 + OH was generally found to decrease slightly with increasing temperature in the 100 to 600 K range, with measured Arrhenius activation energies ranging from –2.3 to 0.0 kcal/mol.[56,64,67,74,82,83] Lower temperature studies have been limited to Leone and coworkers'[83] study over the temperature range from 96 to 296 K using the pulsed Laval nozzle technique. Although relatively low pressures were employed in this study (e.g., less than 1 Torr for the lower temperatures), it was argued that the results still pertained to the high pressure limit due to the increase in the lifetime of the complex with decreasing temperature. The combined experimental data over the 96 to 600 K range provides a stringent test for modern rate theory.

Our initial exploration of the C_2H_4OH system led us to probe the sensitivity of the potential energy surface using quantum chemical calculations. The remainder of this chapter highlights the findings in early considerations. Chapter III presents the two-transition state model in its final form and its predictions compared to a large set of experimental observations. In Chapter IV, we will present the extension of this model to the isoprene-OH system, and compare its predictions against a large set of experimental observations. Our model utilizes quantum chemical calculations, which have been carefully benchmarked as described in Chapter III, to provide the most accurate depiction of the present potential energy surface to date. A two-transition state model is applied to the rate predictions in order to include the effects of both the short-range, inner transition state and the outer transition state located on the long-range part of the potential. The application of this model involves RRKM/ME (RRKM/master equation) calculations at the energy, E, and angular momentum, *J*, resolved level to provide the most detailed kinetics analysis available for the isoprene-OH system as presented in Chapter IV.

B. Preliminary Exploration of the Potential Energy Surface (PES)

The focus of preliminary quantum chemical calculations was twofold. We were interested in how the level of theory employed affected the qualitative features of the PES and on how various fits to the reaction coordinate affected transition state theory calculations for the association of ethylene to OH. Our first exploration of the PES employed B3LYP/6-31G*[91,92] calculations, as implemented in the Gaussian 98 suite of programs,[93] to determine the OH-ethylene dissociation energy as a function of carbon-oxygen separation. The results of these calculations are displayed in Figure II-III.

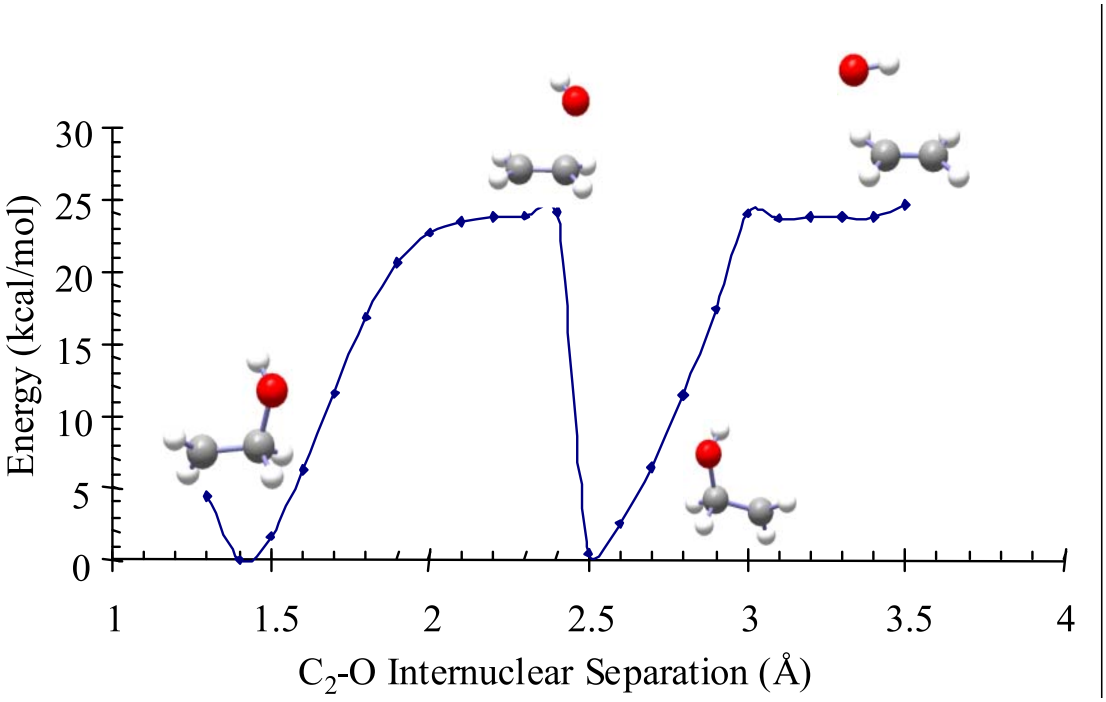

Figure II-III. Energy of the OH-ethylene adduct dissociation as a function of C-O separation in kcal/mol.

Starting with the fully optimized C_2H_4OH geometry, constrained geometry optimizations were performed, allowing full optimization of all coordinates except the C-O separation distance. As the carbon-oxygen bond is stretched, the energy increases monotonically, until a sudden drop in energy occurs around 2.5 Å separation. This drop in energy is associated with the carbon-oxygen bond between the initially bound carbon being of sufficient length for the oxygen to sample the deep well associated with binding to the other carbon in the ethylene molecule. A further increase in the C-O separation results in a rapid increase in energy, approaching the ethylene-OH infinite separation asymptote. Because we were interested in a global potential that stretched from the bound adduct to separate reactants, this constrained optimization method required the additional constraint of the C-C-O angle in order to restrict the sampling of the other deep well on the global potential.

A global PES as a function of C-O separation and C-C-O angle was then determined employing the B3LYP/6-31G* methodology. A three-dimensional plot of this energy as a function of C-O distance with a perpendicular approach of the OH moiety to the planar ethylene is shown in Figure II-III.

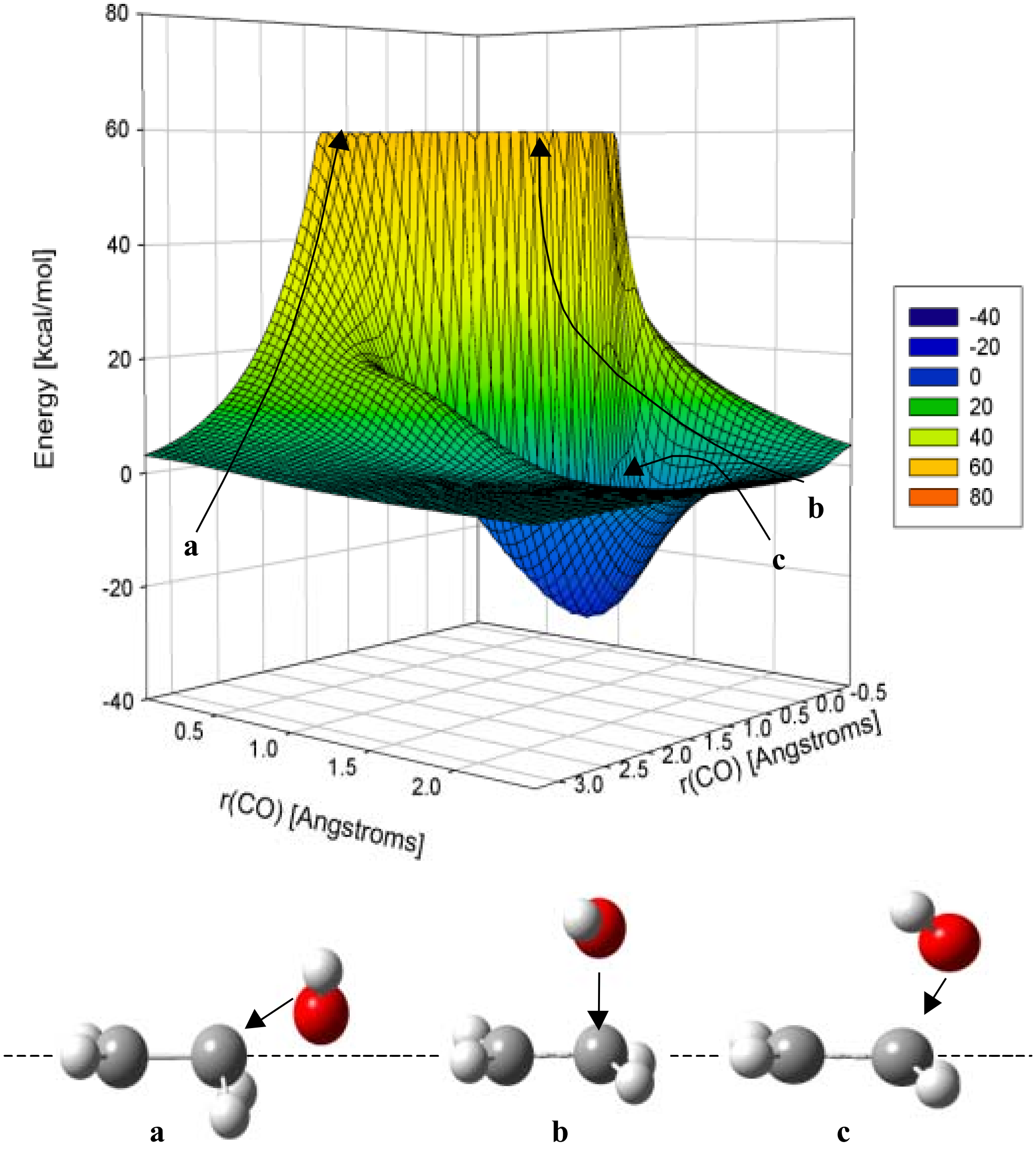

Figure II-IV. Three-dimensional PES for the association of C_2H_4 and OH, as a function of carbon-oxygen separation, spanning the angles of approach from 90 to 180°.

These calculations were performed as a series of geometry optimizations, where the C-O separation and the C-C-O angle were constrained and all other coordinates were optimized. Spline fits were then applied to the calculations to produce the smooth PES seen in Figure II-IV. Figure II-IV displays the energy of ethylene and OH as a function of C-O separation spanning the angles of approach from 90-180^o as illustrated in the molecular pictures below the Figure. The trajectory labeled **a** in the figure displays the angle of OH approach at approximately 170^o. This angle of approach is almost completely repulsive. Trajectory **b** shows the other extreme, where the OH angle of approach is approximately 90^o. Between the two extreme cases, C_2H_4OH adduct formation occurs into a deep well of approximately 32 kcal/mol as shown by the trajectory labeled **c**, at an angle of approach of approximately 110^o. This angle is illustrative of the rehybridization of the electronic structure of the carbon undergoing bonding. Thesp^2 electronic geometry of the planar ethylene must undergo rehybridization to the sp^3 electronic geometry of the bound adduct. At large angles of separation, there is a barrier to formation; however, as the angle decreases to approximately 110^o, a barrierless formation of the adduct occurs.

A series of calculations, employing different computational methodologies, was then applied to slice of this plot corresponding to the minimum energy pathway, i.e. the slice corresponding to the approximately 110^o angle of approach, as shown in Figure II-V.

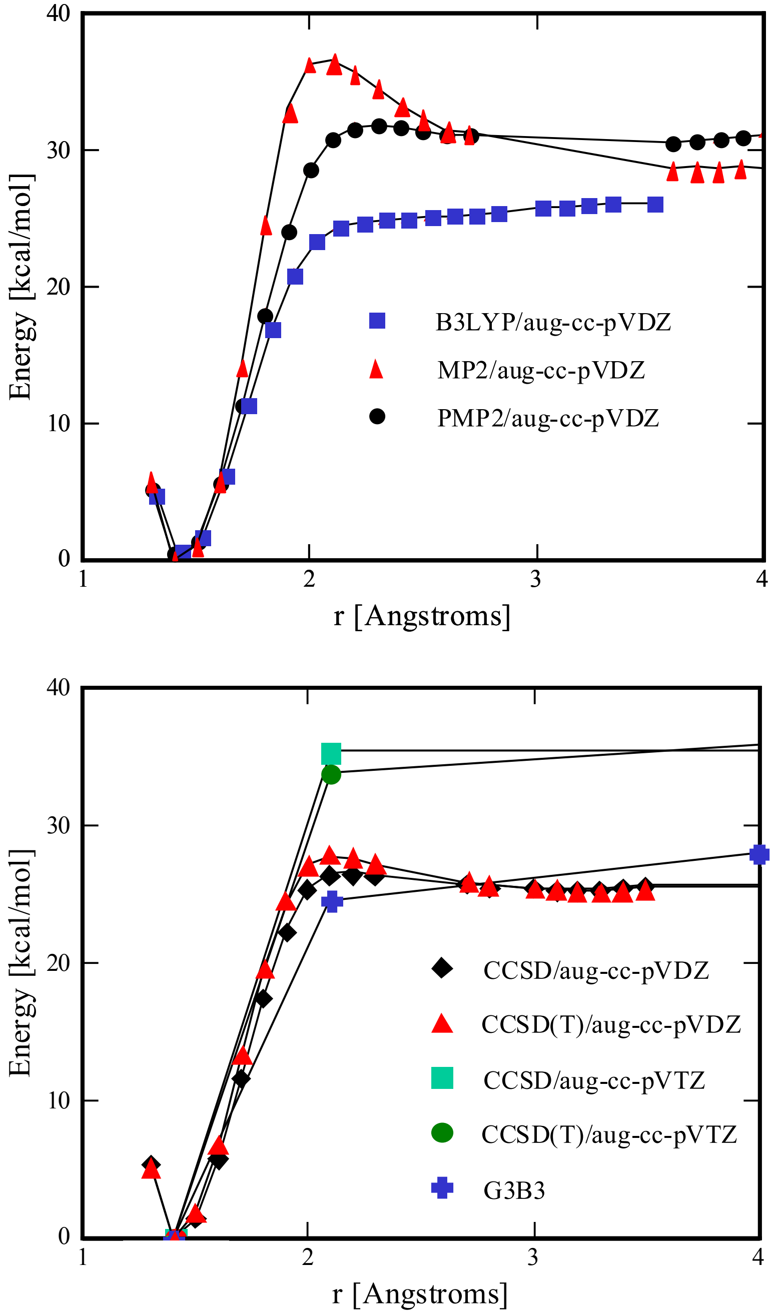

Figure II-V. PESs of the ethylene-OH adduct dissociation as a function of C-O separation along the angle of approach corresponding to the minimum energy pathway employing a variety of methodologies.

From Figure II-III, it is clear that the binding energy of the C_2H_4OH adduct depends on the quantum chemical methodology employed. Additionally, the presence or absence and absolute height of a barrier to formation depends on the computational methodology. Throughout the literature, a variety of computational schemes are used in the case of OH addition to ethylene. It is not obvious *a priori* which calculations most accurately depict the true PES. The test of the accuracy of the PES lies with the reproducibility of experimentally observed reaction rates under varying conditions of temperature and pressure.

C. Preliminary Exploration of the Kinetics

The simplest functional form by which to describe the energy, V(r), of the breaking of a chemical bond is given by an anharmonic Morse oscillator:

$$V(r) = D_e\left[\exp\{r_e - r\} - 1\right]^2 \qquad (2\text{-}1)$$

where r is the length of the bond, D_e is the binding energy of the adduct, r_e is the bond length of the equilibrium geometry, and β is the parameter that describes the tightness of the oscillator given by,

$$\beta = \omega\left[\frac{4\pi^2\mu c}{2hD_e}\right]^{\frac{1}{2}} \qquad (2\text{-}2)$$

where ω is the frequency of the bond, c is the speed of light, h is Plank's constant, and μ is the reduced mass of the system, given by,

$$\mu = \frac{m_1 m_2}{m_1 + m_2} \qquad (2\text{-}3)$$

where m_1 and m_2 are the masses of the moieties separating along the bond being broken. Much effort has been devoted over time to establishing the most realistic potential energy surface by which to describe the breaking of a chemical bond. The spoils of these efforts include other potential energy surfaces such as modified Morse potentials and the Varshni potential. A detailed review of these and many more functions describing potential energy surfaces can be found in a Ref. 94. The Varshni potential tends to be a stiffer, i.e. to approach the asymptotic energy at a faster rate. The Varshni potential utilizes the same terms (except for β) and is given by,

$$V(r) = D_e\left[1 - \frac{r_e}{r}\exp\left\{-\beta\left(r^2 - r_e^2\right)\right\}\right]^2 \quad . \tag{2-4}$$

where

$$\beta = \frac{1}{2r_e}\beta_{morse} - \frac{1}{r_e} \tag{2-5}$$

An extended Morse provides a good fit to quantum chemical calculations, therefor providing an analytical functional form for the calculated PES. The extended Morse function is given by an infinite sum, though in practice, can be truncated after the first few terms and is given by,

$$V(r) = D_e\sum_{i=2}^{\infty} n_i\left[\exp\left\{-\beta\left(r_e - r\right)\right\} - 1\right]^i \tag{2-6}$$

where the n_i's and β are a fitting parameters.

Analytical forms for the PES of ethylene addition to OH were determined employing Morse and Varshni functions determined as described by Eq. (2-1) – Eq. (2-5). Additionally, Morse, Varshni, and extended Morse potentials were employed, where non-linear least squares fits, varying D_e and β (and the n_i's in the case of the extended Morse), to the B3LYP/aug-cc-pVDZ calculations were performed. Plots in all cases can be seen compared to the B3LYP/aug-cc-pVDZ calculations in Figure II-VI.

The top panel of Figure II-VI gives the applications of the Morse potentials, where the lower panel displays the results employing the Varshni potential. All of the applications of the functional forms are in good agreement with the harmonic oscillator like part of the potential. The Morse and Varshni potentials calculated from first principles, as well as the fit of to the Extended Morse, approach the correct asymptotic energy, although the fit to the intermediate energies employing the Morse and Varshni potentials is poor. When allowing the parameters of both functional forms to float in order to determine a best fit to the available calculations, improvement is seen in both cases at intermediate energies, however, this improvement is at the expense of accurate asymptotic energy. The extended Morse potential, employing the first 5 terms, provides a very good fit to the data.

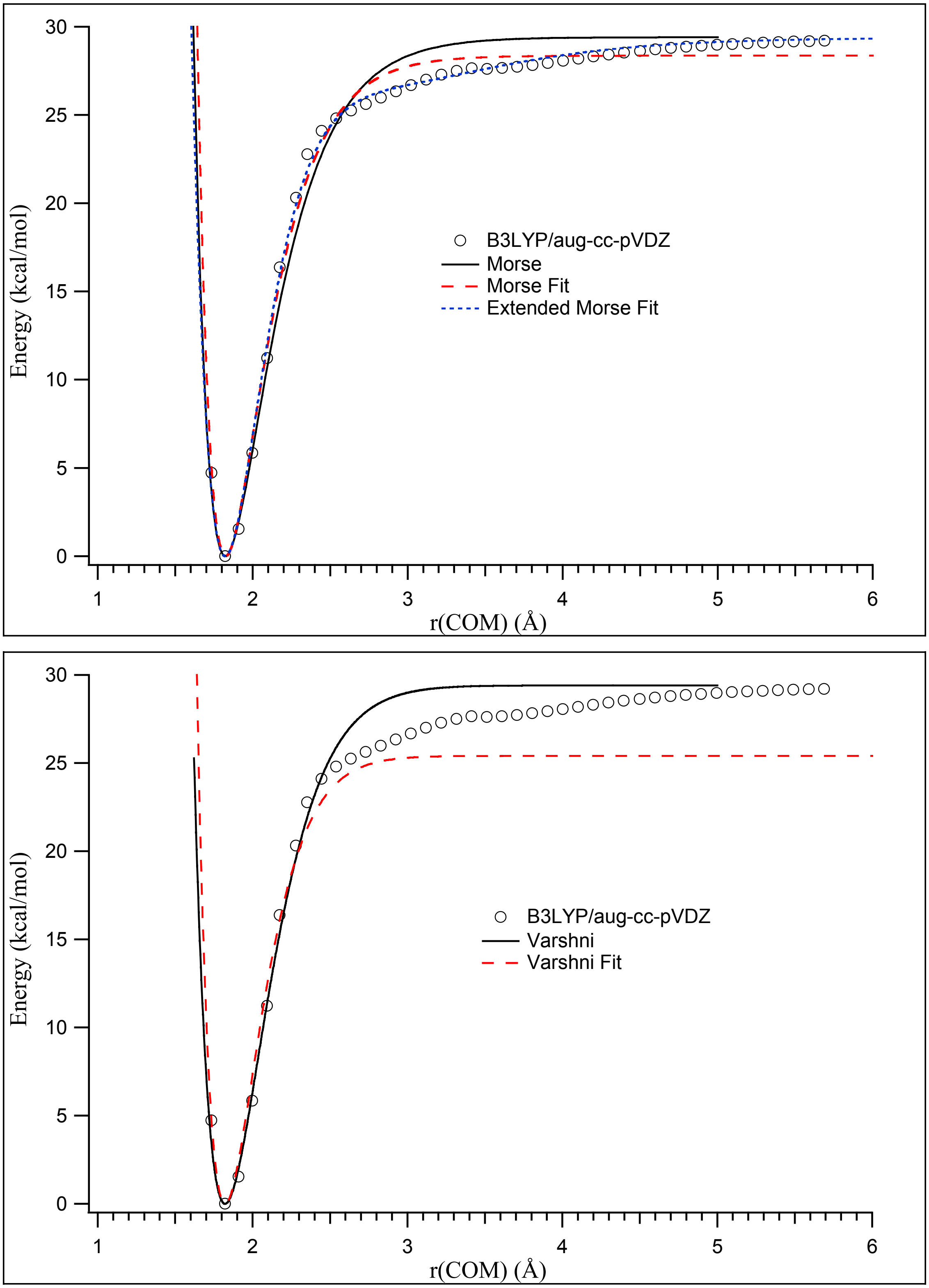

Figure II-VI. Function forms of the PESs for the ethylene + OH system.

In order to establish the sensitivity of the rate constants to the chosen functional form, we performed variational canonical transition state theory (cvTST) rate calculations employing the 3 analytically fit potential energy surfaces. The canonical transition state theory rate constant, *k(T)*, (i.e. employing a canonical ensemble of molecules) is given by,

$$k(T) = \frac{k_b T}{h} \frac{Q^{\ddagger}}{Q_{react}} \exp\left\{ \frac{-E_o}{k_b T} \right\} \qquad (2\text{-}7)$$

where k_b is the Boltzmann constant, T is the temperature, h is Plank's constant, $Q^{\ddagger}$ is the partition function for the transition state, Q_{react} is the product of the reactant molecule partition functions, and E_o is the threshold energy for the reaction. The total partition function, Q, for a reactant molecule or the transition state structure is the product of the translational, rotational, vibrational, electronic, and nuclear partition functions,

$$Q = q_t q_r q_v q_e q_n \qquad (2\text{-}8)$$

where the individual canonical partition functions are given in practical application by,

$$\begin{aligned} q_t &= \frac{k_b T}{m} \left(\frac{2\pi m k_b T}{h^2} \right)^{\frac{3}{2}} \\ q_r &= \frac{(k_b T)^{\frac{3}{2}}}{\sigma} \left(\frac{\pi}{ABC} \right)^{\frac{1}{2}} \\ q_v &= \prod_{i=1}^{n} \left[\frac{\exp\left\{ -\frac{h\nu}{2k_b T} \right\}}{1 - \exp\left\{ -\frac{h\nu}{k_b T} \right\}} \right] \\ q_e &= g_i, \qquad q_n = g_i \end{aligned} \qquad (2\text{-}9)$$

where k_b is the Boltzmann constant, T is the temperature, m is the mass, h is Plank's constant, σ is rotational symmetry number, A, B, and C are the rotational constants of a three-dimensional rotor, n is the number of normal modes of a reactant or the number of normal modes minus one for a transition state, ν is vibrational frequency, and g_i is the electronic or nuclear degeneracy. These partition functions are given employing some approximations to yield practical forms applicable to most chemical systems at about 100 K and higher in temperature.

As all of the above PESs are monotonically increasing, a cvTST treatment was employed. The variational principle states that the most accurate solution is the minimum solution. In other words, the most accurate rate of reaction given a particular potential energy surface is the minimum rate as a function of reaction coordinate. In practical application, for a particular temperature, one should evaluate the TST rate as a function of reaction coordinate and find the minimum rate. This minimum rate determines the thermal rate constant and the position along the reaction coordinate of the transition state.

In order to evaluate rate constants as a function of reaction coordinate, a cvTST code was written in C++ and is available in Appendix A. Rotational constants were determined as a function of reaction coordinate and fit using analytic expressions in order to smoothly evaluate rates over the breadth of the reaction coordinate. The rotational constants were fit using a simple exponential function for each. Vibrational frequencies as a function of reaction coordinate are displayed in Figure II-VII.

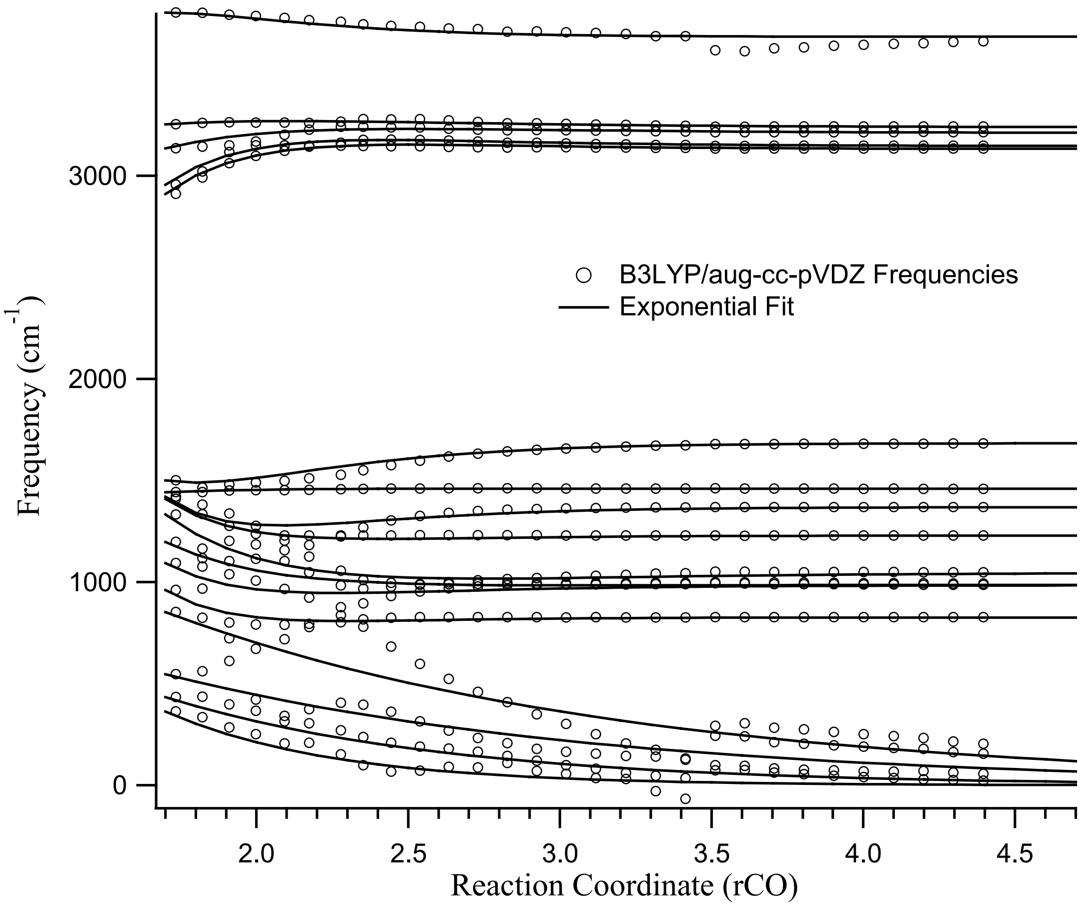

Figure II-VII. Vibrational frequencies determined at the B3LYP/aug-cc-pVDZ level of theory for the addition of OH to ethylene (symbols) overlaid with exponential switching function fits.

Vibrational frequencies are evaluated using quantum chemical calculations and listed in those calculations in descending order. The ordering of the frequencies along the reaction coordinate of interest are not maintained in an order that allows one to easily follow the transitions of the frequencies along the reaction coordinate. For a dissociating molecule, the number of modes remaining in the products are called the conserved modes and will maintain similar values between the reactant molecule and the product molecules in many cases, i.e. in the case of one of the C-H stretches in the C_2H_4OH adduct and the same C-H stretch in the separated ethylene. A number of modes will be disappearing modes. For example, the C_2H_4OH adduct has 18 normal modes, whereas the separated ethylene and OH have a combined 13 normal modes. One of the vanishing degrees of freedom describes the reaction coordinate, and the other 4 will disappear. The following exponential switching function was used in order to switch the frequencies between those determined for the adduct (ν_1) to those determined for separated products (ν_2) or disappearing to zero,

$$\nu(x) = \nu_1 \exp\{-\alpha(x - r_e\} + \nu_2\left(1 - \exp\{-\beta(x - r_e)\}\right) \qquad (2\text{-}10)$$

where α and β are the fitting parameters listed in Table II-I for the case of C_2H_4OH dissociation.

The cvTST calculated rate constants, as a function of reaction coordinate, at 300 K employing the extended Morse potential, in the evaluation of the minimum rate and transition state location are displayed in Figure II-VIII and an Arrhenius plot of the temperature dependent rate constants on the same reaction coordinate are seen in Figure II-IX.

Table II-I. Parameters used in the exponential switching function analytical expression.

v_1	v_2	α	β
2910.0009	3132.27	2.61927	2.78676
2956.0783	3146.53	2.56445	2.74255
3134.9257	3210.72	2.02947	2.09956
853.1496	0	0.65516	0
961.4067	826.417	3.63613	3.1374
1093.1897	984.28	2.99551	2.50253
362.4206	0	1.79308	0
434.4672	0	1.08083	0
547.274	0	0.69205	0
1421.2938	1369.35	3.41877	2.77011
1443.2772	1459.52	1.86286	1.8791
1501.3554	1683.58	3.20227	2.71851
1197.1077	986.901	2.52784	2.33268
1331.8265	1045.52	2.27608	1.84723
1408.9505	1228.84	3.26779	2.92144
3252.4263	3238.65	1.92132	1.96181
3802.4607	3683.57	3.16968	3.27255

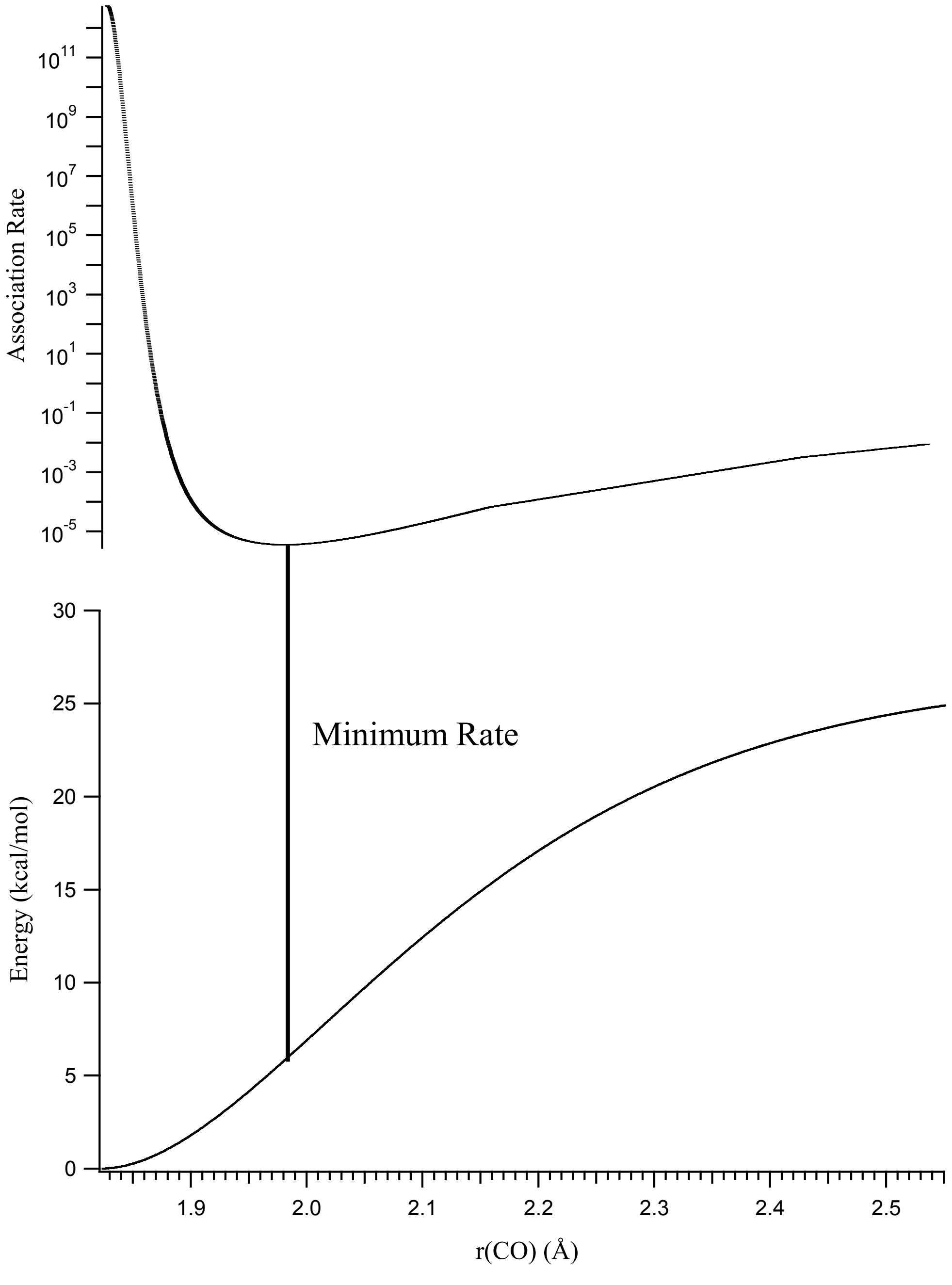

Figure II-VIII. The cvTST calculation as a function of reaction coordinate at 300 K employing the extended Morse potential energy surface.

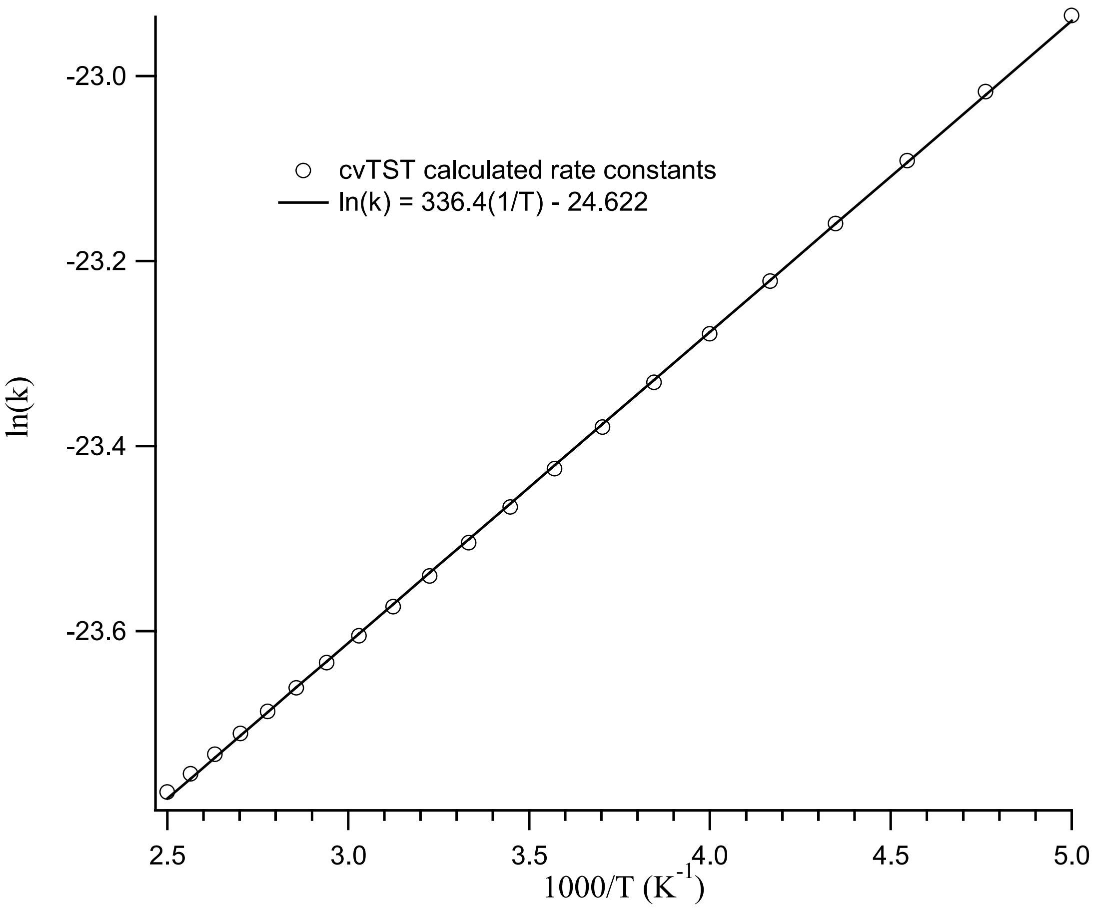

Figure II-IX. Arrhenius plot of the cvTST calculated rate constants as a function of Temperature employing the extended Morse PES.

Temperature dependent rate constants calculated using the cvTST code and evaluated on Morse, Varshni, and extended Morse PESs are summarized in Table II-II along with the corresponding experimental observations.

Table II-II: Computational and experimental rates of reaction and Arrhenius activation energies for the hydroxyl radical addition to ethylene.

	Computational	
	k(300 K) [$\text{cm}^3\text{molecule}^{-1}\text{s}^{-1}$]	Activation Energy [kcal/mol]
Morse	6.29×10^{-12}	0.54
Varshni	3.15×10^{-12}	0.05
Extended Morse	6.59×10^{-11}	-0.83

	Experimental	
	k(300 K) [$\text{cm}^3\text{molecule}^{-1}\text{s}^{-1}$]	Activation Energy [kcal/mol]
Ref. 95	8.8×10^{-12}	---
Ref.96	1.8×10^{-12} - 1×10^{-11}	-1.05*

* This represents an average reported Arrhenius activation energy.

The results outlined in Table II-II demonstrate the sensitivity of cvTST rate constants to the functional form of the employed PES. The Morse potential comes closest to the recommended rate constant of the 1997 NASA JPL publication;[95] however, temperature dependence disagrees with the observed inverse temperature dependence. While the rate constants calculated employing the extended Morse potential decrease with an increase in temperature, as is indicated by the negative value of the Arrhenius activation energy, the 300 K absolute rate constant is off by an order of magnitude. These results are a clear indicator that an accurate representation of the reaction kinetics for this class of reactions required a much more sophisticated treatment than was currently being employed. As such, we entered into a collaboration with Stephen Klippenstein and Yuri Georgievskii at Sandia National Laboratory to develop a more accurate approach to calculation of the reaction kinetics. The details of the two-transition state model developed in that collaboration are given in Chapter III. Based on the success with the C_2H_4OH system, the model was extended to the case of isomeric branching and reaction rates in the isoprene-OH system and the details of that study are given in Chapter IV.

CHAPTER III

HYDROXYL RADICAL INITIATED OXIDATION OF ETHYLENE: A TWO-TRANSITION STATE MODEL*

A. Background

Theoretical studies of the C_2H_4 + OH reaction have considered quantum chemical analyses of the stationary points on the potential energy surface[48,84,85,86,87,88,89,90] as well as transition state theory based analyses of the kinetics.,[48,85,87,88,90] The quantum chemical analyses have provided fairly detailed descriptions of the saddle point connecting the entrance van der Waals complex with the CH_2CH_2OH adduct, as well as mapping out the full reactive potential energy surface. The transition state theory analyses of the addition rate have focused on the effect of only this saddle point on the entrance channel kinetics.[48,85] Other aspects of the kinetics, such as the abstraction kinetics and the isomerization/dissociation kinetics of the initial adduct, have also been considered.[87,88,90]

The appearance of a negative activation energy in the experiments has been correlated with a negative energy of the entrance channel saddle point relative to reactants.[85] However, a negative value for the saddle point energy necessarily implies that, at least in some energy range near the reaction threshold, there is a second transition state at large separations. This "outer" transition state must provide the dominant bottleneck at low energies (or temperatures), while the "inner" transition state, located in the neighborhood of the saddle point, should provide the dominant bottleneck at higher energies (or temperatures). At intermediate temperatures, the bottlenecks in the flux through both the inner and the outer transition state will contribute to determining the

---

* Reprinted with permission from "A Two Transition State Model for Radical-Molecule Reactions: A Case Study of the Addition of OH to C_2H_4" Greenwald, E. E.; North, S. W.; Georgievskii, Y.; Klippenstein, S. J. *J. Phys. Chem. A.* **2005**, *109*, 6031.

overall rate and thus its temperature dependence. A proper rationalization of the negative activation energy must consider the combined effect of these two transition states.

The recent theoretical analysis of the C_2H_4 + OH reaction by Vivier-Bunge and coworkers,[48] building on earlier work of Singleton and Cvetanovic,[49] recognized the significance of the outer transition state preceding the van der Waals complex. Implementing a steady state assumption for the concentration of van der Waals complexes they suggested that the overall addition rate constant is given by

$$k = k_1 k_2 /(k_{-1} + k_2) \tag{3-1}$$

where k_1 and k_{-1} are the thermal rate constants for formation and decomposition of the van der Waals complex from reactants, while k_2 is the thermal rate constant for conversion of the van der Waals complex into the chemical adduct. Vivier-Bunge and coworkers then went on to derive expressions for the activation energy under the assumption that k_{-1} is much greater than k_2 and so the overall rate constant can be simplified to k_1k_2/k_{-1}.

There are multiple problems with this analysis. First, the assumption of $k_{-1} >> k_2$ is not valid in precisely the interesting temperature region where the two transition states provide a comparable bottleneck to the reactive flux. An even more fundamental flaw is that, the standard steady state analysis[97] leading to Eq. (3-1) is implemented at the *canonical* level, which in effect presumes that the van der Waals complexes have a thermal distribution of states. This thermal distribution would only arise if the van der Waals complexes suffer many collisions before reacting. The shallowness of the van der Waals wells suggests that this is seldom if ever true. As a result, Eq. (3-1), with thermal rate constants, is essentially never applicable.

A more appropriate assumption is that the dynamics in the region of the van der Waals complex occurs in a collision free environment with total energy, *E,* and total angular momentum, *J,* conserved.[98] The inner and outer transition states then act as a series of bottlenecks to reaction. A reasonable approximation to the effective flux through both transition states is given by

$$N^{\dagger}_{\text{eff}}\left(E,J\right) = N^{\dagger}_{\text{outer}}\left(E,J\right)N^{\dagger}_{\text{inner}}\left(E,J\right)/\left(N^{\dagger}_{\text{outer}}\left(E,J\right)+ N^{\dagger}_{\text{inner}}\left(E,J\right)\right), \qquad (3\text{-}2)$$

where $N_{\text{inner}}{}^{\dagger}$ and $N_{\text{outer}}{}^{\dagger}$ are the E and J resolved transition state numbers of states at the inner and outer transition states, respectively. In writing Eq. (3-2), we are presuming statistical probabilities for crossing each transition state dividing surface, and further that the maximum in the flux at the van der Waals minimum greatly exceeds that at the two transition states.[99,100] The "high pressure" addition rate constant for this effective transition state model is provided by the standard Boltzmann average of the effective transition state flux

$$k^{\infty}(T) = \frac{1}{hQ_{\text{reactants}}}\int N^{\dagger}_{\text{eff}}(E,J)\exp\left(-\frac{E}{k_B T}\right)dEdJ, \qquad (3\text{-}3)$$

where we are considering a pressure that yields a collision rate that is high relative to redissociation of the chemical adduct, but that is low relative to the dissociation of the van der Waals complex.

Now, in the limit where the flux through the outer bottleneck greatly exceeds that through the inner bottleneck, k^{∞} reduces to k_2, as it should. Note that the expression in Eq. (3-2) is closely related to that of Eq. (3-1), essentially involving the replacement of the canonical rate constants with E and J resolved rate constants. It corresponds to the implementation of a steady state assumption at the E and J resolved level. This replacement will prove to be of crucial importance to the proper modeling of the temperature dependence of the C_2H_4 + OH reaction, and of other related reactions.

In this chapter, we provide a detailed application of Eqs. (3-2) and (3-3) to the evaluation of the high-pressure addition rate constant for the C_2H_4 + OH reaction. In order to make proper comparisons with experiment we also implement Eq. (3-2) for the transition state flux within a 2-dimensional (in *E* and *J*) master equation analysis of the pressure dependence. Related two transition state models for radical molecule reactions were first considered by Benson and coworkers,[101] where they considered the effect of the transition states for an entrance and an exit channel acting in series. Subsequent studies by Rauk and coworkers[102] and by Rayez and coworkers[103] have applied this model to reactions with two separate transition states in the entrance channel, but with somewhat limited models for the outer transition state. Here, we build on these earlier works by applying more accurate, *a priori* models for both the inner and outer transition states, with a specific illustration to the C_2H_4 + OH reaction. The results from this study are of both specific and general interest. Notably, this two transition state picture has already proven to be essential to the quantitative understanding of the dynamics of barrierless reactions such as NC + NO[100] and $^1CH_2$ + CO,[104] where there is no inner saddle point and the presence of separate inner and outer transition states is less obvious.

The models we employ for the inner and the outer transition states are distinctly different. The outer transition state lies at large separations, beyond the van der Waals minimum, where only long-range interactions are important. Considerable effort has been devoted to the implementation of quantized versions of transition state theory[105,106] for such long-range potentials in order to obtain accurate estimates for the low temperature limit rate. Here, we are more interested in somewhat higher temperatures (e.g., above about 10 K), with our primary focus on understanding where the transition from the long-range to the short-range transition state occurs, and what the effects of this transition are. In this temperature regime, classical transition state theory based approaches should be appropriate. Thus, we implement a particularly simple, yet classically accurate, version of variational transition state theory appropriate in the limit of large transition state separations.[107]

The inner transition state is in the neighborhood of the saddle point on the potential energy surface. This saddle point arises as the chemical bond between the carbon and oxygen atoms begins to form, while the CC π bond begins to break. The interplay between these two chemical forces determines the precise location of the saddlepoint, which turns out to be at about 2.2 Å separation between the C and O for the C_2H_4 + OH reaction. At such short separations, the intermolecular forces between the ethylene and hydroxyl moieties are quite strong. As a result, a simple rigid-rotor harmonic-oscillator treatment of all but the HOCC torsional mode, which will be treated as a 1-dimensional hindered rotor, should provide a reasonably satisfactory treatment of the inner transition state. To illustrate this point we also present results for calculations involving the direct evaluation of a classical phase space based representation of the inner transition state partition function. The latter calculations provide a quantitative treatment of the full anharmonicities and couplings of the interfragment modes. Sophisticated ab initio methodologies are employed here in analyzing the energy of the saddlepoint and in obtaining appropriate vibrational frequencies and torsional potentials. For completeness, we also incorporate a variational reaction path treatment of this inner transition state region. However, for the temperatures of interest here, such variational effects are found to be minimal.

The computational methodologies employed for both the *ab initio* determinations, and for the kinetics evaluations are summarized in Sec. B. Then, in Sec C, the quantum chemical results and the predictions for the rate constant are presented and discussed. This discussion focuses on a comparison with experiment and on the effect of the transition from a dominant outer to a dominant inner transition state as the temperature rises. Some concluding remarks are provided in Sec. D.

B. Computational Methodology

Ab Initio Simulations. The focus of the present ab initio quantum chemical simulations is on the accurate evaluation of the rovibrational properties of the reactants, the products, and the reaction path from the inner transition state inwards. The highest level geometry optimizations performed here involve restricted open-shell quadratic configuration interaction calculations with perturbative inclusion of the triples contribution[108] (roQCISD(T)), employing Dunning-style, triple-ζ basis sets (cc-pVTZ).[109] These optimizations are computationally intensive and so were restricted to C_s symmetry. The actual saddlepoint appears to have C_1 symmetry, as does the equilibrium geometry of the adduct.

Both unrestricted second-order Møller-Plesset perturbation theory (uMP2)[110,111] and the unrestricted Becke-3 Lee-Yang-Parr (uB3LYP)[91] density functional were used to explore the reaction pathway in C_1 symmetry and to explore the vibrational properties. In particular, saddle points were located at both possible C_s symmetries and in C_1 symmetry with uMP2/cc-pVTZ calculations. Frequency calculations verified that the saddle point in C_1 symmetry was a first order saddle point (i.e., one imaginary frequency) and the saddle points in C_s symmetry were second order (i.e., two imaginary frequencies). The intrinsic reaction coordinate was followed in both directions (again at the uMP2/cc-pVTZ level) to ensure that the transition states connect reactants (the C_2H_4...OH van der Waal's adduct) to products (the C_2H_4OH molecular adduct). Projected vibrational frequencies were obtained along the pathway from the saddlepoints to the adduct at the same level of theory.

The saddle point vibrational frequencies were examined using molecular visualization to verify that the largest imaginary frequency corresponds to the reaction coordinate, while, in C_s symmetry, the other imaginary frequency corresponds to a symmetry breaking motion that will be treated separately as a 1-dimensional hindered rotor. The C_1 symmetry saddle point was found to have a CCOH dihedral angle of 17°. The torsional potential in the neighborhood of this C_1 saddle point is extremely flat, with the uMP2/cc-pVTZ energy difference between the C_1 and the lower of the C_s saddle points (CCOH dihedral angle of 0°) being less than 0.01 kcal/mol.

Higher level saddlepoint frequency estimates were obtained at the unrestricted QCISD(T)/6-311G** level for a CCOH dihedral angle of 0°. The uQCISD(T)/6-311G** optimizations resulted in a saddle point of a similar geometry to that at the roQCISD(T)/cc-pVTZ level; e.g., at a CO bond length of 2.103 Å versus 2.136 Å. The frequency calculations again suggest that the C_s saddle point is of second order, with the largest imaginary frequency corresponding to the reaction coordinate and the additional imaginary frequency corresponding to the symmetry breaking motion of the CCOH torsion. uQCISD(T)/6-311G** geometry optimizations and frequency calculations for the infinitely separated products were also performed.

The zero-point energy change from reactants to the saddlepoint is substantially greater at the uMP2/cc-pVTZ level (2.43 kcal/mol) than at the uQCISD(T)/6-311G** level (1.67 kcal/mol). This result is not too surprising when one considers the large spin contamination ($<S^2>$~1.00) in the wavefunction near the saddlepoint. Importantly, the QCISD(T) method is generally better able to handle the failures related to this spin contamination. Thus, the large difference strongly suggests some shortcoming in the uMP2/cc-pVTZ frequencies. Their implementation in transition state theory would result in inaccurate rate estimates, at least near room temperature and below, where a 0.8 kcal/mol energy difference correlates with a factor of four change in the rate. Notably, the two saddle point locations are quite similar, with the CO separation at the uMP2/cc-pVTZ level of 2.063 Å being only 0.040 Å shorter. Indeed, a reaction path projected frequency analyses suggests that the zero-point energy should change by only about 0.02 kcal/mol as a result of this difference in geometry. Furthermore, uMP2 evaluations with other basis sets indicate similarly increased zero-point differences, thereby indicating the inaccuracy is a fundamental flaw of second order Møller Plesset perturbation theory.

This apparent error in the uMP2 frequencies led us to also perform uB3LYP/6-311++G** frequency evaluations. The latter approach has only a minor spin contamination, with an $<S^2>$~0.77 at a CO separation of 2.2 Å. Furthermore, B3LYP density functional theory generally provides much more consistent and accurate vibrational frequencies than does MP2. The absence of a saddle point introduces some ambiguity in the uB3LYP frequency evaluations. We have evaluated projected frequencies at the optimized geometries corresponding to constrained CO distances and also at the geometries obtained from an intrinsic reaction coordinate analysis starting at the optimized geometry for a CO separation of 2.2 Å. The latter geometry is chosen as the starting point for the intrinsic reaction coordinate analysis because it represents our best estimate of the transition state location, as discussed below. The former approach assumes that the CO separation provides a good representation of the reaction coordinate in the neighborhood of the saddlepoint. The two approaches yield essentially identical frequencies when correlated by their CO separations, yielding some confidence in either approach.

Table III-I provides a comparison of the frequencies and zero-point energy differences obtained with the uB3LYP/6-311++G**, uMP2/cc-pVTZ, and uQCISD(T)/6-311G** methods. The uB3LYP/6-311++G** results are seen to correlate very well with the uQCISD(T)/6-311G** ones, while the correlation with the uMP2/cc-pVTZ results is not nearly as good. This correlation between the uB3LYP and uQCISD(T) frequencies strongly suggests that both are reasonable and that the uMP2 estimates are flawed. Thus, the uB3LYP/6-311++G** density functional should provide a computationally tractable, and yet accurate, approach for studying the projected frequencies along the reaction path in both C_s and C_1 symmetry. This approach was used in the final kinetics estimates for the inner transition state.

Final energy estimates for the saddle point, reactants, products, reaction path geometries, and van der Waals intermediate, were obtained by computing single point energies using roQCISD(T) calculations with the Dunning-style, triple-ζ and quadruple-ζ (cc-pVQZ) basis sets. These calculations were performed for the roQCISD(T)/cc-pVTZ C_s saddle point and reactant geometries and for all stationary points with the uB3LYP/6-311++G** geometries. Higher-level energies (E_{HL}) were estimated from an extrapolation to the infinite basis set limit via the expression[112,113]

$$E(\infty) = E(l_{\max}) - B/(l_{\max}+1)^4, \qquad (3\text{-}4)$$

where $l_{\max}$ represents the maximum angular momentum in the basis set and B is a fitting parameter. The cc-pVTZ and cc-pVQZ basis sets correspond to $l_{\max} = 3$ and 4, respectively.

Table III-I: Vibrational frequencies for the stationary points

Species	Method	Vibrational Frequencies[a]	ΔE_0 [b]
C_2H_4 + OH	uQCISD(T)/ 6-311G(d,p)	822, 889, 948, 1038, 1229, 1365, 1474, 1663, 3134, 3152, 3216, 3242, 3765	
	uMP2/ cc-pVTZ	827, 959, 983, 1076, 1246, 1384, 1485, 1685, 3180, 3198, 3269, 3295, 3824	
	uB3LYP/ 6-311++G**	835, 973, 976, 1058, 1238, 1377, 1471, 1683, 3122, 3137, 3194, 3223, 3709	
van der Waal's minimum	uB3LYP/ 6-311++G**	74, 104, 105, 280, 363, 836, 986, 994, 1067, 1239, 1377, 1474, 1678, 3123, 3136, 3196, 3224, 3616	1.25
	uMP2/ cc-pvTZ	76, 84, 115, 317, 354, 828, 975, 1000, 1082, 1248, 1383, 1487, 1678, 3180, 3196, 3269, 3295, 3752	
Saddle Point (τ=0)	uQCISD(T)/ 6-311G(d,p)	407i, 169i, 211, 367, 726, 822, 830, 953, 998, 1234, 1314, 1475, 1598, 3142, 3170, 3234, 3268, 3763	1.67
	uMP2/ cc-pVTZ	514i, 55i, 229, 410, 748, 841, 1005, 1069, 1128, 1264, 1388, 1496, 1685, 3201, 3226, 3296, 3329, 3800	2.43
	uB3LYP/ 6-311++G**	------, 82I, 190, 344, 642, 835, 919, 989, 995, 1239, 1333, 1474, 1585, 3132, 3161, 3217, 3257, 3746	1.51
Saddle Point (C_1)	uMP2/ cc-pVTZ	515i, 76, 231, 410, 749, 841, 1007, 1071, 1130, 1264, 1389, 1496, 1688, 3201, 3225, 3296, 3328, 3801	2.56
	uB3LYP/ 6-311++G**	------,105, 213, 348, 645, 832, 923, 973, 994, 1236, 1336, 1472, 1607, 3136, 3160, 3221, 3254, 3752	1.73
Saddle Point (τ=180°)	UMP2/ cc-pVTZ	626i, 188i, 196, 349, 765, 848, 996, 1037, 1104, 1271, 1368, 1495, 1654, 3205, 3213, 3298, 3324, 3802	2.16
	uB3LYP/ 6-311++G**	------,199i, 164, 289, 644, 839, 894, 963, 985, 1244, 1331, 1460, 1570, 3136, 3143, 3222, 3249, 3736	1.24
C_2H_4OH (C_1)	uB3LYP/ 6-311++G**	186, 345, 427, 560, 825, 949, 1077, 1119, 1178, 1354, 1395, 1452, 1483, 2975, 2995, 3136, 3245, 3818	3.60
C_2H_4OH (τ=0)	uB3LYP/ 6-311++G**	301i, 76, 389, 598, 803, 931, 1051, 1164, 1217, 1278, 1401, 1466, 1521, 3026, 3059, 3132, 3237, 3825	3.11
C_2H_4OH (τ=180°)	uB3LYP/ 6-311++G**	129, 254, 416, 484, 858, 951, 1067, 1101, 1214, 1267, 1414, 1456, 1488, 2887, 2954, 3150, 3263, 3843	2.96

[a] Vibrational frequencies in cm^{-1}. For uB3LYP saddle points the values are projected frequencies at R=2.2 Å because there is no saddle point.

[b] Change in zero-point energies from reactants to stationary point in kcal/mol.

Adapted from Table 1 of Ref. 114

The higher-level energy is then calculated from the expression

$$\begin{aligned} E_{\mathrm{HL}} &= E\left[\mathrm{QCISD(T)/cc-pVQZ}\right] + \\ &\quad \left\{E\left[\mathrm{QCISD(T)/cc-pVQZ}\right] - E\left[\mathrm{QCISD(T)/cc-pVTZ}\right]\right\} \times 0.69377 . \end{aligned} \qquad (3\text{-}5)$$

Alternative extrapolation schemes have been presented in the literature (see, e.g., Ref. 115 and its citations). Our experience with heats of formation for a large variety of C/O/H molecules and radicals suggests that the present formula is reasonably representative of any two-point formula and does yield near optimal agreement with experiment. Furthermore, since the extrapolation yields a correction of only 0.6 kcal/mol to the present saddle point energy, it is unlikely that any reasonable alternative extrapolation scheme would yield more than a 0.1 kcal/mol change in this quantity.

Both the spin contamination ($<S^2>\sim 1.00$) in the unrestricted Hartree-Fock evaluations and the Q1 diagnostic[116] (~0.03) in the roQCISD(T) evaluations at the saddle point suggest that there is either significant multi-reference character or dynamic correlation to the wavefunction in that region. As a result, there is somewhat increased uncertainty about the accuracy of a QCISD(T) based energy estimate. For this reason, we have also estimated the saddle point energy relative to reactants with internally contracted multi-reference configuration-interaction calculations with single and double excitations from a complete active space (CAS) self-consistent field (SCF) reference wavefunction. The roQCISD(T)/cc-pVTZ geometries were employed in these evaluations and the results for the cc-pVTZ and cc-pVQZ basis sets were extrapolated to the infinite basis set limit with an expression analogous to Eq. (3-5). Various active spaces were considered with the estimated saddle point energy generally decreasing somewhat with increasing number of active orbitals. The final calculations presented here are for a 7 electron 6 orbital CAS reference space consisting of the CC π and π^* orbitals (occupations of 1.91 and 0.09), the O radical (occupation of 1.00) and A" lone pair orbitals (occupations of 2.00), and the OH σ and σ^* orbitals (occupations of 1.98 and 0.02); where the stated occupations are for a CO separation of 2.2 Å.

A referee suggested that it may be interesting to compare with predictions from the CCSD(T) method. Our own experience is that, contrary to popular belief, the QCISD(T) method tends to provide better predictions than the CCSD(T) method. This is particularly notable when considering the dissociation of a molecule to form two doublet radicals, such as the dissociation of CH_4 to CH_3 + H. In this instance, both the QCISD(T) and CCSD(T) methods have an unphysical turnover in their dissociation curves at large separations. However, the failure for the QCISD(T) method arises at a significantly larger separation (i. e., ~3.2 versus ~2.8 Å). Nevertheless, we have performed CCSD(T)/cc-pVTZ calculations and find that it predicts an increase in the saddle point energy relative to reactants of 0.3 kcal/mol over that obtained at the QCISD(T) /cc-pVTZ level.

The torsional potential in the saddle point region is extremely flat, particularly in the region from the C_1 minimum to the 0° CCOH dihedral angle, τ. Indeed, it is not completely clear whether the true torsional minimum at the saddle point is of C_s or of C_1 symmetry. The high level calculations suggest the two energies differ by only 10 cm^{-1}. The uB3LYP/6-311++G** and uMP2/cc-pVTZ calculations predict very different CCOH dihedral angles of 50° and 17°, respectively.

The flatness of the potential between the minimum and $\tau=0°$, combined with the fairly significant torsional barrier at 180° (2.7 kcal/mol), implies that an accurate treatment of the contribution from the CCOH torsional motion to the transition state partition function requires a hindered rotor treatment based on a full torsional potential. Here, these potentials were based on 5 term cosine Fourier expansions designed to reproduce the three stationary point energies (τ = 0°, 50°, and 180°) and the vibrational frequencies at two of them (τ = 50°, and 180°). These Fourier expansions were obtained for each point along the uB3LYP/6-311++G** reaction path. The energies for the minima were obtained from higher level calculations according to Eq. (3-5), while the frequencies were obtained from uB3LYP/6-311++G** evaluations. Sample calculations on a grid of torsional values indicate that the Fourier expansion provides a very good representation of the torsional potential.

At large separations there are effectively two degenerate electronic states corresponding asymptotically with the $^2\Pi_{1/2}$ and $^2\Pi_{3/2}$ states of OH. Within C_s symmetry these two states correlate with A′ and A″ states, with the A′ state correlating with the ground state of the C_2H_4OH adduct, while the A″ state correlates with a repulsive excited state. At the intermediate separations of the inner transition state, the extent of the separation between these two states is unclear. To explore the possible importance of the A″ state we have optimized the geometry at various constrained CO separations with the uB3LYP/6-311++G** method and then performed higher level energy estimates according to Eq. (3-5).

The uB3LYP/6-31G* method was employed in the direct evaluation of the transitional mode contribution to the transition state partition function within the variable reaction coordinate formalism,[117] as discussed in more detail in the kinetics section. Corresponding reactant and saddle point vibrational analyses were also performed at the uB3LYP/6-31G* level in order to obtain reference rigid-rotor harmonic-oscillator based transition state theory results.

The quadrupole moment of ethylene and the dipole moment of OH are the key parameters in calculating the transition state partition functions for the outer transition state. Dipole moments of 1.68 and 1.69 Debye were evaluated with the uB3LYP/cc-pVQZ and uMP2/cc-pVQZ methods, respectively. These compare favorably with the experimental OH dipole moment of 1.66 Debye.[118] The same calculations yielded largest principle quadrupole moments[107] for C_2H_4 of 6.39 and 6.62 Debye Å, respectively; again agreeing well with the experimental value of 6.48 Debye Å.[119] The asymmetry in the quadrupole is very small, with the quadrupole moments for the other two axes being nearly identical.

All spin-restricted open-shell roQCISD(T) and multi-reference configuration-interaction calculations were carried out using the Molpro[120] quantum chemistry package. The remaining quantum chemical calculations were carried out using the Gaussian 98 suite of programs.[93]

Kinetics. Transition state theory (TST) is now being widely used for the *a priori* calculation of rates.[121] The application of TST to the present reaction, and to other radical-molecule reactions, where the saddle point on the addition path lies lower in energy than reactants, is complicated by the presence of two separate transition states. At low temperatures, the dominant transition state lies at large separations (the outer transition state), while at higher temperatures, the dominant transition state lies in the neighborhood of the saddle point (the inner transition state).

At large separations, the longest ranged term in the potential dominates and one may focus on just its effect on the kinetics. A recently described classical variational transition state theory treatment of the kinetics on long-range potentials is employed here.[107] For the addition of OH to C_2H_4, the dipole-quadrupole interaction provides the longest ranged interaction. For that case, the capture rate on the long-range potential is predicted to be[107]

$$k = C\left|dQ/\mu\right|^{1/2} \tag{3-6}$$

where d is the dipole moment of OH, Q is the largest principal quadrupole moment of C_2H_4, μ is the reduced mass for the C_2H_4, OH collision, and C=4.49 when all quantities are expressed in atomic units. This expression yields a temperature independent rate constant of $3.6\text{x}10^{-10}$ cm^3 molecule^{-1} s^{-1}. Related expressions provided in Ref. 107 allow for the straightforward evaluation of the energy, *E,* and total angular momentum, *J,* resolved transition state number of states. Importantly, the *E* and *J* resolved transition state number of states is what is implemented in the evaluation of the rate constant according to Eq. (3-2).

The two key assumptions in this approach are (i) that the long-range potential provides an adequate description of the intermolecular interactions in the transition state region and (ii) that the moment of inertia for the centrifugal motion of the two fragments greatly exceeds the moments of inertia of the two fragments. The first approximation usually fails at a larger separation than the second one, with a separation of 10 bohr providing a reasonable first approximation to where it begins to fail significantly.[122] For the dipole quadrupole potential, the canonical transition state location $R^\dagger$ is given by

$$R^\dagger = 0.91\left|dQ/T\right|^{1/4} \tag{3-7}$$

For C_2H_4 + OH this expression yields a transition state distance of 10 bohr at 71 K, implying that the long-range transition state treatment should be quite accurate for temperatures below that.

This temperature is somewhat lower than that at which the inner transition state becomes dominant (~130 K). However, it is more appropriate to consider the range of applicability at the microcanonical level. At the microcanonical level the transition state location is given by $1.17|dQ/E|^{1/4}$. For the present case, this implies that the transition state lies at a separation of 10 bohr at an energy of 0.39 kcal/mol. At the microcanonical level the inner and outer transition state numbers of states become equal at about 0.26 kcal/mol. Thus, the present long-range transition state treatment should be valid to beyond the crossing point of the two curves and thus should provide reasonable predictions for the current purposes. Furthermore, at even higher energies, the present treatment should still provide a semiquantitatively correct description of the flux at large separations.

Two quite different treatments of the inner transition state are considered here. The primary focus will be on a fairly standard approach based on direct summation over the rigid-rotor harmonic-oscillator (RRHO) energy levels. The parameters for these energy levels are determined from high level quantum chemical simulations at a number of points along the reaction path[123] as described above. For the CCOH torsional motion, a harmonic description is clearly of limited accuracy. Thus, a one-dimensional classical phase space integral based treatment, which is again quite standard, is instead employed for this mode. A Pitzer-Gwinn approximation is applied to approximately correct for quantum effects.[124,125] For completeness a one-dimensional, Eckart-based tunneling treatment is incorporated for the reaction coordinate in the evaluation of the inner transition state number of states. In reality, however, this tunneling, which occurs from the van der Waals complex to the molecular complex, is expected to be of little importance in this reaction, because the saddle point on the potential energy surface lies below reactants.

In a number of prior studies of barrierless radical-radical reactions we have considered fully anharmonic treatments of all the interfragment modes via classical phase space integration.[117,126] An important aspect of these prior analyses involved the consideration of multiple shapes (or reaction coordinates) for the transition state dividing surface. For the present radical-molecule case, the relatively short separation between the two reactants at the inner transition state (e.g., a CO separation of 2.2 Å at the saddle point) suggests that the simple harmonic-oscillator based description should be quite accurate. Nevertheless, it is interesting to study the extent of any anharmonic effects via the implementation of this variable reaction coordinate approach.

For the present application of the variable reaction coordinate (VRC) transition state theory (TST) approach, we employ the multi-faceted dividing surface (MDS) formalism described in Ref. 127. With this approach, the dividing surface is defined by a fixed distance *r* between sets of pivot points on each of the fragments. For the OH fragment the pivot point is taken to be at the O atom. For the C_2H_4 fragment four symmetry related pivot points are considered; with two pairs located a distance *d* above and below each C atom along a line perpendicular to the CC axis and passing through the C atom. For each different choice of *d* the distance *r* between the two pivot points is fixed so that the CO separation at the minimum energy point is effectively that of the high level saddle point (i.e., 2.2 Å). *d* values ranging from 0 to 2 bohr are considered here. These MDS-TST evaluations are performed with the direct evaluation of the interaction potential at the uB3LYP/6-31G* level. In order to make a proper comparison with the related RRHO based analyses, we have also repeated the transition state vibrational analyses with the same uB3LYP/6-31G* method.

In prior VRC-TST applications, we have generally considered the fragment geometries to be constrained to those at infinite separation, thereby neglecting any effects due to structural rearrangement of the fragments as they react. At the 2.2 Å separation of the present inner saddle point, it is not clear that this rearrangement can be ignored. Indeed, the results presented below clearly indicate that the structural relaxation is a key aspect of the analysis. Thus, we have also considered a novel implementation of the VRC-TST approach in which the internal structures of each fragment for each configuration sampled in the direct evaluation of the transition state configurational integrals are optimized as part of the energy analysis.

This calculation of the geometry relaxation energy of the fragments employs a novel iterative process based on the normal mode representation of the internal vibrational modes of the separated fragments. For a given overall configuration, at each step in the iteration, the Cartesian forces are evaluated analytically and transformed into internal fragment normal mode displacements using the normal modes of the fragments at infinite separation. These displacements were found to provide a reasonable description of the direction towards the potential energy minimum, but the distance to the minimum was generally overestimated. This deviation from the infinite separation quadratic model arises from both the change in the normal mode frequencies and geometries, and the distortion of the potential energy from the quadratic form due to the interaction between the fragments. This distortion is taken into account by introducing a scaling factor for the normal mode displacements, which itself is calculated iteratively so that the energy is approximately minimized along the previously found direction in the normal modes coordinates space.

This procedure is followed to convergence with the required convergence varying with the interaction strength. For configurations with a negative interaction energy (relative to infinitely separated fragments), a high degree of convergence is requested (e.g., ~0.1 kcal/mol), while for points that are modestly repulsive a more modest convergence is requested. Highly repulsive geometries make little contribution to the transition state partition function and no attempt is made to evaluate their relaxation energy. With this procedure, the direct evaluation of the relaxation energy only increased the computational time by about a factor of two.

The two bottlenecks to the reactive flux are combined to provide an effective transition state number of states $N^{\dagger}_{\mathrm{eff}}$ given by[99,100]

$$\frac{1}{N^{\dagger}_{\mathrm{eff}}} = \frac{1}{N^{\dagger}_{\mathrm{inner}}} + \frac{1}{N^{\dagger}_{\mathrm{outer}}} - \frac{1}{N_{\mathrm{max}}}. \tag{3-8}$$

This expression assumes ergodicity between the inner and outer transition state, with statistical probabilities for crossing a given transition state. The quantities $N^{\dagger}_{\mathrm{inner}}$ and $N^{\dagger}_{\mathrm{outer}}$ are the number of available states at the inner and outer transition states, respectively, while N_{max} is the maximum flux between the two transition states. Although the van der Waals complex is not very deep (~1.7 kcal/mol), in a relative sense it is much lower than the saddle point. Furthermore, the vibrational frequencies in the van der Waals complex are much lower than those at the saddlepoint. Thus, it is reasonable to neglect the term in N_{max}, which reduces Eq. (3-8) to Eq. (3-2).

All of the present transition state theory evaluations are carried out at the energy, *E,* and total angular momentum, *J,* resolved level. The high-pressure limit capture rate is then obtained via Eq. (3-3). The experimental studies of the addition process have largely been performed at pressures of about 1 bar or lower. At such pressures, there may be some deviation of the rate constant from the high-pressure limit. Thus, we have also considered a 2-dimensional master equation analysis of the temperature and pressure dependent kinetics. This master equation analysis is based on the methodology described in Ref. 128. An exponential down model of energy transfer and Lennard Jones collision rates are employed. The Lennard Jones parameters for C_2H_4OH, He, and N_2 were taken to be $\sigma = 4.46$, 3.68, and 2.58 Å and $\varepsilon = 390$, 92, and 10 K, respectively.

One subtlety in the evaluation of Eq. (3-2) involves the treatment of the rovibronic states in the two, nearly degenerate, electronic states of OH (and thus of the interacting fragments) within the evaluation of $N^{\dagger}_{\mathrm{inner}}$ and $N^{\dagger}_{\mathrm{outer}}$. In the inner transition state region the spin-orbit splitting is simply ignored, because it should be greatly reduced from its value at infinite separation. Furthermore, as illustrated below, the A′′

state is high enough in energy at the inner transition state that it can be ignored and only one electronic state is considered. Thus, for the inner transition state, the sole effect of the spin-orbit interactions of the OH radical is assumed to involve an increase in the calculated interaction energy by 70 cm^{-1}, correlating with the spin-orbit lowering of the asymptotic OH ground electronic state, because this splitting is ignored in the present ab initio simulations. The present evaluation of $N^{\dagger}_{\mathrm{outer}}$ effectively involves an electronically decoupled classical evaluation of the OH rotational partition functions. Furthermore, we presume, because the fragments are only weakly interacting at large separations, that the spin-orbit splitting of the OH radicals is geometry independent. The overall $N^{\dagger}_{\mathrm{outer}}$ then includes one contribution from each spin-orbit state, with that from the second spin-orbit state shifted up by the spin-orbit splitting.

At low temperatures, the electronically decoupled classical evaluation of $N^{\dagger}_{\mathrm{outer}}$ necessitates an equivalent evaluation of the free OH rovibronic partition function for use in Eq. (3-3). However, at higher temperatures, where the inner transition state is the dominant bottleneck, it is best to employ the correct free OH rovibronic partition function obtained from a direct summation over the coupled quantized rovibronic energy levels. Here, we employ the decoupled classical evaluation of the free OH partition function as a reference and then incorporate an *ad hoc* correction factor to interpolate between the correct high and low temperature limits. This correction factor is taken to be $[k_{\mathrm{inner}}{}' (T)\, k_{\mathrm{outer}} (T) / (k_{\mathrm{inner}}{}' (T) + k_{\mathrm{outer}} (T))] / [k_{\mathrm{inner}} (T)\, k_{\mathrm{outer}} (T) / (k_{\mathrm{inner}} (T) + k_{\mathrm{outer}} (T))]$ where $k_{\mathrm{inner}} (T)$ and $k_{\mathrm{outer}} (T)$ are evaluated with the decoupled classical OH partition function and $k_{\mathrm{inner}}{}'(T)$ is evaluated with the correct coupled quantum OH rovibronic partition function. This *ad hoc* correction factor is always less than unity and takes a minimum value of 0.78 at about 150 K. An improved treatment, involving, for example, quantized rovibronic energy evaluations in the outer transition state region, would not affect the conclusions reached below and was deemed beyond the scope of this work.

C. Results and Discussion

Potential Energy Surface. An illustrative plot of the lowest A′, A, and A′′ potential energy surfaces along the minimum energy path for various orientations is provided in Figure III-I. The results plotted in Figure III-I are from HL//B3LYP/6-311++G(d,p)[129] calculations and do not include zero-point energy corrections. The maximum on the A surface for the optimal τ value arises at R_{CO} = 2.2 Å, and is at –1.74 kcal/mol relative to reactants. This A state correlates with the A′ state in C_s symmetry. At this separation the A′′ state is more than 10 kcal/mol higher in energy, clearly indicating the irrelevance of the A′′ state to the flux through the inner transition state.

In the neighborhood of the saddle point the τ=0 and τ~50° potential values are nearly equivalent, while the τ=180° value is about 3 kcal/mol higher. A more detailed plot of the torsional dependence of the potential in the neighborhood of the saddlepoint is provided in Figure III-II. The torsional potential gradually develops a sharper minimum near τ=50° as the CO separation decreases. At the equilibrium CH_2CH_2OH geometry the potential for the optimal torsional angle of 53.5° is 1.35 kcal/mol lower in energy than that for τ=0. In contrast, for the transition state separation, R_{CO} = 2.2 Å, it is not completely clear whether the minimum is at 0 or at 50°. The extraordinarily flat behavior f the torsional potential from zero to 50°, coupled with the stronger dependence from 50° to 180°, strongly suggests that a harmonic treatment of this mode would be inadequate.

The present HL predictions for the zero-point corrected energies of the key stationary points are summarized in Table III-II, along with the results of other high level calculations from Refs. 89 and 86. Also included therein are the Q1 diagnostics for the QCISD(T)//B3LYP calculations. The geometries corresponding to these stationary points are illustrated schematically in Fig. III-III, with the relevant geometric parameters.[130]

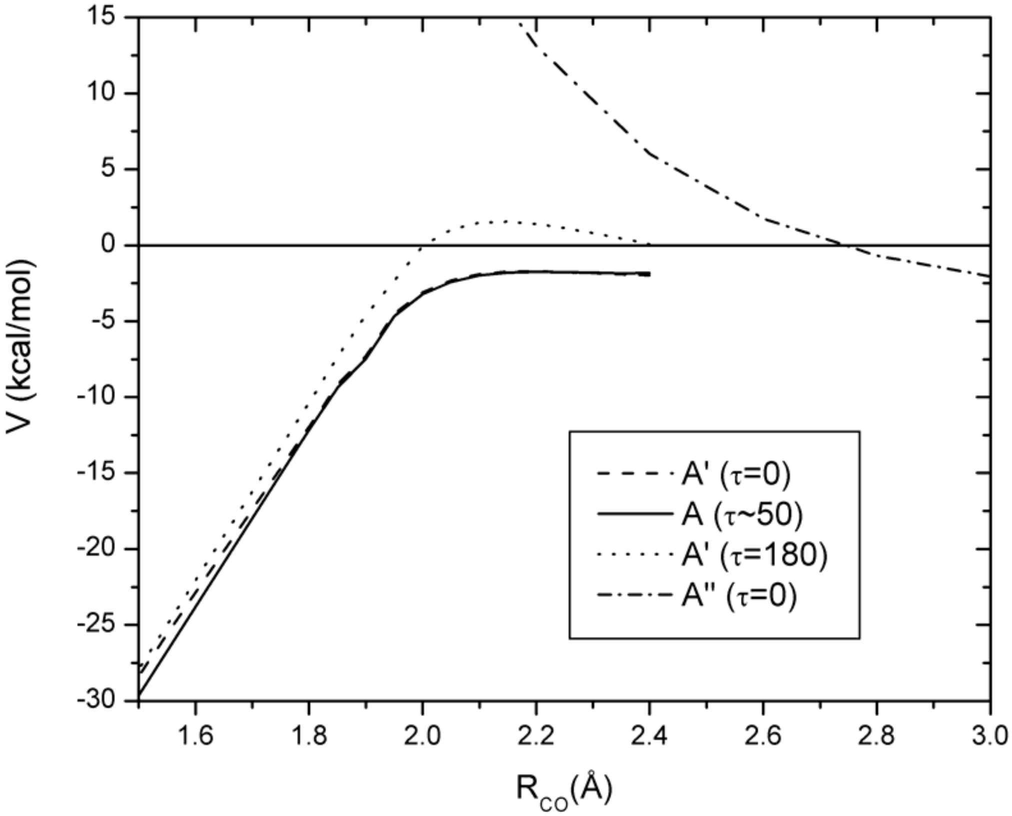

Figure III-I. Plot of the minimum energy path potentials from HL//B3LYP calculations as a function of the constrained CO separation for the A' surface with τ = 0° and 180°, for the A'' surface with τ = 0°, and for the ground state with an optimized τ value of ~50°. Adapted from Figure 1 of Ref. 114

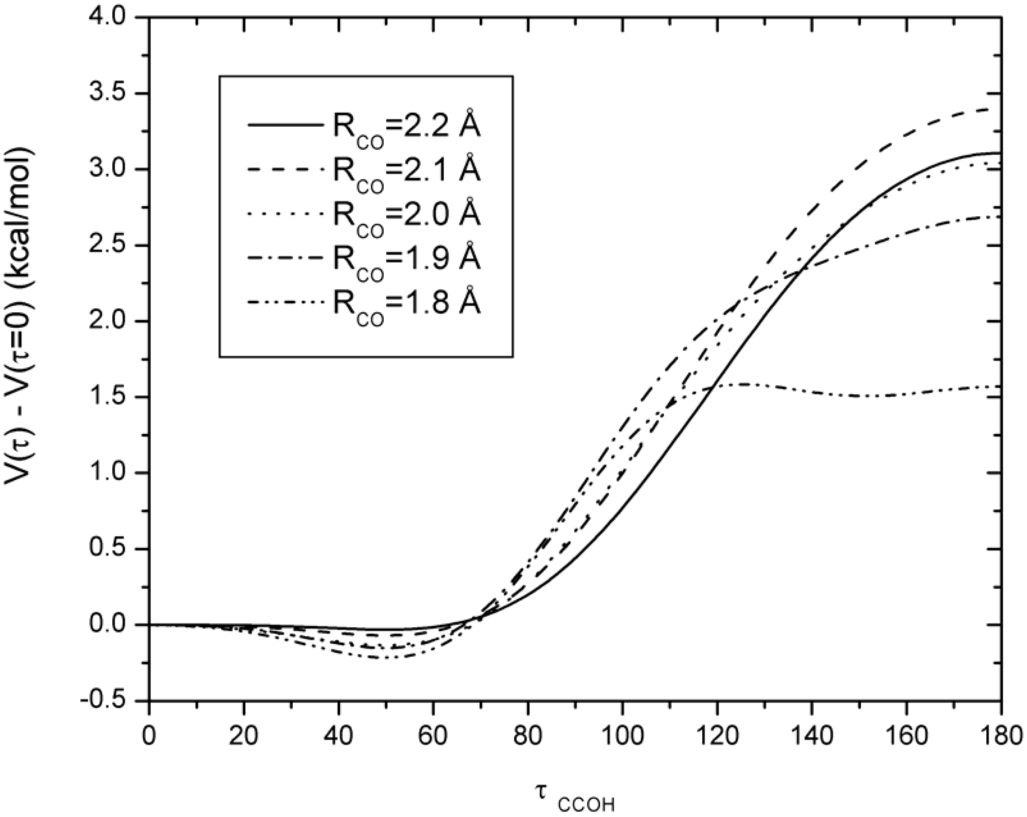

Figure III-II. Plot of the HL//B3LYP CCOH torsional potential for a number of constrained CO separations. Adapted from Figure 2 of Ref. 114.

Table III-II: Stationary point energies[a]

Species	B3LYP[b]	HL// B3LYP[c]	HL// QCISD(T)[d]	G2[e]	BAC-G2[f]	CBS-Q[g]	Q1 Diag.[h]
van der Waal's min.	-1.35	-1.70	-1.72	-2.07	-2.06	-1.94	0.010
Saddle Point (C_1)	-3.52	-0.01		-1.23 *1.39*	-2.00	-2.90	0.026
Saddle Point (τ=0)	-3.61	-0.20	-0.38 (-0.30)[i]				0.026
Saddle Point (τ=180°)	-0.98	3.02					0.026
C_2H_4OH (C_1)	-24.61	-26.98		-26.5 *-26.0*	-26.4	-26.9	0.012
C_2H_4OH (τ=0)	-23.44	-26.12	-26.15				0.012
C_2H_4OH (τ=180°)	-22.88	-25.52					0.010

[a] All energies in kcal/mol relative to C_2H_4 + OH including uB3LYP/6-311++G(d,p) zero-point corrections.

[b] uB3LYP/6-311++G(d,p) energies.

[c] Basis set extrapolated roQCISD(T) energies (cf. Eq. (3-5)) evaluated at the uB3LYP/6-311++G(d,p) geometry. For the saddle point the R_{CO}=2.2 Å constrained uB3LYP/6-311++G(d,p) optimized geometry is used, which corresponds to the maximum in the HL//B3LYP/6-311++G(d,p) minimum energy path potential.

[d] Basis set extrapolated roQCISD(T) energies (cf. Eq. (3-5)) evaluated at the roQCISD(T)/cc-pVTZ geometry.

[e] G2 energies from Ref. 89 and Ref. 86, with the latter in italics.

[f] BAC-G2 energies from Ref. 89.

[g] CBS-Q energies from Ref. 89.

[h] Q1 diagnostic for roQCISD(T)/cc-pvqz//B3LYP/6-311++G(d,p) calculation. For comparison the C_2H_4 and OH values are 0.011 and 0.009, respectively.

[i] The number in parentheses denotes the maximum along the distinguished reaction path obtained from R_{CO} constrained optimizations with the roQCISD(T)/cc-pvtz method.

Adapted from Table 2 of Ref. 114.

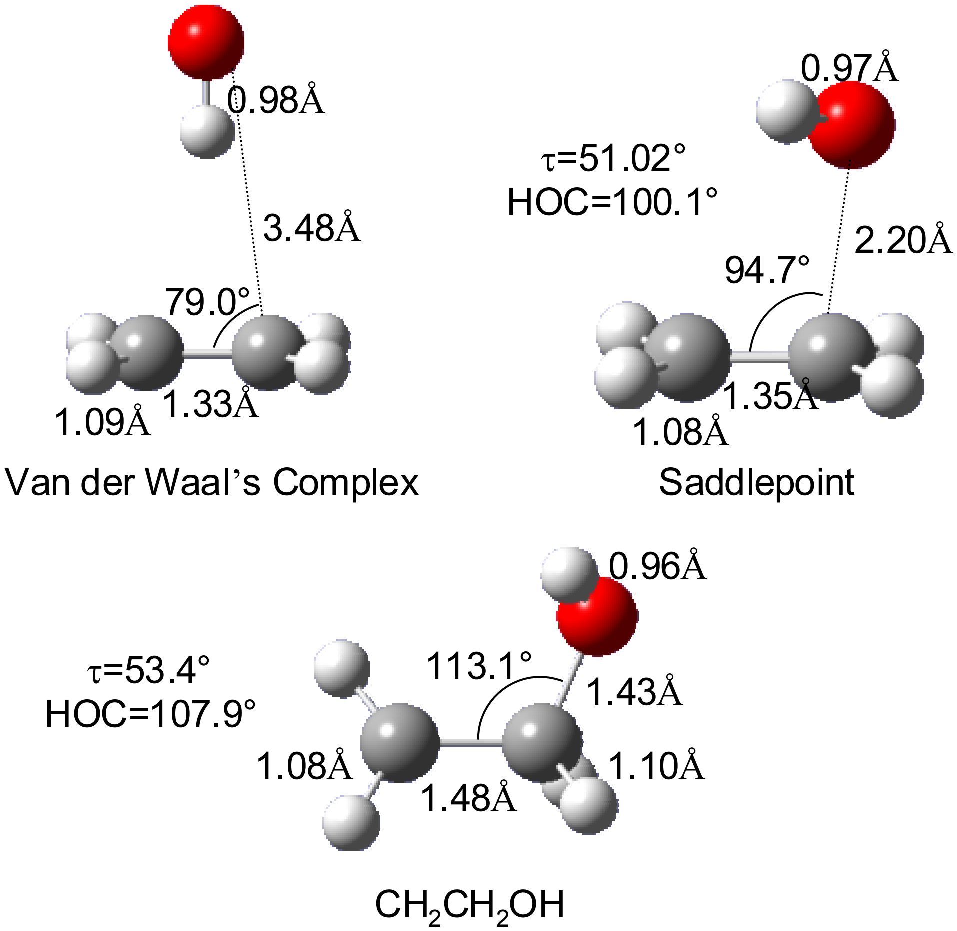

Figure III-III. Illustration of the uB3LYP/6-311++G** optimized geometries for the van der Waal's minimum, the optimized geometry for C_1 symmetry at R_{CO} = 2.2 Å, and for the C_2H_4OH molecular complex. Adapted from Figure 3 of Ref. 114.

The two HL predictions for the saddle point and C_2H_4OH energies in C_s symmetry are in good agreement. Notably, the HL//B3LYP prediction for the saddlepoint energy is higher for the C_1 geometry than for the τ=0° geometry. This result is primarily due to the inclusion of the zero-point energy for the torsional mode in the C_1 estimate but not in the τ=0° estimate, because the harmonic frequency for the latter is imaginary. The best estimate for the saddle point energy from the present calculations is –0.1 kcal/mol, which is obtained from the HL//roQCISD(T) calculation for τ=0°, added to the difference between the HL//B3LYP predictions for τ~50° and τ=0°. This estimate also includes a spin-orbit lowering of the ground reactant state by 70 cm^{-1} and a reduction in the saddle point energy by the harmonic zero-point energy for the torsional mode (52 cm^{-1}), because an anharmonic treatment would likely yield a frequency close to zero.

The G2, BAC-G2, and CBS-Q predictions from Ref. 89 yield lower saddle point energies, with the CBS-Q prediction being 2.8 kcal/mol lower. The variation in these estimates indicates a significant uncertainty in the estimated saddle point energy, as does the relatively large Q1 diagnostic of 0.03. For this reason we have also performed multi-reference configuration-interaction (MRCI) calculations employing a 7-electron 6-orbital CAS reference wavefunction. These calculations employed roQCISD(T)/cc-pVTZ R_{CO} constrained geometries and were again extrapolated from cc-pVTZ and cc-pVQZ results to the infinite basis set limit. The τ=0° saddle point was again found to occur at R_{CO} = 2.2 Å, with an energy of 1.66 kcal/mol after inclusion of the uB3LYP/6-311++G(d,p) zero-point energy correction. This result includes the Davidson correction for higher order excitations, while its neglect yields a saddle point energy of 3.64 kcal/mol. The difference between these two results is somewhat indicative of the uncertainty in the MRCI estimates. For the cc-pVQZ basis set the results are 1.98 and 3.84 kcal/mol, suggesting only a few tenths of a kcal/mol uncertainty from the basis set extrapolation. The relatively high value for the MRCI barrier height suggests that there is significant dynamic correlation in this system. Taken together, the MRCI, QCISD(T), and other high level calculations suggest that the saddlepoint energy is –0.1 ± 2 kcal/mol.

The various high level predictions for the energy of the C_2H_4OH complex are in better agreement, differing by less than 1.0 kcal/mol. The experimental studies of Diau and Lee[80] and of Hippler and coworkers[82] have yielded estimated reaction enthalpies of –30.2 ± 0.5 and –29.4 ± 1.4 kcal/mol, respectively. These values are considerably lower than the present 0 K estimate of –27.0 kcal/mol. However, the experimental values are for temperatures ranging from about 550 to 800 K. A direct comparison of the predicted and observed temperature dependent equilibrium constants, as in Figure III-IV, provides a better indication of the accuracy of the theoretical predictions. The present predictions are seen to be in remarkable agreement with the experimental results of Diau and Lee,[80] while the order of magnitude discrepancy with the data of Hippler and coworkers[82] suggests some shortcoming in that work.

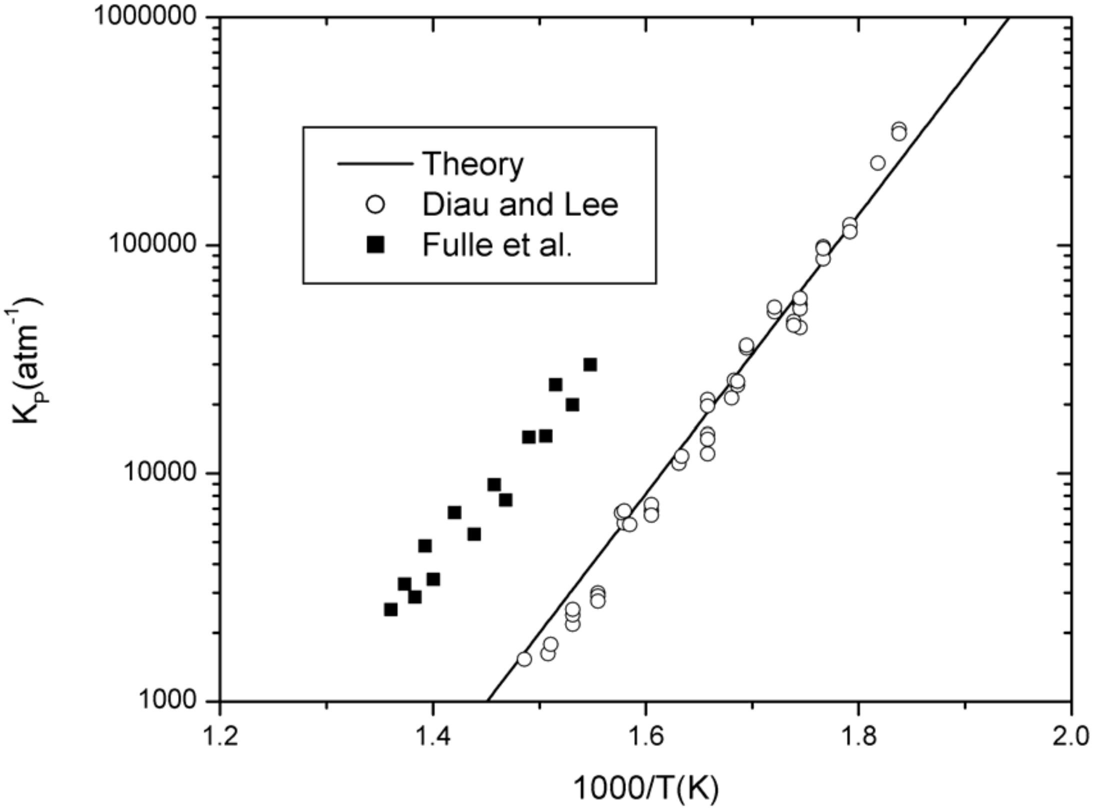

Figure III-IV. Plot of the predicted and experimentally observed temperature dependence of the equilibrium constant, K_p. Adapted from Figure 4 of Ref. 114.

Kinetics. The present predictions for the temperature dependence of the high pressure C_2H_4 + OH addition rate are illustrated in Figure III-V for a variety of saddle point energies. For comparison the available experimental data for pressures of 600 torr or higher, where the observed rate should be close to the high pressure limit, are also plotted therein, as well as the low temperature (and low pressure) data of Leone and coworkers.[83]

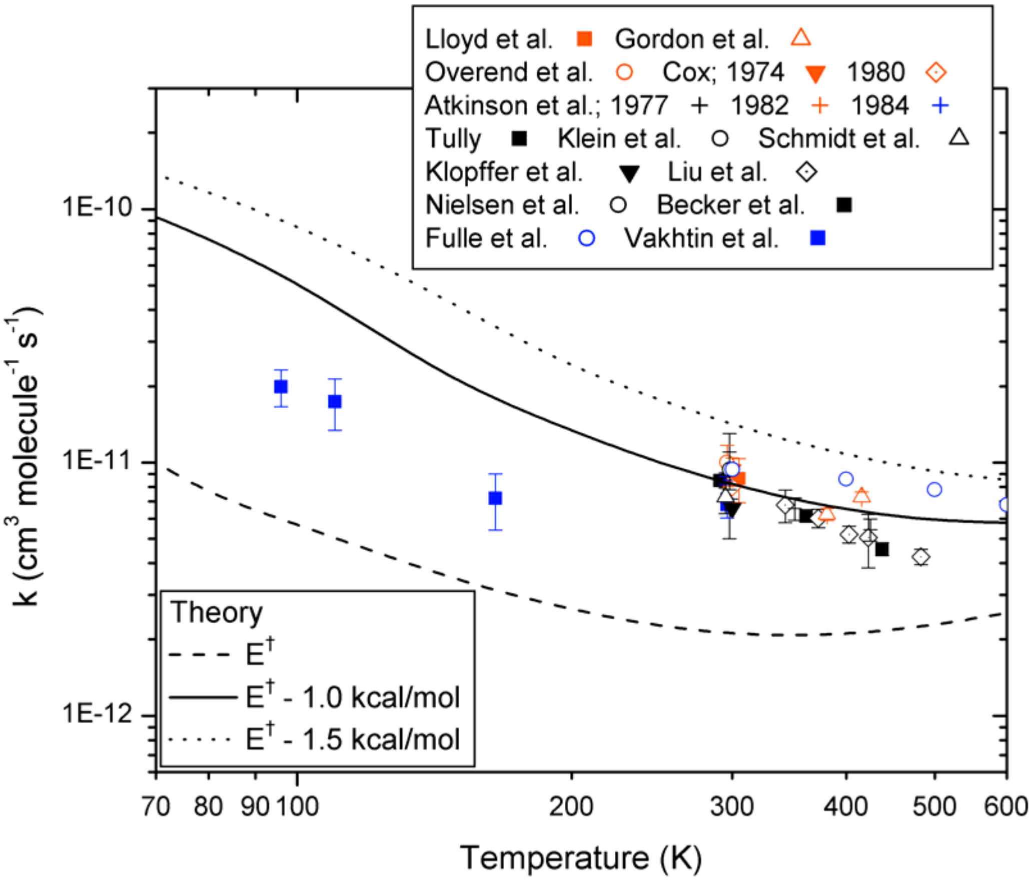

Figure III-V. Plot of the temperature dependence of the high-pressure addition rate constant as predicted by the present effective transition state model for three different assumed inner saddle point energies. Also plotted are the available experimental rate constants determined for pressures of 1 bar or higher and the experimental data of Leone and coworkers[83] measured at lower temperatures and pressures.
Adapted from Figure 5 of Ref. 114.

The predictions based on the current best estimate of -0.1 kcal/mol for the saddle point energy, given by the dashed line, are clearly lower than the experimental observations. Decreasing the ab initio predicted saddle point energy by 1.0 kcal/mol, to –1.1 kcal/mol, yields good agreement with the experimental data from 300 K on, while the reduction by 1.5 kcal/mol yields a rate that is somewhat too high. An adjustment by 1.0 kcal/mol is well within the bounds of the expected accuracy of the *ab initio* calculations, particularly in light of the large Q1 diagnostic for the QCISD(T) calculations in the neighborhood of the saddle point. Nevertheless, there are of course also significant uncertainties in the procedures for extracting kinetic estimates from the quantum chemical data. Thus, one should take the downwards revision in the saddle point energy by 1.0 kcal/mol to be only suggestive of a likely error in the quantum chemical estimates. All further calculations presented here employ this adjusted barrier height. Note that we restrict our attention here to temperatures of 600 K or lower, because the abstraction reaction begins to interfere with measurements of the addition rate at that temperature.[75]

Below room temperature the agreement between the adjusted predictions and Leone and coworkers'[83] experimental observation appears to be unsatisfactory. However, these experiments are at quite low pressures (below 1 torr) and, thus, the discrepancy may simply be an indication of some falloff from the high-pressure limit. Leone and coworkers have argued that this should not be the case. Nevertheless, we have performed our own 2-dimensional master equation simulations of the pressure dependence. The results for a N_2 collider, employing a downwards energy transfer parameter $<\Delta E_{\mathrm{down}}>$ of 200 $(T/298)^{0.85}$ cm^{-1}, are illustrated in Figure III-VI together with various experimental observations for N_2, Ar, and air (which are expected to behave quite similarly to N_2). The functional form for the energy transfer parameter was chosen on the basis of prior findings for similar systems.[128,131] The 298 K value of 200 cm^{-1} is the value, which best reproduces the data at 298 K, and again is completely reasonable in comparison with related studies. The agreement between theory and experiment is seen to be remarkably good.

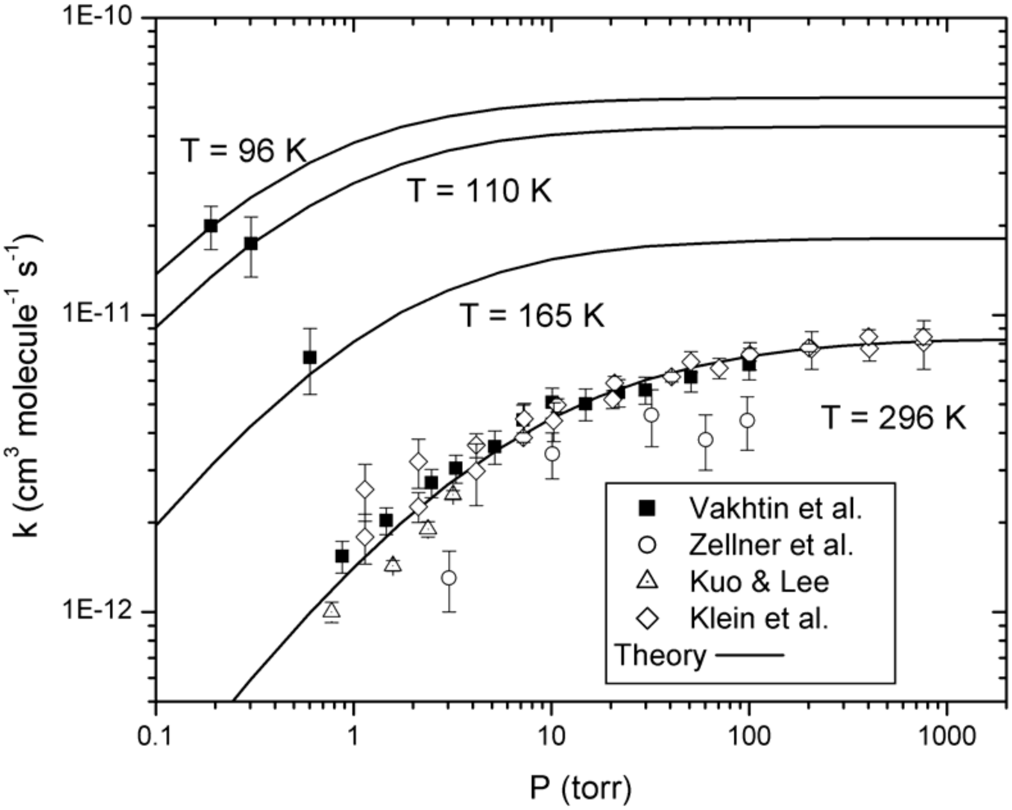

Figure III-VI. Plot of the predicted pressure dependence of the C_2H_4 + OH addition rate constant for N_2 as the bath gas at various temperatures. Also plotted are the corresponding experimentally observed rate constants for N_2, O_2, and air as the bath gases. Adapted from Figure 6 of Ref. 114.

Related plots of the pressure dependence for the case of a He collider are shown in Figure III-VII for results at ~300 K, and in Figure III-VIII for the results of Kuo and Lee for temperatures ranging from 251 to 430 K. In these simulations for a He collider we have chosen an equivalent functional form for the downwards energy transfer parameter, but have set the 298 K value to be 100 cm^{-1} rather than 200 cm^{-1}. Again, this quite reasonable energy transfer parameter yields satisfactory agreement with experiment, particularly at 300 K, where the data is more extensive. The modest overpredictions (~30%) at higher temperatures in Figure III-VIII may be indicative of errors in the theoretical model (e.g., in the temperature dependence of either the energy transfer parameter or the high-pressure limit) or in the experimental data.

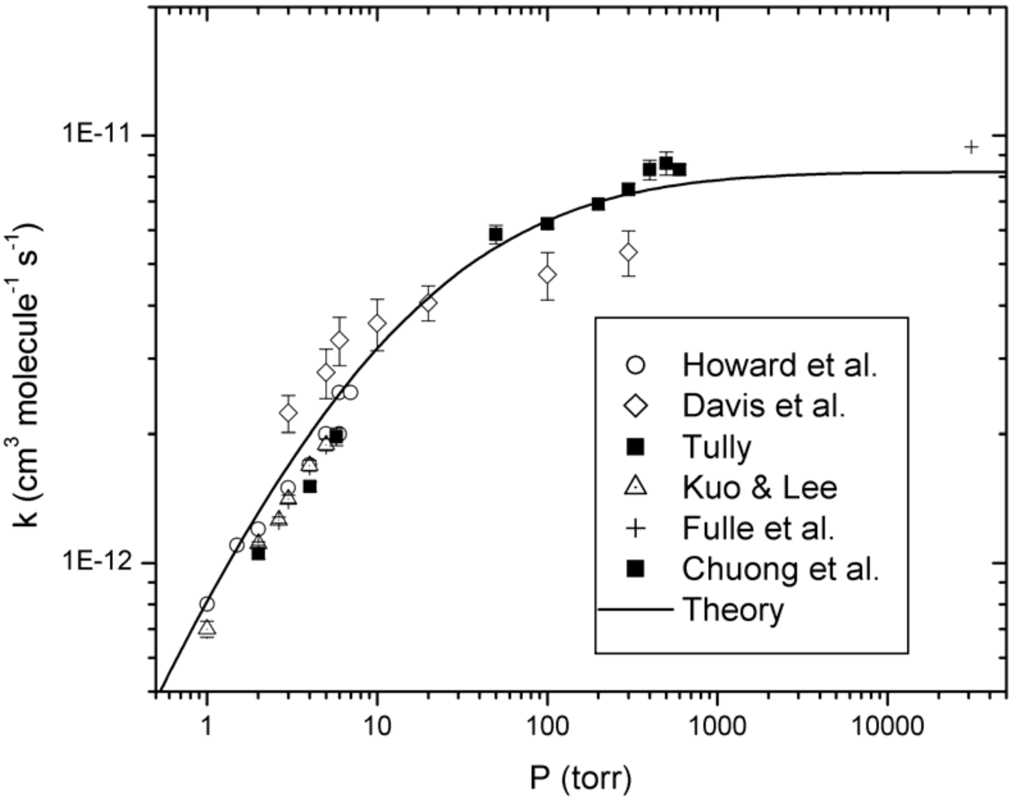

Figure III-VII. Plot of the predicted and observed pressure dependence of the C_2H_4 + OH addition rate constant for He as the bath gas at room temperature. Adapted from Figure 7 of Ref. 114.

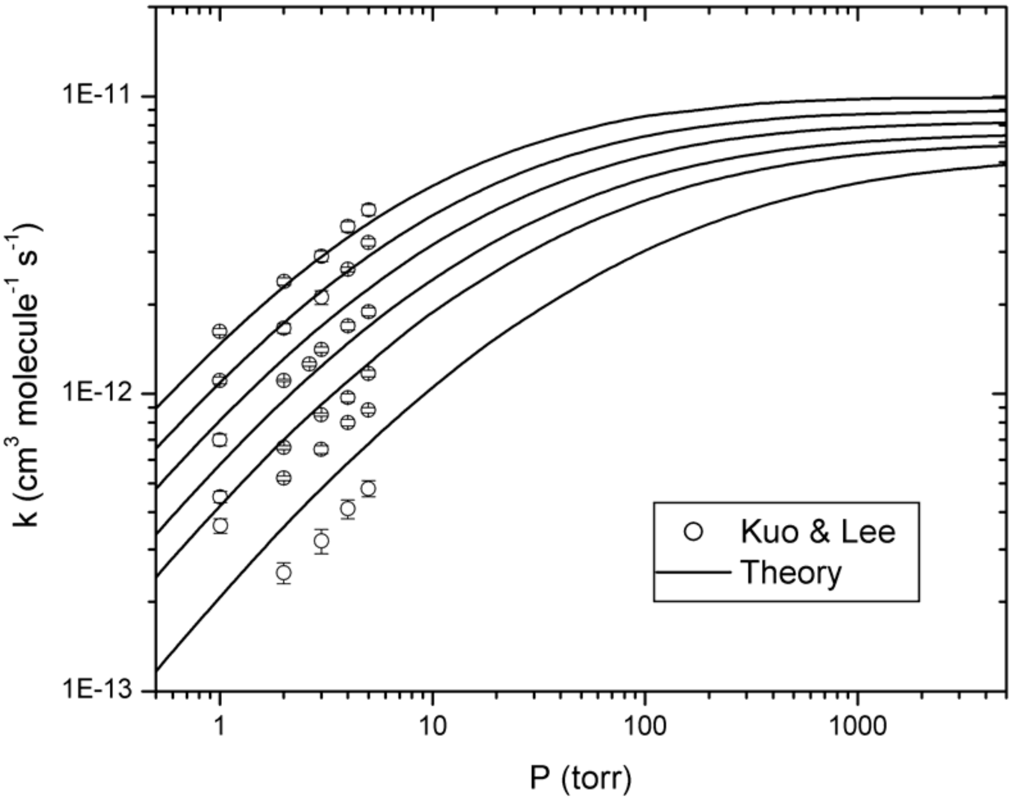

Figure III-VIII. Plot of the predicted and observed pressure dependence of the C_2H_4 + OH addition rate constant for He as the bath gas at temperatures of 251, 275, 300, 330, 360, and 430 K. The rate constants decrease with increasing temperature. Adapted from Figure 8 of Ref. 114.

With this good agreement between theory and experiment for a wide range of temperatures and pressures, it is interesting to consider the relative contributions from the inner and outer transition states. The temperature dependence of these components are illustrated in Figure III-IX. The long-range transition state theory of Ref. 107, predicts a temperature independent capture rate of 3.6x10^{-10} cm^3 molecule^{-1} s^{-1} for the present reaction. In contrast, the present negative saddle point energy corresponds to an inner transition state rate constant that is about 1x10^{-11} cm^3 molecule^{-1} s^{-1} near room temperature and then rapidly rises to infinity as the temperature decreases towards zero.

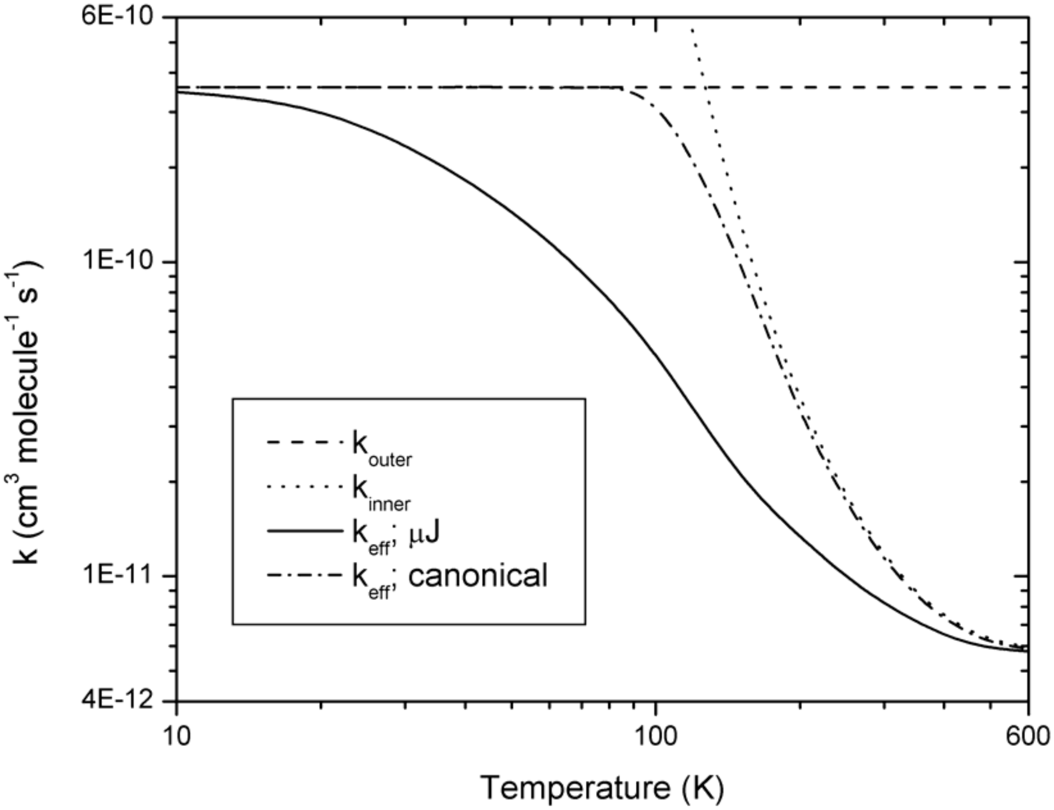

Figure III-IX. Plot of the temperature dependence of the high pressure addition rate constant as predicted by the present effective transition state model, the inner transition state model, and the outer transition state model. For the effective transition state model, both *E/J* resolved evaluations (solid line; according to Eq. (3-2)) and canonical evaluations (dashed-dotted line; according to Eq. (3-1)) of the inner and outer transition state partition functions are illustrated. Adapted from Figure 9 of Ref. 114.

The two rate constants cross at about 130 K. The *E,J*-resolved effective high pressure addition rate constant (from Eq. (3-2)) is significantly below (i.e., by more than 10%) each of the individual rate constants all the way from 10 to 400 K. At the crossing point of the inner and outer transition state predictions, the *E,J*-resolved effective rate constant is more than a factor of 10 lower. Notably, with canonical cvTST evaluations of the transition state effective partition function (according to Eq. (3-1)), this difference cannot exceed a factor of two, as illustrated by the dashed-dotted line. At 300 K the *E,J*-resolved effective rate is still 30% lower than that from the inner transition state prediction. Clearly, the proper consideration of the two individual transition state regions at the *E,J*-resolved level is essential to the accurate modeling of the temperature dependence of this reaction.

The effect of neglecting the variational, the tunneling, or the 1-dimensional hindered rotor treatments of the inner transition state are illustrated in Figure III-X. The variational considerations yield a reduction in the inner transition state rate constant by at most 15%, with, as expected, the maximum reduction at the highest temperature considered of 600 K. The Eckart tunneling estimate provides a greater increase in the inner transition state rate constant, but only at lower temperatures, where the effect is ameliorated by the increasing dominance of the outer transition state bottleneck. The replacement of the hindered rotor treatment of the CCOH dihedral angle with a harmonic oscillator treatment has the greatest effect on the predicted capture rate.

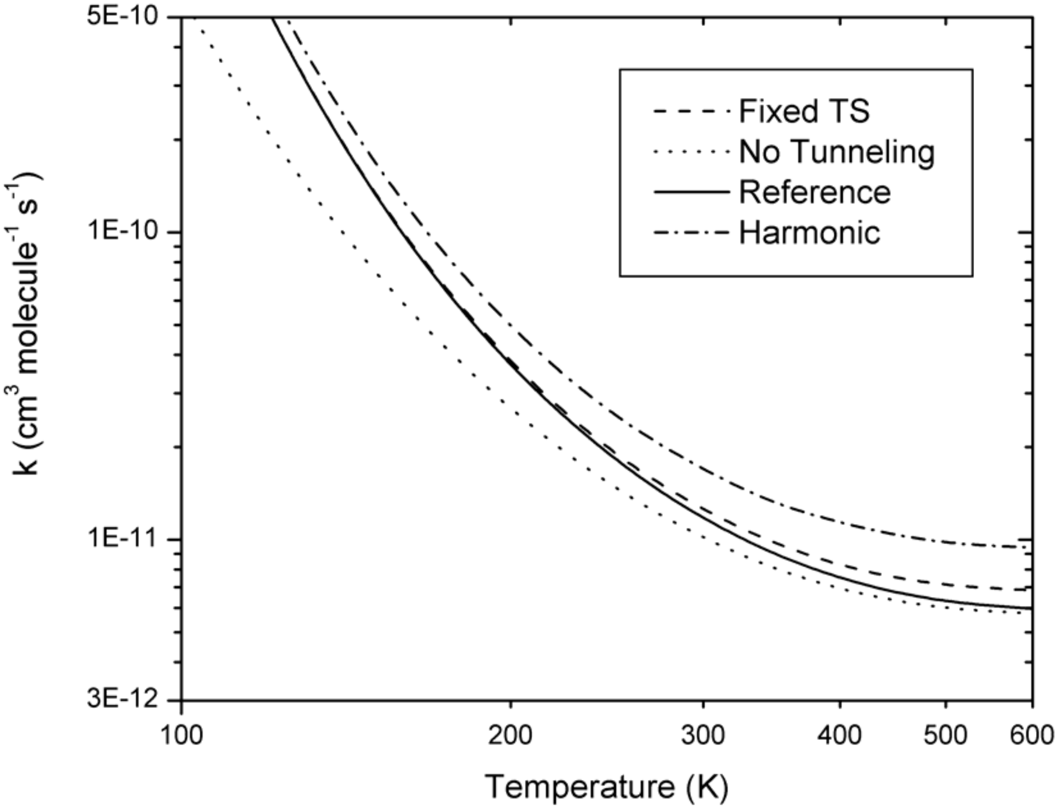

Figure III-X. Plot of the predicted temperature dependence of the high-pressure addition rate constant for the inner transition state model, and ignoring tunneling, or anharmonicities in the torsional mode, or variational effects for the inner transition state. Adapted from Figure 10 of Ref. 114.

A more global estimate of the effect of anharmonicities on the inner transition state predictions is provided by a comparison of phase-space integral (PSI) based mulitfaceted-dividing-surface variable-reaction-coordinate TST predictions with the corresponding rigid-rotor harmonic-oscillator (including a 1-dimensional hindered rotor treatment) based TST results. The ratio of these two predictions is illustrated in Figure III-XI for a variety of pivot point locations, *d*.

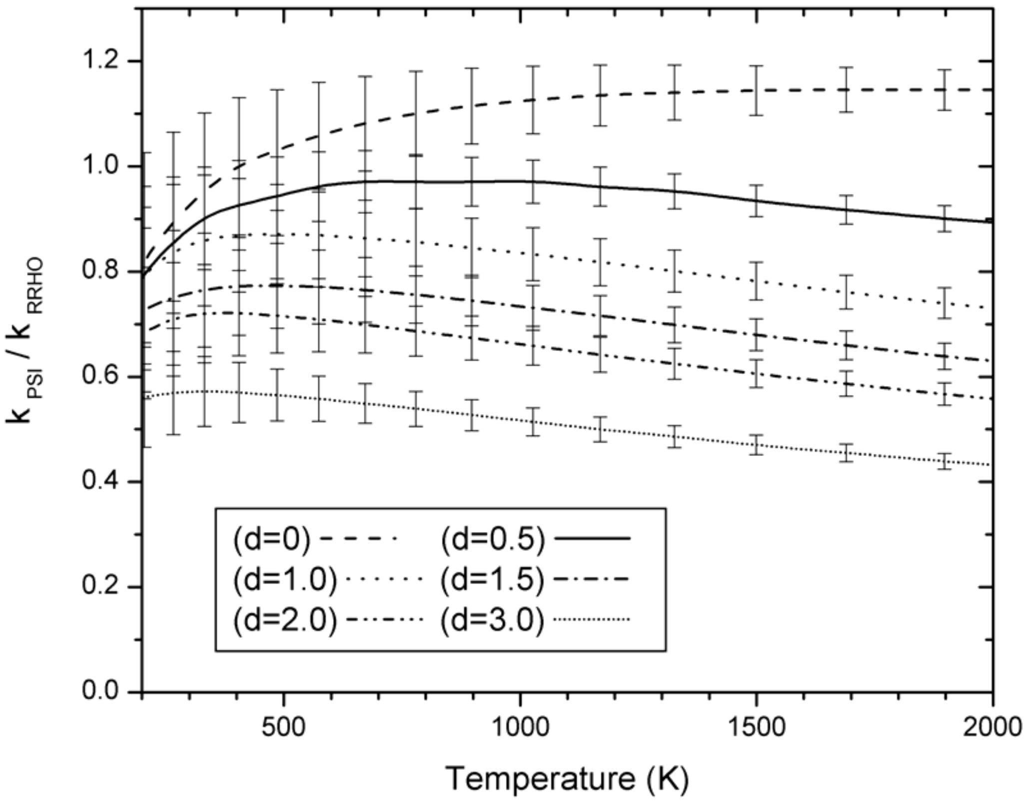

Figure III-XI. Plot of the ratio of the corrected multifaceted-dividing-surface variable-reaction-coordinate TST predicted high-pressure rate constant to that from the rigid rotor harmonic oscillator based inner transition state model. Adapted from Figure 11 of Ref. 114.

In making this plot, we have included an approximate correction for quantum effects in the PSI-based results, because the vibrational frequencies for the transitional modes at the saddle point are large enough to have significant quantum effects. In particular, the ratio of the quantum harmonic to classical harmonic canonical partition function for the transitional modes, which is illustrated in Figure III-XII, is applied as a correction factor to the PSI-based results, in order to make a proper comparison. The large deviation of this correction factor from unity, up to temperatures well beyond that at which the inner transition state becomes dominant, clearly indicates the importance of including quantum effects for these modes at lower temperatures. In contrast, for radical-

radical reactions the vibrational frequencies for the transitional modes are considerably lower and quantum effects can be safely neglected.[132]

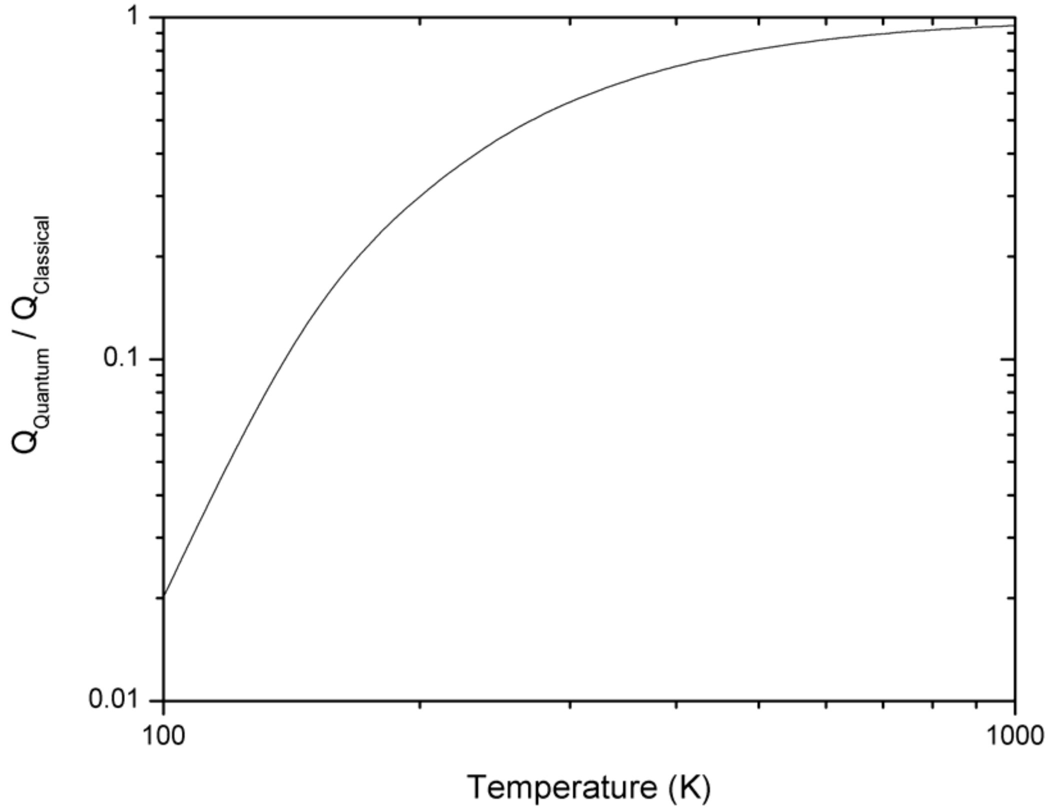

Figure III-XII. Plot of the ratio of the quantum harmonic to classical harmonic canonical partition function for the transitional modes as a function of temperature. Adapted from Figure 12 of Ref. 114.

Another more modest correction factor involves the effect of the internal relaxation of the C_2H_4 and OH fragments in the neighborhood of the inner transition state. This effect can generally be neglected for radical-radical reactions, again due to the relatively large separations between the two fragments in that case. However, in the present radical-molecule reaction this effect is much larger and so, for the plot in Figure

III-XI, we have corrected the PSI results by a Boltzmann factor in the uB3LYP/6-31G* relaxation energy at the saddle point. This correction assumes that the relaxation energy is independent of the relative orientation of the fragments within the inner transition state dividing surface.

With these corrections we see that the deviation of the ratio from unity, which is likely attributable to anharmonic effects, is quite small. However, there is one serious difficulty. In particular, the PSI-based predictions decrease monotonically with increasing pivot point distance *d*, and thus there is no variational minimum. If we had allowed *d* to continue to increase beyond 3 bohr, the PSI-predicted rate would have gradually gone to zero. The problem lies in the approximation of an orientation independent fragment relaxation energy.

To study this effect we have also performed a PSI-based analysis where the internal fragment structures are optimized for each orientation sampled in the configurational integral. The resulting predictions for the ratio of the PSI-based calculations to the RRHO-based calculations are illustrated in Figure III-XIII. In this case, the ratio does go through a minimum at a pivot point of about *d* = 1.0 bohr, which corresponds to the typical pivot point location that we have observed in various related studies of radical-radical reactions. Now the effect of global anharmonicities and transitional mode-couplings is predicted to be very small, with the ratio being about 1.0 +/- 0.1 throughout the temperature range from 300 to 2000 K.

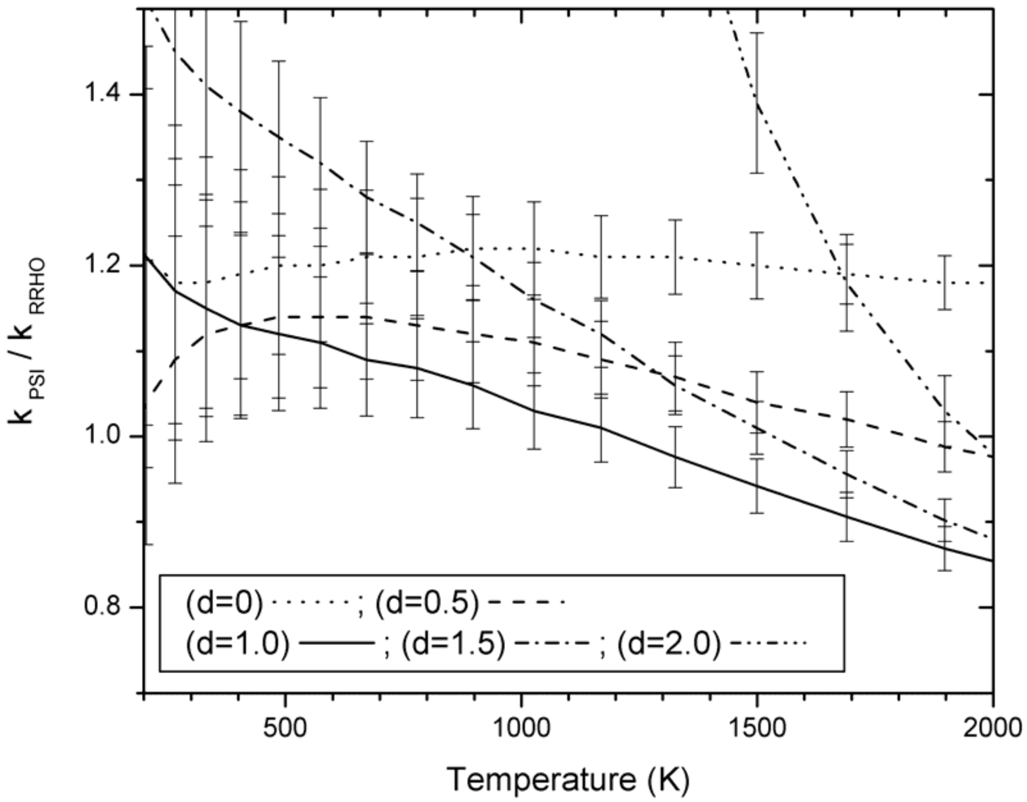

Figure III-XIII. As in Figure III-XI, but including a direct calculation of the effect of geometry relaxation on the multifaceted dividing surface variable reaction coordinate predictions. Adapted from Figure 13 of Ref. 114.

At this point it is perhaps worthwhile to return to a discussion of the activation energy defined as –R d ln k / d (1/T). The predicted absence of significant anharmonic effects suggests that the present prediction for the inner saddle point energy of -1.1 kcal/mol should be quite reliable. Furthermore, this negative value for the saddle point does correlate, at least qualitatively, with the observed and predicted negative activation energy near room temperature. However, the slope of the rate versus temperature plot near room temperature is quite different for the effective and inner transition state models, as seen in Figure III-IX. Indeed, the calculated room temperature activation energies for the present effective and inner transition state models are -0.5 and -1.2 kcal/mol, respectively.

Activation energies similar to the present inner transition model were obtained in the studies of Villa et al.[85] (-0.92 kcal/mol) and of Vivier-Bunge and coworkers.[48] (-1.08 kcal/mol). Again, these activation energies were obtained with canonical transition theory state models that do not consider the effects of the outer transition state and thus do not provide reliable predictions, particularly for lower temperatures. Importantly, canonical implementations of transition state theory, in which the transition state partition function is optimized only as a function of *T*, are incapable of adequately describing the effect of the two transition states. The variational minimizations at the *E,J*-resolved level are a key component of the present model. For example, an effective transition state treatment implemented at the canonical level would yield a high pressure rate constant of 1.8×10^{-10} cm^3 $molecule^{-1}$ s^{-1} at the crossing point between the inner and outer transition state model predictions (~130 K). This rate constant is about a factor of 6 greater than that obtained from the *E,J*-resolved effective transition state model. In the case of Vivier-Bunge and coworkers[48] the contribution from the temperature dependence of the partition functions has also been ignored.

D. Conclusions

We have examined the low to moderate temperature addition of the hydroxyl radical to ethylene in the high pressure limit, and as a function of pressure, via high level quantum chemical calculations, sophisticated cvTST evaluations, and 2-dimensional master equation simulations. By simply reducing the inner saddle point energy by 1.0 kcal/mol from its ab initio predicted value (to -1.1 kcal/mol) we are able to satisfactorily reproduce the available experimental data from 100 to 600 K. The pressure dependence of the addition rate constant is also satisfactorily reproduced with reasonable parameters for the energy transfer function. The theoretically predicted capture rate is reproduced to within 10% by the expression $[4.93 \times 10^{-12}(T/298)^{-2.488}\exp(-107.9/RT) + 3.33 \times 10^{-12} (T/298)^{0.451}\exp(117.6/RT)$; with R=1.987 and T in K] cm^3 $molecules^{-1}$ s^{-1}over the 10 to 600 K range.

The use of an effective transition state model, incorporating effects from both the inner and outer transition states, is an essential element of the present predictions. It is particularly important that these effects be included at the energy, *E,* and total angular momentum, *J,* resolved level. At the point where the two transition states are of equal importance, the *E/J* resolved treatment yields a reduction in the rate by an order of magnitude. The long-range transition state theory of Ref. 107 provides a useful procedure for treating the outer transition state, while more standard rigid-rotor harmonic-oscillator plus 1-dimensional torsional treatments provide an appropriate model for the inner transition state. Other anharmonic effects appear to be minimal, at least for the present reaction.

The present calculations clearly show that a single transition state model is only appropriate for temperatures of about 400 K or higher. The convergence of the inner transition state model to the effective transition state model occurs at a temperature that roughly corresponds to the energy of the saddle point below reactants. This finding is likely quite general and can be used to estimate whether a single inner transition state treatment is sufficient for other reactions with negative saddle point energies.

The present model indicates that, for the C_2H_4 + OH system at low temperatures, the decrease in the capture rate constant with increasing temperature is due to the increasing importance of the inner transition state. This finding likely provides an explanation for some related observations of the temperature dependence of radical-molecule reactions. For example, in the reaction of butenes with OH, where rates have been measured down to 23 K,[133] the experimental observations are remarkably analogous to those illustrated in the present Figure III-IX.

CHAPTER IV

HYDROXYL RADICAL INITIATED OXIDATION OF ISOPRENE: A TWO-TRANSITION STATE MODEL*

A. Background

Here, we will present a new theoretical model for the association of OH and isoprene and compare its predictions with a large set of experimental observations. This model improves on the prior models in a variety of ways. First, our model is based on a higher level and more complete quantum chemical analysis. Furthermore, this quantum chemical analysis is carefully benchmarked against higher level calculations for the much smaller ethylene + OH system. Perhaps more importantly, we make significant improvements in the transition state theory parts of the kinetic analysis. In particular, a key aspect of the addition of OH radicals to alkenes involves the presence of two distinct transition state regions. An outer transition state describes the initial formation of a long range van der Waals complex, while an inner transition state describes the transformation from the van der Waals complex to a chemical adduct. Here, the combined effect of these two transition states is treated at an energy, E, and total angular momentum, *J*, resolved level. Other models have either simply neglected the outer transition state or else employed wholly inadequate treatments of its effect. Finally, we also include a two-dimensional master equation (ME) based analysis of the pressure dependence of the addition kinetics.

The two-transition state RRKM/ME model employed here was previously used to model the addition of hydroxyl radicals to ethylene (Chapter III) and provided excellent agreement with the extensive available temperature and pressure dependent experimental data. [114] The ethylene-OH system permits benchmarking of various aspects

---

* Preprinted with permission from "A Two Transition State Model for Radical-Molecule Reactions: Application to Isomeric Branching in the OH-Isoprene Reaction" Greenwald, E. E.; North, S. W.; Georgievskii, Y.; Klippenstein, S. J. *J. Phys. Chem. A* **2007**, submitted.

of the present treatment such as the level of theory used in the quantum chemical calculations, inclusion of variational effects, the effects of tunneling, hindered rotor treatments of low frequency motions, and anharmonicity, as well as the significance of including both an outer and an inner transition state. In the ethylene-OH system, at 300 K, the E,J-resolved effective rate was 30% lower than that predicted by inclusion of only the inner transition state. This divergence should increase as the inner saddle point lowers in energy. Including only the inner transition state was found to be an inadequate representation of the kinetics below temperatures comparable to the energy of the saddle point below the reaction asymptote. In the isoprene-OH system, the energies of the saddle points for formation of the 4 isomers are 2.43, 0.94, 0.08, and 2.13 kcal/mol (including zero point energy) below the reaction asymptote for isomers 1, 2, 3, and 4, respectively. This implies that inclusion of only the inner transition state will be insufficient below temperatures as high as about 1200 K.

The models we employ for the inner and the outer transition states are distinctly different. The outer transition state lies at large separations, beyond the van der Waals minimum, where only long-range interactions are important. Considerable effort has been devoted to the implementation of quantized versions of transition state theory for such long-range potentials to obtain accurate estimates for the low temperature limit rate. Here, we are more interested in somewhat higher temperatures (e.g., above about 10 K), with our primary focus on understanding where the transition from the long-range to the short-range transition state occurs. In this temperature range a recently derived classical long-range transition state theory approach is appropriate.[134] The derivation of this approach included an application to the addition of hydroxyl radical to isoprene, and the results of this analysis provide the basis for the present treatment of the outer transition state.

The inner transition state region for the isoprene + OH reaction is somewhat more complex than for ethylene + OH as there are now four separate inner transition states corresponding to the formation of the four different isomers of the adduct. Each inner transition state is near a saddle point on the potential energy surface. The saddle point arises as the chemical bond between the carbon and oxygen atoms forms and the CC π bond weakens. The interplay between these two chemical forces determines the precise location of the saddle point, which corresponds to carbon-oxygen separations of 2.1-2.35 Å for the four different isomers (1-4). At such short separations, the intermolecular forces between the isoprene and hydroxyl moieties are quite strong. As a result, a simple rigid-rotor harmonic-oscillator treatment of all but the HOCC torsional modes, the cis-trans isomer conversion modes, and the torsional modes of the methyl rotations, which are treated as one-dimensional (1D) hindered rotors, provides a reasonably satisfactory treatment of the inner transition state. A standard energy, E, and total angular momentum, J, resolved RRKM kinetics analysis is then performed to evaluate the reaction rates.

The computational methodologies employed for both the *ab initio* determinations, and for the kinetics evaluations are summarized in section B. In section C, the quantum chemical results and the predictions for the rate constants are presented and discussed. This discussion focuses on a comparison with experiment and on the effect of the transition from a dominant outer to a dominant inner transition state as the temperature rises as well as providing an accurate prediction of the initial branching ratio under tropospheric conditions. Some concluding remarks are provided in section D.

B. Computational Methodology

***An Initio* Calculations.** The focus of the present *ab initio* quantum chemical calculations is the accurate evaluation of the rovibrational properties of the reactants, the products, and of the reaction path in the transition state region. All geometry optimizations used for the kinetics simulations were performed using the unrestricted Becke-3 Lee-Yang-Parr (uB3LYP)[91] density functional with the Pople-style triple-ζ polarized split-valence basis sets with diffuse functions 6-311++G** [135,136] as implemented in the Gaussian 03 suite of programs.[137] Single point energy calculations were performed on those geometries using restricted open-shell quadratic configuration interaction calculations with perturbative inclusion of the triples contribution (roQCISD(T)),[108] employing the Pople-style double-ζ polarized split valence basis sets with diffuse functions, 6-31++G**, as well as using restricted open-shell Möller-Plesset perturbation theory (roMP2)[110,138] employing both the 6-31++G** basis sets and the Pople-style triple-ζ polarized split valence basis sets with diffuse functions 6-311++G(3df,2pd) as employed in the Molpro suite of programs.[120]

When considering the equilibrium structures of the individual isoprene-OH adducts, care must be taken to ensure that the global minimum for each structure is determined. In the deep wells of the adducts, many local minima corresponding to different rotational isomers of the adducts exist. As such, B3LYP/6-31G* [92] was used to optimize structures and calculate energies in order to determine the lowest energy rotational conformation of each isoprene-OH adduct. For the four isoprene-OH adducts, 58 local minima were found. The optimized geometry of the lowest energy conformation for each adduct was then used as the starting geometry for all subsequent calculations.

We have re-examined the ethylene-OH potential energy surface (PES) in the region of the inner transition state in order to develop a more tractable methodology, i.e. one which is computationally less expensive than was used in the ethylene-OH study but that quantitatively captures the high level potential energy surface. Figure IV-I is a plot of energy vs. C-O internuclear separation for the ethylene-OH system calculated at the roQCISD(T)/6-31++G**//B3LYP/6-311++G** level of theory including a basis set correction at the roMP2 level of theory (X's in Figure IV-I) as described by,

$$\begin{aligned} E_\infty = & \left[roQCISD(T)/6-31++G^{**}//B3LYP/6-311++G^{**}\right] \\ & +\left[roMP2/6-311++G(3df,2pd)//B3LYP/6-311++G^{**}\right] \\ & -\left[roMP2/6-31++G^{**}//B3LYP/6-311++G^{**}\right] \end{aligned} \tag{4-1}$$

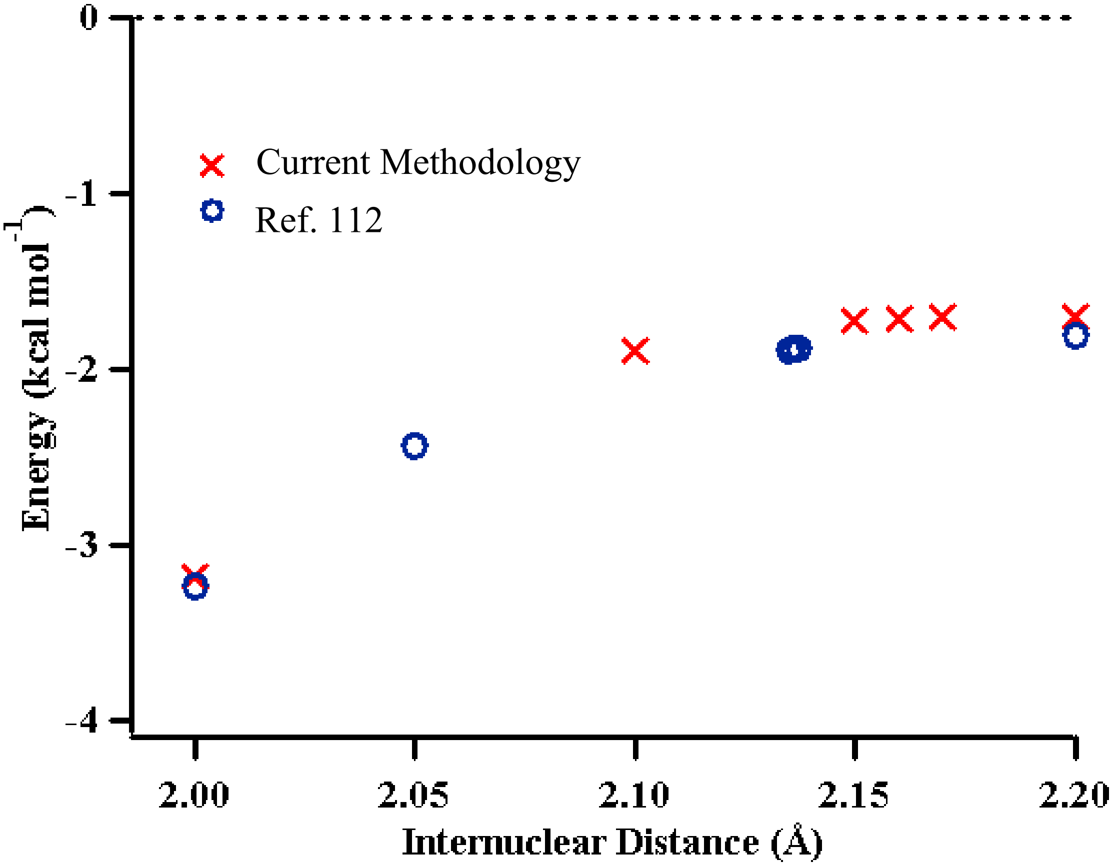

Figure IV-I. Energies in the region of the inner saddle point for the C_2H_4+OH reaction employing the current computational scheme (equation 4-1, Xs) as compared to the previously published extrapolation scheme of Ref. 114 (circles). Energies are relative to infinite separation energy of the C_2H_4+OH of 0 kcal/mol in both cases. Zero point energy is not included. Adapted from Figure 1 of Ref. 38.

Overlaid in Figure IV-I (circles) is the plot of energy vs. C-O internuclear separation for calculations at the more computationally expensive method published previously.[114] The saddle point optimized along the C-O internuclear-separation employing the present methodology is within 0.015 Å and 0.17 kcal mol^{-1} of that previously reported.

Given the success of the above computational methodology, we have adopted this approach to treat the isoprene-OH system. In the case of isomers 2 and 3, direct B3LYP/6-311++G** saddle point optimizations located a transition state along the reaction coordinate and these were used in subsequent calculations. However, no such transition states were found for isomers 1 and 4. Instead, constrained geometry optimizations at the B3LYP/6-311++G** level of theory, along a coordinate of C-O internuclear separation, were performed. Saddle points at the composite level of scheme IV-I were then found along the individual PESs. The energies from those calculations were used to construct the present PESs.

Harmonic frequencies and rigid rotor rotational constants were calculated for all stationary points at the B3LYP/6-311++G** level and those frequencies were used to include zero point energy. Vibrational frequencies obtained for the stationary points are given in Table IV-I.

One-Dimensional torsional potentials for the CCOH torsional motions, the methyl rotations, and the cis-trans isomerization motions were calculated as shown in Figure IV-II. Constrained optimizations, starting with the B3LYP/6-311++G** geometry for the lowest energy conformation of a particular stationary point, were performed as a function of dihedral angle and then computational scheme IV-I was applied. These torsional potentials were then fit to an analytical Fourier expansion (including only the first 6 terms) for the inclusion in density and number of state calculations.

Isomers 1 and 4 have 3 hindered rotors each, which correspond to the methyl rotations, the CCOH torsional motions, and the cis/trans isomerization motions. Isomers 2 and 3 have 4 hindered rotors each, which correspond to the methyl rotations, the CCOH torsional motions, the cis/trans isomerization motions, and the rotation of the CH_2 radical sites. Transition states 1-4 have 2 hindered rotors each, which correspond to the methyl rotations and the CCOH torsional motions.

Table IV-I: Frequencies of stationary points. (*Projected frequencies)

Species	Frequencies (B3LYP/6-311++G**)													
Isoprene	162	201	278	410	431	536	644	783	790	927	936	960	1011	1027
	1068	1088	1324	1328	1410	1429	1458	1483	1502	1652	1692	3023	3070	3109
	3131	3135	3144	3217	3223									
Exp.[139]	153	199	288	401	412	523	622	755	780	891	903	953	990	1012
	1034	1069	1219	1303	1388	1414	1425	1442	1466	1603	1638	2910	2928	2956
	2978	2988	3020	3092	3097									
OH	3709													
Exp.[140]	3738													
TS 1	138I	74	85	144	175	180	281	410	426	537	566	661	782	795
	935	944	961	1011	1019	1056	1086	1322	1338	1406	1421	1454	1479	1500
	1596	1646	3027	3076	3126	3134	3147	3159	3230	3254	3762			
TS 1*	72	85	142	175	178	281	406	426	537	563	661	780	795	923
	944	961	1011	1018	1055	1086	1322	1338	1406	1421	1454	1479	1500	1596
	1645	3027	3076	3126	3134	3147	3152	3230	3249	3755				
TS 2	269I	118	187	201	227	267	297	364	419	528	599	712	730	779
	867	955	956	1008	1023	1049	1083	1326	1331	1394	1417	1454	1479	1499
	1556	1683	3035	3106	3131	3134	3145	3148	3229	3244	3771			
TS 3	255I	76	147	176	202	265	287	424	455	532	608	704	740	793
	874	935	959	1001	1014	1070	1091	1293	1326	1408	1421	1457	1484	1504
	1568	1688	3025	3080	3114	3136	3153	3166	3219	3248	3765			
TS 4	160I	70	90	133	211	226	284	427	458	538	593	652	769	798
	926	948	963	985	1014	1069	1088	1307	1331	1408	1424	1457	1484	1507
	1593	1637	3027	3081	3114	3133	3138	3172	3222	3261	3761			
TS 4*	70	89	131	210	223	284	427	458	538	591	652	768	798	922
	927	961	984	1014	1069	1088	1307	1331	1408	1424	1457	1484	1507	1593
	1637	3027	3081	3114	3133	3138	3172	3222	3260	3760				
Adduct 1	65	87	183	277	287	325	377	454	549	609	780	801	930	971
	985	1002	1027	1056	1179	1229	1248	1335	1384	1398	1414	1455	1493	1494
	1499	1524	2993	3005	3048	3068	3107	3116	3149	3238	3815			
Adduct 2	105	115	245	280	298	323	347	418	433	547	582	699	736	878
	952	960	983	1020	1034	1044	1186	1242	1314	1320	1391	1436	1446	1482
	1490	1696	3034	3110	3114	3126	3136	3142	3223	3248	3803			
Adduct 3	75	104	168	229	261	337	359	438	478	565	588	743	796	884
	933	964	1023	1058	1069	1097	1233	1282	1311	1376	1406	1443	1446	1476
	1497	1695	2944	3026	3077	3109	3124	3151	3204	3267	3825			
Adduct 4	55	135	139	243	331	375	465	493	515	563	746	801	833	921
	996	1005	1032	1054	1141	1187	1272	1339	1378	1397	1420	1463	1487	1499
	1503	1516	3013	3030	3044	3081	3109	3137	3144	3232	3818			

Adapted from Table 1 in Ref. 38.

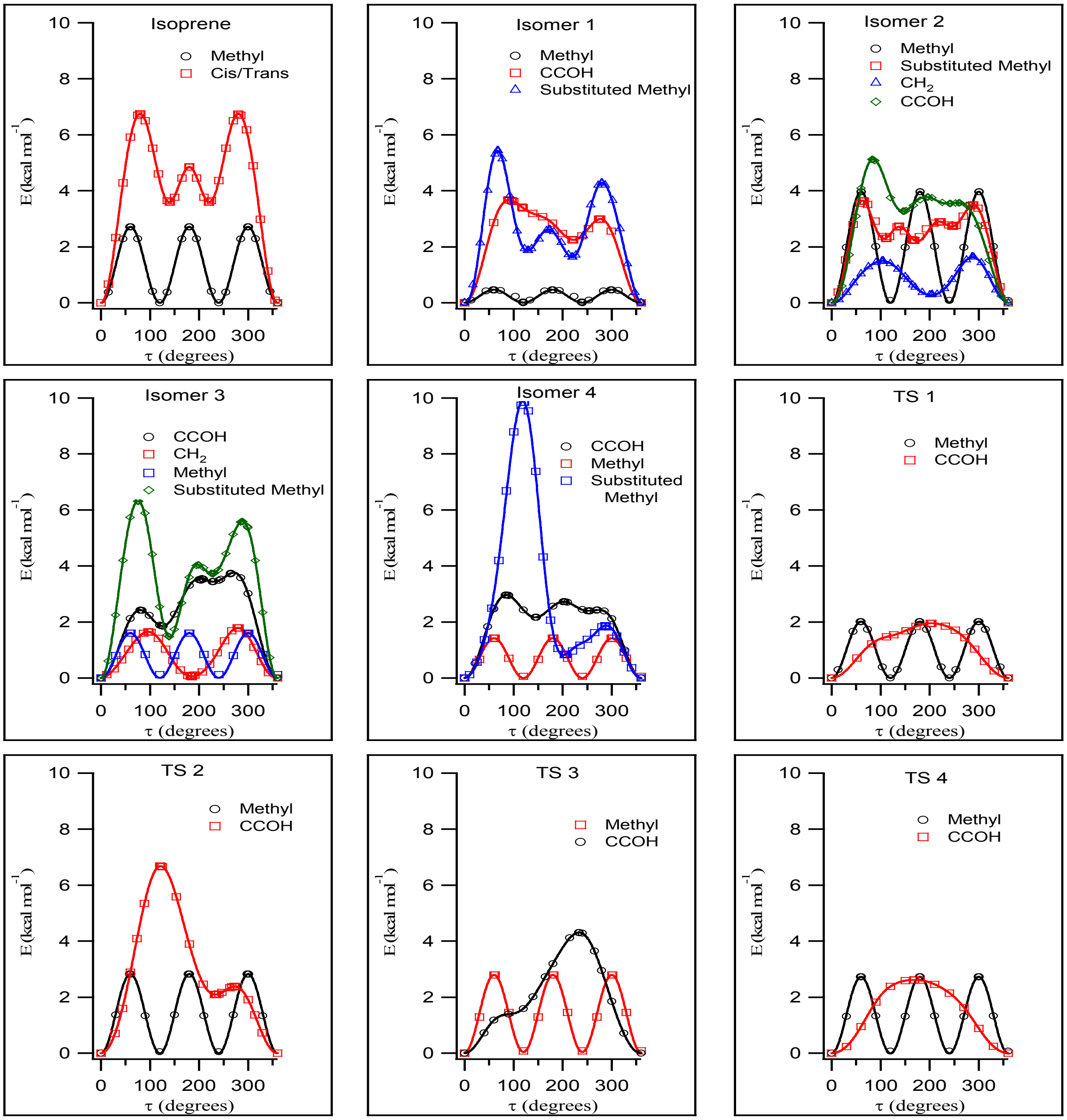

Figure IV-II. Torsional potentials (symbols) and Fourier expansion fits (lines) for the hindered rotors considered for isoprene, isomers 1-4, and transition states 1-4.

Rate Calculations. In order to compare our theoretical results to the experimental data, which measure the overall production rates of all four isomers, one must calculate the overall rate of OH addition to isoprene. This overall production rate incorporates an effective number of states, which includes reactive flux through a long-range outer transition state in combination with the reactive flux through the shorter-range inner transition state. All rate calculations, including both the high-pressure limit rate constants and those employing a 2D master equation (ME) analysis, were carried out using the VARIFLEX code.[141]

High-pressure Limit Rate Constants. In the case of OH addition to ethylene, a modest reduction in the *ab initio* predicted saddle point energy yielded a theoretically predicted capture rate which reproduced experimental data to within 10% on the temperature range from 10 to 600 K. In the present case of OH addition to isoprene, we find that a similar reduction in the *ab initio* predicted saddle point energy is necessary to reproduce temperature dependent experimental observations to a similar accuracy. Variational effects were found to be small, resulting in a reduction of the inner transition state rate constant of at most 15%, with the maximal reduction occurring at the highest temperature considered, 600 K. Eckart tunneling estimates contributed a non-negligible increase in the predicted inner transition state rate constant; however, this effect was pronounced only at lower temperatures, where the effect was ameliorated by the increasing dominance of the outer transition state. As such, variational effects and tunneling have been neglected in the present model.

The hindered rotor replacement of the low frequency CCOH torsional mode had the most substantial effect on the rate constant predictions in the case of OH addition to ethylene. In the present rate calculations, the low frequency CCOH, CH_3, and cis-trans conversion torsional modes are treated with hindered rotors where applicable. For C_2H_4 + OH estimates of the effects of anharmonicities on the inner transition state were performed using phase space integral calculations, but the effects of global anharmonicities and transitional mode coupling were found to be very small. A ratio of the rate constants calculated via a phase space integral (PSI) based multifaceted-dividing-surface variable-reaction-coordinate method and calculated via the corresponding rigid-rotor harmonic oscillator method (including a hindered rotor treatment) was equal to 1.0 ± 0.1 throughout the entire temperature range from 300-2000 K. Similarly small effects are expected here and so such global anharmonicity calculations were not repeated for the present system.

The model presented for the addition of OH to ethylene illustrated the importance of incorporating the effects from both the inner and outer transition states, in particular at the energy, E, and total angular momentum, *J*, resolved level. The E,*J*-resolved effective high-pressure addition rate constant is significantly below (i.e., by more than 10%) each of the individual rate constants all the way from 10 to 400K. In fact, at the crossing point of the inner and outer transition state predictions, the E,*J*-resolved effective rate constant is more than a factor of 10 lower. The present model also demonstrates the importance of including both transition states and combining the flux through each at the energy, E, and total angular momentum, *J*, resolved level as described in section C.

The flux through the outer transition state for the addition of OH to isoprene was explored in a recent derivation of classical variational transition state theory on long-range potentials,[142] and only a brief description of the results of that work will be presented in section C. The rate through the outer transition state is simply the long-range capture rate given by, [142]

$$k_{outer} = AT^{n} \times 10^{-10}\,\mathrm{cm^{3}molecule^{-1}s^{-1}} \tag{4-2}$$

where A and n in k_{outer} are dictated by the particular long-range interaction of the potential as seen in Table IV-II.

Table IV-II: **Long-range transition state theory predictions for rate constants (10^{-10} cm^3 molecule^{-1} s^{-1}) for the various long-range interactions between isoprene and OH from Ref.142.**

Interaction Potential	Rate
Dipole-Dipole	$1.27/T^{(1/6)}$
Dipole-Quadrupole	3.85 (T-independent)
Dipole-Induced Dipole	$1.27T^{(1/6)}$
Dispersion Forces	$2.15T^{(1/6)}$
Sum	5.54[a]

[a] cvTST capture rate for a potential represented by the sum of the dipole-dipole, dipole-quadrupole, dipole-induced-dipole, quadrupole-quadrupole, and the dispersion terms at 58 K.
Adapted from Table 2 of Ref. 38.

To obtain the number of states, $N^{\dagger}_{outer}$, associated with the outer transition state, the number of states was calculated using classical phase space theory. The coefficient for an r^{-6} interaction potential between neutral fragments was adjusted until the phase space theory rate constant at 58 K was in agreement with the theoretical result of Ref. 142 when considering the sum of the electrostatic interactions.

The long-range part of the potential is fragment orientation-dependent, though the separations described by this region of the PES are sufficiently large that orientation preferences here are expected to have no bearing on reactive probability at the inner parts of the PES. As such, all four reaction channels are assumed to share a single long-range capture rate.

At large separations, there are effectively two degenerate electronic states corresponding asymptotically to the $^2\Pi_{1/2}$ and $^2\Pi_{3/2}$ states of OH. The effects of this degeneracy on the reaction coordinate near the inner transition state were considered in the ethylene-OH system and it was found that there is sufficient energetic separation of electronic states in that region of the PES that only the lowest electronic state need be considered.[114] The higher energy electronic state originating from the spin-orbit splitting of the reactant hydroxyl moiety has been neglected in this study in the region of the inner transition state. The effect of the spin-orbit coupling does however increase the energy at the transition state relative to reactants by 70 cm^{-1}. This shift is incorporated here

As the inner saddle points amongst the four isomers vary in location and height, the formation rate at the inner transition state for each isomer is distinct. The rate constants associated with the inner transition states for formation of each isomer are the E,*J*-resolved microcanonical rate constants. However, in considering the effective rate constant on the global potential energy surface, one must consider reactive flux through the inner transition state region as a whole. As such, the total reactive flux through this region of the potential energy surface related to $N^{\dagger}_{inner}$ can be considered as a series of parallel reactions where formation of each isomer is unique. The flux through the transition states can then be summed to obtain the total flux through the inner transition state region,

$$N^{\dagger}_{inner} = \sum_{i=1}^{4} N^{\dagger}_{i} \tag{4-3}$$

where $N^{\dagger}_{i}$ is the reactive flux through the inner transition state corresponding to isomer i.

The inner and outer transition states act as a series of bottlenecks to reaction. A reasonable approximation to the effective flux through both transition states is given by

$$\frac{1}{N^{\dagger}_{\text{eff}}} = \frac{1}{N^{\dagger}_{\text{inner}}} + \frac{1}{N^{\dagger}_{\text{outer}}} \tag{4-4}$$

where $N^{\dagger}_{inner}$ and $N^{\dagger}_{outer}$ are the *E*,*J*-resolved transition state numbers of states at the inner and outer transition states, respectively. In writing eqn. 4-4, we assume statistical probabilities for crossing each transition state dividing surface, and further that the maximum in the flux at the van der Waals minimum greatly exceeds that at the two transition states.[99,100] Given equation 4-3, equation 4-4 becomes

$$N^{\dagger}_{\mathrm{eff}} = \frac{N^{\dagger}_{\mathrm{outer}}\left[\sum_{i=1}^{4} N^{\dagger}_{i}\right]}{N^{\dagger}_{outer} + N^{\dagger}_{inner}} \tag{4-5}$$

At low temperatures, the temperature dependence of the outer transition state will dominate the overall temperature dependence of the reaction rate, just as at high temperatures, the temperature dependence of the inner transition state will dictate the temperature dependence of the effective rate. At intermediate temperatures, the flux through both transition states contributes significantly to the overall rate and thusly the temperature dependence. The total reactive flux in eqn. 4-5 can be divided into the reactive probability of forming each individual isomer, providing a branching ratio $N^{\dagger}_{1} : N^{\dagger}_{2} : N^{\dagger}_{3} : N^{\dagger}_{4}$.

Pressure-Dependent Rate Constants. To model the pressure dependence of the system, we have employed a 2-dimensional master equation analysis of the temperature and pressure-dependent kinetics. The master equation analysis is based on the methodology described in Ref. 128. This treatment includes a temperature dependent exponential down model of energy transfer along with Lennard-Jones collision rates. The Lennard-Jones parameters for C_5H_8OH, Ar, and He were taken to be σ = 6.02, 3.47, and 2.55 Å and ε = 490.2, 114.0, and 9.99 K, respectively.

C. Results and Discussion

Potential Energy Surface. Results for the binding energetics of the isoprene-OH adducts, employing a variety of *ab initio* and density functional calculations, are tabulated in Table IV-III.

Table IV-III: **Relative energies (not including zero point energy) of the OH+Isoprene reaction in kcal/mol.**

Level of Theory	Isomer 1	Isomer 2	Isomer 3	Isomer 4
B3LYP/6-311++G** [a]	-39.8	-21.9	-22.6	-37.3
roQCISD(T)/6-31++G**//a [1]	-38.0	-25.3	-24.2	-35.5
roMP2/6-311++G(3df,2pd)//a [1]	-47.1	-32.1	-31.7	-44.0
roMP2/6-31++G**//a [1]	-43.8	-30.0	-29.1	-40.6
Computational Scheme 1 [1]	-41.4	-27.4	-26.8	-38.9
HF/6-31G** [2]	-31.5	-13.4	-14.6	-29.6
MP2/6-31G** [2]	-37.6	-30.2	-29.2	-34.7
MP2/6-311G** [2]	-37.3	-30.5	-29.4	-34.3
MP4(SDTQ)/6-311G**//b [2]	-35.9	-27.7	-26.4	-33.1
PMP4(SDTQ)/6-311G**//b [2]	-41.7	-28.0	-26.7	-39.1
B3LYP/6-31G** [2]	-47.7	-29.7	-30.2	-45.0

[1] From current work [2] From Ref. 31 a) geometry optimizations at the B3LYP/6-311++G** level of theory b) geometry optimizations at the MP2/6-311G** level of theory. Adapted from Table 3 of Ref. 38.

The variation in the results confirms the need for benchmarking. While the binding energies will only have a direct effect on the pressure dependent calculations, they will also indirectly affect the steepness of the PESs from the saddle-point inward. Furthermore, errors in the adduct energetics are indicative of likely errors in the transition state properties. The HF results appear to severely underestimate the binding energy of all four adducts. The B3LYP/6-31G** results overestimate the binding energies of all the adducts and overestimate the relative stability of adducts 1 and 4 as compared to 2 and 3. The B3LYP/6-311++G** results are in qualitative agreement with the higher level results, though they are not at the accuracy one would require for quantitative kinetics calculations. This large improvement over the B3LYP/6-31G** results reflects a strong dependence on basis set. The MP2 and MP4 results determine all four well depths to be within 10 kcal/mol of one another.[31] This is inconsistent with all other calculations performed. The roMP2 results restrict the paired electrons and include diffuse functions in the basis sets, improving upon the MP2 energies. The PMP4 results are the most closely aligned with those employed vide infra. The present computational scheme was applied to the ethylene-OH system, where the PES has already been used to very accurately determine rate constants varying both temperature and pressure, and the present computational scheme reproduces the ethylene-OH well depth to within 0.8 kcal/mol. The pressure dependence for the ethylene-OH system is particularly sensitive to the well depth.

An illustrative plot of the potential energy surfaces for formation of the 4 isomers (1-4) in the region of the inner transition state is shown in Figure IV-III. The energies seen in Figure IV-III do not include zero point energy. Isomers 1 and 4 (corresponding to the more stable, allylic radicals) have significantly larger binding energies, and thusly steeper PESs in the region between the inner saddle points and the deep wells of the adducts.

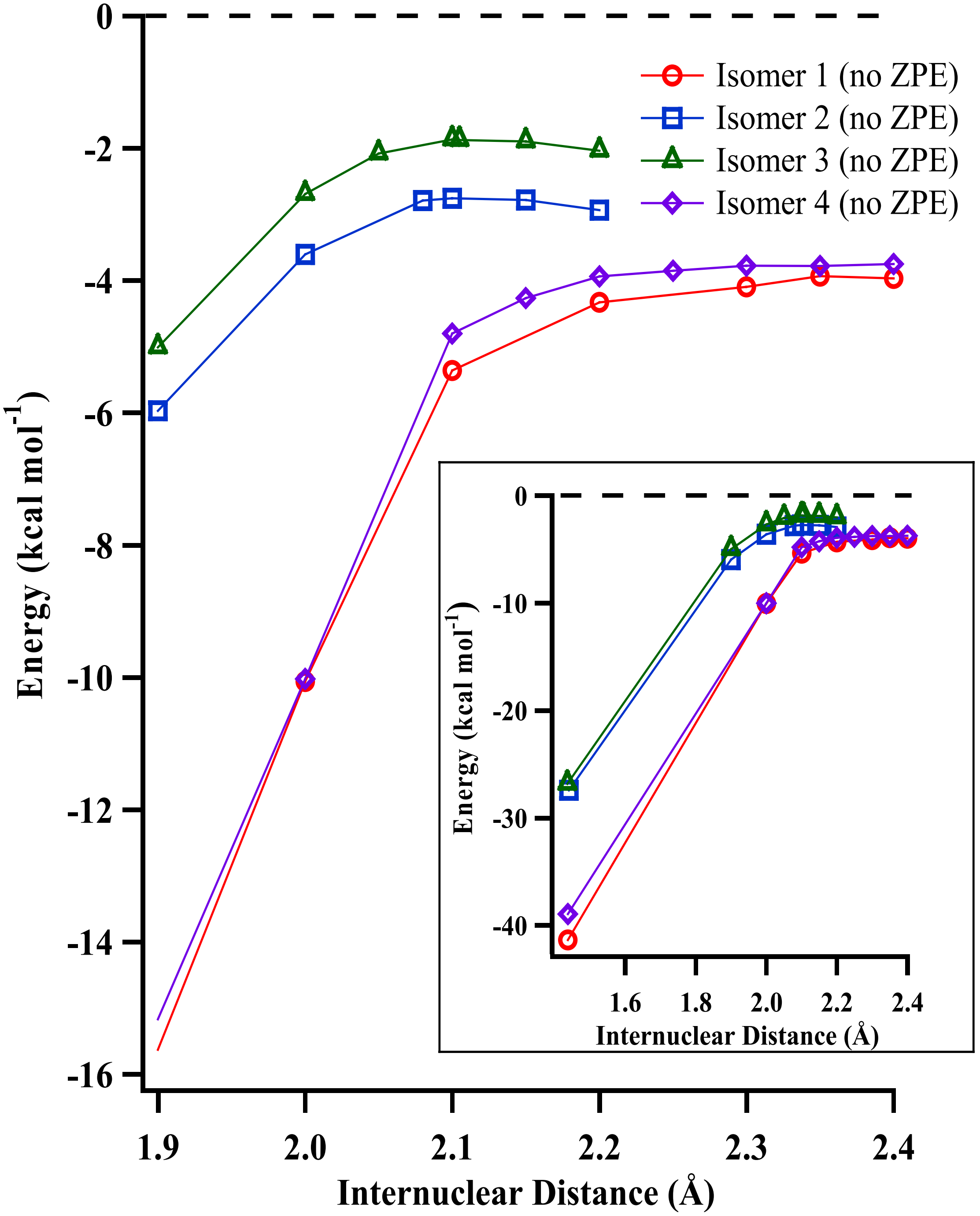

Figure IV-III. Reaction coordinate diagrams, in the region of the inner transition state, with relative energy (equation 4-1) as a function of C-O separation for the formation of each of the four isomers. Zero point energy is not included. (There is also no correction for the spin orbit splitting of OH.) Adapted from Figure 2 of Ref. 38.

Table IV-IV: Energies of stationary points (kcal/mol) relative to the isoprene-OH asymptote, including zero point energy.

Species	Energy (kcal/mol)[1]	Energy (kcal/mol)[2]
Isoprene + OH	0	0
TS 1	-2.4	-1.7
TS 2	-0.9	5.3
TS 3	-0.1	2.7
TS 4	-2.1	-1.8
Adduct 1	-37.3	-35.9
Adduct 2	-24.9	-20.9
Adduct 3	-24.1	-21.0
Adduct 4	-35.0	-33.4

1) Current methodology (equation 4-1) including zero point energy and the spin orbit splitting of the hydroxyl radical. 2) BHandHLYP/6-311G** level of theory, including zero point energy, as reported by Francisco-Marquez et al.[44] Adapted from Table 4 of Ref. 38.

The most notable feature of these PESs is that the inner saddle points to formation of each of the four isoprene-OH adducts are found *below* the reaction asymptote. This result is contrary to those previously reported by Francisco-Marquez et al.,[44] which suggested that formation of isomers 2 and 3 involves surmounting a barrier above the OH-isoprene reaction asymptote (Table IV-IV). In such a model, the rates of formation of isomers 1 and 4 are so much faster, than for isomers 2 and 3, that isomers 2 and 3 should never be formed at room temperature. Experimental studies support the formation of isomers 2 and 3 in non-negligible quantities.[33]

Saddle points for isomers 1 and 4 were located using computational scheme (IV-I) at 2.35 Å carbon-oxygen separation and 2.3 Å carbon-oxygen separation, respectively. This method was also applied to the location of saddle points for isomers 2 and 3, where saddle points were located at 2.15 Å carbon-oxygen separation and 2.1 Å carbon-oxygen separation, respectively. These saddle points are in relatively good agreement with those found on the B3LYP surface at 2.08 Å carbon-oxygen separation and 2.105 Å carbon-oxygen separation for isomers 2 and 3.

B3LYP is known to give credible geometric parameters and frequencies for organic molecules.[143] Traaeteberg et al.[139] experimentally determined structural parameters for isoprene using a gas-phase electron diffraction technique. Experimentally determined geometrical parameters compared with the calculated parameters are in good agreement as seen in Figure IV-IV. In addition, the vibrational frequencies for isoprene are in good agreement with those determined experimentally[139] (Table IV-I).

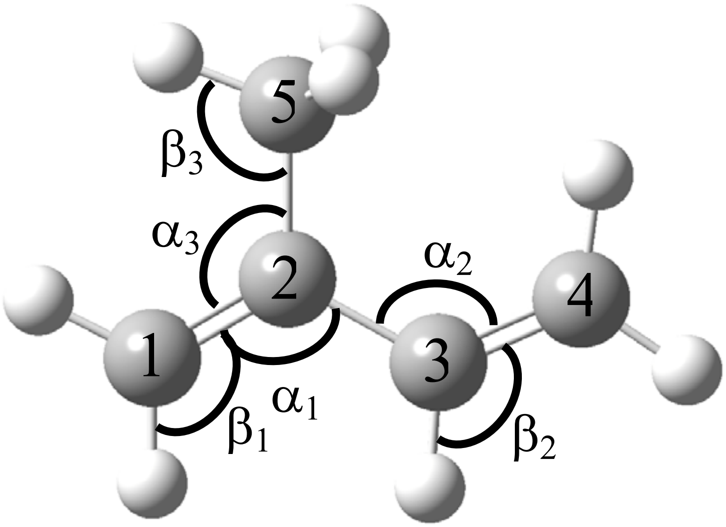

Parameter	B3LYP/6-311++G**	Experiment
C=C	1.342 Å	1.350 Å
C_2-C_3	1.467 Å	1.463 Å
C_2-C_5	1.508 Å	1.512 Å
$C_{sp}{}^2$-H	1.084 Å	1.076 Å
$C_{sp}{}^3$-H	1.091 Å	1.110 Å
$\angle\alpha_1$	119.7°	121.4°
$\angle\alpha_2$	126.1°	127.3°
$\angle\alpha_3$	121.5°	121.0°
$\angle\beta_1$	121.4°	124.3°
$\angle\beta_2$	118.6°	123.4°
$\angle\beta_3$	111.0°	109.1°

Figure IV-IV. Computationally determined structure of isoprene with relevant geometrical parameters compared to geometrical parameters determined by the gas-phase electron diffraction method presented in Ref. 139. Adapted from Figure 3 of Ref. 38.

High frequency motions are reasonably described by harmonic oscillator potentials and errors in these frequencies do not result in large errors in the rate predictions. Moreover, as rate calculations involve ratios of partition functions, one can often expect cancellation of errors. Firstly, the frequency calculations for both species need to be performed at the same level of theory. Secondly, the conserved modes would be estimated either high or low in the same direction for both the transition state and the reactant(s). It is clear that only the lowest frequency motions, on the order of a couple hundred cm^{-1} need to be considered as a possible source of error to the kinetics evaluations. We treat the majority of these low frequency motions as hindered rotors, which should provide a quite accurate treatment.

Rate Constants in the High-Pressure Limit. In calculating the capture rate on the long-range part of the potential for OH addition to isoprene, it is not obvious, *a priori*, which electrostatic interaction will be dominant. Capture rates considering the dipole-quadrupole, dipole-dipole, dipole-induced dipole, and dispersion forces were all considered as well as a capture rate considering the sum of these interactions (where the sum is dominated by dispersion forces). The temperature dependent capture rates for the various interactions can be found in Table IV-II.

The present predictions for the OH + isoprene rate constant in the high-pressure limit are illustrated in Figure IV-V, together with the available experimental data. The solid line in Figure IV-V is the simulation excluding any adjustment to the *ab initio* determined saddle point energy. A modest adjustment in the saddle point energy to formation of each OH-isoprene adduct of –0.8 kcal/mol yields high-pressure rate constants in better agreement with the experimentally determined rate constants as can be seen by the higher dotted line in Figure IV-V. The adjustment affords a 300 K rate constant of 1.06×10^{-10} cm^3 $molecule^{-1}$ s^{-1}, which is in good agreement with the recommended value. The lower dashed line reflects an increase in the saddle point energy of 0.8 kcal/mol. Nearly all of the available high-pressure limit rate constants fall within a few percent of the dotted line. A consistent use of the saddle point adjustment of –0.8 kcal/mol was chosen based on the excellent agreement between the model and the high-pressure limit data.

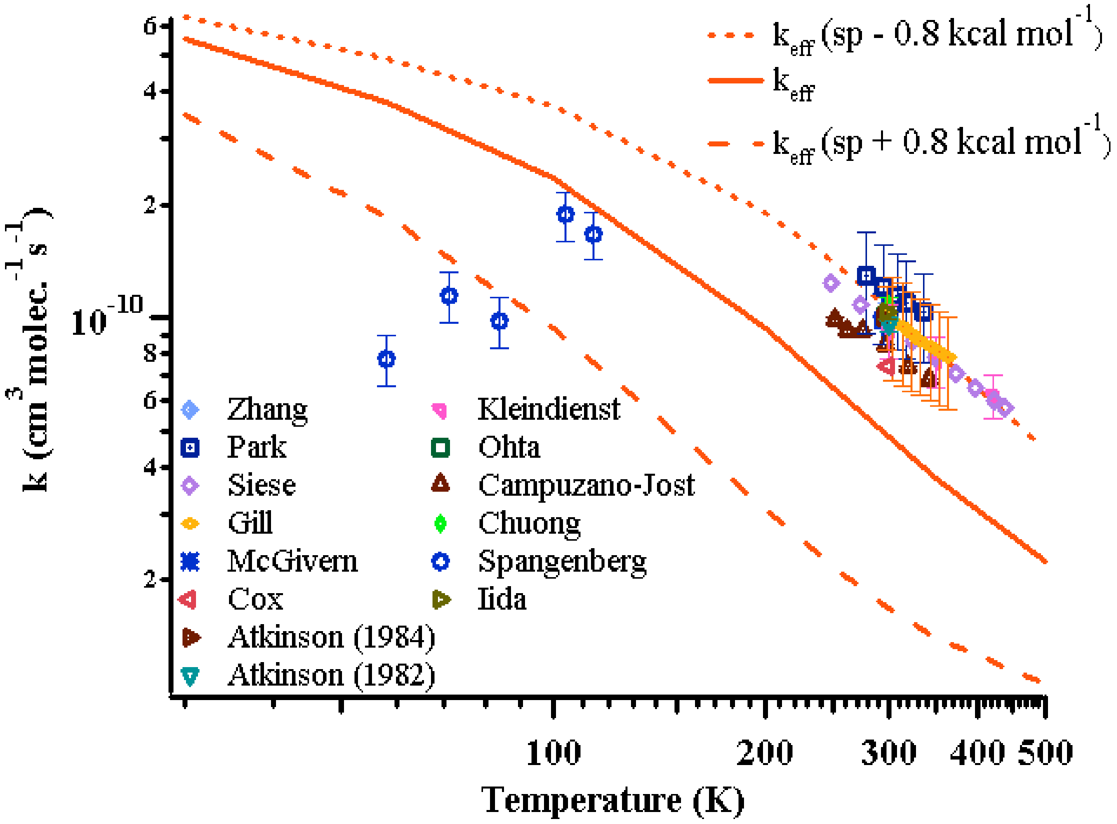

Figure IV-V. Effective high-pressure rate constants employing a ± 0.8 kcal mol^{-1} adjustment to the saddle point energy as a function of temperature for all four isoprene-OH adducts compared to experimental data. (Zhang Ref. 32, Kleindienst Ref. 25, Park Ref. 28, Ohta Ref. 27, Siese Ref. 29, Campuzano-Jost Ref. 15, Gill Ref. 23, Chuong Ref. 22, McGivern Ref. 26, Spangenberg Ref. 30, Cox Ref. 21, Iida Ref. 24, Atkinson (1984) Ref. 17, Atkinson (1982) Ref. 18) Adapted from Figure 4 of Ref. 38.

This decrease is similar to what was found to be necessary for describing the reaction kinetics in the OH-ethylene system. Importantly, this decrease in the *ab initio* predicted saddle point is well within the expected uncertainty of the quantum chemical calculations and should be considered as a likely error in these calculations. Errors of this magnitude are consistent with multi-reference effects of the wavefunction using the employed *ab initio* methodology. Benchmarking with the ethylene-OH case, however, offers substantial confidence to the accuracy of this methodology and as an analogous model, one expects a decrease on the order of ~1 kcal/mol to the predicted saddle point energy.

The lower rate constants, when compared to the average in Figure IV-V, by Campuzano-Jost et al.[15] are in very good agreement with the temperature dependence seen. In that work, isoprene concentrations were measured in situ via UV absorption. The authors note that an error in the absorption cross section of isoprene would directly translate to a systematic error in the measured rate constants. The faster than average rate constants determined by Park et al.[28] are likely due to the difficulties in accurately extrapolating low pressure measurements to the high-pressure limit.

The low temperature data points of Spangenberg et al.,[30] are consistent with an appreciable positive temperature dependence of approximately $T^{3/2}$. Such a temperature dependence differs from standard long-range electrostatic capture rates and may be the result of errors due to the challenges associated with low temperature measurements and the authors cite several sources of plausible error. Similar low-temperature experiments have been employed for the addition of OH to ethylene, propene, and 1-butene[83] and to a series of butenes.[133] In these studies, a monotonic increase in the observed rate constants with a decrease in temperature is observed. An explanation for the substantial differences in the temperature dependence exhibited in the OH addition to isoprene is not obvious. One would expect, as the present calculations predict, that a similar trend in the low temperature rate constants would be observed. Sims et al. note that the low-temperature rate constants are only limited by the capture rate. We have shown, in the previous study on the OH addition to ethylene, that inclusion of the long-range electrostatic potential provides rate constant estimates in excellent agreement with those experimentally determined at low temperatures. One aspect of this analysis involved the realization that Leone and coworkers measurements for the ethylene-OH system were not in the high pressure limit. A similar deviation from the high pressure limit might help explain some of the discrepancies between our predictions and the Spangenberg et al.[30] measurements. However, explicit master equation simulations indicated that the isoprene-OH system is in the high pressure limit for the experimental conditions of Ref. 30.

The reproduction of the observed temperature dependence provides a stringent test for theory. The activation energy, defined as –Rd(lnk)/d(1/T), has been of interest for this and analogous systems due to its negative value under ambient conditions. This is not quantitatively identical to the negative value of the saddle point energy relative to separated products (threshold energy in a transition state theory context) as has been proposed in previous reports.[44] The present calculations are in excellent agreement with experimental observations, which indicate an Arrhenius activation energy of −1 kcal/mol at room temperature. The calculated activation energy is –0.77 kcal/mol. At higher temperatures, the temperature dependence changes sign due in the large part to the change of mechanism to a predominant hydrogen abstraction mechanism.

Figure IV-VI compares the rate constants when including only the flux through the outer transition state, only the flux through the inner transition state, and the effective flux when considering both transition states. Furthermore, the dashed line presents the effective rate constants including both the inner and outer transition state rate constants, but combined at the *canonical* level. It is evident that over the entire temperature range, the effects of both transition states are prevalent. At 300 K, there is a 62% reduction in the addition rate upon including the effects of both transition states, at the E,*J*-resolved level, as compared to considering the inner transition state alone. Even at 500 K, the rate constant including both transition states is substantially (18%) lower than that determined using only the inner transition state. It is also clear from the results that the flux through each transition state must be combined at the E,*J*-resolved level. At 300 K, there is still a 35% reduction in the rate constant achieved by combining flux at the E,*J*-resolved level of theory over combining the rate constants at a canonical level. This effect is significant (i.e. by more than 10%) over the entire temperature range from 58-350 K.

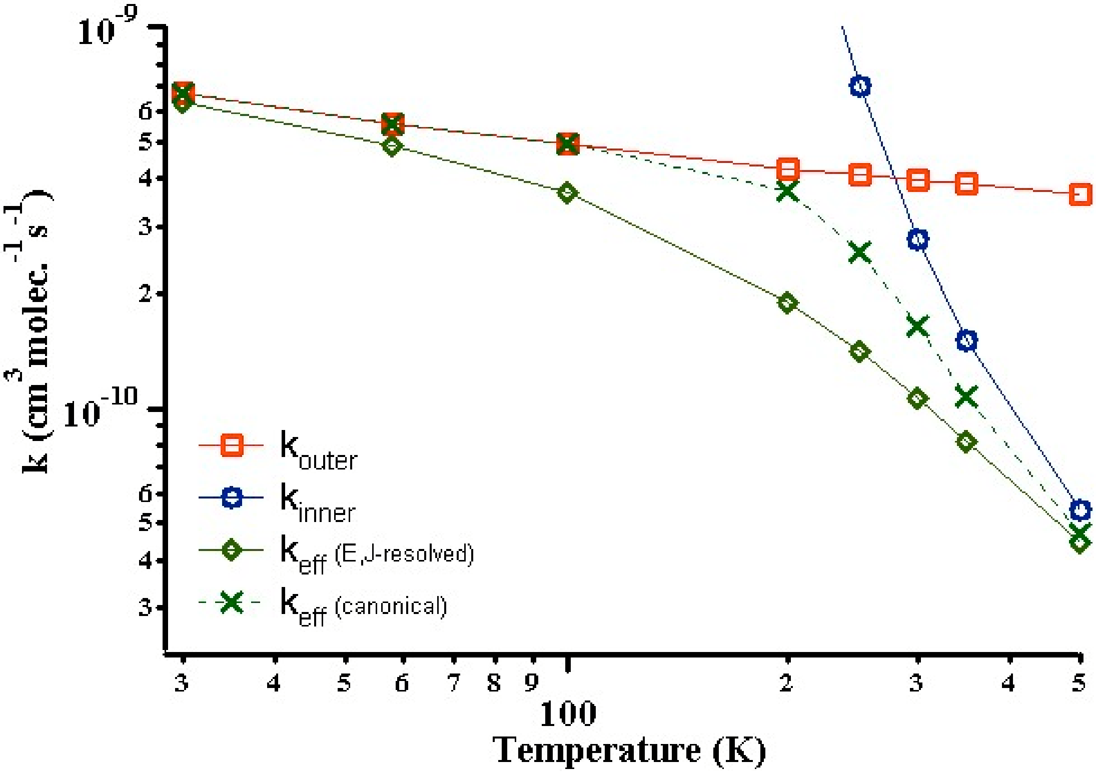

Figure IV-VI. High-pressure rate constants as a function of temperature for the flux through the outer transition state, the inner transition state and combined flux through both transition states considering both a combination of flux at the canonical level and a combination of flux at the E,J-resolved level. Adapted from Figure 5 of Ref. 38.

Although Francisco-Marquez et al.[44] did consider flux through two transition states, the long range transition state was considered in the context of an equilibrium constant describing the formation and dissociation of a loosely bound van der Waals complex. This treatment relied on the implicit assumption that the van der Waals complexes suffer many collisions before reaction such that a thermal distribution of states is maintained, permitting the use of *canonical* rate constants. The shallowness of the van der Walls wells suggests that this is seldom if ever true in the present reaction. Additionally, their overall rate constant calculation relies a steady-state approximation as described in Eq. (3-1). Furthermore, k_{-1} was then assumed to be much larger than k_2 leading to the expression $k=K_{eq}k_2$ over the range of temperatures considered. Such an assumption was invalid in precisely the interesting temperature region where the two transition states provide a comparable bottleneck to the reactive flux.

Branching Ratio Determination. The present predictions for the branching ratios as a function of temperature are provided in Table IV-V. At room temperature, the branching ratio is determined to be 0.67:0.02:0.02:0.29 (1:2:3:4). This ratio is fairly insensitive to temperature spanning the entire range from 30-500K. Differences in the errors in the quantum chemical estimates for the addition of OH to one of the inner positions of isoprene vs. the addition of OH to one of the outer positions may arise from having transition states of different quality (i.e. the transition states to formation of isomers 1 and 4 are looser than that of 2 and 3). It is reasonable to assume that the errors in the quantum chemical estimates for isomers 1 and 4 (and their corresponding transition states) are of similar magnitude and in the same direction, as is the case for isomers 2 and 3. However, this is not necessarily the case between the two sets of isomers 1,4 and 2,3. In order to assess the possible impact of errors in the quantum mechanical calculations on the branching ratios, branching ratio ranges are determined.

High-pressure limit rate calculations were performed where the saddle point energies of the dominant pathways (formation of isomers 1 and 4) were held at constant saddle point reductions of 0.8 kcal/mol for each saddle point and the other two saddle point energies were adjusted by ± 1 kcal/mol of this adjustment (i.e. saddle points corresponding to each of isomers 2 and 3 were adjusted up by a total of 0.2 kcal/mol and down by a total of 1.8 kcal/mol). Such adjustments are fairly representative of the possible errors in the relative barrier heights. While this adjustment has only a minimal effect on the total rate constant, as there is only a few percent contribution from the inner addition positions, the effect on the branching ratio is more substantial. The ± limits on the branching ratios were calculated in this way (Table IV-V).

Table IV-V: Branching ratios, as a function of temperature, for the OH addition to isoprene leading to formation of isomers 1, 2, 3, and 4 at the high-pressure limit.

Temperature (K)	Isomers			
	1	2	3	4
30	0.68 ± 0.03	0.03 ± 0.03	0.01 ± 0.01	0.28 ± 0.01
58	0.68 ± 0.03	0.03 ± 0.03	0.01 ± 0.01	0.28 ± 0.01
100	0.68 ± 0.02	0.03 ± 0.03	0.01 ± 0.01	0.29 ± 0.01
200	0.67 ± 0.02	0.02 ± 0.02	0.01 ± 0.01	0.29 ± 0.01
250	0.67 ± 0.02	0.02 ± 0.02	0.01 ± 0.01	0.29 ± 0.01
300	0.67 ± 0.03	0.02 ± 0.02	0.02 ± 0.01	0.29 ± 0.01
350	0.66 ± 0.03	0.02 ± 0.02	0.02 ± 0.01	0.29 ± 0.01
500	0.64 ± 0.03	0.03 ± 0.02	0.03 ± 0.02	0.30 ± 0.01

Adapted from Table 5 of Ref. 38.

We find that the branching ratios are insensitive to changes in pressure, and as shown in Table IV-V, relatively insensitive to temperature. The branching ratios determined here are in good agreement with those determined previously using structure additivity relationships. Structure additivity relationships yield a branching ratio of 0.618:0.044:0.044:0.294 for isomers 1, 2, 3, and 4, respectively.[42,43] Lee et al.[35] adopted the branching ratio proposed by Jenkin[36] of 0.60:0.05:0.05:0.31 (1:2:3:4) in the interpretation of their experimental result. The work of Park et al.[28] included a branching of 93% OH addition to the terminal positions of isoprene in the extension of their cycling mechanism used to predict the first generation end product distribution with good agreement with the reports of Atkinson,[144] Jenkin,[36,145] Zhao,[146] and Paulson.[41]

In the work of Stevens et al.,[31] termolecular rate constants were calculated in the low pressure limit and a branching ratio of 0.72:<0.01: <0.01:0.28 (1:2:3:4) was determined. The authors argued that an equal production of all 4 isomers under tropospheric conditions was likely since the differences between the transition states would be negligible, leading to adduct formation of comparable yields for all four isomers. In the model presented by McGivern et al.,[26,45] a simple Morse function was used to represent the potential energy surface of the OH addition to form each of the four isoprene-OH adducts (1-4). Rates of reaction were then determined employing variational RRKM theory. That work presents a computational result of 0.56:0.023:0.046:0.37 (1:2:3:4), which is in general agreement with the present result. Their monotonically increasing potential energy surface (PES) neglects reaction coordinate saddle points and other (PES) intricacies. Of particular importance at low to moderate temperatures, these treatments neglect a proper inclusion of the outer transition state. The work of Francisco-Marquez et al.[44] excludes contributions from OH addition to either of the internal positions due to inner transition states which lie above the reaction asymptote. The reported branching ratio is 0.69:0.00:0.00:0.31 (1:2:3:4).

It is noteworthy that the absolute energies of the inner saddle points are not the only factors, which determine the branching ratio of the OH-isoprene adducts, though this is the most significant factor. Another contribution to each rate is dictated by geometrical parameters. Saddle points are located at carbon-oxygen separations of 2.35, 2.08, 2.105, and 2.3 Å for isomers 1-4, respectively. Saddle points are found at larger carbon-oxygen separations for isomers 1 and 4 and the corresponding motions for these transition states are slightly looser, contributing to faster rates. For example, the imaginary frequencies (denoted with an "I" in Table IV-I) are, on average, approximately 40% larger for saddle points 2 and 3 as compared to saddle points 1 and 4. This is indicative of saddle points 1 and 4 having less curvature in the reaction coordinate, where the curvature is related to the forces acting on the reaction coordinate. For all of the frequencies below ~700 cm^{-1}, saddle points 1 and 4 are markedly smaller than the corresponding frequencies in saddle points 2 and 3.

Pressure-Dependent Rate Constants. We have performed 2D master equation simulations of the pressure dependence in both Ar and He carrier gasses. The results for each case employing a downward energy transfer parameter, $\langle \Delta E_{down} \rangle$, of $150(T/298)^{0.7}$ cm^{-1} are illustrated in Figure IV-VII. Included in the figure are experimental observations for Ar (top panel) and He (bottom panel). This functional form for the energy transfer parameter was employed previously in the 2D master equation simulations of the OH addition to ethylene, where the pressure-dependent calculations provided an excellent fit to experimental data. In the ethylene-OH case, the fall-off regime spans much higher pressures (up to several hundred Torr) and accurate determination over a large data set in this regime provides a stringent test for the theoretical model.

The isomerization between adduct isomers has not been considered in the present simulations. Lei et al.[45] determined barriers to isomerization at the CCSD(T)/6-311G**//B3LYP/6-31G** level of theory and RRKM/ME calculations were used to assess the impact of the isomerization reactions on the overall pressure dependence of the OH addition to isoprene. Isomerization rates were found to be 3 orders of magnitude slower than dissociation rates and therefore, considered to have a negligible impact on the overall kinetics. The slow isomerization rates, despite comparable barrier heights to adduct dissociation, are a result of the tightness of the isomerization transition states compared to the loose nature of the transition states associated with adduct formation/dissociation. Additionally, the authors reported that the isomerization pathway had a negligible effect on the branching into the 4 isoprene-adduct wells.

The results of Park et al. (open symbols)[28] and McGivern et al. (solid symbols)[26] for the pressure dependent rate constants are presented in the upper panel of Figure IV-VII. The data of McGivern et al. was measured at the single temperature of 295 K. As discussed previously, the extrapolation to the infinite pressure limit provided by a Troe Formalism fit in each case, compared to the recommended value at 298 K, indicates that the values reported by McGivern et al. are slightly low; whereas, the values of Park et al. are slightly high. We note that a 298 K value of $\langle \Delta E_{down} \rangle$ = 50 cm^{-1} provides a much better fit to the available data measured in Ar; although, this is a low value for the energy transfer parameter. Considering the challenges associated with measurements of low pressure rate constants, we find reasonable agreement between the present calculations and the available pressure-dependent data.

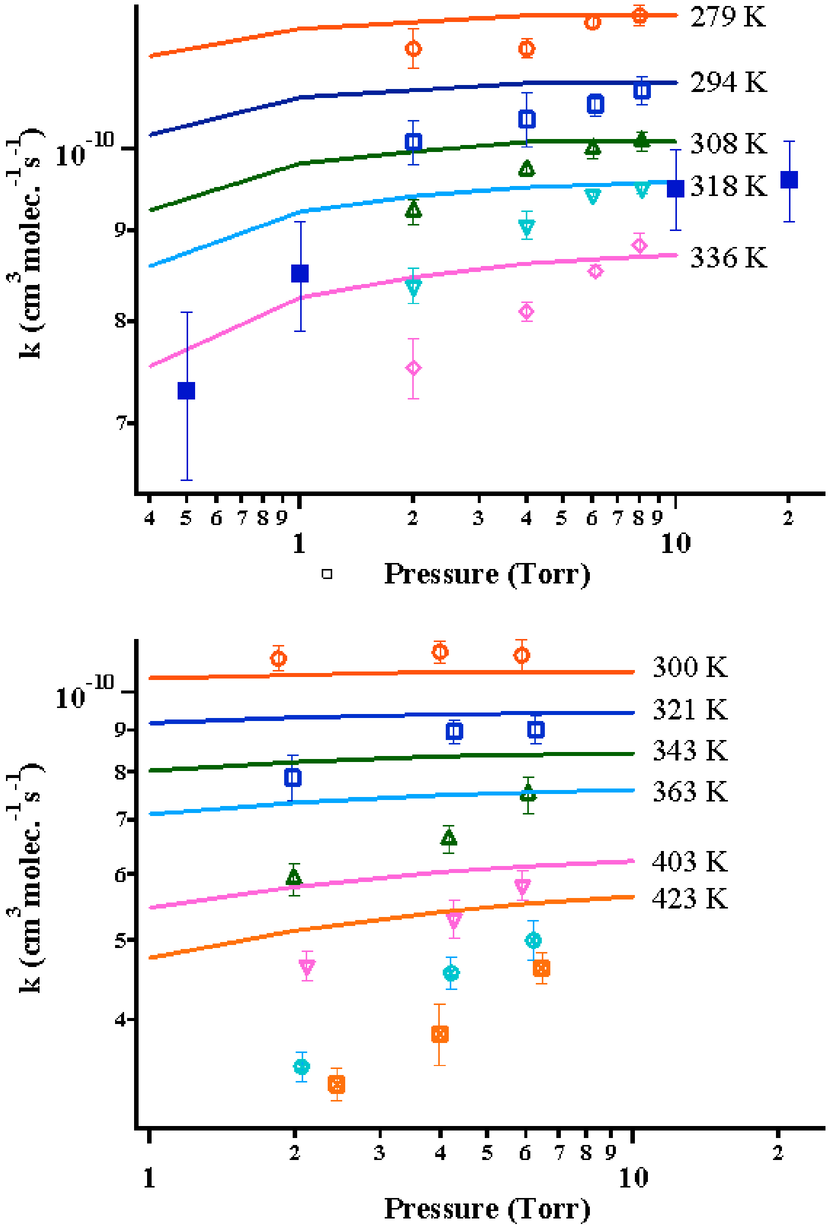

Figure IV-VII. Pressure-dependent rate constants for the association of isoprene and OH at a variety of temperatures in Ar and He carrier gasses. Top: Effective rate constants as a function of pressure (in Ar carrier gas) for all four isoprene-OH adducts compared to the experimental works of Park et al. (open symbols, Ref. 28) and the experimental works of McGivern et al. at 295 K (closed symbols, Ref. 26). Bottom: Effective rate constants as a function of pressure (in He carrier gas) for all four isoprene-OH adducts compared to the experimental works of Chuong et al. (Ref. 33). Adapted from Figure 6 of Ref. 38.

The pressure dependent results of Chuong and Stevens[33] are presented for a series of temperatures in the lower panel of Figure IV-VII. We are unsure as to the origins of the differences between our calculations and the experimental data at higher temperatures. The discrepancy may suggest that the experimental rates have a systematic error, which caused an underestimation in the lower pressure rates at higher temperatures and lead to the strong pressure dependence. Alternatively, some aspect of the pressure dependent calculations causes an overly gradual approach to the high-pressure limit for these temperatures.[147]

D. Conclusions

We have extended the previously developed two-transition state model for OH addition to ethylene to the case of OH addition to isoprene. We have calculated the rates of reaction under ambient conditions as well as examined low temperature rates of reaction and rates of reaction as a function of pressure and temperature in the fall-off regime. We combined phase space theory calculations with standard RRKM theory calculations to determine the contribution to the rates of reaction from both an outer and an inner transition state.

With a modest adjustment of the saddle point energies to each of the four OH-isoprene isomers (1-4) of –0.8 kcal/mol, we were able to accurately reproduce the high-pressure limit, temperature dependent rate constants. The high-pressure limiting 300 K rate constant of the OH addition to isoprene calculated here of 1.06×10^{-10} cm^3 $molecule^{-1}$ s^{-1} is consistent with the recommended value. The theoretically predicted capture rate is reproduced to within 10% by the expression $[1.71\text{x}10^{-10}(T/298)^{-2.58}\exp(-608.6/RT) + 5.47\text{x}10^{-11}(T/298)^{-1.78}\exp(-97.3/RT)$; with $R = 1.987$ and T in K] cm^3 $molecule^{-1}$ s^{-1} over the 30-500 K range. A 300 K, high-pressure limit branching ratio of 0.67:0.02:0.02:0.29 was determined for isomers, 1, 2, 3, and 4, respectively. An Arrhenius activation energy of –0.77 kcal/mol was determined for the high-pressure addition rate constants around 300 K. The branching ratio was determined to be relatively insensitive to changes in temperature and independent of pressure. Using reasonable parameters for collisional energy transfer in the exponential down model, we were able to satisfactorily reproduce the pressure dependence of these reactions at a variety of temperatures in Ar and He buffer gasses.

CHAPTER V

INTRODUCTION TO EXPERIMENTAL TECHNIQUES[*]

A. Background

There is considerable interest in the atmospheric oxidation of unsaturated hydrocarbons due to their role in ozone production, aerosol formation, and acid rain.[5] Although significant progress has been made toward unraveling the detailed mechanisms of OH initiated oxidation, questions persist. In the case of larger unsaturated hydrocarbons, like isoprene, the electrophilic addition of OH results in multiple radical isomers. Often the number of intermediate species increases following the reaction with O_2 and further branching can occur during subsequent steps on the way to first generation end products. Although recent *ab initio* studies[26,31,38,45,148,149,150,151,152] have made a substantial impact in providing *a priori* predictions of these branching ratios in isoprene oxidation, direct experimental confirmation is unavailable. Recent kinetic studies have relied on OH-regeneration to infer information about the isomeric branching.[15,22,28,153,154] Analysis of the results suggests qualitative agreement with theoretical predictions but the complexity of the reaction systems has precluded a quantitative treatment. To date all of the kinetic data reflects “lumped,” non-isomeric selective rate constants.

Direct measurements of the intermediates using either chemical ionization mass spectrometry[155] or transient absorption have also been unable to extract isomeric specific rate constants and branching ratios. Zalyubovsky and co-workers have recently demonstrated the feasibility of using cavity ring-down spectroscopy on the resolved A-X

---

[*] Parts of this chapter are preprinted with permission from “The OH Initiated Oxidation of Isoprene in the Presence of O_2 and NO: A Photolytic Route to Study Isomeric Selective Reactivity” Greenwald, E. E.; Ghosh, B.; Anderson, K. A.; Dooley, K. S.; North, S. W. *J. Phys. Chem. A.* **2007**, in preparation. Additional parts of this chapter are reprinted with permission from "The OH Initiated Oxidation of 1,3-Butadiene in the Presence of O2 and NO: A Photolytic Route to Study Isomeric Selective Reactivity" Greenwald, E. E.; Anderson, K. C.; Park, J.; Kim, H.; Reich, B. J. E.; Miller, S. A.; North, S. W. *J. Phys. Chem.. A* **2005**, *109*, 7915.

transition of peroxy radicals to obtain selective detection.[156] In those studies, the peroxy radicals were generated *via* reaction of a hydrocarbon with OH in the presence of O_2. As the hydrocarbons become more complex and the resulting number of isomers increases, however, the spectroscopic assignments will be challenging. Ideally one would like to isolate the isomers and thus simplify the ensuing kinetics. In addition to making kinetic studies more tractable, isomeric selective studies permit the investigation of minor, yet important, channels that are difficult to study in the presence of major channel kinetics. The photodissociation of a suitable precursor can, in principle, provide a route to the formation of a single isomer.

OH addition to isoprene to form the allylic radicals (isomers 1 and 4) is the dominant addition pathway in the troposphere, while OH addition to form the primary radicals (isomers 2 and 3) is the minor addition pathway. The majority of the literature concurs that the primary radicals are formed with a yield of only a few percent under tropospheric conditions. The most recent theoretical study of Greenwald and coworkers[38] provides a branching ratio of approximately 4% of the total OH addition to isoprene resulting in one of the two primary radicals. In the presence of O_2 and NO, further branching ensues in the case of all four radicals. The initial branching into the first four isomers essentially “locks in” subsequent kinetics, although this initial branching ratio is difficult to ascertain as further branching occurs. Additionally, many of the fundamental chemical steps from early on in the reaction are invisible to typical experimental setups as minor channels in the reaction are flooded by species of similar chemical identity being generated by the major channels. The widely accepted photooxidation mechanism fates all 4 isoprene-OH adducts (1-4) with O_2 addition to form peroxy radicals. Isomers 1 and 4 have a cis and a trans conformation, so 6 peroxy radicals result from OH addition to one of the inner positions of isoprene in the presence of O_2. In recent years, the mechanistic details pertaining to the isoprene-OH adduct primary radicals have been challenged.

It was proposed that the primary radicals formed via OH addition to a conjugated unsaturated hydrocarbon would undergo a prompt cyclic isomerization, which would then undergo a facile hydrogen abstraction to produce an aldehyde or ketone products rather than peroxy radicals in the presence of O_2. The reaction of α-hydroxyalkyl radicals with O_2 proceeds *via* hydrogen abstraction, resulting in carbonyls and HO_2, whereas the dominant fate of β-hydroxyalkyl radicals in the presence of O_2 is addition to yield peroxy radicals.[157,158,159,160] Ideally, one could study the chemistry of each OH-isoprene addition product (isomers 1-4) individually. As there is no way to direct the OH addition to isoprene in the gas phase, other methods must be pursued to pare down the mechanism to obtain detailed kinetic information.

In 1976, Jack Baldwin established a number of empirical rules in order to predict the "*relative facility*" of ring formation.[161] The rules are applied through a naming scheme, where three characteristics for the ring to be formed are considered and the name takes the format 'ring size'-'*Exo*/*Endo*'-'*Tet*/*Trig*/*Dig*'. The ring size denotes the size of the ring being formed, Exo or Endo describes whether the radical will be attacking an unsaturated site from an internal (*Exo*) (an exocylcic attack, forming the smallest ring) or end-on (*Endo*) site as described in Figure V-I, and the final term denotes the geometry of the carbon undergoing the ring closure, i.e. *Tet* for sp^3 geometry, *Trig* for sp^2 geometry, and *Dig* for sp geometry.

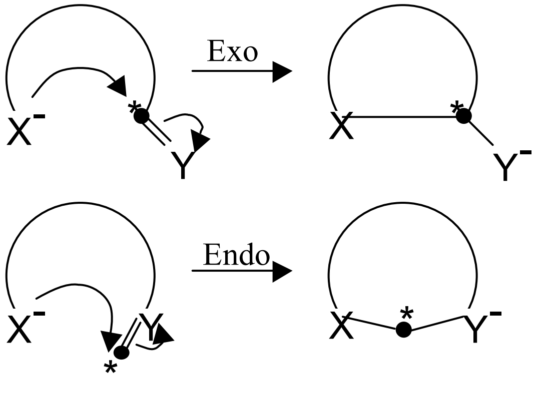

Figure V-I. Schematic representation of *Exo* vs. *Endo* ring closure as defined by Baldwin's rules. Asterisks denote the carbon under attack (i.e. the position corresponding to the *Tet*, *Trig*, or *Dig*) and the '–' corresponds to the radical. Adapted from Scheme 1 of reference 161.

In the case of β-hydroxyalkyl radicals formed upon OH addition to the inner position of 1,3-butadiene or one of the inner positions of isoprene (isomers 2 and 3), two possibilities for ring closure exist. The 3-*Exo-Trig* and 4-*Endo-Trig* ring closure possibilities for the β-hydroxyalkyl radical formed upon OH addition to the internal carbon of butadiene, are displayed in Figure V-II.

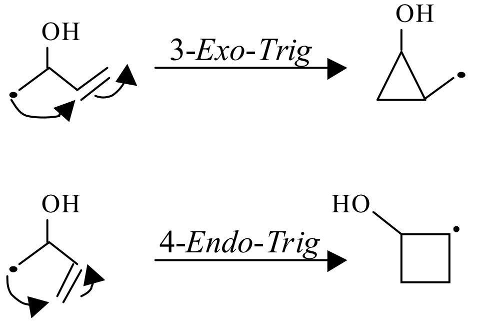

Figure V-II. 3-*Exo-Trig* and 4-*Endo-Trig* ring closure possibilities for the β-hydroxyalkyl radical formed upon OH addition to the inner position of 1,3-butadiene.

As the rules are based on considerations of the steric hindrance of the attacking radical, (i.e. p-orbital overlap of the radical with the p-orbital of the receiving carbon), it is no surprise that the 3-*Exo-Trig* ring formation is favored over the 4-*Endo-Trig* formation. Although this isomerization pathway, 3-*Exo-Trig*, is well known in solution,[161] to our knowledge, the first discussion of this chemistry in the gas-phase appeared in the context of isoprene oxidation, as the result of addition of OH to conjugated, unsaturated hydrocarbons.[37]

Investigations into the cyclic isomerization pathway of conjugated unsaturated hydrocarbons have included both computational and experimental explorations. In the case of the primary β-hydroxyalkyl radical formed when OH adds to the second or third position of isoprene, Park and coworkers[37] performed a computational study, which included detailed calculations of the potential energy surface along with RRKM rate calculations coupled with a 1D Master Equation (ME) treatment of the pressure dependence. This study concluded that not only is the cyclic isomerization pathway shown in Figure V-III feasible, it is favorable. Based on the RRKM/ME analysis, OH addition to isoprene producing the β-hydroxyalkyl radical (isomer 2) will isomerize through a 3-membered cyclic intermediate (2b) forming the corresponding α-hydroxyalkyl (2c) radical with nearly 100% yield. OH addition to isoprene producing the β-hydroxyalkyl radical (isomer 3) will isomerize through a 3-membered cyclic intermediate (3b) forming the corresponding α-hydroxyalkyl radical (3c), but only with a ~50% yield.

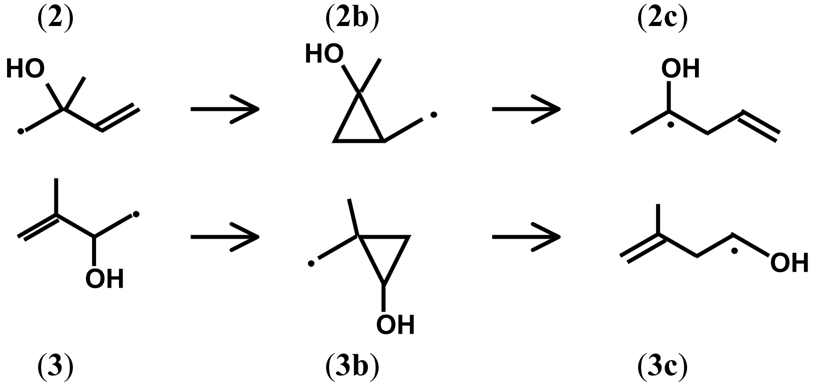

Figure V-III. Cyclic isomerization pathways for the β-hydroxyalkyl radicals formed upon OH addition to one of the inner positions of isoprene.

In the presence of O_2, there will be negligible peroxy radical formation for isomer 2 as there will be complete conversion of the β-hydroxyalkyl radicals to the α-hydroxyalkyl radicals, which then undergo facile hydrogen abstraction by O_2 to produce 1-penten-4-one. Isomer 3 reactivity is slightly different, as about half of it will react to produce peroxy radicals while the other half will undergo cyclic isomerization followed by hydrogen abstraction by O_2 to produce 2-methyl-1-butenaldehyde. Mechanistic differences, such as these, create a need to study these mechanisms on an isomeric specific level.

In the present studies, we focus on the photolytic production of one of two possible isomers following OH addition to 1,3-butadiene, the addition of OH to the inner carbon, to demonstrate the feasibility of this approach. It is expected that this is the minor channel, based on the analogous methyl-substituted butadiene (2-methyl-1,3-butadiene, isoprene) where there is preferential addition of OH to one of the terminal carbons. We then extend our study to focus on the photolytic production of one of the four possible isomers following OH addition isoprene, the addition of OH to the methyl-substituted carbon, to determine the subsequent kinetics of this reactive intermediate.

There are several requirements, which must be considered prior to selecting a photolytic precursor. The synthetic preparation of the photolytic precursor should be feasible. The photodissociation should have an appreciable absorption cross-section at the photolysis wavelength and result in a single product channel with near unit quantum yield. And, there is an additional, subtler, requirement, which is particularly relevant in the present study. The thermal addition of OH to 1,3-butadiene or isoprene results in highly activated radicals with internal energies in excess of the exothermicity of the reactions. Thus, in order to mimic subsequent reactivity of these radicals under thermal conditions, the photolytic route must result in a nascent internal energy distribution consistent with thermal activation. Halogenated compounds are suitable precursors since excitation in the UV/Vis region typically involves an $n \rightarrow \sigma^*$ transition on the C-X moiety resulting in prompt dissociation of this bond. Given the relative bond strengths of the carbon-halogen bonds, the location of the corresponding absorption maxima in the UV/Vis region, and the energy partitioning predicted for a direct dissociation on a repulsive potential[162], we find that the iodine substituted compounds, shown in Figure V-VI, are ideal.

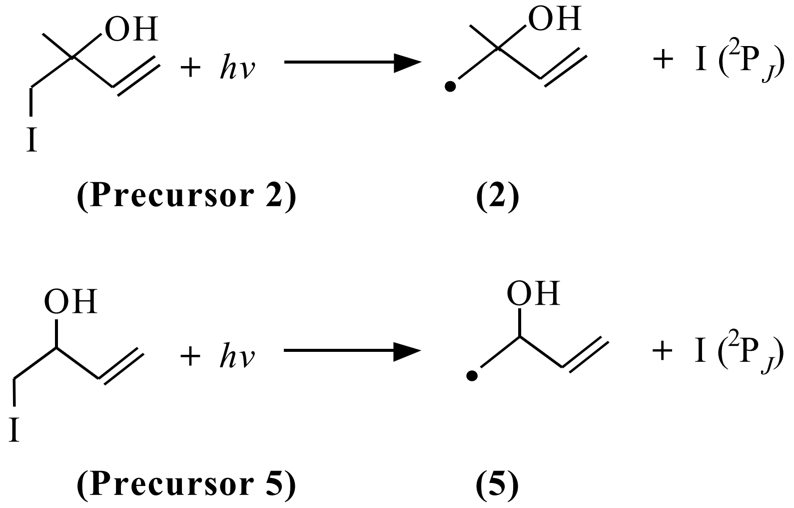

(Precursor 2) **(2)**

(Precursor 5) **(5)**

Figure V-IV. Iodohydrin photolytic precursors for the isomeric selective studies of β-hydroxyalkyl radicals formed upon addition of OH to one of the inner positions of isoprene (**2**) and butadiene (**5**).

To this end, we have synthesized the photolytic precursors, 1-iodo-2-methyl-3-buten-2-ol (**Precursor 2**) and 1-iodo-3-buten-2-ol (**Precursor 5**). Photolysis at 248 nm or 266 nm should produce activated β-hydroxyalkyl radical **2** and **5**, respectively. We are particularly interested in this radical due to the cyclic rearrangement pathway, which leads to an α-hydroxyalkyl radical.

The first direct experimental study of this chemistry in the gas phase,[39] presented in Chapter VI, provided the corresponding theoretical predictions in the same work. 1,3-butadiene, an analogous conjugated unsaturated hydrocarbon to isoprene, was chosen due to simplification compared to the isoprene system. OH addition to butadiene leads to 2 distinct isomers, as opposed to the 4 distinct isomers formed upon OH addition to isoprene. Computational work predicted nearly identical subsequent chemistry for the butadiene case as had been predicted for isoprene. The cyclic isomerization pathway was shown to be both a feasible and energetically favorable fate for the primary β-hydroxyalkyl radical. A photolytic precursor to the OH addition to the inner position of butadiene was synthesized and photolyzed to produce only the primary β-hydroxyalkyl radical. The velocity map ion imaging technique was used to measure the internal energy distribution of the nascent radicals and the LP/LIF technique was then used to observe the subsequent kinetics. The hydroxyl radical was used as a proxy to following the time dependent kinetics as it was generated from the reduction of the HO_2 produced during the hydrogen abstraction from the α-hydroxyalkyl radical. Regeneration of OH on the time scale of ~80 μs, as opposed to the regeneration of OH on the time scale of ~300 μs in the case standard cycling measurements which primarily probe OH regeneration due to the cycling mechanism of the allylic radicals, provided strong evidence toward the cyclic isomerization pathway. A judicious choice of initial conditions, careful modeling, and utilization of sensitivity coefficients allowed confirmation of the cyclic isomerization pathway in the case of OH addition to the inner position of butadiene.

Upon completion of the butadiene study, a proof of principles to the methodology, precursor **2** was prepared and the subsequent kinetics investigated. The results of that study are provided in Chapter VII. Slight variations were made in this study, which are outlined throughout the text. The most significant addition to that study over the butadiene was the addition of a time-dependent multiplexed mass spectrometer analysis of the reaction kinetics.

The remainder of this chapter details the experimental aspects of these studies, i.e. details of the synthesis, the VELMI experimental apparatus, the time-dependent multiplexed mass spectrometer experiment (used in the precursor 2 studies, and the LP/LIF experimental apparatus. The results of the corresponding studies are presented in Chapter VI in the case of the butadiene iodohydrin and Chapter VII in the case of the isoprene iodohydrin.

The coalescence of these experimental techniques provides strong support for the cyclic isomerization pathway and builds on a new approach in determining detailed kinetic and mechanistic information for tropospheric hydrocarbon chemistry.

B. Experimental Techniques

Iodohydrin Synthesis. The synthesis of 1-iodo-3-buten-2-ol was based on an approach to iodohydrins reported by Barluenga *et al.*[163] Identification and purity of the sample was confirmed by comparison of NMR spectra with the report of Masuda *et al.*[164] Mono-deuteration of the 1-iodo-3-buten-2-ol was achieved by shaking 1-iodo-3-buten-2-ol in an ether/D_2O mixture.

The synthesis of the 1-iodo-2-methyl-3-buten-2-ol is also based on the synthetic preparation by Barluenga and coworkers.[163] As this synthesis is not explicitly presented in that work, the detailed steps are presented here. 14.82 grams of sodium iodide (98.9 mmol, EM Science, 99.5%) were added to a mixture of 25 mL of distilled water and 120 mL of tetrahydrofuran (EMD Chemicals, GR ACS). The solution was stirred rapidly in an ice bath until the reaction flask cooled to 0^{o}C. An excess of 15 mL of isoprene (150 mmol, Alfa Aesar, 99%) was added. To the reaction flask was added 83 mL of sulfuric acid[165] (7.2 M, Em Chemicals, 95-98.0%) dropwise. Additionally, 33 mL of 30% hydrogen peroxide (Em Science, 30% solution) was added dropwise. The reaction flask was stirred for 8-12 hours while ice bath was allowed to melt. The reaction was then quenched with 300 mL of 5% sodium thiosulfate solution (Mallinckrodt, AR). THF was then removed via distillation under vacuum, and the remaining solution was extracted in 3 times 75 mL diethylether (EMD) and washed with brine solution. The ether was removed via distillation under vacuum. Typically, the product was purified via flash column chromatography in diethylether to remove polymer formed throughout the reaction process. Many attempts were made to separate out the minor product (the iodohydrin corresponding to isomer 3) via column chromatography. A variety of solvent mixtures were tested using thin layer chromatography including 15% ethanol in hexanes, 20% ethanol in hexanes, pure ethanol, pure hexanes, 5% ether in hexanes, 10% ether in hexanes, 25% ether in hexanes, 50% ether in hexanes, along with variations of the prescribed separations outlined by Barluenga et al.[163] We found that even though multiple spots were seen on TLC plates, in practice, during the fractional collection, no separation was achieved. Additionally, the hexanes were very difficult to remove completely from the final product. It is speculated that the THF, which is difficult to entirely remove from the sample, created challenges during the column chromatography step. The final product, after the flash column chromatography step, was distilled under vacuum to remove the ether.

It is worth noting that some heat during the distillation steps would have increased the removal of THF and hexanes. However, the product is not well characterized, and based on the darkening of the product (to a deep red) upon heating, we were concerned that, though we may have been completely removing organic impurities obtained during the synthesis, we were degrading our product and forming polymer impurities.

Product characterization was achieved via proton NMR. The H-NMR is shown in Figure V-V. Further evidence of the constitutionality of the product is evidenced in the mass spectra described vide infra. Kinetics consistent with those predicted for the product offers further confidence as to the synthetic product. Photolysis characteristics were determined via UV/VIS absorption spectroscopy, and the resultant absorption cross section as a function of wavelength is shown in Figure V-VI.

The proposed synthetic reaction mechanism is described in Figure V-VII.

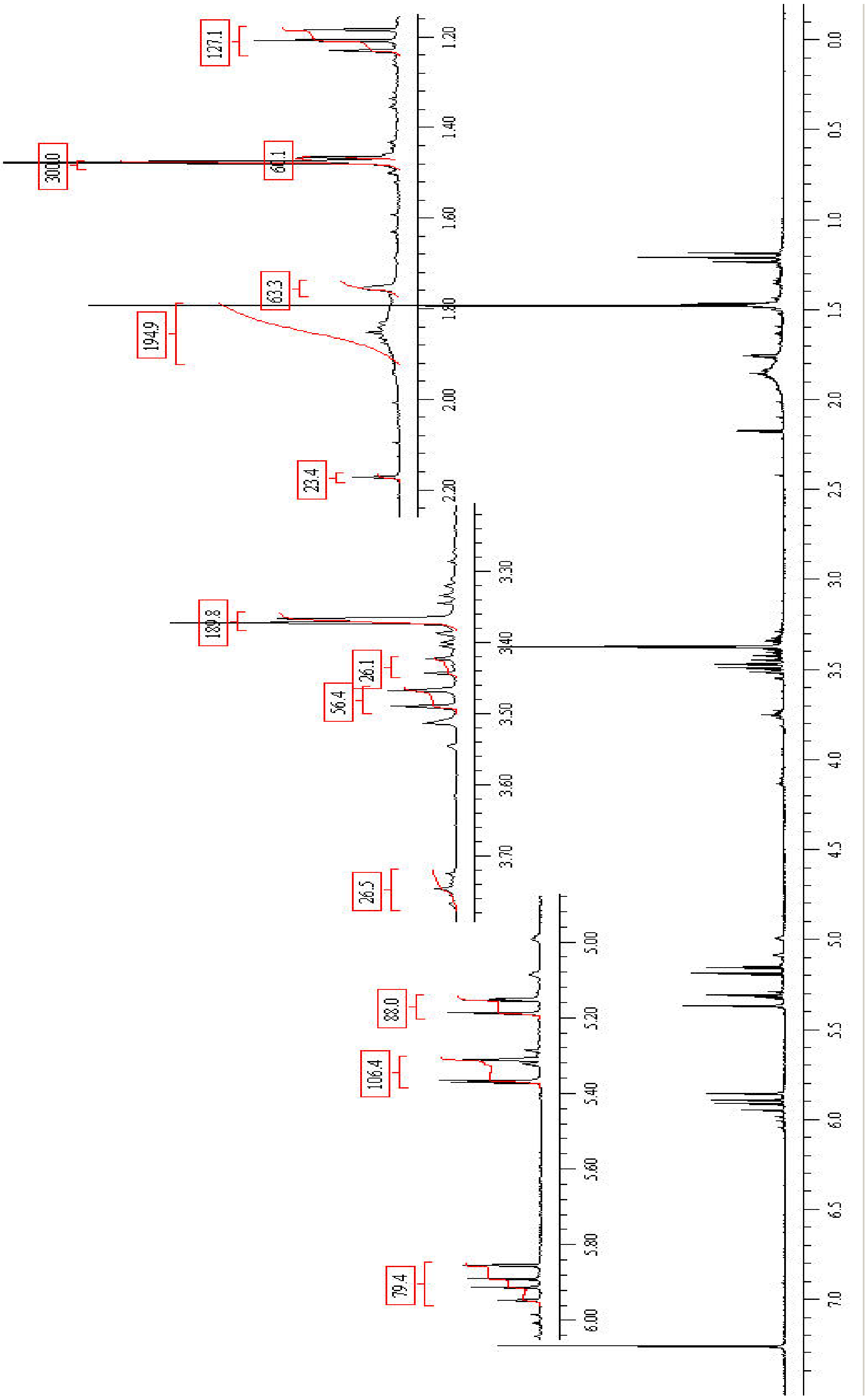

Figure V-V. Proton NMR spectra of precursor 2.

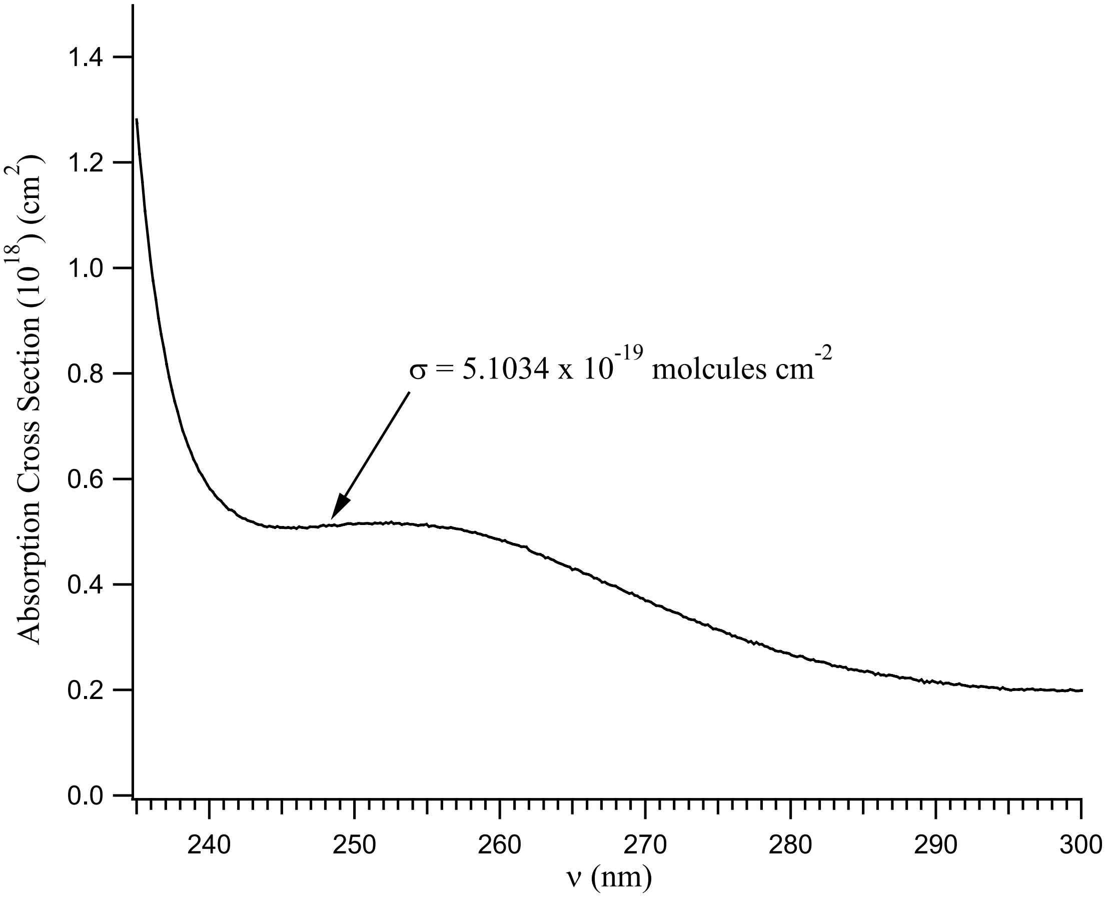

Figure V-VI. Absorption cross section, σ, as a function of wavelength for precursor 2.

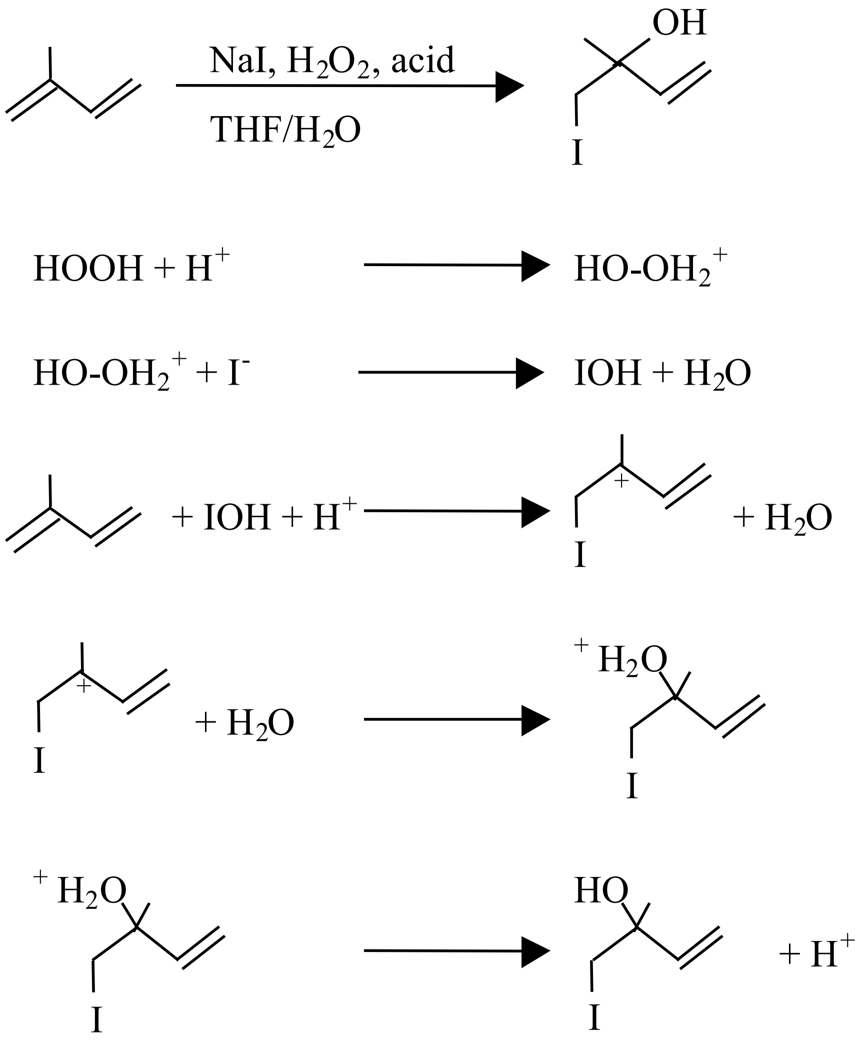

Figure V-VII. Proposed mechanism for the preparation of iodohydrin **2** from isoprene.

The unsaturated hydrocarbon reaction with IOH is well documented, even at the sophomore organic level.[166] In this one-pot synthetic preparation, IOH is prepared in situ via the reaction of hydrogen peroxide with sodium iodide in an acidic, aqueous medium. IOH reacts with unsaturated hydrocarbons via a carbocation intermediate. As such, OH addition to the most highly substituted carbon is favorable due to stabilization of the cation. In our synthetic preparation, we find an approximate 5:1 ratio of the reaction product shown in Figure V-VII (the major product) to the minor addition product where IOH adds across the alternative double bond.

Velocity Map Ion Imaging (VELMI). This technique has been described elsewhere[167] and only a brief summary will be presented here. The photodissociation dynamics of 1-iodo-3-buten-2-ol at 266 nm and 1-iodo-2-methyl-3-buten-2-ol at 248 nm were studied using velocity-map imaging (VELMI). Briefly, a pulsed molecular beam of 1% iodohydrin (precursor 2 or 5) in He (1 atm) was collimated by a conical skimmer and crossed at 90° by the focussed output of a tunable pulsed laser beam. In the photodissociation study of 1-iodo-3-buten-2-ol (precursor 5), a single color near 266 nm was used for both photolysis and state-selective ionization of the iodine atom photofragments using 2+1 resonance-enhanced multiphoton ionization (REMPI).[168] The light near 266 nm was generated by doubling the output of an Nd:YAG (Spectra-Physics LAB-150-10) pumped dye laser (LAS) running Coumarin-500. In the photodissociation of 1-iodo-2-methyl-3-buten-2-ol (precursor 2), a 248 nm photolysis beam was coupled with a beam probe beam near 304 nm for state-selective ionization of the iodine atom fragments using 2+1 REMPI (304.6 nm for I($^2P_{3/2}$), hereafter notated as I and 303.9 nm for I($^2P_{1/2}$), hereafter notated as I*). The 248 nm light was generated by doubling the output of an ND:YAG (Spectra-Physics Lab 150-10) pulsed dye laser (PDL) running DCM and mixing with the 1064 nm fundamental of the YAG. The light near 304 was generated by doubling the output of an ND:YAG (Spectra-Physics Lab-150-10) pumped dye laser (LAS) running Rhodamine-640+Rhodamine-610. The resulting ions were accelerated the length of a 50 cm flight tube using ion optics and detected by a 40 mm diameter dual microchannel plate (MCP) coupled to a phosphor screen assembly, as shown in Figure V-VIII. The MCP plates were gated to collect only *m/z*=127. Images were collected with a fast scan charge-coupled device camera and integrated using a data acquisition system. A PMT assembly was used to measure ion arrival times in order to select the timing-gate of the MCP.

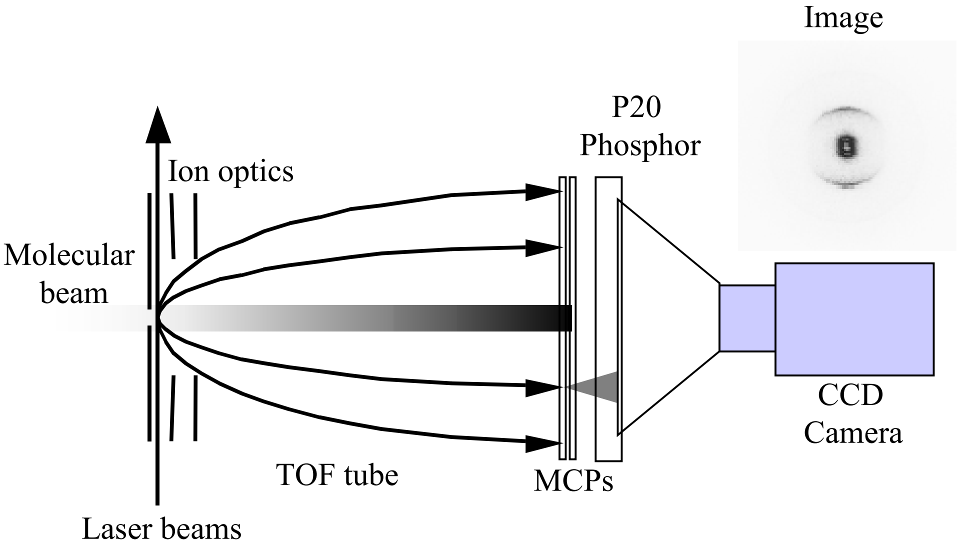

Figure V-VIII. Velocity Map Ion Imaging (VELMI) experimental apparatus.

A raw photofragment images is shown in Figure V-VIII. The electric field vector of the laser is vertical in the plane of the image. The images represent 2D projections of the 3D velocity distributions. Conversion of the raw images into speed and angular distributions was achieved using the basis set expansion program (BASEX) for image reconstruction developed by Reisler and co-workers.[169] The photofragment angular distributions can be described by the form,[170]

$$P(\theta) \propto \frac{1}{4\pi}\left[1+\beta P_2(\cos\theta)\right] \qquad (5\text{-}1)$$

where β is the spatial anisotropy parameter and $P_2(\theta)$ is the second Legendre polynomial. We have determined a best fit speed-independent anisotropy parameter of β=1.4±0.1 for the case of 1-iodo-3-buten-2-ol for both channels and a speed-independent anisotropy parameter of β=1.9±0.5 for the case of 1-iodo-2-methyl-3-buten-2-ol for both channels, consistent with parallel transition to repulsive excited state potentials.

The I/I* branching ratio was determined by integration of the Doppler profiles for the I/I* transitions using identical laser power. The integrated Doppler profiles were weighted by the relative detection efficiencies of I and I* at 248 nm and 266nm.[171] Independent confirmation of the detection efficiencies was obtained using the photodissociation of CH_3I at 266nm. The energy partitioning and I/I* branching ratio are very similar to the results of previous alkyl iodide photolysis near 260 nm.[172,173,174] The radial distance of the collected image, as shown in Figure V-VIII, yields a speed distribution of the iodine ions. Through linear momentum and energy conservation, an internal energy distribution of the unseen fragments formed in coincidence with either I or I* is determined given,

$$h\nu - D_o^o(C-I) = E_{avail} = E_{trans} + E_e^I + E_{e,v,r}^{C_5H_8OH} \tag{5-2}$$

where $h\nu$ is the photon energy of dissociation, $D_o^o(C-I)$ is the bond dissociation energy of the carbon-iodine bond, E_{avail} is the available energy to the system, E_e^I is the electronic energy of the iodine fragment (which is optically selected), $E_{e,v,r}^{C_5H_8OH}$ is the internal energy of the unseen hydroxyalkyl fragment, and E_{trans} is the translation energy of the fragments and is measured as the radial distance of the collected image,

$$E_{trans} = \frac{1}{2}\mu g^2, \quad \mu = \frac{m_I m_{C_5H_8OH}}{m_I + m_{C_5H_8OH}}, \quad g = -\left(\frac{m_I + m_{C_5H_8OH}}{m_{C_5H_8OH}}\right)v_I \tag{5-3}$$

where m_I is the mass of the iodine atom, $m_{C_5H_8OH}$ is the mass of the hydroxyalkyl fragment, and v_I is the speed of the iodine ions. The final energy distributions, representing weighted averages of the I and I* components, are shown in Chapters VI and VII.

Since the I/I* branching ratio will be dependent on the dissociation wavelength and a change to this ratio can significantly alter the nascent energy distribution, careful measurements of the I/I* ratio must be performed to asses this affect. Increasing the dissociation wavelength could, in fact, result in an internal energy distribution of nascent hydroxyalkyl radicals which is hotter than that at 266 nm if the I/I* branching ratio increased.

Time-Dependent Mass Spec (precursor 2 only). The details of this experimental technique are presented elsewhere and only a brief summary is presented here.[175] A 248 nm pulsed photolysis laser beam (4 Hz) from an Excimer laser shines down the length of a quartz reactor (nearing 1 m in length) where iodohydrin and oxygen are mixed and buffered to 4 torr total pressure in He where constant pressure is maintained using a throttle valve. The system is under slow-flow conditions, where the gas in the reactor tube is replenished between photolysis pulses by insuring fast enough flow through the reactor tube considering total pressure and flow rates. A typical flow rate for a reactor tube approaching 1 m in length with a 4 torr total pressure is approximately 100 sccm (standard cubic cm per minute) yielding a flow velocity near 4 m/s. A pinhole in the reactor tube allows a small stream of gas-phase reaction products to diffuse into the relatively high vacuum source region of the chamber. Typical pressures in this region are on the order of 10^{-5} torr. The diffused molecules are collimated through a conical skimmer into an ionization region, which is typically about half of the total pressure of the source region. The molecular beam is then crossed by a tunable VUV laser source (from the synchrotron light source at the Advanced Light Source at Lawrence Berkeley National Laboratory). The ions created from the soft-fragment ionization are then accelerated by a series of ion optics and separated by mass using a 0.9 T magnet. Single ion counts of all masses in coincidence are then detected by a time and position sensitive mass spectrometer in the ultra-high vacuum region of the chamber ($\sim10^{-9}$ torr). The schematic of the chamber is shown in Figure V-VIX.

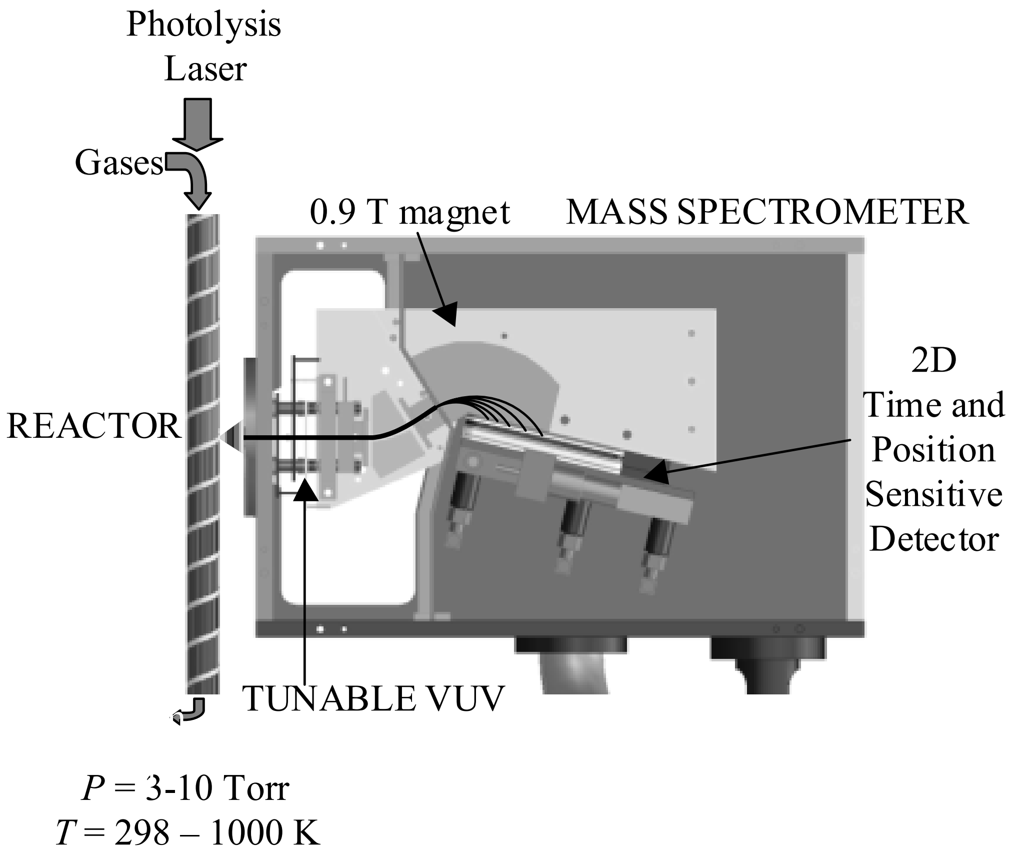

Figure V-IX. Time dependent multiplexed mass spectrometer. Figure created and provided by David L. Osborn of Sandia.

LP/LIF. The laser photolysis/ laser induced fluorescence technique (LP/LIF) has been discussed in detail elsewhere[26] though a detailed description compliments that discussion here. A schematic outlining the optical setup is displayed in Figure V-X. The 266 nm beam from an ND:YAG laser (Spectra Physics GCR-150-10) or a 248 nm photolysis beam from an EX10 Excimer laser (Gam laser inc.) is colinearly aligned through the reaction cell with a probe beam generated using a KDP crystal to double the output of a pulsed dye laser (Quantel TDL-51) running Rhodamine 590 or Rhodamine 610 dye pumped by the 532 nm second harmonic from an Nd-Yag Laser (Spectra Physics Quanta Ray INDI). The OH radical concentration was monitored using the LIF technique to monitor OH or OD excited on the $Q_1(1)$ transition of the A←X(1,0) vibrational band near 282 nm or 287 nm, respectively.

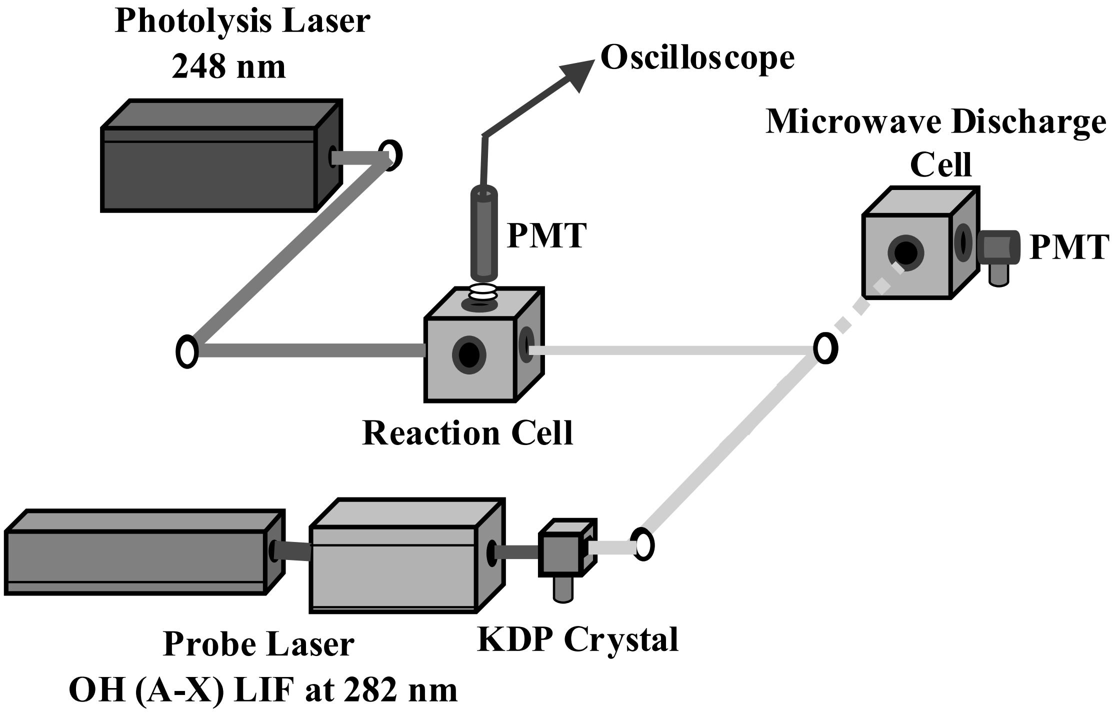

Figure V-X. Optical setup for Laser Photolysis/Laser Induced Fluorescence (LP/LIF).

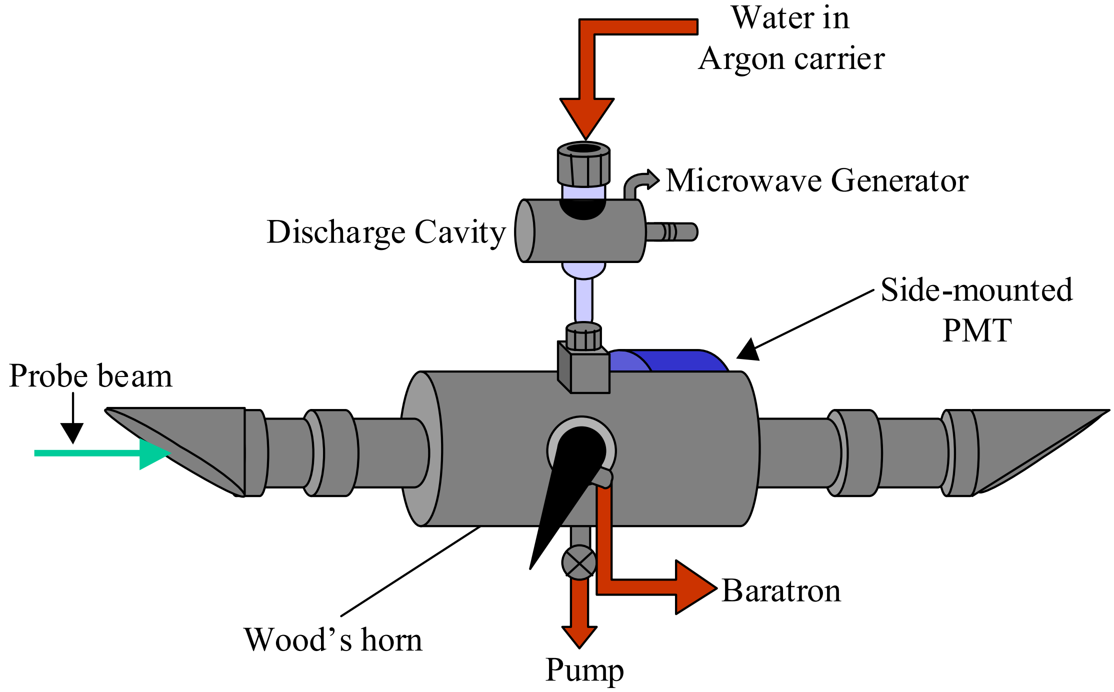

Figure V-XI. Microwave Discharge cell for calibration of OH/OD LIF

A rotatable mounted prism is located between the KDP output and the LIF reaction cell. The prism can be rotated away from the probe beam such that the probe beam is redirected into a microwave discharge cell. The microwave discharge cell provides the ability to calibrate the probe beam to the precise wavelength for OH (or OD) detection. A detailed schematic of the microwave discharge setup is displayed in Figure V-XI. High frequency radiation in the GHz range is generated by a microwave generator (Opthos) and transferred to the gaseous water source (in Ar carrier gas) via an Evenson cavity (Opthos). A Tesla coil initiates a discharge creating a plasma and free electrons dissociate the water molecules resulting in plasma containing OH radicals. The OH radicals are produced in sufficient yield such that many LIF peaks (transitions on the $A \leftarrow X(1,0)$ vibrational band) are observed. Scanning the probe beam maps out the LIF peaks such that maximum OH LIF signal on the $Q_1(1)$ transition is achieved as shown in Figure V-XII.

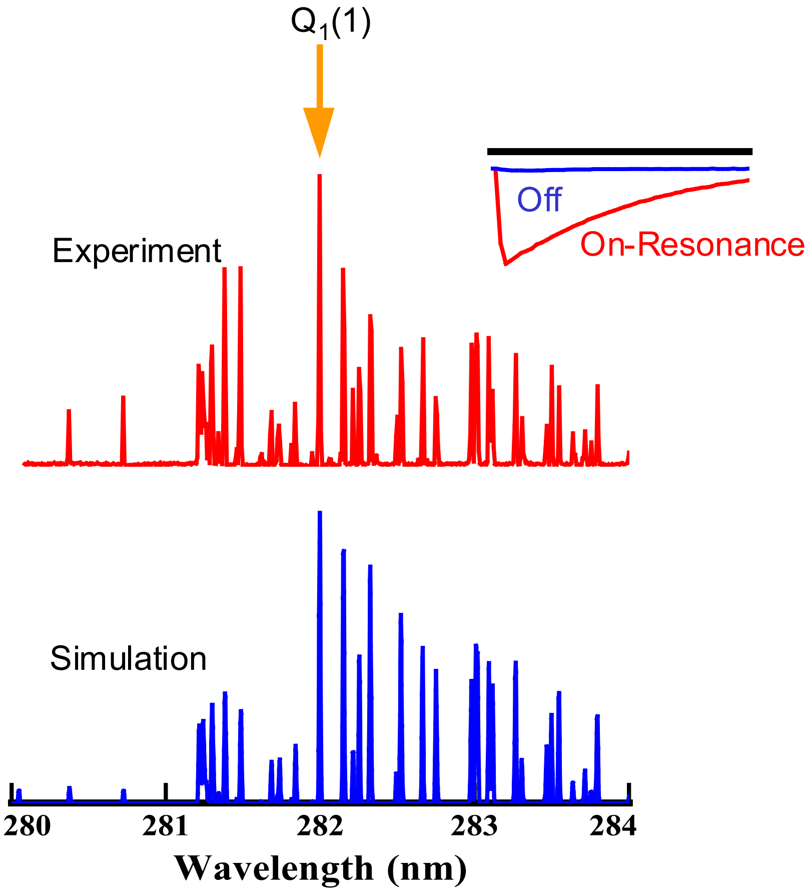

Figure V-XII. OH experimental and simulated LIF spectra on the A← X(1,0) vibrational band.

After the probe beam is tuned, the mounted prism is rotated back into place, redirecting the probe beam through the LIF cell. A schematic of the LIF reaction cell is given in Figure V-XIII. Premixed gasses are flowed into the stainless steel LP/LIF reaction cell. The cell is also being evacuated through a dry ice/acetone trap by a mechanical pump such that the reactant molecules are replenished between laser shots where the lasers operate at a frequency of 10 Hz. A baratron monitors the total pressure of the cell and a thermocouple inside the reaction cell monitors the temperature of the gasses. The probe and dissociation beams are colinearly aligned through opposite quartz windows, which are placed at a Brewster angle to minimize reflected light.

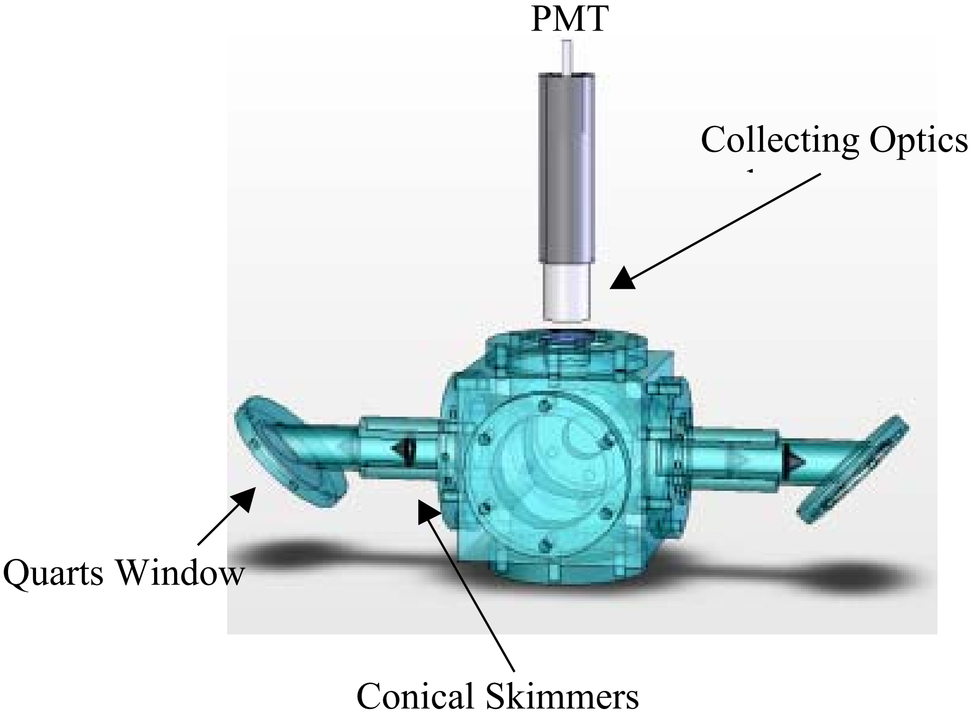

Figure V-XIII. Laser Photolysis/Laser Induced Fluorescence (LP/LIF) reaction cell.

The conical skimmers reduce the respective beam sizes such that the photolysis beam diameter at the monitoring region is much larger (~10 times) than the probe laser beam diameter to minimize the fly out effect. A set of collection optics expands and refocuses a pinpoint of light from along the photodissociated and probed cylinder of reacted molecules. The resulting fluorescence at 308 nm was collected through an optical filter and detected by a photo multiplier tube (PMT) and integrated using an oscilloscope. The delay between photolysis and probe laser pulses is controlled by a digital delay/ pulse generator (Stanford Research System, DG 535).

The kinetics were monitored by measuring the integrated fluorescence as a function of time. Each fluorescence decay was typically averaged over 80-100 shots and followed for at least 300 μs. Argon was flowed through a bubbler containing the precursor iodohydrin molecule and introduced into the cell through an MKS flow meter. The NO (Sigma Aldrich, 98.5%) was flowed through an ascarite trap and a bulb of known concentration was prepared with an Argon buffer. O_2 (BOTCO, 99.995%) was also buffered with argon (BOTCO) to make a bulb of known concentration. Experiments were run at fixed concentration of iodohydrin, while varying the concentration of NO and O_2. The total pressure of the reaction cell was always buffered to 50 ± 4 Torr.

The LP/LIF technique was employed for kinetics measurements of both the 1-iodo-3-buten-2-ol and the 1-iodo-2-methyl-3-buten-2-ol. The details applicable to the specific systems, reaction conditions, results, and analysis are given in Chapters VI and VII.

CHAPTER VI

ISOMERIC SELECTIVE HYDROXYL RADICAL INITIATED OXIDATION OF BUTADIENE[*]

A. Results and Discussion – 1-iodo-3-buten-2-ol

Ion Imaging Experiments. Raw photofragment images for I($^2P_{3/2}$) and I($^2P_{1/2}$) (hereafter referred to as I and I*, respectively) are shown in Figure VI-I.

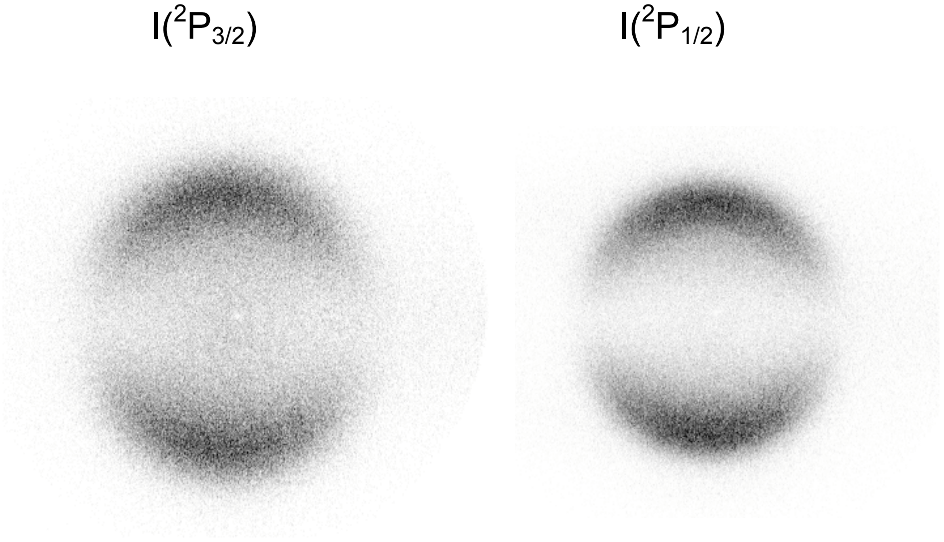

Figure VI-I. Raw ion images for I($^2P_{3/2}$) (left) and I($^2P_{1/2}$) (right) atoms from the photodissociation of 1-iodo-2-butene-3-ol at 266 nm. Adapted from Figure 1 of Ref. 39.

The final energy distribution derived from these imagines, as described in Chapter V, is shown as the solid line in Figure VI-II. For comparison a 300 K Boltzmann energy distribution, shifted by the exothermicity of the addition of OH to the inner position of

---

[*] Reprinted with permission from "The OH Initiated Oxidation of 1,3-Butadiene in the Presence of O2 and NO: A Photolytic Route to Study Isomeric Selective Reactivity" Greenwald, E. E.; Anderson, K. C.; Park, J.; Kim, H.; Reich, B. J. E.; Miller, S. A.; North, S. W. *J. Phys. Chem.. A* **2005**, *109*, 7915.

1,3-butadiene, as would be predicted for chemical activation, is shown as the dashed line in Figure VI-II. The distributions are qualitatively similar suggesting that the subsequent kinetics of the radicals produced *via* photolysis of 1-iodo-3-buten-2-ol should effectively mimic the radicals formed by thermal recombination. The measured internal energy distribution is bimodal as a result of the large spin orbit splitting between the two atomic states of iodine. The large peak, centered around 22 kcal/mol corresponds to the excited state I*; whereas, the small peak centered around 40 kcal/mol corresponds ground state I. The I/I* branching ratio weights the relative heights of these peaks.

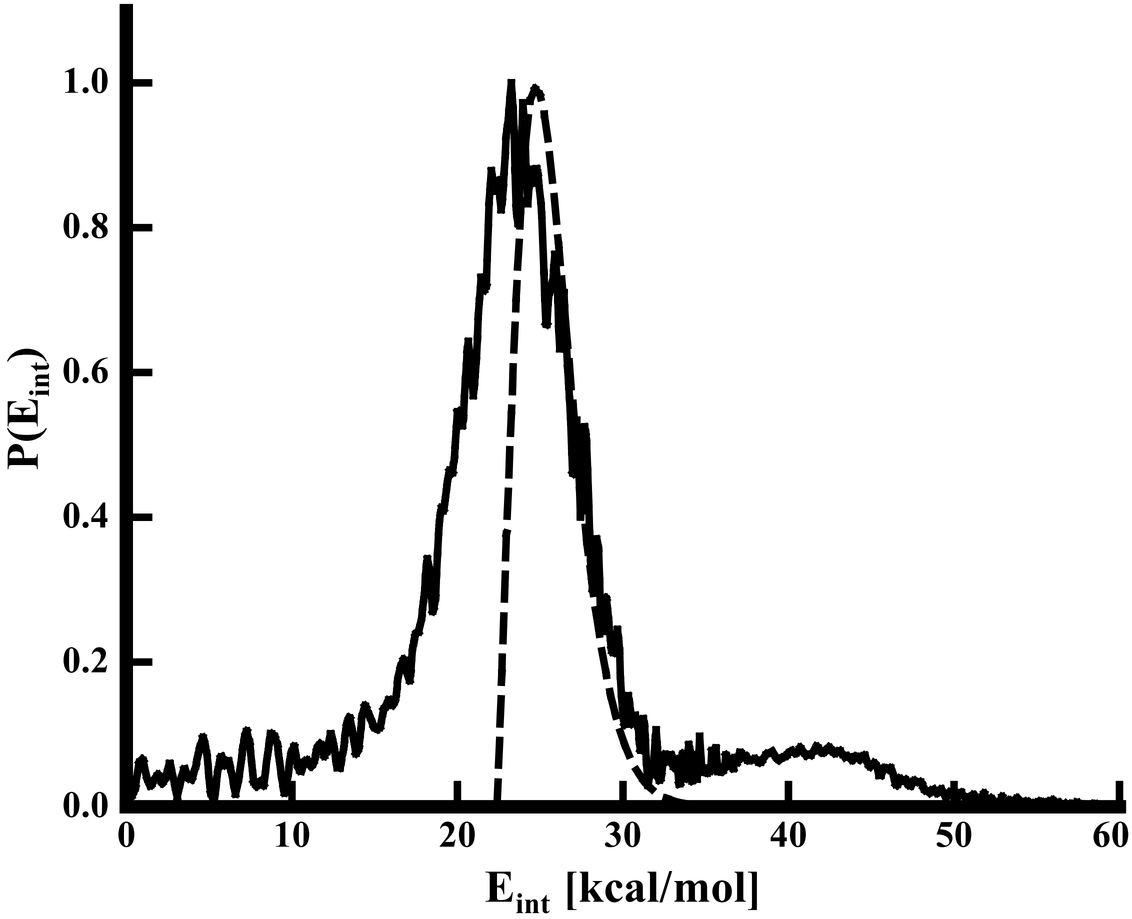

Figure VI-II. Nascent β-hydroxyalkyl radical internal energy distribution (solid line) based on the measured translational energy derived from the ion imaging data shown in Figure VI-I. The dashed line represents a shifted, to the OH-butadiene asymptote, 300 K Boltzmann distribution. Adapted from Figure 2 of Ref. 39.

Calculations of the Cyclic Isomerization Reactions Quantum chemical calculations using the Gaussian 03[137] software package were performed to provide all relevant energetics, geometries, and frequencies to obtain state counts as a function of energy for the OH-butadiene radical cyclic isomerization reaction. The highest level calculations performed, which were used in the kinetic modeling, include optimized geometries of reactants, intermediate species, products and transition states using density functional theory (DFT). Becke's three-parameter hybrid method employing the LYP correlation functional (B3LYP)[91,176] in conjunction with the Pople-style triple-ζ split valence polarized basis sets was used (6-311++G**)[135,177] Single-point energy calculations were performed on these stationary points using coupled-cluster theory with single and double excitations with perturbative inclusion of the triples contribution (CCSD(T))[108,110] with the Dunning-style triple-ζ basis sets (cc-pVTZ).[109] Energies from density functional theory and *ab initio* calculations are listed in Table VI-I and a schematic energy diagram is shown in Figure VI-III.

Table VI-I. Relative energies (in kcal/mol), including spin orbit splitting for the OH and zero point energy, for the isomers at various levels of theory.

Method and Basis Set	C_4H_6 + OH	2a	ts1	2b	ts2	2c
B3LYP/6-31G*	22.4	0.0	9.7	3.0	8.6	-6.1
B3LYP/6-311++G**	18.9	0.0	10.1	4.5	8.9	-6.3
CCSD(T)/cc-pVDZ// B3LYP/6-311++G**	23.4	0.0	12.7	5.1	12.8	-4.9
CCSD(T)/cc-pVTZ// B3LYP/6-311++G**	22.4	0.0	11.5	4.5	11.6	-4.9

CCSD(T) calculations include zero point energy from the B3LYP/6-311++G** frequency calculation.
Adapted from Table 1 of Ref. 39.

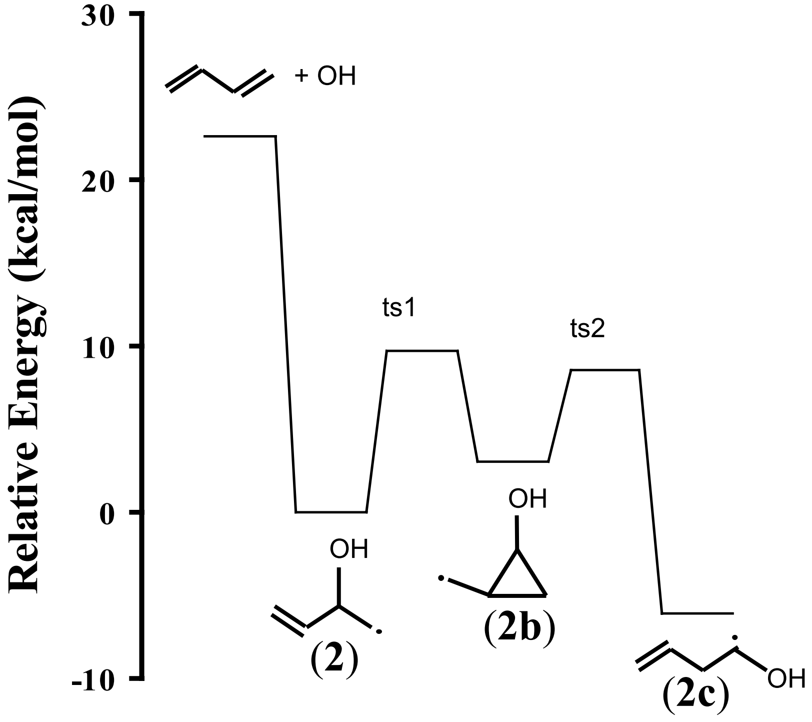

Figure VI-III. Schematic reaction diagram for the cyclic isomerization reaction of the OH-butadiene radical obtained using CCSD(T)/cc-pVTZ//B3LYP/6-311++G** energies (including B3LYP/6-311++G** zero point energy). Adapted from Figure 3 of Ref. 39.

The initially activated β-hydroxyalkyl radicals are subject to a competition between collisional stabilization, dissociation, and isomerization.[37] We have employed RRKM theory coupled with the master equation (ME) formalism to calculate reaction rate constants as well as branching ratios among the isomers and into the dissociative channel, to give 1,3-butadiene and OH. Since the OH-butadiene radicals isomerize through well-defined transition states along the potential energy surface, standard (non-variational) RRKM theory can be used to calculate microcanonical rate. The dissociation of the OH-butadiene adducts takes place on a nearly monotonically increasing potential energy surface. An accurate description of the dissociation requires a two transition state model, which includes variational treatments of both the inner and the outer transition states. Recently, this treatment has been applied to the case of the hydroxyl radical addition to ethylene.[38] At high temperatures, the outer transition state becomes unimportant and including only the inner transition state can accurately approximate the kinetic model. At 300 K, the inner transition state serves as the dominant bottleneck such that an inclusion of both transition states only reduces the rate by 30%. Furthermore, high level *ab initio* calculations revealed that the potential energy surface for the adduct dissociation includes a saddle point below the asymptotic energy of separated products and the saddle point appears at carbon-oxygen separation distances in the neighborhood of 2.2 Å. For the purposes of this model, a 2.2 Å carbon-oxygen separation was assumed to adequately describe the saddle point for the adduct dissociation channel. A B3LYP/6-311++G** geometry optimization constraining the carbon-oxygen bond distance to 2.2 Å and frequency calculation was used to determine harmonic frequencies and rotational constants in order to evaluate the microcanonical number of states for the adduct dissociation channel. The threshold energy was assumed to be the asymptotic energy for separated butadiene and OH. Neglecting variational effects introduces an error of less than 15% to the dissociation rate in the case of ethylene and have, therefore, been excluded from the current work.

CCSD(T)/cc-pVTZ//B3LYP/6-311++G** energies, unscaled vibrational frequencies, and rotational constants were used to calculate the RRKM rate constants through the tight transition states. For all species, the density and sum of states were obtained through an exact count procedure by the Stein-Rabinovitch extension[178] of the Beyer-Swinehart algorithm[179] implemented in the MultiWell program suite.[180,181] There was no reaction path degeneracy for the isomerization reactions. The dissociation channel for the butadiene-OH adduct was considered to be irreversible, and the isomerization steps were considered to be reversible. The transformation from the microcanonical rates to thermal rate constants, and the short-time evolution of the initial OH-butadiene radical distribution, was treated using the one-dimensional, energy grained ME formalism. Implementation of the ME formalism includes activation and deactivation processes as well as unimolecular rate constants for reacting molecules. The strong collision approximation is not valid for the treatment of small monatomic or diatomic colliders such as N_2. A more appropriate treatment includes a weak collision model, which has been implemented by applying the exponential down model of energy transfer. We have calculated the collision frequency based on a Lennard-Jones interaction potential. The necessary quantities for the self-collisions of many bath gases (*e.g.* N_2) and several reactant molecules are listed in the literature.[182] In the case of the hydroxyalkyl radicals, it is necessary to estimate ε and σ since these are not available. We calculated their values using empirical formulae. The values of $\varepsilon = 146.4$ and 225.6 K and $\sigma = 4.8$ and 4.5 Å have been adopted as Lennard-Jones parameters for the interactions between the hydroxyalkyl radicals with N_2 and Ar, respectively.

RRKM/ME calculations were performed at 298 K and 760 Torr in a Nitrogen atmosphere, applicable to tropospheric conditions, where a Boltzmann distribution, shifted by the exothermicity of the addition reaction, was used for the initial energy distribution of β-hydroxyalkyl radicals.[183] The measured internal energy distribution for the nascent hydroxyalkyl radicals from the photodissociation experiment was used as an initial energy distribution for a simulation at 50 torr in an Argon bath gas to model the chemistry in the laboratory experiment. The fractional populations of the isomers as a function of time under laboratory conditions are shown in Figure VI-IV.

At 50 torr total pressure in Ar, the conditions of the present experiment, the fractional populations of isomers 2, 2b, and 2c reach quasi steady-state values after $1\mathrm{x}10^{-8}$s, which can be considered prompt on the time scale of subsequent reactivity. Following collisional stabilization and in the absence of bimolecular reaction channels, the system approaches equilibrium at a significantly slower rate. Since the α-hydroxyalkyl radicals are thermodynamically favored, at sufficiently long times, there will be quantitative conversion to the α-hydroxyalkyl radicals. At the smallest and largest O_2 concentrations used in the kinetics experiment, the lifetimes of the β-hydroxyalkyl radical in the presence of O_2 are 1 ms and 300 μs, respectively. Long time simulations indicate that this system approaches equilibrium on a similar time scale such that O_2 addition to the β-hydroxyalkyl radicals is competitive with the cyclic isomerization pathway after the initial collisional stabilization, which determines the short-time fractional population of α-hydroxyl radicals.

In the troposphere, the fractional populations of isomers 2, 2b, and 2c reach quasi steady-state values faster than $1\mathrm{x}10^{-8}$ s, which can also be considered prompt on the time scale of subsequent reactivity. The lifetime of β-hydroxyalkyl radicals in the troposphere is less than 1 μs. The ratio of β-hydroxyalkyl radicals to α-hydroxyalkyl radicals in the troposphere is essentially determined by the initial collisional stabilization, where the majority of the population (0.64) is already in the α-hydroxyalkyl radical form. Since the fractional populations of α-hydroxyalkyl radicals and β-hydroxyalkyl radicals do not change significantly both in the temperature range from 240 K to 340 K at 760 Torr and in the pressure range from 50 Torr to 760 Torr at 298 K, we predict that the reactions of both β-hydroxyalkyl radicals and α-hydroxyalkyl radicals with molecular oxygen are important pathways in the atmosphere when considering OH addition to the inner positions of conjugated olefins. A change in the average collisional energy transfer ($<\Delta E_{\mathrm{down}}>$) by ±100 cm^{-1} causes the final steady-state population of 2c to change by ±16%. Increasing $<\Delta E_{\mathrm{down}}>$, as with increasing the pressure or decreasing the temperature, results in a larger initial fraction of β-hydroxyalkyl radicals, reflecting more efficient collisional stabilization. Quasi steady-state fractional populations as a function of condition can be seen in Table VI-II.

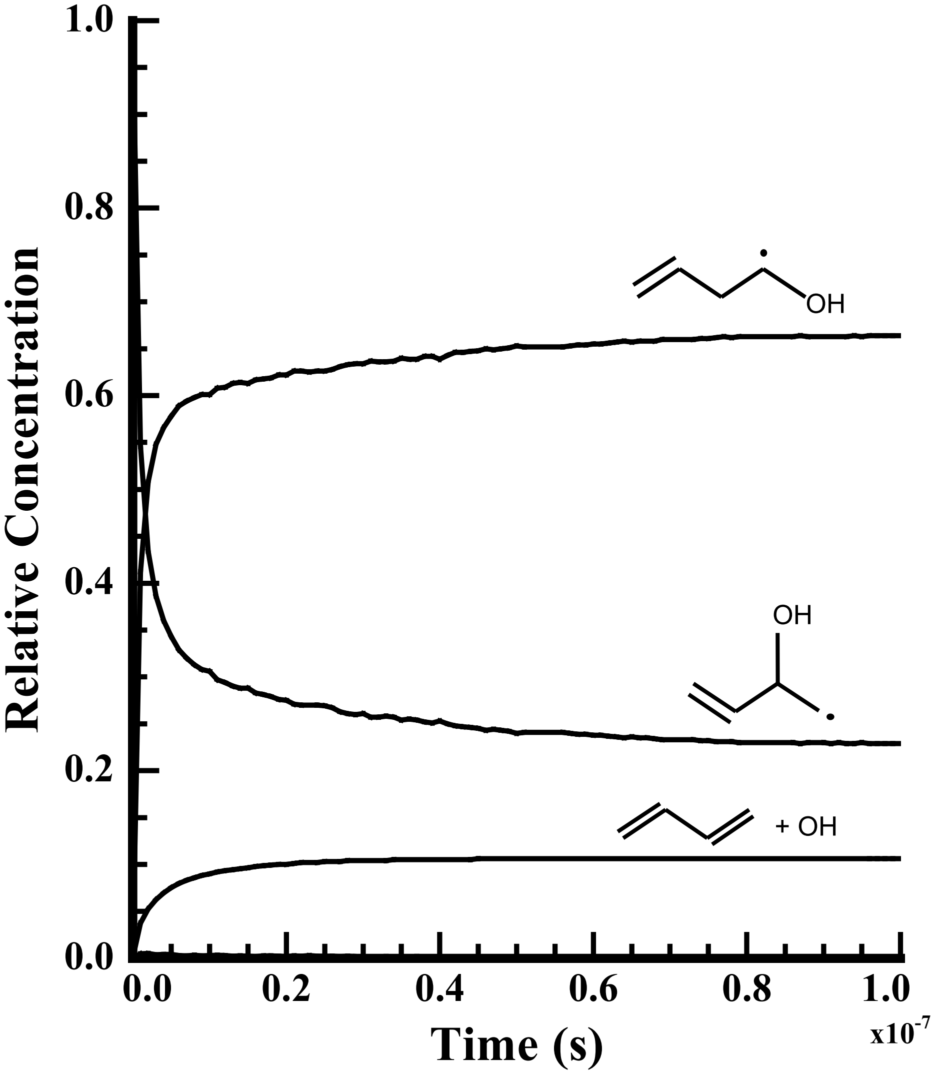

Figure VI-IV. RRKM/ME modeling of the fractional populations of isomers as a function of time under laboratory conditions. Adapted from Figure 4 of Ref. 39.

Table VI-II. Quasi steady state fractional populations as a function of conditions. All temperatures are modeled by the shifted Boltzmann except for *hv* which is the internal energy distribution measured by the VELMI.

Temperature/K	*hv*	298	298	298	298	240	340
Pressure/Torr	50[a]	50[a]	760[b]	760[b]	760[b]	760[b]	760[b]
$<\Delta E_{down}>$	300	300	200	300	400	300	300
C_4H_6 + OH	0.11	0.02	<0.01	<0.01	<0.01	<0.01	<0.01
2a	0.22	0.15	0.26	0.36	0.46	0.48	0.30
2b	<0.01	<0.01	<0.01	<0.01	<0.01	<0.01	<0.01
2c	0.67	0.83	0.74	0.64	0.54	0.52	0.69

[a] Argon bath gas and populations taken at $t=1x10^{-7}$ seconds.
[b] N_2 bath gas and populations taken at $t=1x10^{-8}$ seconds.
Adapted from Table 2 of Ref. 39.

The Kinetics of OD Formation. The kinetics experiments rely on the time-dependent formation of OD as a function of O_2 and NO concentrations to provide information about rate constants of intermediate reactions. The technique has been shown to be effective with judicious choice of experimental conditions guided by sensitivity analysis. These studies seek to confirm the importance of the β-hydroxyalkyl radical isomerization pathway and to determine the 298 K rate constant for the O_2 reaction with the α-hydroxyalkyl radical. Based on sensitivity analysis we focus our attention on the initial OD formation at short times (<100 μsec) where the kinetics are dominated by a limited number of reactions. At later times, termination involving NO and OD-regeneration reactions with 1-iodo-3-buten-2-ol becomes increasingly important. The RRKM/ME results demonstrated that the cyclic isomerization and collisional deactivation of the nascent β-hydroxyalkyl radicals is 'prompt' on the time scale of the subsequent kinetics. As a result, the kinetics simulations fix the initial fraction of β-hydroxyalkyl and α-hydroxyalkyl radicals. The formation of OD from each of these radicals proceeds by a significantly different mechanism and this difference permits isolation of the reaction of α-hydroxyalkyl radical with O_2. The production of OD from β-hydroxyalkyl radicals involves several intermediate steps: the addition of $O_2$184, the reaction of the resulting peroxy radicals with NO to form alkoxy radicals, decomposition of these radicals, the reaction of the decomposition products with O_2 to yield DO_2, and finally the conversion of DO_2 to OD *via* reaction with NO. Recent OH/OD cycling experiments on isoprene,[28] for which the β-hydroxyalkyl radicals are the dominant species following OH/OD addition, suggest that, under the conditions employed in the present experiment, the onset of OD regeneration from the β-hydroxyalkyl radicals should occur at times near 200 μsec. In contrast, the formation of OD from α-hydroxyalkyl radicals requires only two reaction steps: D-abstraction by O_2 followed by conversion of the DO_2 to OD by reaction with NO. Figure VI-V shows a typical set of time-dependent OD data using concentrations of 1-iodo-3-buten-2-ol and NO of $4.80\text{x}10^{14}$ molecules cm^{-3} and $6.49\text{x}10^{14}$ molecules cm^{-3}, respectively. The individual curves represent various concentrations of O_2 ranging from $4.20\text{x}10^{14}$ molecules cm^{-3} to $1.69\text{x}10^{15}$ molecules cm^{-3}. The experimental time-dependent OD curves exhibit a rapid increase during the initial 100 μsec consistent with a significant yield of α-hydroxyalkyl radicals. Figure 6.6 shows data obtained by fixing the O_2 concentration at $8.40\text{x}10^{14}$ molecules cm^{-3} and varying the NO concentration between $2.99\text{x}10^{14}$ molecules cm^{-3} and $1.30\text{x}10^{15}$ molecules cm^{-3}.

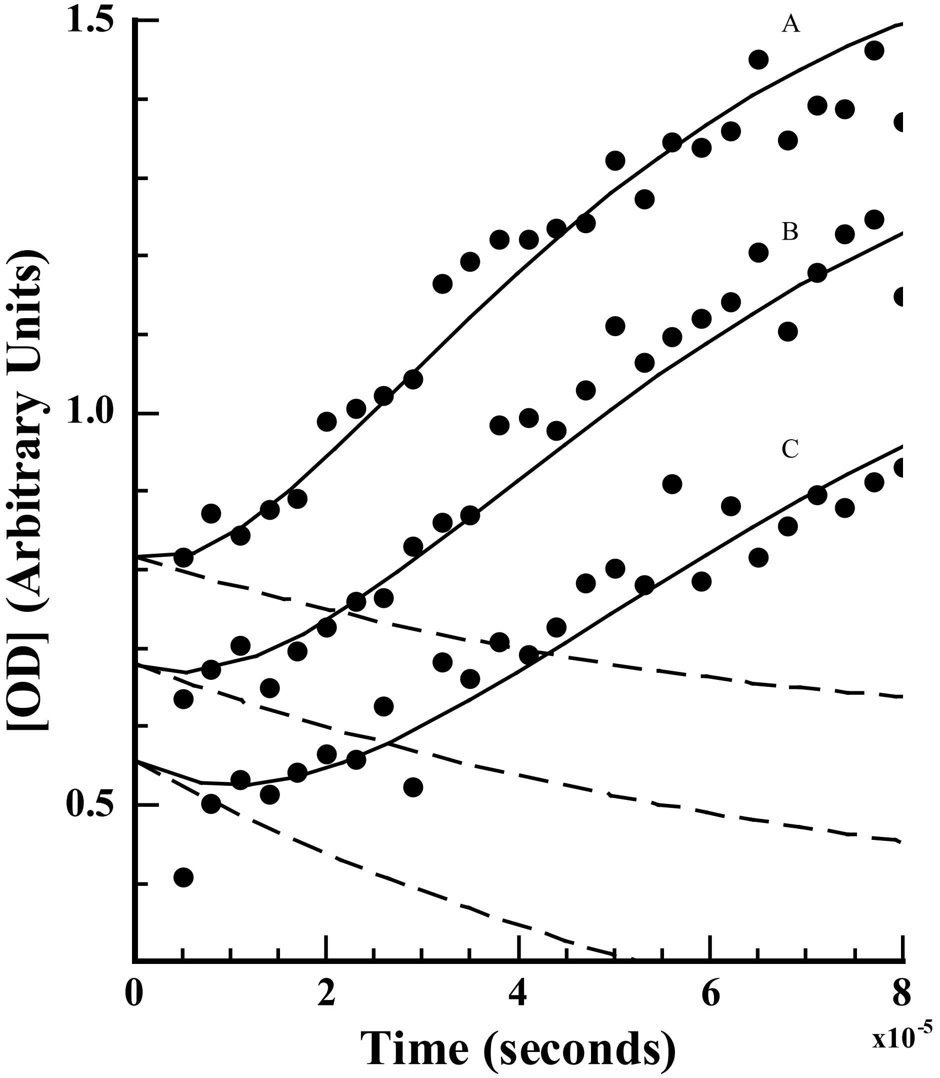

Figure VI-V. Temporal OD fluorescence intensity at several O_2 concentrations. Symbols represent experimental data and solid lines represent the fits using the reaction mechanism and rate constants in Table 6.2 with [NO]=6.49x10^{14} molecules cm^{-3}. The O_2 concentrations were varied. (A: 1.69x10^{15} molecules cm^{-3}. B: 8.40x10^{14} molecules cm^{-3}. C: 4.20x10^{14} molecules cm^{-3}.) The dashed lines are simulations assuming the initial concentration of α-hydroxyalkyl radical is zero. Adapted from Figure 5 of Ref. 39.

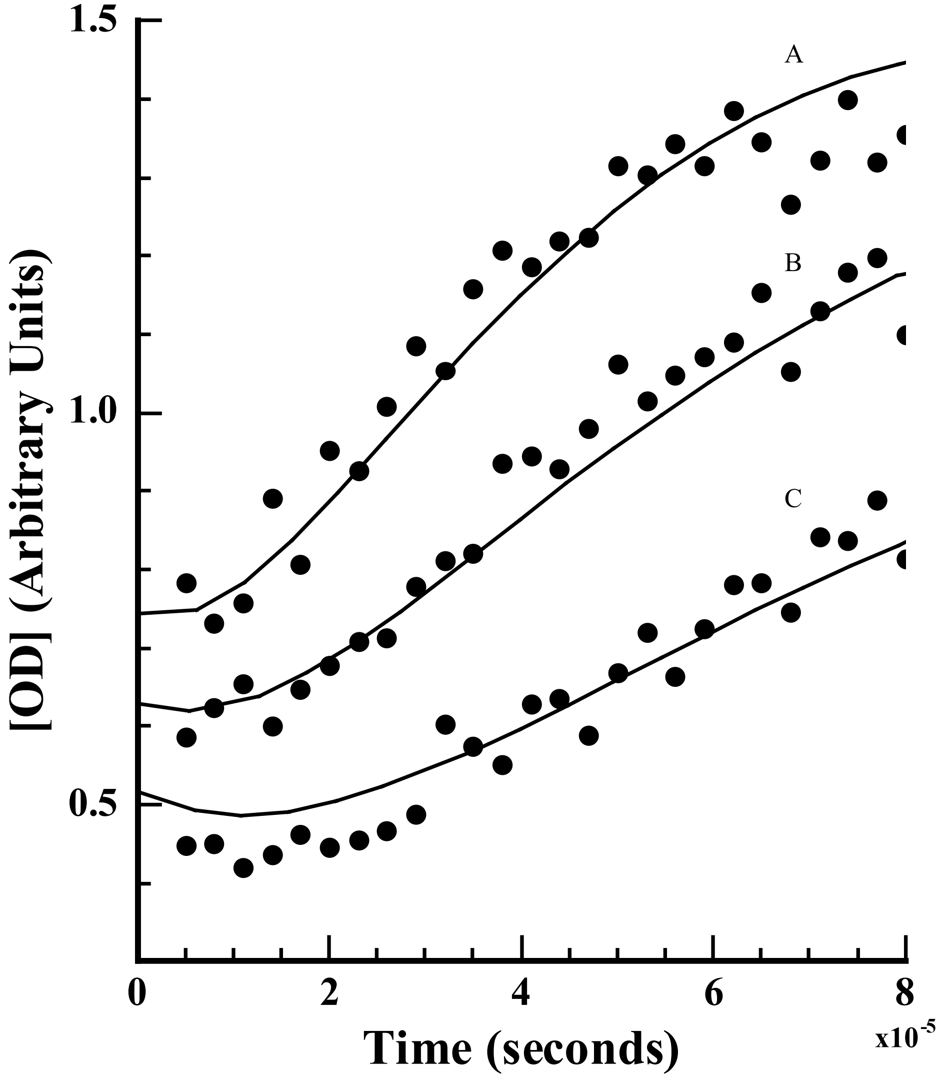

Figure VI-VI. Temporal OD fluorescence intensity at several NO concentrations. Symbols represent experimental data and solid lines represent the fits using the reaction mechanism and rate constants in Table 6.2 with $[O_2]=8.40x10^{14}$ molecules cm^{-3}. The NO concentrations were varied.
(A: 1.3x10^{15} molecules cm^{-3}. B: 6.49x10^{14} molecules cm^{-3}. C: 2.99x10^{14} molecules cm^{-3}.) Adapted from Figure 6 of Ref. 39.

A numerical program, KINTECUS,[185] was used to simulate the kinetics data and the sensitivity analysis was performed using the same software. The 16 reactions used in the simulations are given in Table VI-III along with the rate constants corresponding to each step.

Table VI-III. Reaction mechanism and corresponding rate constants (298 K) used for simulation. (Rates constants are in the unit of molecules^{-1}cm^{3}s^{-1} unless the unit is specified)

	Reaction	Rate
k_1	α-hydroxyalkyl radical ($CH_2CH(OD)CHCH_2$)	70 %
k_2	β-hydroxyalkyl radical (CH_2CHCH_2CHOD)	30 %
k_3	$CH_2CHCH_2CHOD + O_2 \rightarrow CH_2CHCH_2CHO + DO_2$	3.30×10^{-11}
k_4	$CH_2CHCH_2CHOD + NO \rightarrow CH_2CHCH_2CH(OD)NO$	2.20×10^{-11}
k_5	$CH_2CH(OD)CHCH_2 + NO \rightarrow CH_2CH(OD)(NO)CHCH_2$	2.20×10^{-11}
k_6	$CH_2CH(OD)CHCH_2 + O_2 \rightarrow O_2CH_2CH(OD)CHCH_2$	2.30×10^{-12}
k_7	$O_2CH_2CH(OD)CHCH_2 + NO \rightarrow OCH_2CH(OD)CHCH_2 + NO_2$	8.50×10^{-12}
k_8	$O_2CH_2CH(OD)CHCH_2 + NO \rightarrow ONO_2CH_2CH(OD)CHCH_2$	4.50×10^{-13}
k_9	$OCH_2CH(OD)CHCH_2 \rightarrow CH_2O + DOCHCHCH_2$	5.00×10^{5} s^{-1}
k_{10}	$OCH_2CH(OD)CHCH_2 + NO \rightarrow ONOCH_2CH(OD)CHCH_2$	3.00×10^{-11}
k_{11}	$DOCHCHCH_2 + O_2 \rightarrow OCHCHCH_2 + DO_2$	3.00×10^{-11}
k_{12}	$DOCHCHCH_2 + NO \rightarrow DOCHCHCH_2NO$	3.00×10^{-11}
k_{13}	$DO_2 + NO \rightarrow OD + NO_2$	8.80×10^{-12}
k_{14}	$OD + NO \rightarrow DONO$	9.40×10^{-13}
k_{15}	$OD + NO_2 \rightarrow DONO_2$	2.22×10^{-12}
k_{16}	$OD + IODCH_2CHCHCH_2$	1.50×10^{-11}

Adapted from Table 3 of Ref. 39.

The best fits of the simulations to the data are shown as solid lines in Figures VI-V and VI-VI. The dashed lines in Figure VI-V represent the simulations predicted if the kinetics involved β-hydroxyalkyl radicals exclusively. The reaction scheme includes reactions for which the simulations were sensitive and were required for adequate fitting. Figure VI-VII shows normalized sensitivity coefficients for all the rate constants in the reaction mechanism evaluated at 30 μsec and NO and O_2 concentrations of 6.49×10^{14} molecules cm^{-3} and 8.40×10^{14} molecules cm^{-3}, respectively. The figure demonstrates that the OD concentration profiles depend sensitively on few rate constants; in particular, the relative branching between α-hydroxyalkyl and β-hydroxyalkyl radicals (k_1 and k_2),[186] the rate of O_2 reaction with α-hydroxyalkyl radicals (k_3), the rate constant for the reaction between NO and DO_2 (k_{13}), and the rate between OD and 1-iodo-3-buten-2-ol

(k_{16}). However, the rate constant between NO and DO_2 (k_{13}) is established as $1.1\pm0.4\times10^{-11}$ cm^{3}molecules^{-1}s^{-1} [187,188] and a rate constant of $1.5\pm0.1\times10^{-11}$ cm^{3}molecules^{-1}s^{-1} was independently measured for the reaction between OD and the photolytic precursor (k_{16}). The simulations are relatively insensitive to the remaining rate constants. In order to fit the data we must include a contribution of 'prompt' OD equal to 2-5% of the initial hydroxyalkyl radical concentration. The source is the small fraction of highly excited radicals (Figure VI-III) which undergo decomposition to OD and 1,3-butadiene and is predicted by the RRKM/ME calculations.

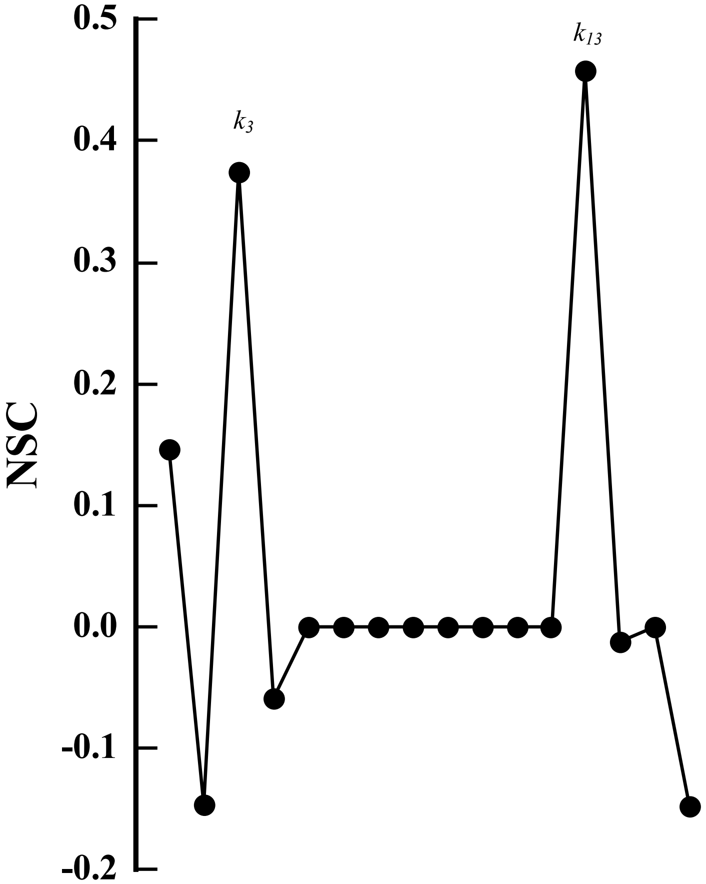

Figure VI-VII. Normalized sensitivity coefficients evaluated at the delay time of 30 μs and with [NO]=6.49×10^{14} molecules cm^{-3} and [O_2]=8.40×10^{15} molecules cm^{-3}. Adapted from Figure 7 of Ref. 39.

We find that good agreement between the data and the simulations can be achieved using an initial distribution corresponding to 70±10% α-hydroxyalkyl and 30±10% β-hydroxyalkyl radicals which is consistent with the RRKM/ME predictions. Our value of $3.3 \pm 1.0\text{x}10^{-11}$ $\text{cm}^3\text{molecules}^{-1}\text{s}^{-1}$ for D-abstraction from the α-hydroxyalkyl radicals by O_2 is consistent with the range of $1.2\text{x}10^{-11}$ to $3.7\text{x}10^{-11}$ molecules cm^{-3} s^{-1} reported by Miyoshi and co-workers[160] for several α-hydroxyalkyl radicals with O_2.

B. Conclusions

We have demonstrated a photolytic route to studying isomeric selective kinetics of OH-initiated oxidation of unsaturated hydrocarbons using the UV photolysis of iodohydrins. The present study focuses on the reactivity of the nascent β-hydroxyalkyl radical formed when butadiene undergoes oxidation by hydroxyl radical addition. Velocity map ion imaging permits the direct determination of the internal energy distribution of the nascent radical ensuring that the energy distribution of the radicals can be ‘tuned’ to mimic the kinetics of radicals formed from electrophilic-OH addition. The theoretical predictions modeling isomerization vs. collisional relaxation of the β-hydroxyalkyl radicals predict a significant proportion of β-hydroxyalkyl radicals isomerize to the α-hydroxyalkyl radical form before collisional relaxation. Prompt OD generation during the kinetics experiments offers conclusive evidence supporting the cyclic isomerization to α-hydroxyalkyl radicals.

CHAPTER VII

ISOMERIC SELECTIVE HYDROXYL RADICAL INITIATED OXIDATION OF ISOPRENE[*]

A. Results and Discussion – 1-iodo-2-methyl-3-buten-2-ol

VELMI. β-hydroxyalkyl radicals formed via OH addition to isoprene in the atmosphere have an internal energy distribution consistent with chemical activation. The internal energy distribution is reasonably described by a Boltzmann distribution of energy characterized by the ambient temperature and shifted by the exothermicity of the reaction. This internal energy distribution provides the β-hydroxyalkyl radicals with sufficient internal energy that further reaction competes with collisional relaxation. β-hydroxyalkyl radicals in the troposphere will either undergo O_2 addition or cyclic isomerization to form α-hydroxyalkyl radicals. Kinetics measurements, which are pertinent to atmospheric conditions, must be initiated with a distribution of radicals whose energy mimics that of chemical activation. Should less energy be available to the nascent radicals, collisional relaxation will have a delusive dominance over redissociation. Careful measurements and interpretation of the internal energy distribution of the nascent radicals formed via photolysis should offer insight into the relevance of the kinetics to the troposphere as well as provide requisite information for the interpretation of the kinetics.

Shown in Figure VII-I are the raw photo fragment images of the I and I* from the iodohydrin photolysis at 248 nm. The image of the I atoms is larger in diameter, consistent with the higher velocity of those fragments due to the excess energy available to the fragments as compared to the I*, where a portion of the available energy is used in the electronic excitation of the iodine atom.

---

[*] Preprinted with permission from “The OH Initiated Oxidation of Isoprene in the Presence of O_2 and NO: A Photolytic Route to Study Isomeric Selective Reactivity” Greenwald, E. E.; Ghosh, B.; Anderson, K. A.; Dooley, K. S.; North, S. W. *J. Phys. Chem. A.* **2007**, in preparation.

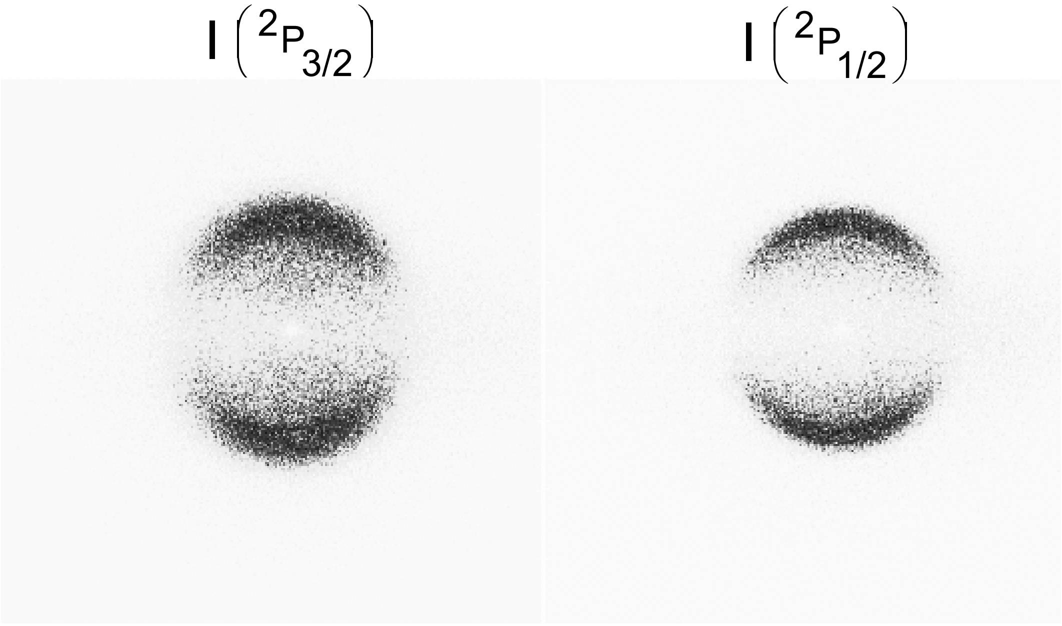

Figure VII-I. Raw photofragment images of the I and I* formed in coincidence with β-hydroxyalkyl radicals upon the photolysis of 1-iodo-2-methyl-3-buten-2-ol at 248 nm.

Shown in Figure VII-II is the internal energy distribution of the hydroxyalkyl radicals formed via the photodissociation of 1-iodo-2-methyl-3-buten-2-ol at 248 nm.

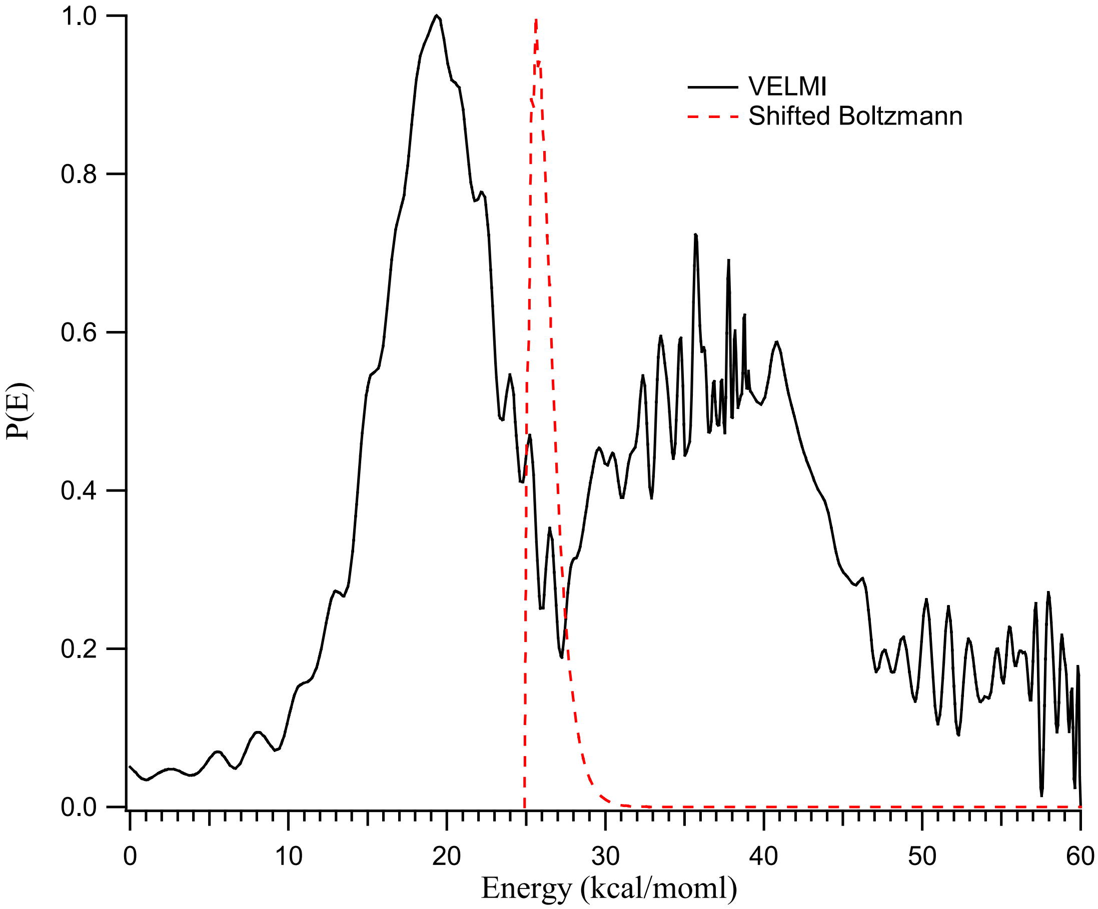

Figure VII-II. Internal energy distribution of the β-hydroxyalkyl radicals formed upon photolysis of 1-iodo-2-methyl-3-buten-2-ol as measured by VELMI (solid lines) overlaid with the Boltzmann distribution of energies expected upon OH addition to the second position of isoprene.

The Boltzmann distribution of energies that one would expect upon addition of OH to isoprene to form the β-hydroxyalkyl radical is overlaid in Figure VII-II. The are two peaks in the measured speed distribution, one at ~19 kcal/mol corresponding to the radicals formed in coincidence with I* with an average energy 20.3 kcal/mol and one at ~37 kcal/mol corresponding to those formed in coincidence with I, with an average energy of 39.6 kcal/mol. The expected average energy formed via collisional activation is 26.3 kcal/mol. Preliminary measurements of the I/I* branching ratio suggest equal yields of I and I*, as displayed in Figure VII-II. The resultant internal energy distribution is expected to produce a substantial proportion (~22 %) of radicals with sufficient internal energy to undergo prompt dissociation to form isoprene and OH, leaving only the radicals constituting the slower peak to subsequently react. A prompt OH signal, consistent with this dissociation is observed in the LP/LIF experiment and will be discussed in that section. The similarity between the remaining “cooler” radicals and the thermal distribution suggests tropospheric relevance of the ensuing kinetics.

Time-Dependent Mass Spec. One method of probing the subsequent kinetics of the β-hydroxyalkyl radicals formed via OH addition to the second position of isoprene (isomers 2) involves photolysis of the corresponding iodohydrin in the presence of O_2 and measuring the time evolution of reaction products by mass spectrometry.

Figure VII-III displays the two possible fates of the β-hydroxyalkyl radicals in the presence of O_2 with the corresponding mass to charge (m/z) ratios observed in a mass spectrometry experiment. Prompt cyclic isomerization of β-hydroxyalkyl radicals (m/z 85) followed by hydrogen abstraction yields 4-penten-2-one (m/z 84) and HO_2 (m/z 33); whereas O_2 addition to the β-hydroxyalkyl radicals produces peroxy radicals (m/z 117). The primary m/z ratios of interest in this study are m/z = 33, 84, 85, 117, and 127, which correspond to HO_2, 4-penten-2-one, α-,β-hydroxyalkyl radical, peroxy radical, and iodine atom, respectively. It is noteworthy that the tunability of the synchrotron light source, varying the ionization energy, allows additional chemical species information for species with known ionization energies. Scanning the synchrotron light source affords the ability to characterize species, not only by respective m/z ratios, but by the onset energy of the observed signal. Photoionization energies are not known for all species; however, one can estimate the energy based on similar species.

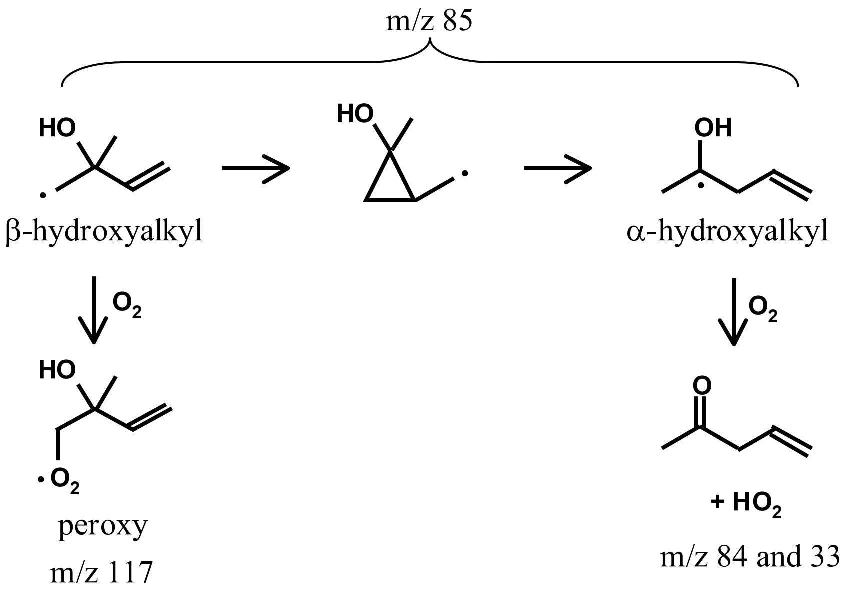

Figure VII-III. The fate of β-hydroxyalkyl radicals in the presence of O_2 and corresponding mass to charge (m/z) ratios.

We tuned the photon energy of the synchrotron light source above and below the ionization energies of the known species, which are HO_2 and I at 11.35 and 10.45 eV, respectively. We were able to use a the similar structures of 1-penten-3-one and 3-penten-2-one, with ionization energies of 9.5 and 9.39 eV, respectively, to provide an estimate of the ionization energy expected for the 4-peten-2-one. Signal corresponding to the m/z ratios of HO_2, I, and 4-penten-2-one were only seen above the ionization energies for each species. A complete time-dependent mass spectrum of all species is shown in Figure VII-II at an ionization photon energy of 12.0 eV.

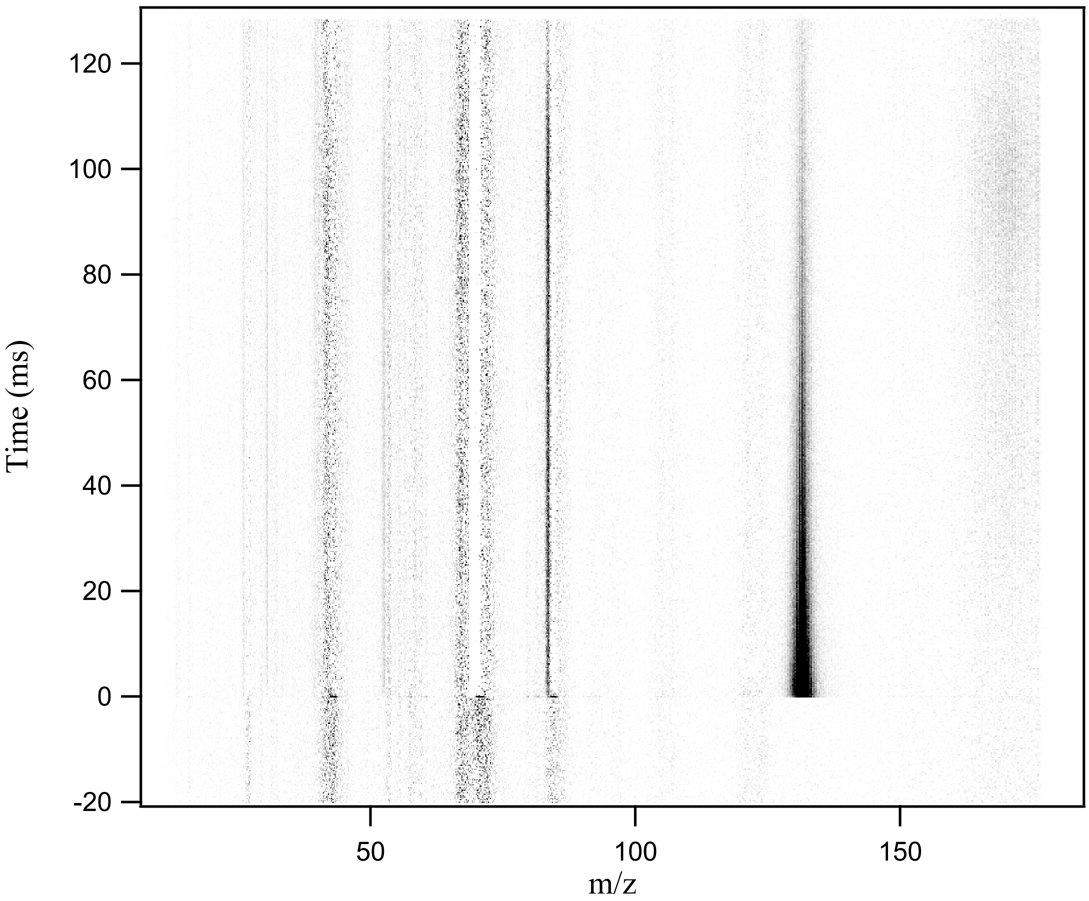

Figure VII-IV. Time and mass resolved mass spectra of the photodissociation of 1-iodo-2-methyl-3-buten-2-ol at 248 nm in the presence of O_2.

Because of the high photon energy, impurities in the sample and impurities on the walls of the tube are readily detected. One substantial advantage to this particular experiment is the ability to measure the time dependence of all species simultaneously. Anything formed before zero ms (the trigger time of the photolysis laser) is an impurity or the result of dissociative ionization. However, in the case of dissociative ionization, a species will not lose the time dependence beginning with the dissociation pulse. Such is the case for the hydroxyalkyl radical (m/z 85) where some radicals are produced before the dissociation pulse when the precursor molecule falls apart in the ionization region, however a distinctive time dependence is seen at zero ms as is shown in Figure VII-V. The plot is a slice through the 3-D, background-subtracted image (Figure VII-IV). There is a non-negligible concentration of hydroxyalkyl radical before the photolysis pulse, and so after background subtraction, the negative value of intensity is indicative of radical depletion. The radicals are formed promptly upon photolysis, and then rapidly decay within the first few time steps of the experiment which are typically 250 μs. While the absolute concentration of O_2 was unknown, fits to the decay of the hydroxyalkyl radicals and the rise of the ketone, employing the kinetic model described in the context of the LP/LIF experiment, suggest an O_2 concentration of approximately 5 x 10^{14} molecules cm^{-3}.

The decay of the hydroxyalkyl radical corresponds to a nearly instantaneous rise of 4-penten-2-one and HO_2. The time profile of 4-penten-2-ol and HO_2 are shown in Figures VII-VI and VII-VII, respectively.

The ionization cross section of the HO_2 is much smaller than the ketone and is thusly more difficult to detect and leading to much smaller absolute signal. We have overlaid the two plots from Figures VII-VI and VII-VII, and after enlarging the total intensity of the HO_2 by a multiplicative scaling factor in order to compare the time constant of the rise visually, we observe nearly identical rises.

The 4-penten-2-one is long lived and the time trace is level after the initial rise, whereas the HO_2 decays due to subsequent reactions. There was no evidence seen of m/z 117 associated with the peroxy. The m/z 33 appearance in coincidence with the m/z 84 appearance and the m/z 85 disappearance is compelling evidence toward a hydrogen abstraction mechanism. Nevertheless, one would like to follow the time dependence of the kinetics on a smaller time scale. Unfortunately, to follow the time dependence along shorter time steps, one must sacrifice the ability to watch all species simultaneously. Instead, the OH radical (NO reduction of HO_2) can be followed as a proxy while employing the LP/LIF technique.

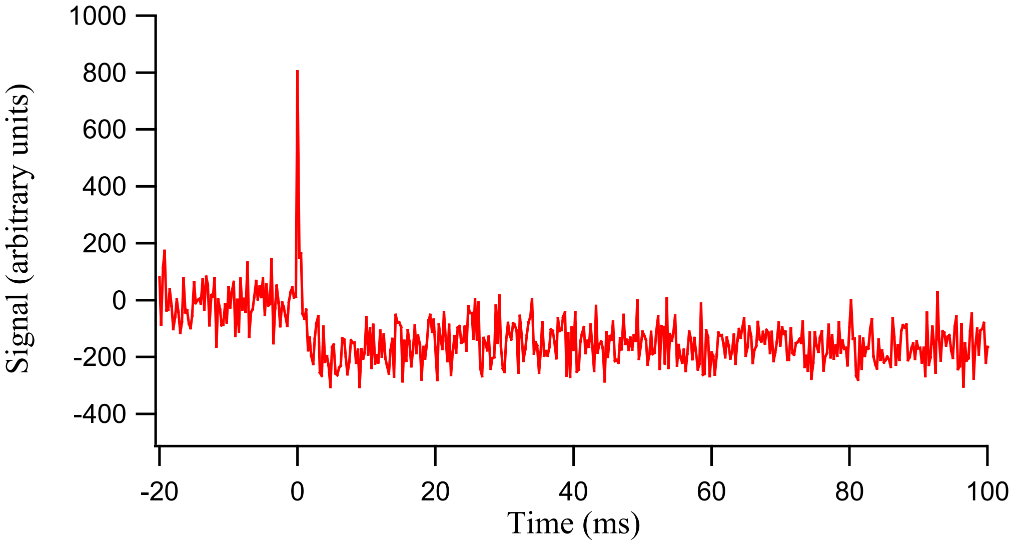

Figure VII-V. Time trace of the m/z = 85 corresponding to the hydroxyalkyl radical formed upon photolysis of 1-iodo-2-methyl-3-buten-2-ol.

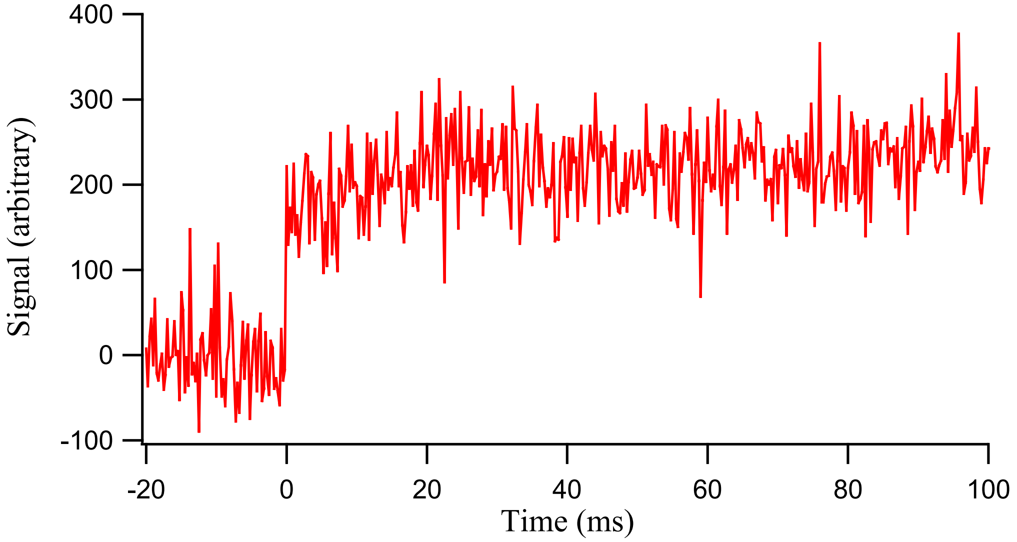

Figure VII-VI. Time trace of the m/z = 84 corresponding to the 4-penten-2-one formed upon hydrogen abstraction from the α-hydroxyalkyl radical.

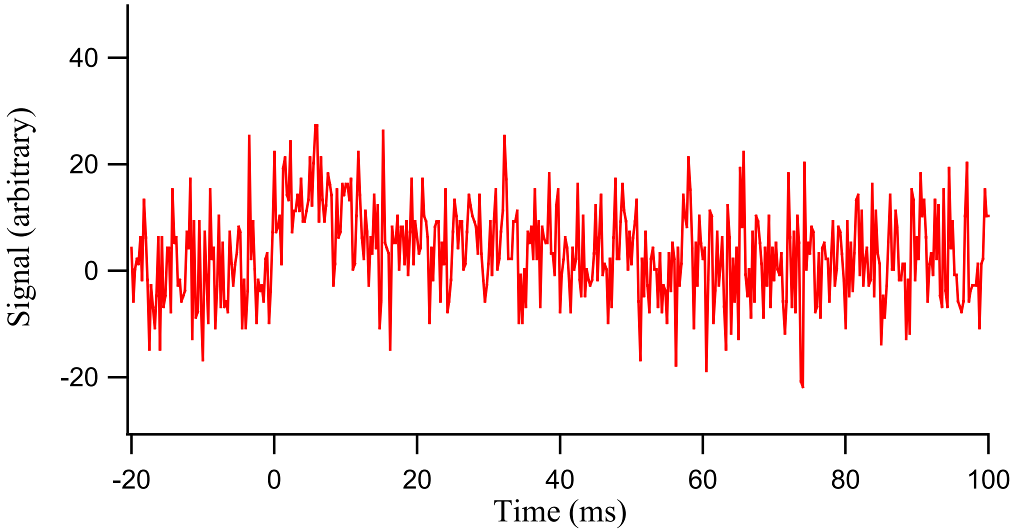

Figure VII-VII. Time trace of the m/z = 33 corresponding to the HO_2 formed upon O_2 hydrogen abstraction from the α-hydroxyalkyl radical.

LP/LIF. The present LP/LIF studies are nearly identical to those presented in the previous chapter for precursor 5 and the experimental details have been described in Chapter V. Here, photolysis at 248 nm of precursor 2 is monitored following the temporal profiles of OH. Reactions were all conducted at room temperature (298 K). Additionally, all experiments were performed on the same day in order to minimize systematic errors associated with temperature and laser power fluctuations.

A judicious choice of initial conditions and careful sensitivity analysis allows us to model our experimental observations. Figure VII-VIII shows OH temporal profiles under 9 different reaction conditions, in which the concentrations of O_2 and NO are varied, overlaid with fits of the data. In each of the three panels, a plot of the temporal profiles of OH for three different O_2 concentrations, spanning (3.99-16.2) x 10^{14} molecule cm^{-3}, at a constant concentration of NO is given along with the decay of OH without any O_2 or NO. The top panel displays OH temporal profiles including the varied O_2 concentrations given an NO concentration of 1.08 x 10^{15} molecule cm^{-3}, the middle panel includes the similar results for an NO concentration of 1.62 x 10^{15} molecule cm^{-3}, and the bottom panel displays the results for an NO concentration of 2.16 x 10^{15} molecule cm^{-3}. Additional experiments were conducted to verify that the both NO and O_2 were required in the observation of OH rise. OH temporal profiles were followed under conditions including NO in the absence of O_2, and including O_2 in the absence of NO, and in both cases, no rise in OH concentrations were observed. In all cases, the model is in excellent agreement with the data.

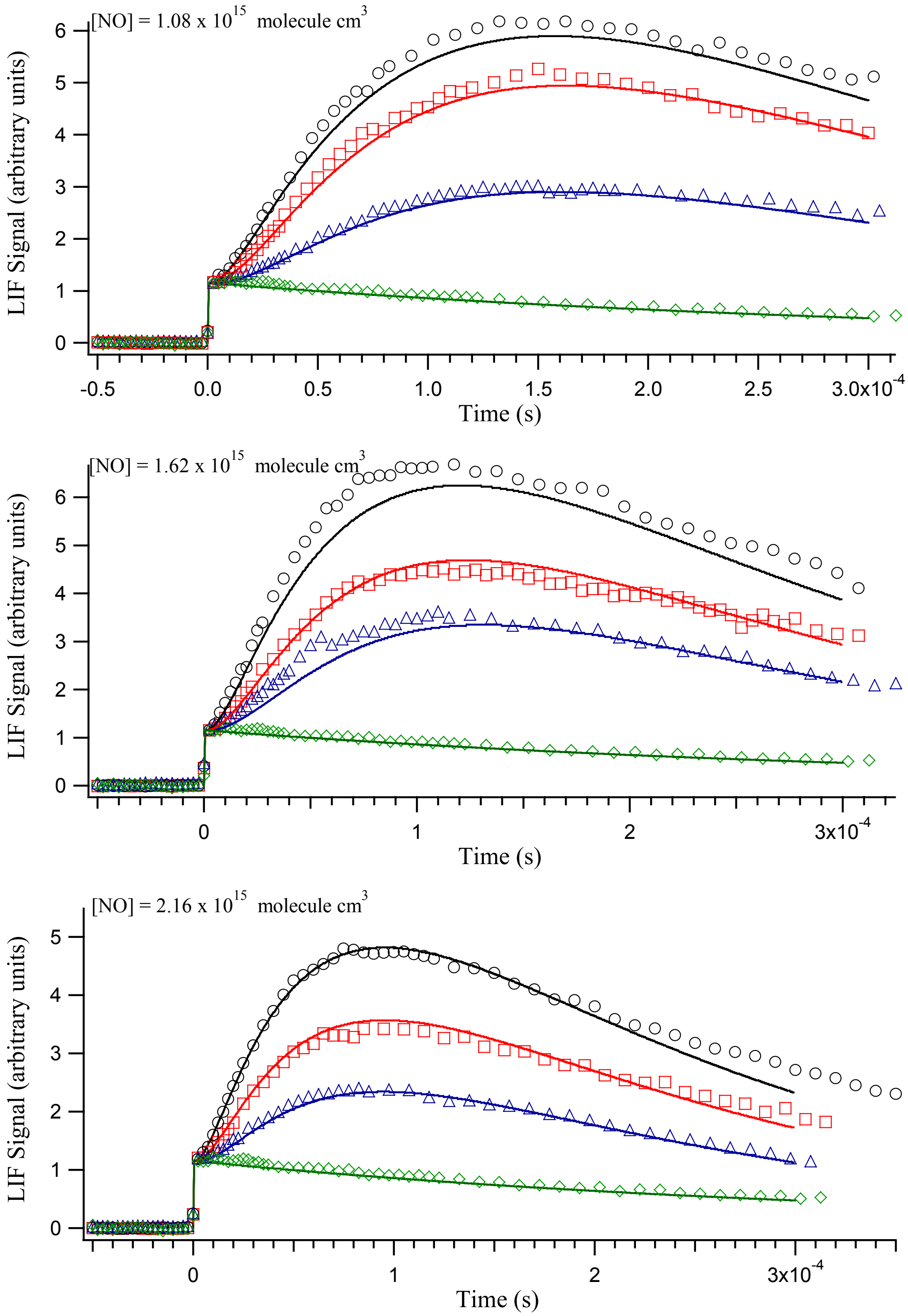

Figure VII-VIII. Temporal profiles of OH under varying conditions of NO and O_2 for the addition of OH to the second position of isoprene.

Table VII-I. Reaction mechanism for the OH addition to the second position of isoprene in the presence of NO and O_2.

Reaction				Rate Constant	
k_1	IC_5H_8OH	$\longrightarrow$	$OH + C_5H_8$	$8.0 \times {}^{9}$	s^{-1}
k_2	IC_5H_8OH	$\longrightarrow$	$C_5H_8OH + I$	9.2×10^{10}	s^{-1}
k_3	C_5H_8OH	$\longrightarrow$	α-C_5H_8OH	9.94×10^{11}	s^{-1}
k_4	C_5H_8OH	$\longrightarrow$	β-C_5H_8OH	6.0×10^{9}	s^{-1}
k_5	α-$C_5H_8OH + O_2$	$\longrightarrow$	α-$C_5H_8O + HO_2$	3.72×10^{-11}	cm^3 molecule^{-1} s^{-1}
k_6	α-$C_5H_8OH + NO$	$\longrightarrow$	α-C_5H_8OHNO	2.34×10^{-11}	cm^3 molecule^{-1} s^{-1}
k_7	β-$C_5H_8OH + NO$	$\longrightarrow$	β-C_5H_8OHNO	2.34×10^{-11}	cm^3 molecule^{-1} s^{-1}
k_8	β-$C_5H_8OH + O_2$	$\longrightarrow$	β-$C_5H_8OHO_2$	2.30×10^{-12}	cm^3 molecule^{-1} s^{-1}
k_9	β-$C_5H_8OHO_2 + NO$	$\longrightarrow$	β-$C_5H_8OHO + NO_2$	8.50×10^{-12}	cm^3 molecule^{-1} s^{-1}
k_{10}	β-$_5H_8OHO_2 + NO$	$\longrightarrow$	β-$C_5H_8OHONO_2$	4.50×10^{-13}	cm^3 molecule^{-1} s^{-1}
k_{11}	β-C_5H_8OHO	$\longrightarrow$	$CH_2O + C_4H_6OH$	5.00×10^{5}	s^{-1}
k_{12}	β-$C_5H_8OHO + NO$	$\longrightarrow$	β-C_5H_8OHONO	3.00×10^{-11}	cm^3 molecule^{-1} s^{-1}
k_{13}	$C_4H_6OH + O_2$	$\longrightarrow$	$C_4H_6O + HO_2$	3.00×10^{-11}	cm^3 molecule^{-1} s^{-1}
k_{14}	$C_4H_6OH + NO$	$\longrightarrow$	C_4H_6OHNO	3.00×10^{-11}	cm^3 molecule^{-1} s^{-1}
k_{15}	$HO_2 + NO$	$\longrightarrow$	$OH + NO_2$	8.80×10^{-12}	cm^3 molecule^{-1} s^{-1}
k_{16}	$HO_2 + NO_2$	$\longrightarrow$	HO_2NO_2	2.23×10^{-13}	cm^3 molecule^{-1} s^{-1}
k_{17}	$HO_2 + HO_2$	$\longrightarrow$	$H_2O_2 + O_2$	1.60×10^{-12}	cm^3 molecule^{-1} s^{-1}
k_{18}	$OH + NO$	$\longrightarrow$	$HONO$	9.40×10^{-13}	cm^3 molecule^{-1} s^{-1}
k_{19}	$OH + NO_2$	$\longrightarrow$	$HONO_2$	2.22×10^{-12}	cm^3 molecule^{-1} s^{-1}
k_{20}	$OH + NO_2$	$\longrightarrow$	$HO_2 + NO$	5.34×10^{-14}	cm^3 molecule^{-1} s^{-1}
k_{21}	$OH + OH$	$\longrightarrow$	H_2O_2	8.97×10^{-13}	cm^3 molecule^{-1} s^{-1}
k_{22}	$OH + OH$	$\longrightarrow$	$H_2O + O$	1.48×10^{-12}	cm^3 molecule^{-1} s^{-1}
k_{23}	$OH + HO_2$	$\longrightarrow$	$O_2 + H_2O$	1.10×10^{-10}	cm^3 molecule^{-1} s^{-1}
k_{24}	$OH + H_2O_2$	$\longrightarrow$	$H_2O + HO_2$	1.70×10^{-12}	cm^3 molecule^{-1} s^{-1}
k_{25}	$OH+HONO$	$\longrightarrow$	$H_2O + NO_2$	6.00×10^{-12}	cm^3 molecule^{-1} s^{-1}
k_{26}	$OH+HO_2NO_2$	$\longrightarrow$	products	4.70×10^{-12}	cm^3 molecule^{-1} s^{-1}
k_{27}	$OH+HONO_2$	$\longrightarrow$	$H_2O + NO_3$	1.50×10^{-13}	cm^3 molecule^{-1} s^{-1}
k_{28}	$OH + IC_5H_8OH$	$\longrightarrow$	IC_5H_8OHOH	1.50×10^{-11}	cm^3 molecule^{-1} s^{-1}

The mechanism, shown in Table VII-I, involves 28 reaction rates. This model is an extremely constrained model. Only rates k_1-k_7 were actually adjusted in the fitting procedure. The rate of OH reaction with the iodohydrin precursor was measured employing the LP/LIF technique in our lab yielding a bimolecular rate constant of 1.5 x 10^{-11} cm^3 $molecule^{-1}$ s^{-1}. It is noteworthy that the absolute magnitudes of rates k_1-k_4 are unimportant and only the relative values of k_1/k_2 and k_3/k_4 are considered. These four reactions are considered prompt on the time scale of the reaction. The ratio of k_1 to k_2 represents the proportion of precursor molecules that undergo photolysis, which is about 0.5% of the total precursor molecule concentration based on the absorption cross section of the iodohydrin and the power density of the laser. A proportion of the nascent β-hydroxyalkyl radicals promptly dissociates to generate an initial concentration of OH. The kinetic model very sensitively depends on the percentage of β-hydroxyalkyl radicals, which promptly dissociate to form OH and isoprene. Figure VII-IX shows a kinetics simulation where 34% of the β-hydroxyalkyl radicals undergo prompt dissociation as compared to the similar simulation including 8% prompt dissociation. The larger percent prompt limits the total concentration of hydroxyalkyl radicals available to regenerate OH. This is clearly demonstrated by the much smaller rise of OH compared to prompt OH in the simulation including 34% prompt OH dissociation. As such, our kinetics data indicates that about 8% of the β-hydroxyalkyl radicals will promptly dissociate, which is consistent with an I/I* branching ratio of 0.05 as opposed to the I/I* branching ratio of 0.5 determined in the preliminary VELMI analysis. The origin of the discrepancy between the VELMI results and the LP/LIF results are not clear at this time.

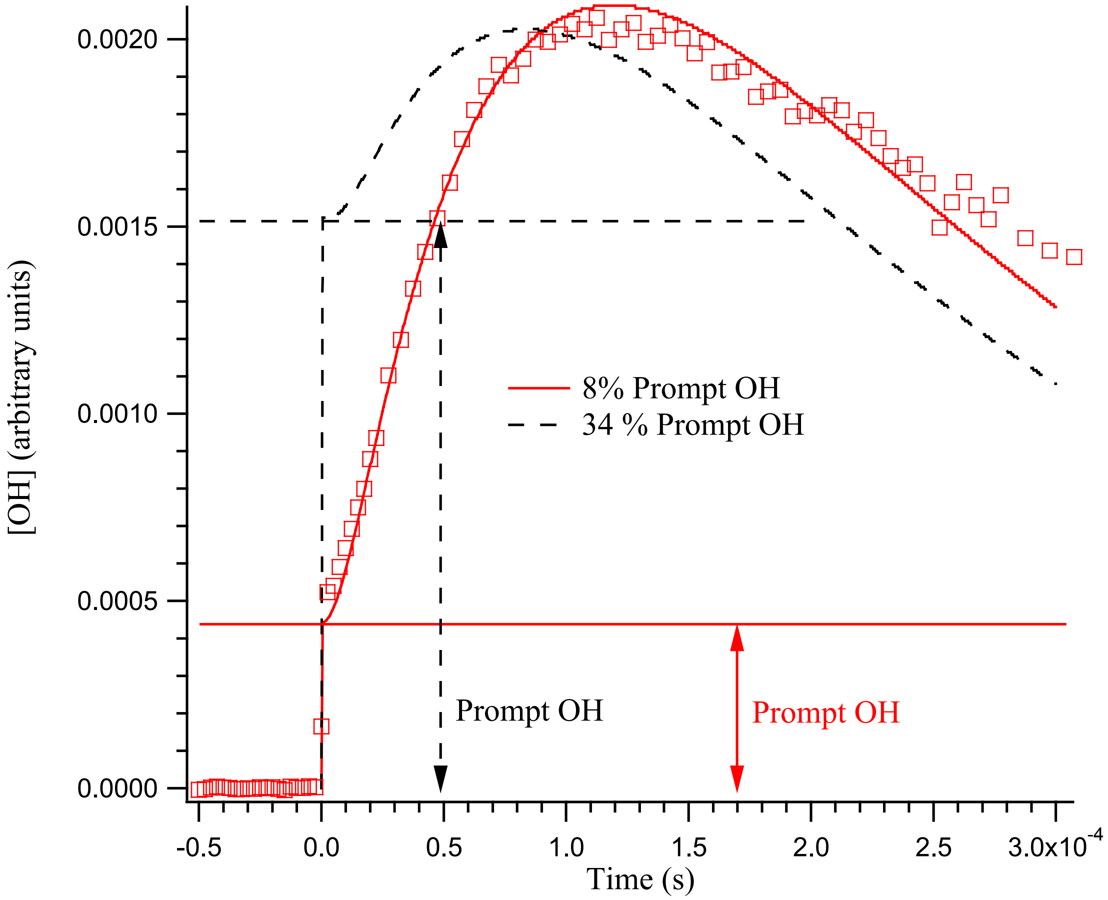

Figure VII-IX. Simulations from the kinetic model including 34% prompt dissociation of β-hydroxyalkyl radicals as compared to 8%.

Of the surviving β-hydroxyalkyl radicals, the ratio of k_3 to k_4 represents the proportion which will cyclically isomerize to form α-hydroxyalkyl radicals to the proportion which collisionally relax into the deep well of the β-hydroxyalkyl adducts.

The fates of the α-hydroxyalkyl radicals are either hydrogen abstraction by O_2 or NO termination. The β-hydroxyalkyl radicals are assumed to follow the conventional hydrocarbon oxidation scheme as shown in Figure I-I and either undergo NO termination or O_2 addition. Further reactions of the peroxy radicals resulting from O_2 addition to β-hydroxyalkyl radicals ultimately lead to a regeneration of OH radicals, but on a time scale much longer than the observed OH rise in the data. Additional simulations excluding the cyclic isomerization to form α-hydroxyalkyl radicals were performed as shown in Figure VII-X. It is clear that the time dependence seen in the OH temporal profiles relies on the cyclic isomerization.

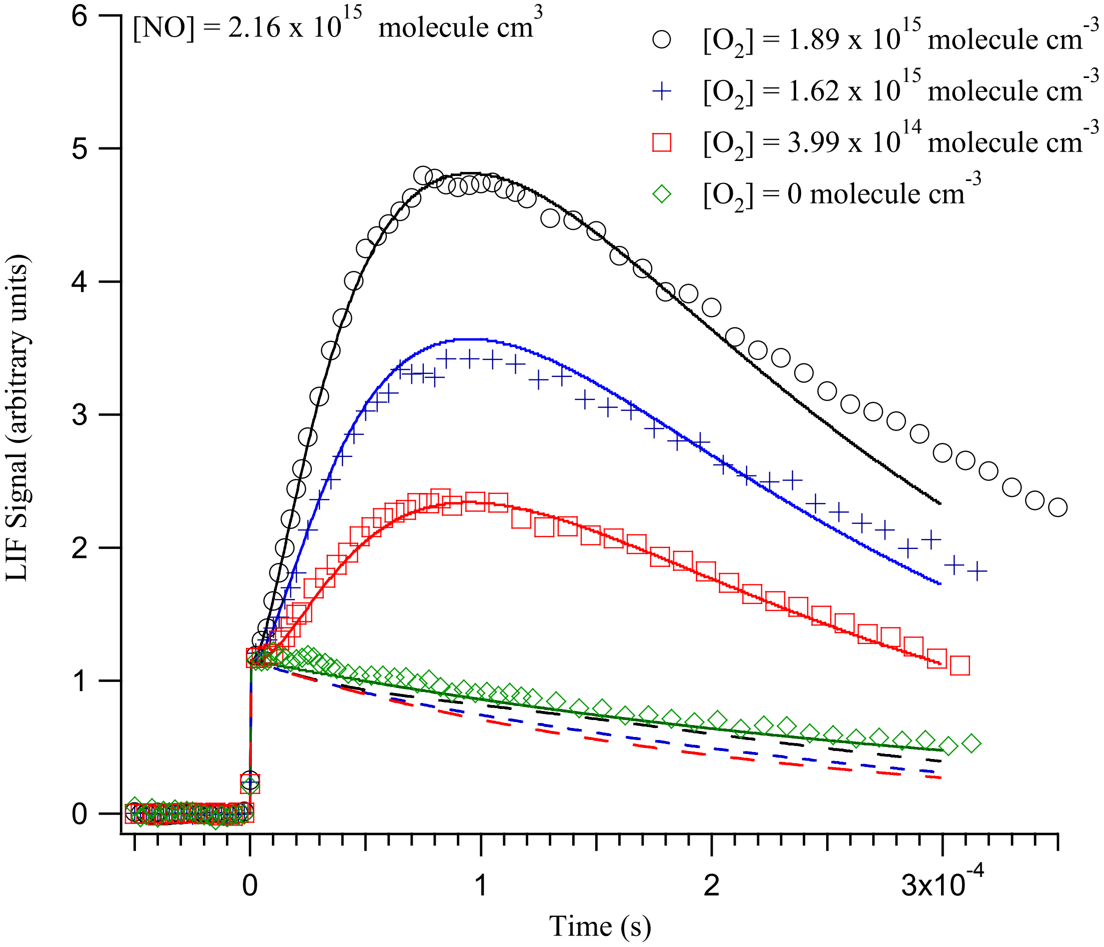

Figure VII-X. OH temporal profiles for the reaction of OH addition to the second position of isoprene in the presence of O_2 and NO. The data is shown in symbols overlaid with fits including the cyclic isomerization pathway (solid lines) and excluding the cyclic isomerization pathway (dashed lines.)

Sensitivity analysis, such as that presented in the previous chapter, is shown in Figure VII-XI. Of the rates, which exhibit high sensitivity, only rates k_1-k_5 are adjustable rates. Based on this model, the hydrogen abstraction rate from the α-hydroxyalkyl radical is determined to be (3.72 ± 0.37) x 10^{-11} cm^3 $molecule^{-1}$ s^{-1}, where the error bars reflect 2 standard deviations from the average. We are also able to establish an α/β branching ratio of 7 (87.5% of the β-hydroxyalkyl radicals cyclically isomerize.)

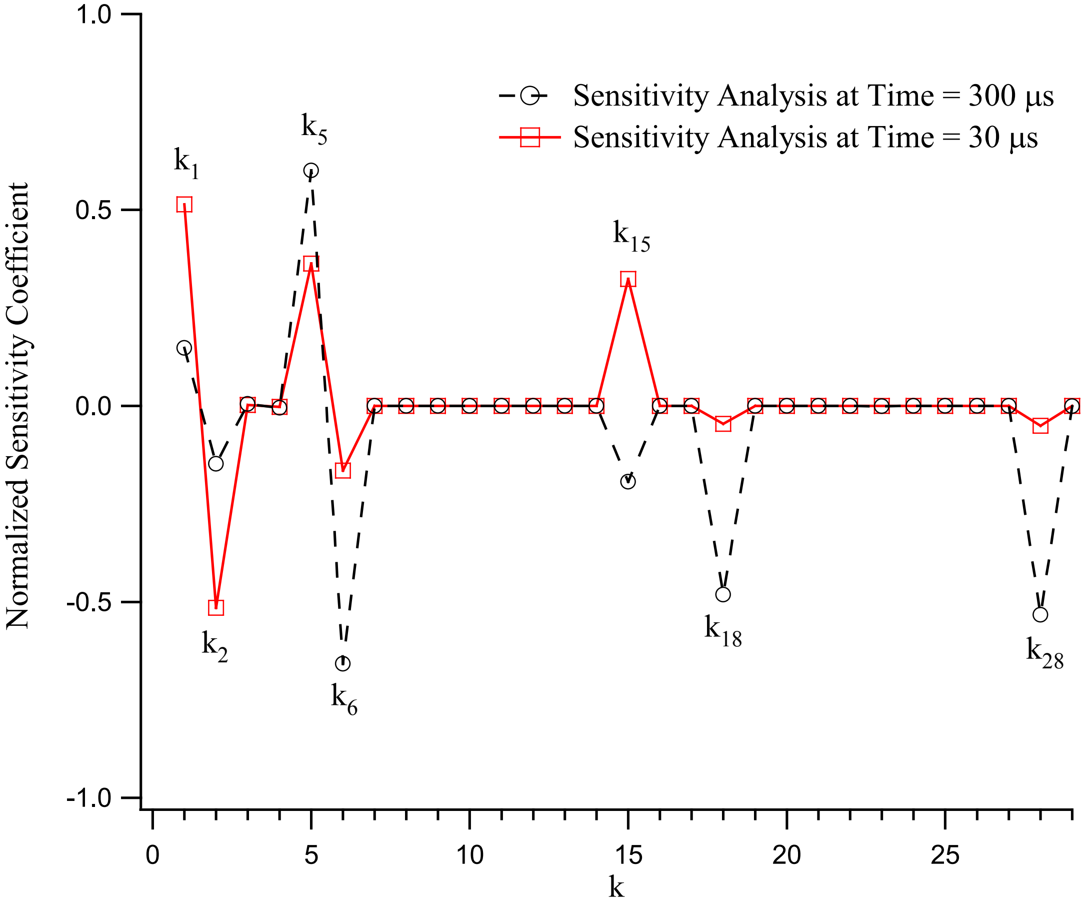

Figure VII-XI. Normalized sensitivity coefficients for the reaction mechanism of the OH addition to the second position of isoprene in the presence of O_2 and NO at short times (T = 30 µs) and long times (T = 300 µs.)

B. Conclusions

We have demonstrated a photolytic route to studying isomeric selective kinetics of OH-initiated oxidation of unsaturated hydrocarbons using the UV photolysis of iodohydrins. The present study focuses on the reactivity of the nascent β-hydroxyalkyl radical formed when isoprene undergoes oxidation by hydroxyl radical addition. Velocity map ion imaging permits the direct determination of the internal energy distribution of the nascent radical ensuring that the energy distribution of the radicals can be 'tuned' to mimic the kinetics of radicals formed from electrophilic-OH addition. Time resolved mass spectrometry affords additional confirmation of the cyclic isomerization pathway by monitoring the time dependent depletion of reactants and formation of products. Prompt OH generation during the kinetics experiments offers addition evidence supporting the cyclic isomerization to α-hydroxyalkyl radicals and affords a hydrogen abstraction rate constant from the α-hydroxyalkyl radical of $(3.72 \pm 0.37) \times 10^{-11}$ cm^3 $molecule^{-1}$ s^{-1}.

CHAPTER VIII

CONCLUSIONS[*]

A. Concluding Remarks

We have examined the mechanistic details of the early oxidation steps of unsaturated hydrocarbons in the troposphere, employing both theoretical and experimental techniques. We have developed a robust theoretical model to predict temperature and pressure dependent kinetics of the OH addition to unsaturated hydrocarbons, first applied to the case of OH addition to ethylene, and later expanding to the OH addition to isoprene.

By simply reducing the inner saddle point energy by 1.0 kcal/mol from its ab initio predicted value (to -1.1 kcal/mol) we are able to satisfactorily reproduce the available experimental data from 100 to 600 K of the OH addition to ethylene. The pressure dependence of the addition rate constant is also satisfactorily reproduced with reasonable parameters for the energy transfer function. The theoretically predicted capture rate is reproduced to within 10% by the expression [$4.93\text{x}10^{-12}(T/298)^{-2.488}\exp(-107.9/RT) + 3.33\text{x}10^{-12} (T/298)^{0.451}\exp(117.6/RT)$; with R=1.987 and T in K] cm^3 $molecules^{-1}$ s^{-1}over the 10 to 600 K range.

---

[*] Parts of this chapter are preprinted with permission from "A Two Transition State Model for Radical-Molecule Reactions: Application to Isomeric Branching in the OH-Isoprene Reaction" Greenwald, E. E.; North, S. W.; Georgievskii, Y.; Klippenstein, S. J. *J. Phys. Chem. A* **2007**, submitted and “The OH Initiated Oxidation of Isoprene in the Presence of O_2 and NO: A Photolytic Route to Study Isomeric Selective Reactivity” Greenwald, E. E.; Ghosh, B.; Anderson, K. A.; Dooley, K. S.; North, S. W. *J. Phys. Chem. A.* **2007**, in preparation. Additional parts of this chapter are reprinted with permission from “A Two Transition State Model for Radical-Molecule Reactions: A Case Study of the Addition of OH to C_2H_4” Greenwald, E. E.; North, S. W.; Georgievskii, Y.; Klippenstein, S. J. *J. Phys. Chem. A.* **2005**, *109*, 6031 and "The OH Initiated Oxidation of 1,3-Butadiene in the Presence of O2 and NO: A Photolytic Route to Study Isomeric Selective Reactivity" Greenwald, E. E.; Anderson, K. C.; Park, J.; Kim, H.; Reich, B. J. E.; Miller, S. A.; North, S. W. *J. Phys. Chem.. A* **2005**, *109*, 7915.

We have extended the previously developed two-transition state model for OH addition to ethylene to the case of OH addition to isoprene. We have calculated the rates of reaction under ambient conditions as well as examined low temperature rates of reaction and rates of reaction as a function of pressure and temperature in the fall-off regime. We combined phase space theory calculations with standard RRKM theory calculations to determine the contribution to the rates of reaction from both an outer and an inner transition state.

With a modest adjustment of the saddle point energies to each of the four OH-isoprene isomers (1-4) of –0.8 kcal/mol, we were able to accurately reproduce the high-pressure limit, temperature dependent rate constants. The high-pressure limiting 300 K rate constant of the OH addition to isoprene calculated here of 1.06×10^{-10} cm^3 $molecule^{-1}$ s^{-1} is consistent with the recommended value. The theoretically predicted capture rate is reproduced to within 10% by the expression $[1.71\text{x}10^{-10}(T/298)^{-2.58}\exp(-608.6/RT) + 5.47\text{x}10^{-11}(T/298)^{-1.78}\exp(-97.3/RT)$; with $R = 1.987$ and T in K] cm^3 $molecule^{-1}$ s^{-1} over the 30-500 K range. A 300 K, high-pressure limit branching ratio of 0.67:0.02:0.02:0.29 was determined for isomers, 1, 2, 3, and 4, respectively. An Arrhenius activation energy of –0.77 kcal/mol was determined for the high-pressure addition rate constants around 300 K. Using reasonable parameters for collisional energy transfer in the exponential down model, we were able to satisfactorily reproduce the pressure dependence of these reactions at a variety of temperatures in Ar and He buffer gasses.

The use of an effective transition state model, incorporating effects from both the inner and outer transition states, is an essential element of the present predictions. It is particularly important that these effects be included at the energy, *E,* and total angular momentum, *J,* resolved level. At the point where the two transition states are of equal importance, the *E/J* resolved treatment yields a reduction in the rate by an order of magnitude.

The present calculations clearly show that a single transition state model is only appropriate for temperatures of about 400 K or higher. The convergence of the inner transition state model to the effective transition state model occurs at a temperature that roughly corresponds to the energy of the saddle point below reactants. This finding is likely quite general and can be used to estimate whether a single inner transition state treatment is sufficient for other reactions with negative saddle point energies.

We have demonstrated a photolytic route to studying isomeric selective kinetics of OH-initiated oxidation of unsaturated hydrocarbons using the UV photolysis of iodohydrins. The present studies focus on the reactivity of the nascent β-hydroxyalkyl radical formed when butadiene and isoprene undergo oxidation by hydroxyl radical addition. Velocity map ion imaging permits the direct determination of the internal energy distribution of the nascent radical ensuring that the energy distribution of the radicals can be 'tuned' to mimic the kinetics of radicals formed from electrophilic-OH addition. The theoretical predictions modeling isomerization vs. collisional relaxation of the β-hydroxyalkyl radicals predict a significant proportion of β-hydroxyalkyl radicals isomerize to the α-hydroxyalkyl radical form before collisional relaxation. Prompt OH/OD generation during the kinetics experiments offers conclusive evidence supporting the cyclic isomerization to α-hydroxyalkyl radicals.

We have theoretically predicted and experimentally observed a novel route to C5 carbonyl formation for OH addition to inner positions of isoprene employing time resolved mass spectrometry and laser photolysis/ laser induced fluorescence. These results offer insight into previously unexplained products in remote measurements and smog chamber experiments.

B. Future Directions

While the initial steps of the OH addition to unsaturated hydrocarbons is now generally understood under tropospheric conditions, the extension of these models to higher temperatures is useful for applications such as combustion. In a combustion setting, hydrogen abstraction by OH becomes important and many energetically inaccessible under ambient conditions become accessible. For the case of OH addition to ethylene, this analysis was performed by Miller and coworkers[189] immediately following the publication of our model. It would be instructive to follow suite for other combustion important molecules such as propene.

Additionally, the two-transition state model would provide a useful application for the subsequent O_2 addition to the allylic radicals formed by OH addition to one of the outer positions of isoprene. In the case of O_2 addition to these isomers, further branching ensues as shown in Figure VIII-I. The two allylic radicals have two possible positions for O_2 addition, each, and those isomers have E and Z conformations, resulting in 6 possible peroxy radicals from the initial 2 hydroxyalkyl radicals.

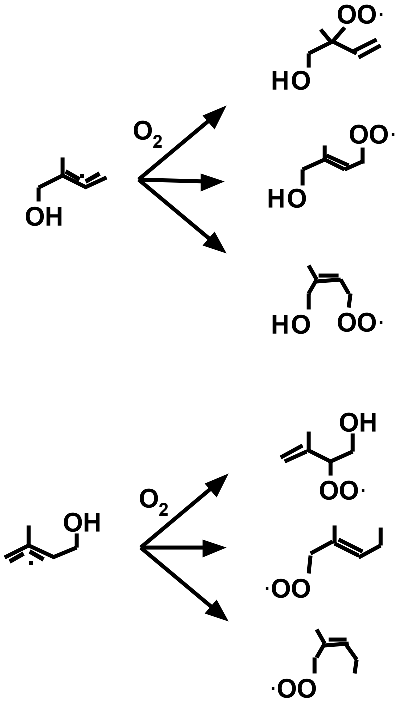

Figure VIII-I. Branching in the O_2 addition to the allylic hydroxyalkyl OH-isoprene isomers 1 and 4.

One could employ a similar methodology as was used to model the OH to isoprene in order to understand the branching and isomeric specific rate constants to formation of each of the 6 peroxy radicals. Additionally, one could prepare photolytic precursors to pare down the reaction to an extent that employing chemical ionization mass spectrometry,[155] or cavity ring-down spectroscopy on the resolved A-X transition of peroxy radicals to obtain selective detection[156] would extract meaningful branching ratios.

Another interesting application of the isomeric selective studies would be to study the temperature and pressure dependent kinetics of the hydrogen abstraction step from α-hydroxyalkyl radicals to expand the relatively limited previous determinations of this reaction mechanism.[157,190,191,192,193,194,195] The inverse temperature dependence previously observed for this reaction is indicative of a mechanism that first involves O_2 addition followed by HO_2 elimination. Theoretical predictions confirm this mechanism. [193,195] Further pressure dependent and temperature dependent studies would be insightful into the generality of this observed trend. Additionally, isotopic labeling may aide in the distinction between a mechanism where the O_2 first adds to the radical site, followed by intramolecular hydrogen abstraction, and then dissociation to form HO_2 as compared to direct hydrogen abstraction by O_2. Preparation of the mono-deuterated iodohydrin, such as that presented in Chapter VI, should show a kinetic isotope effect in the observed reaction kinetics for a mechanism involving direction H/D abstraction from the α-hydroxyalkyl radical.

REFERENCES AND NOTES

(1) Riehl, H. *Introduction to the Atmosphere*, 3rd ed.; McGraw-Hill: New York, 1978.

(2) Brasseur, G. P.; Orlando, J. J.; Tyndall, G. S. *Atmospheric Chemistry and Global Change*; Oxford University Press, Inc.: New York, 1999.

(3) Finlayson-Pitts, B. J.; James N. Pitts, J. *Chemistry of the Upper and Lower Atmosphere: Theory, Experiments, and Applications*; Academic Press: San Diego, 2000.

(4) Guenther, A.; Hewitt, C. N. ; Erickson, D. ; Fall, R. ; Geron, C. ; Graedel, T. ; Harley, P. ; Klinger, L. ; Lerdau, M. ; et al. *J. Geophys. Res.* **1995**, *100*, 8873.

(5) Fuentes, J. D.; Lerdau, M.; Atkinson, R.; Baldocchi, D.; Bottenheim, J. W.; Ciccioli, P.; Lamb, B.; Geron, C.; Gu, L.; Guenther, A.; Sharkey, T. D.; Stockwell, W. *Bulletin of the American Meteorological Society* **2000**, *81*, 1537.

(6) Kroll, J. H.; Ng, N. L.; Murphy, S. M.; Flagan, R. C.; Seinfeld, J. H. *Geophys. Res. Lett.* **2005**, *32*, L18808.

(7) Kroll, J. H.; Ng, N. L.; Murphy, S. M.; Flagan, R. C.; Seinfeld, J. H. *Environ. Sci. Technol.* **2006**, *40*, 1869.

(8) Surratt, J. D.; Murphy, S. M.; Kroll, J. H.; Ng, N. L.; Hildebrandt, L.; Sorooshian, A.; Szmigielski, R.; Mermeylen, R.; Maenhaut, W.; Claeys, M.; Flagan, R. C.; Seinfeld, J. H. *J. Phys. Chem. A* **2006**, *110*, 9665.

(9) Dommen, J.; Metzger, A.; Duplissy, J.; Kalberer, M.; Alfarra, M. R.; Gascho, A.; Weingartner, E.; Prevot, A. S. H.; Verheggen, B.; Baltensperger, U. *Geophys. Res. Lett.* **2006**, *33*, L13805.

(10) Edney, E. O.; Kleindienst, T. E.; Jaoui, M.; Lewandowski, M.; Offenberg, J. H.; Wang, W.; Claeys, M. *Atmos. Environ.* **2005**, *39*, 5281.

(11) Lim, H.-J.; Carlton, A. G.; Turpin, B. J. *Environ. Sci. Technol.* **2005**, *39*, 4441.

(12) Altieri, K. E.; Carlton, A. G.; Lim, H.-J.; Turpin, B. J.; Seitzinger, S. P. *Environ. Sci. Technol.* **2006**, *40*, 4956.

(13) Carlton, A. G.; Turpin, B. J.; Lim, H.-J.; Altieri, K. E.; Seitzinger, S. *Geophys. Res. Lett.* **2006**, *33*, L06822.

(14) Santos, L. S.; Dalmázio, I.; Eberlin, M. N.; Claeys, M.; Augusti, R. *Rapid Commun. Mass Spectrom.* **2006**, *20*, 2104.

(15) Campuzano-Jost, P.; Williams, M. B.; D'Ottone, L.; Hynes, A. *Geophys. Res. Lett.* **2000**, *27*, 693.

(16) Despite a range of 7.4x10^{-11} to 1.1x10^{-10} cm^3 $molec^{-1}$ s^{-1} throughout the literature, a general consensus has been reached that the literature value of the OH addition to isoprene converges to 1x10^{-10} $molec.^3cm^{-3}s^{-1}$.

(17) Atkinson, R.; Aschmann, S. *Int. J. Chem. Kinet.* **1984**, *16*, 1175.

(18) Atkinson, R.; Aschmann, S. M.; Winer, A. M.; Pitts, J. N., Jr. *Int. J. Chem. Kinet.* **1982**, *14*, 507.

(19) Atkinson, R. *J. Phys. Chem. Ref. Data* **1994**, *2*, 1.

(20) Atkinson, R. *Chem. Rev.* **1985**, *85*, 69.

(21) Cox, R. A.; Derwent, R. G.; Williams, M. R. *Environ. Sci. and Technol.* **1980**, *14*, 57.

(22) Chuong, B.; Stevens, P. S. *J. Geophys. Res.* **2002**, *107*, 4162.

(23) Gill, K. J.; Hites, R. A. *J. Phys. Chem. A* **2002**, *106*, 2538.

(24) Iida, Y.; Obi, K.; Imamura, T. *Chem. Lett.* **2002**, *8*, 792.

(25) Kleindienst, T. E.; Harris, G.W.; Pitts, J. N., Jr. *Environ. Sci. Technol.* **1982**, *16*, 844.

(26) McGivern, W. S.; Suh, I.; Clinkenbeard, A. D.; Zhang, R.; North, S. W. *J. Phys. Chem. A* **2000**, *104*, 6609.

(27) Ohta, T. *J. Phys. Chem.* **1983**, *87*, 1209.

(28) Park, J.; Jongsma, C. G.; Zhang, R.; North, S. W. *J. Phys. Chem. A* **2004**, *108*, 10688.

(29) Siese, M.; Koch, R. Fittschen, C.; Zetzsch, C. The Proceedings of EUROTRAC Symposium '94 edited by PmM. Borrell et al., pp. 115-119. **1994**, SPB Academic Publishing bv. The Hague, The Netherlands.

(30) Spangenberg, T.; Köhler, S.; Hansmann, B.; Wachsmuth, U.; Abel, B.; Smith, M. A. *J. Phys. Chem. A* **2004**, *108*, 7527.

(31) Stevens, P. S.; Seymour E.; Li, Z. *J. Phys. Chem. A* **2000**, *104*, 5989.

(32) Zhang, R.; Suh, I.; Lei, W.; Clinkenbeard, A.; North, S. W. *J. Geophys. Res*. **2000**, *105*, 24627.

(33) Chuong, B.; Stevens, P.S. *J. Phys. Chem. A* **2000**, *104*, 5230.

(34) Atkinson, R.; Arey, J. *Atmos. Environ.* **2003**, *37*, S197.

(35) Lee, W.; Baasandorj, M.; Stevens, P. S.; Hites, R. A. *Environ. Sci. Technol.* **2005**, *39*, 1030.

(36) Jenkin, M. E.; Boyd, A. A.; Lesclaux, R. *J. Atmos. Chem.* 1998, *29*, 267. Jenkin, M. E.; Hayman, G. D. *J. Chem. Soc. Faraday Trans.* **1995**, *91*, 1911.

(37) Park, J.; Jongsma, C. G.; Zhang, R.; North, S. W. *Phys. Chem. Chem. Phys.* **2003**, *5*, 3638.

(38) Greenwald, E. E.; North, S. W.; Georgievskii, Y.; Klippenstein, S. J. *J. Phys. Chem. A* **2007**, in press.

(39) Greenwald, E. E.; Anderson, K. C.; Park, J.; Kim, K.; Reich, B. J. E.; Miller, S. A.; Zhang, R.; North, S. W. *J. Phys. Chem. A* **2005**, *109*, 7915.

(40) Greenwald, E. E.; Ghosh, B.; Anderson, K. C.; Zhang, R.; North, S. W. *J. Phys. Chem. A* **2007**, in preparation.

(41) Paulson, S. E.; Flagan, R. C.; Seinfeld, J. H. *Int. J. Chem. Kinet.* **1992**, *24*, 79.

(42) Peeters, J.; Boullart, W.; Hoeymissen, J. V. The Proceedings of EUROTRAC Symposium '94 edited by PmM. Borrell et al., Vol. 14, pp. 110-. **1994**, SPB Academic Publishing bv. The Hague, The Netherlands.

(43) Peeters, J.; Boullart, W.; Pultau, V.; Vanderberk, S.; Vereecken, L. *J. Phys. Chem. A* **2007**, ASAP.

(44) Francisco-Márquez, M.; Alvarez-Idaboy, J. R.; Galano, A.; Vivier-Bunge, A. *Phys. Chem. Chem. Phys.* **2003**, *5*, 1392.

(45) Lei, W.; Zhang, R. J. ; McGivern, W. S.; Derecskei-Kovacs, A.; North, S. W. *Chem. Phys. Lett.* **2000**, *326*, 109.

(46) Wortmann-Saleh, D.; Engels, B.; Peyerimhoff, S. D. *J. Phys. Chem.* **1994**, *98*, 9541. Engels, B.; Peyerimhoff, S. D. *J. Phys. Chem.* **1989**, *93*, 4462. Engles, B.; Peyerimhoff, S. D.; Skell, P. S. *J. Phys. Chem.* **1990**, *94*, 1267.

(47) Villa, J.; Gonzalez-Lafont, A.; Lluch, J. M.; Corchado, J. C.; Espinosa-Garcia, J. *J. Chem. Phys.* **1997**, *107*, 7266.

(48) Alvarez-Idaboy, J. R.; Mora-Diez, N.; Vivier-Bunge, A. *J. Am. Chem. Soc.* **2000**, *122*, 3715.

(49) Singleton, D. L.; Cvetanovic, R. J. *J. Am. Chem. Soc.* **1997**, *98*, 6812.

(50) Greiner, N. R. *J. Chem. Phys.* **1970**, *53,* 1284.

(51) Morris, E. D.; Stedman, D. H.; Niki, H. *J. Am. Chem. Soc.* **1971**, *93,* 3570.

(52) Smith, I. W. M.; Zellner, R. *J. Chem. Soc: Faraday Trans. II* **1973**, *69,* 1617.

(53) Bradley, J. N.; Hack, W.; Hoyermann, K.; Wagner, H. G. *J. Chem. Soc. Trans. 1,* **1973**, *69,* 1889.

(54) Stuhl, F. *Ber. Bunsenges. Phys. Chem.* **1973**, 77, 674.

(55) Cox, R. A. *Int. J. Chem. Kinet. Symp.*, **1975**, *1*, 379.

(56) Gordon, S.; Mulac, W. A. *Int. J. Chem. Kinet. Symp.* **1975**, *1*, 289.

(57) Davis, D. D.; Fischer, S.; Schiff, R.; Watson, R. T.; Bollinger, W. *J. Chem. Phys.* **1975**, *63,* 1707.

(58) Atkinson. R.: Pitts. J. N.. Jr. *J. Chem. Phvs.* **1975**, *63,* 3591.

(59) Pastrana, A. V.; Carr, R. W. *J. Phys. Chem.* **1975**, *79,* 765.

(60) Howard, C. J. *J. Chem. Phys.* **1976**, *65,* 4771.

(61) Lloyd, A. C.; Darnall, K. R.; Winer, A. M.; Pitts, J. N. *J. Phys. Chem.* **1976**, *80,* 789.

(62) Bradley, J. N.; Capey, W. D.; Fair, R. W.; Pritchard, D. K. *Int. J. Chem. Kinet.* **1976**, *8,* 549

(63) Overend, R.; Paraskevopaulos, G. *J. Chem. Phys.* **1977**, *67,* 674.

(64) Atkinson, R.; Perry, R. A.; Pitts, J. N. *J. Chem. Phys.* **1977**, *66,* 1197.

(65) Atkinson, R.; Perry, R. A.; Pitts, J. N., Jr. *J . Chem. Phys.* **1977**, *67,* 3170.

(66) Farquharson, G. K.; Smith, R. H. *Aust. J. Chem.* **1980**, *33,* 1425.

(67) Tully, F. P. *Chem. Phys. Lett.* **1983**, *96,* 148.

(68) Klein, T.; Barnes, I.; Becker, K. H.; Fink, E. H.; Zabel, F. *J. Phys. Chem.* **1984**, *88,* 5020.

(69) Zellner, R.; Lorenz, K. *J. Phys. Chem.* **1984**, *88,* 984.

(70) Atkinson, R.; Aschmann, S. M. *Int. J. Chem. Kinet.* **1984**, *16,* 1175.

(71) Schmidt, V.; Zhu, G. Y.; Becker, K. H.; Fink, E. H.; *Ber. Bunsenges. Phys. Chem.,* **1985**, *89,* 321.

(72) Klopffer; V. W.; Frank, R.; Kohl, E.-G.; Haag, F.; *Chem Ztg.* **1986**, *110,* 57.

(73) Liu,A-. D.; Mulac, W. A.; Jonah, C. D. *Int. J. of Chem. Kinet.* **1987**, *19,* 25.

(74) Liu, A.; Mulac, W. A.; Jonah, C. D. *J. Phys. Chem.* **1988**, *92,* 3828.

(75) Tully, F. P. *Chem. Phys. Lett.* **1988**, *143,* 510.

(76) Westbrook, C. K.; Thornton, M. M.; Pitz, W. J.; Malte, P. C. *Proc. Combust. Inst.* **1989**, *22,* 863.

(77) Nielsen, O. J.; Jorgensen, O.; Donlon, M.; Sidebottom, H. W.; O'Farrell, D. J.; Treacy, T. *Chem. Phys. Lett.* **1990**, *168,* 319.

(78) Becker, K. H.; Geiger, H.; Wiesen, P. *Chem. Phys. Lett.* **1991**, *184*, 256.

(79) Bott, J. F.; Cohen, N. *Int. J. Chem. Kinet.* **1991**, *23,* 1075.

(80) Diau, E. W.; Lee, Y.-P. *J. Chem. Phys.* **1991**, *96,* 377.

(81) Kuo, C.-H.; Lee, Y.-P. *J. Phys. Chem.* **1991**, *95*, 1253.

(82) Fulle, D.; Hamann, H. F.; Hippler, H.; Jansch, C.P. *Ber. Bunsenges. Phys. Chem.* **1997**, *101,* 1433.

(83) Vakhtin, A. B.; Murphy, J. E.; Leone, S. R.; *J. Phys. Chem. A* **2003**, *107,* 10055.

(84) Sosa, C.; Schlegel, H. B. *J. Am. Chem. Soc.* **1987**, *109,* 4193.

(85) Villa, J.; Gonzalez-Lafont, A.; Lluch, J. M.; Corchado, J. C.; Espinosa-Garcia, J. *J. Chem. Phys.* **1997**, *107,* 7266.

(86) Sekusak, S.; Liedl, K. R.; Sabljic, A. *J. Phys. Chem. A,* **1998**, *102,* 1583.

(87) Yamada, T.; Bozzelli, J. W.; Lay, T. *J. Phys. Chem. A,* **1999**, *103,* 7646.

(88) Hippler, H.; Viskolcz, B. *Phys. Chem. Chem. Phys.* **2000**, *2,* 3591.

(89) Piqeuras, M. C.; Crespo, R.; Nebot-Gil, I.; Tomas, F. *J. Molec. Struc.* **2001**, *537,* 199.

(90) Liu, G.-X.; Ding, Y.-H.; Li, Z.-S.; Fu, Q.; Huang, X.-R.; Sun, C.-C.; Tang, A.-C. *Phys. Chem. Chem. Phys* **2002**, *4,* 1021.

(91) Lee, C.; Yang, W.; Parr, R. G. *Phys. Rev. B* **1988**, *37*, 785. Miehlich, B.; Savin, A.; Stoll, H.; Preuss, H. *Chem. Phys. Lett.* **1989**, *157*, 200. Becke, A. D. *J. Chem. Phys.* **1993**. *98*, 5648.

(92) Ditchfield, R.; Hehre, W. J.; Pople, J. A. *J. Chem. Phys.* **1971**, *54*, 724. Hehre, W. J.; Ditchfield, R.; Pople, J. A. *J. Chem. Phys.* **1972**, *56*, 2257. Hariharan, P. C.; Pople, J. A. *Mol. Phys.* **1974**, *27*, 209. Gordon, M. S. *Chem. Phys. Lett.* **1980**, *76*, 163. Hariharan, P. C.; Pople, J. A. *Theo. Chim. Acta* **1973**, *28*, 213. Blaudeau, J.-P.; McGrath, M. P.; Curtiss, L. A.; Radom, L. *J. Chem. Phys.* **1997**, *107*, 5016. Francl, M. M.; Pietro, W. J.; Hehre, W. J.; Binkley, J. S.; DeFrees, D. J.; Pople, J. A.; Gordon, M. S. *J. Chem. Phys.* **1982**, *77*, 3654. Binning, R. C., Jr.; Curtiss, L. A. *J. Comp. Chem.* **1990**, *11*, 1206. Rassolov, V. A.; Pople, J. A.; Ratner, M. A.; Windus, T. L. *J. Chem. Phys.* **1998**, *109*, 1223. Rassolov, V. A.; Ratner, M. A.; Pople, J. A.; Redfern, P. C.; Curtiss, L. A. *J. Comp. Chem.* **2001**, *22*, 976.

(93) Frisch, M. J.; Trucks, G. W.; Schlegel, H. B.; Scuseria, G. E.; Robb, M. A.; Cheeseman, J. R.; Zakrzewski, V. G.; Montgomery, J. A., Jr.; Stratmann, R. E.; Burant, J. C.; Dapprich, S.; Millam, J. M.; Daniels, A. D.; Kudin, K. N.; Strain, M. C.; Farkas, O.; Tomasi, J.; Barone, V.; Cossi, M.; Cammi, R.; Mennucci, B.; Pomelli, C.; Adamo, C.; Clifford, S.; Ochterski, J.; Petersson, G. A.; Ayala, P. Y.; Cui, Q.; Morokuma, K.; Salvador, P.; Dannenberg, J. J.; Malick, D. K.; Rabuck, A. D.; Raghavachari, K.; Foresman, J. B.; Cioslowski, J.; Ortiz, J. V.; Baboul, A. G.; Stefanov, B. B.; Liu, G. Liashenko, A.; Piskorz, P.; Komaromi, I.; Gomperts, R.; Martin, R. L.; Fox, D. J.; Keith, T.; Al-Laham, M. A.; Peng, C. Y.; Nanayakkara, A.; Challacombe, M.; Gill, P. M. W.; Johnson, B.; Chen, W.; Wong, M. W.; Andres, J. L.; Gonzalez, C.; Head-Gordon, M.; Replogle, E. S.; Pople, J. A. *Gaussian 98*, revision A.11; Gaussian, Inc.: Pittsburgh, PA, 2001.

(94) Varshni, Y. P. *Rev. Mod. Phys.* **1957**, *29*, 664.

(95) DeMore, W. B.; Howard, C. J.; Sander, S. P.; Ravishankara, A. R.; Golden, D. M.; Kolb, C. E.; Hampson, R. F.; Molina, M. J. *JPL Publication 97-4* **1997**, *12*, 1.

(96) This is a compilation of results derived from the references for the association rate of ethylene to OH.

(97) Johnston, H. S. *Gas Phase Reaction Rate Theory*, Ronald, New York, 1966.

(98) Alternatively, one could include the van der Waal's well in a multiple well master equation analysis of the time dependent populations. However, the very short lifetime of the van der Waals complex suggests that the limiting assumption of a collision free environment should be completely satisfactory for all but extraordinarily high pressures.

(99) Hirschfelder, J. O.; Wigner, E. *J. Chem. Phys.* **1939**, *7,* 616. Miller, W. H.; *J. Chem. Phys.* **1976**, *65,* 2216. Chesnavich, W. J.; Bass, L.; Su, T.; Bowers, M. T. *J. Chem. Phys.* **1981**, *74,* 2228. Rai, S. N.; Truhlar, D. G. *J. Chem. Phys.* **1983**, *79,* 6046.

(100) Klippenstein, S. J.; Khundkar, L. R.; Zewail, A. H.; Marcus, R. A. *J. Chem. Phys.* **1988**, *89,* 4761.

(101) Mozurkewich, M.; Benson, S. W. *J. Phys. Chem.* **1984**, *88,* 6429. Mozurkewich, M.; Lamb, J. J.; Benson, S. W. *J. Phys. Chem.* **1984**, *88,* 6435; Lamb, J. J.; Mozurkewich, M.; Benson, S. W. *J. Phys. Chem.* **1984**, *88,* 6441.

(102) Chen, Y.; Rauk, A.; Tschuikow-Roux, E. *J. Phys. Chem.* **1991**, *95,* 9900. Chen, Y.; Tschuikow-Roux, *J. Phys. Chem.* **1993**, *97,* 3742.

(103) Jodkowski, J. T.; Rayez, M.-T.; Rayez, J.-C.; Berces, T.; Dobe, S. *J. Phys. Chem. A,* **1998**, *102,* 9219. Jodkowski, J. T.; Rayez, M.-T.; Rayez, J.-C.; Berces, T.; Dobe, S. *J. Phys. Chem. A,* **1998**, *102,* 9230.

(104) Klippenstein, S. J.; Marcus, R. A. *J. Chem. Phys.* **1989**, *91*, 2280. Klippenstein, S. J.; Marcus, R. A. *J. Chem. Phys.* **1990**, *93,* 2418. Klippenstein, S. J.; East, A. L. L.; Allen, W. D. *J. Chem. Phys.* **1996**, *105*, 118. Klippenstein, S. J. Allen, W. D. *Ber. Bunsen. Phys. Chem.* **1997**, *101*, 423.

(105) Clary, D. C.; *Ann. Rev. Phys. Chem.* **1990**, *41,* 61; and references cited therein.

(106) Troe, J. *Adv. Chem. Phys.* **1997**, *101,* 819; and references cited therein.

(107) Georgievskii, Y.; Klippenstein, S. J. *J. Phys. Chem. A,* **2005**, *122*, 194103.

(108) Pople, J. A.; Head-Gordon, M.; Raghavachari, K. *J. Chem. Phys.* **1987**, *87,* 5968.

(109) Dunning, T. H. *J. Chem. Phys.* **1989**, *90,* 1007.

(110) Head-Gordon, M.; Pople, J. A.; Frisch, M. J. *Chem. Phys. Lett.* **1988**, *153,* 503.

(111) Moller, C.; Plesset, M. C. *Phys. R*ev. **1934**, *46,* 618.

(112) D. Feller and D. A. Dixon, J. Chem. Phys., **2001**, 115, 3484-3496.

(113) Martin, J. M. L. *Chem. Phys. Lett.* **1996**, *259,* 669.

(114)Greenwald, E. E.; North, S. W.; Georgievskii, Y.; Klippenstein, S. J. *J. Phys. Chem. A* **2005**, *109*, 6031.

(115) Helgaker, T.; Klopper, W.; Koch; H.; Noga, J. *J. Chem. Phys.* **1997**, *106,* 9639.

(116) Lee, T. J.; Taylor, P. R. *Int. J. Quant. Chem. Symp.* **1989**, *23,* 199. Lee, T. J.; Rendell, A. P.; Taylor, P. R. *J. Phys. Chem.* **1990**, *94,* 5463.

(117) Klippenstein, S. J. *J. Chem. Phys*. **1992**, *96*, 367. Klippenstein, S. J. *Chem. Phys. Letts.* **1993**, *214*, 418. Klippenstein, S. J. *J. Phys. Chem.* **1994**, *98*, 11459.

(118) Peterson, K. I.; Fraser, G. T.; Klemperer, W. *Can. J. Phys.* **1984**, *62,* 1502.

(119) Dagg, I. R.; Read, L. A. A; Smith, W. *Can. J. Phys.* **1982**, *60*, 1431.

(120) MOLPRO, version 2002.1, is a package of ab initio programs written by Werner, H.-J.; Knowles, P. J.; with contributions from Amos, R. D.; Bernhardsson, A.; Berning, A.; Celani, P.; Cooper, D. L.; Deegan, M. J. O.; Dobbyn, A. J.; Eckert, F.; Hampel, C.; Hetzer, G.; Korona, T.; Lindh, R.; Lloyd, A. W.; McNicholas, S. J.; Manby, F. R.; Meyer, W.; Mura, M. E.; Nicklaâ, A.; Palmieri, P.; Pitzer, R.; Rauhut, G.; Schu¨tz, M.; Schumann, U.; Stoll, H.; Stone A. J.; Tarroni, R.; Thorsteinsson, T.; Werner, H.-J.

(121) Truhlar, D. G.; Garrett, B. C.; Klippenstein, S. J. *J. Phys. Chem.* **1996**, *100*, 12771.

(122) Sample calculations suggest that at this separation, additional terms in the potential, such as those due to dispersion interactions, will yield only a modest (<35%) increase in the long-range predictions for the rate constant.

(123) Miller, W. H.; Handy, N. C.; Adams, J. E. *J. Chem. Phys.* **1980**, *72,* 99.

(124) Pitzer, K. S.; Gwinn, W. D. *J. Chem. Phys.* **1942**, *10,* 428.

(125) Miller, J. A.; Klippenstein, S. J.; Robertson, S. H. *J. Phys. Chem. A,* **2000**, *104,* 7525.

(126) Klippenstein, S. J.; Harding, L. B. *Phys. Chem. Chem. Phys*. **1999**, *1,* 989. Klippenstein, S. J.; Harding, L. B. *J. Phys. Chem. A*, **1999**, *103*, 9388. Klippenstein, S. J.; Harding, L. B. *Proc. Comb. Inst.*, **2000**, *28*, 1503.

(127) Georgievskii, Y.; Klippenstein, S. J. *J. Phys. Chem. A*, **2003**, *107*, 9776. Georgievskii, Y.; Klippenstein, S. J. *J. Chem. Phys.*, **2003**, *118,* 5442.

(128) Miller, J. A.; Klippenstein, S. J.; Raffy, C. *J. Phys. Chem. A*, **2002**, *106*, 4904.

(129) The notation HL//B3LYP/6-311++G(d,p) refers to using the high level energy estimates from the extrapolation scheme shown in equation (5) at B3LYP/6-311++G(d,p) optimized geometries.

(130) Supporting Information Available: The Cartesian coordinates of the key stationary points obtained at the B3LYP/6-311++G(d,p) level are available free of charge via the Internet at http://pubs.acs.org

(131)Miller, J. A.; Klippenstein, S. J. *J. Phys. Chem. A,* **2003**, *107,* 2680.

(132) Klippenstein, S. J.; Marcus, R. A. *J. Chem. Phys.* **1987**, *87,* 3410; Yu, J.; Klippenstein, S. J. *J. Phys. Chem.* **1991**, *95*, 9882.

(133) Sims, I. R; Smith, I. W. M.; Bocherel, P.; Defrane, A.; Travers, D.; Rowe, B. R. *J. Chem. Soc. Faraday Trans.,* **1994**, *90,* 1473.

(134) Georgievskii, Y. and Klippenstein, S. J. *J. Chem. Phys.* **2005**, *122*, 194103.

(135) McLean, A. D.; Chandler, G. S. *J. Chem. Phys.* **1980**, *72*, 5639. Krishnan, R.; Binkley, J. S.; Seeger, R.; Pople, J. A. *J. Chem. Phys.* **1980**, *72*, 650.

(136) Clark, T.; Chandrasekhar, J.; Spitznagel, G. W.; Schleyer, P. v. R. *J. Comp. Chem.* **1983**, *4*, 294. Frisch, M. J.; Pople, J. A.; Binkley, J. S. *J. Chem. Phys.* **1984**, *80*, 3265.

(137) Frisch, M. J.; Trucks, G. W.; Schlegel, H. B.; Scuseria, G. E.; Robb, M. A.; Cheeseman, J. R.; Montgomery, Jr., J. A.; Vreven, T.; Kudin, K. N.; Burant, J. C.; Millam, J. M.; Iyengar, S. S.; Tomasi, J.; Barone, V.; Mennucci, B.; Cossi, M.; Scalmani, G.; Rega, N.; Petersson, G. A.; Nakatsuji, H.; Hada, M.; Ehara, M.; Toyota, K.; Fukuda, R.; Hasegawa, J.; Ishida, M.; Nakajima, T.; Honda, Y.; Kitao, O.; Nakai, H.; Klene, M.; Li, X.; Knox, J. E.; Hratchian, H. P.; Cross, J. B.; Bakken, V.; Adamo, C.; Jaramillo, J.; Gomperts, R.; Stratmann, R. E.; Yazyev, O.; Austin, A. J.; Cammi, R.; Pomelli, C.; Ochterski, J. W.; Ayala, P. Y.; Morokuma, K.; Voth, G. A.; Salvador, P.; Dannenberg, J. J.; Zakrzewski, V. G.; Dapprich, S.; Daniels, A. D.; Strain, M. C.; Farkas, O.; Malick, D. K.; Rabuck, A. D.; Raghavachari, K.; Foresman, J. B.; Ortiz, J. V.; Cui, Q.; Baboul, A. G.; Clifford, S.; Cioslowski, J.; Stefanov, B. B.; Liu, G.;

Liashenko, A.; Piskorz, P.; Komaromi, I.; Martin, R. L.; Fox, D. J.; Keith, T.; Al-Laham, M. A.; Peng, C. Y.; Nanayakkara, A.; Challacombe, M.; Gill, P. M. W.; Johnson, B.; Chen, W.; Wong, M. W.; Gonzalez, C.; and Pople, J. A. *Gaussian 03, Revision C.02* Gaussian, Inc.: Wallingford CT, 2004.

(138) Frisch, M. J.; Head-Gordon, M.; Pople, J. A. *Chem. Phys. Lett.* **1990**, *166*, 275. Frisch, M. J.; Head-Gordon, M.; Pople, J. A. *Chem. Phys. Lett.* **1990**, *166*, 281. Head-Gordon, M.; Head-Gordon, T. *Chem. Phys. Lett.* 1994, *220*, 122. Saebo, S.; Almlof, J. *Chem. Phys. Lett.* **1989**, *154*, 83.

(139) Traetteberg, M.; Paulen, G.; Cyvin, S. J.; Panchenko, Y. N.; Mochalov, V. I. *J. Molec. Struc.* **1984**, *116*, 141. (and citations therein including Compton, D.A.C. *J. Chem. Soc. Perkin Trans. 2* 1977, 1311.)

(140) Huber, K. P.; Herzberg, G. *Molecular Spectra and Molecular Structure. IV. Constants of Diatomic Molecules*. Van Nostrand Reinhold Co. 1979. http://srdata.nist.gov Accessed January 2007.

(141) Klippenstein, S. J.; Wagner, A. F.; Robertson, S. H.; Dunbar, R. C.; Wardlaw, D.M. *VARIFLEX, A Program for Flexible Transition State Theory* http://chemistry.anl.gov/chem.- dyn/VariFlex/index.html, Program made available by Stephen J. Klippenstein 2004.

(142)Georgievskii, Y. and Klippenstein, S. J. *J. Chem. Phys.* **2005**, *122*, 194103.

(143) Young, D. Computational Chemistry. *A Practical Guide for Applying Techniques to Real World Problems.* Wiley-Interscience, New York, 2001.

(144) Atkinson, R.; Aschmann, S. M.; Tuazon, E. C.; Arey, J.; Zielinksa, B. *Int. J. Chem. Kinet.* **1989**, *21*, 593.

(145) Jenkin, M. E.; Hayman, G. D. *J. Chem. Soc. Faraday Trans.* **1995**, *91*, 1911.

(146) Zhao, J.; Zhang, R.; Fortner, E. C.; North, S. W. *J. Am. Chem. Soc.* **2004**, *126*, 2686.

(147) One inadequacy of the present master equation treatment is that it ignores any flux that goes from a well to the van der Waals region and then back to a different well. However, such effects are expected to be minimal, and furthermore should increase the stabilization rate and thus make our predictions even more discordant with experiment.

(148) Lei, W.; Zhang, R. *J Phys. Chem. A* **2001**, *105,* 3808.

(149) Park, J.; Stephens, J. C.; Zhang, R.; North. S. W. *J. Phys. Chem. A* **2003**, *107,* 6408.

(150) Dibble, T.S. *J. Phys. Chem. A* **2002**, *106,* 6643.

(151) Zhao, J.; Zhang. R.; North, S. W. *Chem. Phys. Lett*. **2003**, *369,* 204.

(152) Zhang, D.; Zhang, R.; Park, J.; North, S. W. *J. Am. Chem. Soc.*, **2002**, *124,* 9600.

(153) Stevens, P.; L'Esperance, D.; Chuong, B.; Martin, G. *Int. J. Chem. Kinet.*, **1999**, *31,* 637.

(154) Reitz, J. E.; McGivern, W. S.; Church, M. C.; Wilson, M. D.; North, S. W. *Int. J. Chem. Kinet.*, **2002**, *34,* 255.

(155) Zhang, D.; Zhang, R.; Church, C,; North, S. W. *Chem. Phys. Lett. A*, **2001**, *343,* 49.

(156) Zalyubovsky, S. J.; Glover, B. G.; Miller, T. A.; Hayes, C.; Merle, J. K.; Hadad, C. M. *J. Phys. Chem. A* **2005**, *109,* 1308.

(157) Carter, W. P. L.; Darnall, K. R.; Graham, R. A.; Winer, A. M.; Pitts, J. N. Jr. *J. Phys. Chem.*, **1979**, *83,* 2305.

(158) Ohta, T.; Bandow, H.; Akimoto, H.; *Int. J. Chem. Kinet.* **1982**, *14,* 173.

(159) Washida, N. *J. Chem. Phys.*, **1981**, *75,* 2715.

(160) Miyoshi, A.; Matsui, H.; Washida, N. *J. Phys. Chem.*, **1990**, *94,* 3016.

(161) Baldwin, J. E. *J. C. S. Chem. Comm.* **1976**, *18,* 734.

(162) Busch, G. E.; Wilson, K. R. *J. Chem. Phys.* **1972**, *56*, 3639.

(163) Barluenga, J.; Marco-Arias, M.; González-Bobes, F.; Ballesteros, A.; González, J. M. *Chem. Eur. J.* **2004**, *10*, 1677.

(164) Masuda, H.; Takase, K.; Nishio, M.; Hasegawa, A.; Nishiyama, Y.; Ishii, Y. *J. Org. Chem.* **1994**, *59*, 5550.

(165) It was found that diluting 33 mL of 18 M sulfuric acid with half of the prescribed solvent distilled water to produce 83 mL of 7.2 M sulfuric acid was preferable as predissociating the acid and cooling reduced the amount of heat added to the reaction solution.

(166) McMurry, J. *Organic Chemistry* Pacific Grove, Brooks/Cole, 2000.

(167) Zou, P.; Kim, H.; North, S. W. *J. Chem. Phys.* **2002**, *116*, 4176. Kim, H.; Park, J.; Niday, T. C.; North, S. W. *J. Chem. Phys.* **2005**, *123*, 174303.

(168) Felps, S.; Hochmann, P.; Brint, P.; Mcglynn, S. P. *J. Mol. Spectrosc.* **1976**, *59,* 355.

(169) Dribinski, V.; Ossadtchi, A.; Mandelshtam, V. A.; Reisler, H. *Rev. Sci. Instrum.* **2002**, *73,* 2634.

(170) Zare, R. N. *Mol. Photochem.* **1972**, *4*, 1.

(171) Hess, W. P.; Kohler, S. J.; Haugen, H. K.; Leone, S. R. *J. Chem. Phys.* **1986**, *84,* 2143.

(172) Krajnovich, D.; Butler, L. J.; Lee, Y. T. *J. Chem. Phys.* **1984**, *81,* 3031.

(173) Minton, T. K.; Felder, P.; Brudzynski, R. J.; Lee, Y. T. *J. Chem. Phys.* **1984**, *81,* 1759.

(174) Minton, T. K.; Nathanson, G. M.; Lee, Y. T. *J. Chem. Phys.* **1987**, *86,* 1991.

(175) Meloni, G.; Zou, P.; Klippentstein, S. J.; Ahmed, M.; Leone, S. R.; Taatjes, C. A.; Osborn, D. L. *J. Am. Chem. Soc.* **2006**, *128*, 13559.

(176) Becke, A. D. *J. Chem. Phys*., **1993**, *98*, 5648.

(177) Krishnan, R.; Binkley, J. S.; Seeger, R.; Pople, J. A. *J. Chem. Phys.* **1980**, *72*, 650.

(178) Stein, S. E.; Ravinovitch, B. S. *J. Chem. Phys.* **1973**, *58*, 2438.

(179) Beyer, T. Swinehart, D. R. *ACM Commun*. **1973**, *16*, 379.

(180) Barker, J. R. *MultiWell Software Ver. 1.3.1*; http://aoss.engin.umich.edu/multiwell/, Ann Arbor, MI, **2002**.

(181) Barker, J. R. *Int. J. Chem. Kinet.* **2001**, *33,* 232.

(182) Gilbert, R. G.; Smith, S. C. *Theory of Unimolecular and Recombination Reactions* Blackwell: Oxford, 1990.

(183) A Boltzmann internal energy distribution for the OH-butadiene adduct was calculated, including vibrational and rotational contributions to the density of states, and then offset by the association energy of hydroxyl radical and butadiene (22.4 kcal/mol), which includes zero point energy as well as spin orbit splitting.

(184) The reaction of the β-hydroxy radicals with molecular oxygen is thought to occur exclusively via O_2 addition yielding hydroxy peroxy radicals. The hydrogen abstraction reaction is a relatively minor channel. Recommended rate constants for O_2 addition and hydrogen abstraction are $3x10^{-12}$ molecules cm^{-3} s^{-1} and $8x10^{-15}$ molecules cm^{-3} s^{-1}, respectively. Atkinson, R.; Baulch, D. L.; Cox, R. A.; Hampson, R. F.; Ker, J. A.; Rossi, M. J.; Troe, J. *J. Phys. Chem. Ref. Data* **1997**, *26,* 521.

(185) Ianni, J. C. *Kintecus* Windows Version 2.80, 2002, www.kintecus.com.

(186) It should be noted that the absolute values of k_1 and k_2 are not meaningful, only their relative values. The rates are made sufficiently fast to be considered instantaneous on the time scale of the kinetics.

(187) Glaschick-Schimpf, I.; Leiss, A.; Monkhouse, P. B.; Schurath, U.; Becker, K. H.; Fink, E. H. *Comm. Eur. Communities* **1980**, (EUR 6621, Proceedings European Symposium Physical Chemistry: Behavior of Atmospheric Pollutants, 1st, 1979), 122.

(188) Glaschick-Schimpf, I.; Leiss, A.; Monkhouse, P. B.; Schurath, U.; Becker, K. H.; Fink, E. H. *Chem. Phys. Lett.* **1979**, *67,* 318.

(189) Senosiain, J. P.; Klippenstein, S. J.; Miller, J. A. *J. Phys. Chem. A*, **2006**, *110*, 6960.

(190) Miyoshi, A.; Matsui, H. *J. Phys. Chem.* **1990**, *94*, 3016.

(191) Grotheer, E. E.; Riekert, G.; Walter, D.; Just, T. *J. Phys. Chem.* **1988**, *92*, 4028.

(192) Grotheer, E. E.; Riekert, G.; Meier, U.; Just, T. *Berichte der Bunsen-Gesellschaft* **1985**, *89*, 187.

(193) Olivella, S.; Bofill, J. M.; Sole, A. *Chem.-Eur. J.* **2001**, *7*, 3377.

(194) Dibble, T. S. *Chem. Phys. Lett.* **2002**, *355*, 193.

(195) Hermans, I.; Muller, J.; Nguyen, T. L.; Jacobs, P. A.; Peeters, J. *J. Phys. Chem. A* **2005**, *109*, 4303.

APPENDIX A

```
#include <iostream.h>
#include <stdlib.h>
#include <math.h>
#include <fstream.h>
#include <stdio.h>
#include <iomanip.h>
int main()
{
// Constants that will never change
  double const kb = 1.38065e-23;
  double const h = 6.62608e-34;
  double const ccm = 3e10;
  double const R = 8.314;
  double const Rkcal = 0.001987;
  double const u = 1.66054e-27;
  double const Av = 6.02214e23;
  double const pi = 3.14159265359;

// Constants that will vary with the system
  double const re = 1.822027603;  //equilibrium bond length
  double const massadd = u*45.03404;   // mass of the adduct in kg
  double const masseth = u*28.03130;   // mass of ethylene in kg
  double const massoh = u*17.00274;    // mass of oh in kg
  double const masstst = u*45.03404;   // mass of the tst in kg
  float const symmnumadd = 1;          // symmetry numbers for the adduct, eth,
                                       //oh and the tst
  float const symmnumeth = 4;
```

```
  float const symmnumoh = 1;
  float const symmnumtst = 1;

  int const numsteps = 5000;          // number of steps to take along the reaction
                                     // coordinate

  int const numethfreqs = 12;         // number of frequencies
  int const numohfreqs = 1;
  int const numtstfreqs = 17;
  int const numaddfreqs = 18;

  double const inittemp = 100; // initial temperature  usually 200 with
numsteps=21
  int const numtempsteps = 41; // number of different temperatures to get rates
  double const tempincs = 10;  // incremental difference btwn temp steps

  int const numohBs = 1;        // number of rotational constants
  int const numethBs = 3;
  int const numaddBs = 3;

  double const E = 25.94486;  // this should be the energy difference between the
                  // infinately seperated peices and the adduct with zpe
  double const scalefact = 1;

/* ---------------------------------------------------------------------------
-----------------------------------------------------------------------------
 Here, we will give a number for potential to signify which potential we are using
   if (potential==1) en = tightmorse;
   if (potential==2) en = extendmorse;
```

```
    if (potential==3) en = varshni;
    if (potential==4) en = lj;  <-- Lennard Jones 6-12
    if (potential==5) en = lj2; <-- Lennard Jones from paper (exntended?)
-------------------------------------------------------------------------------
-----------------------------------------------------------------------------*/
  int const potential = 2;
// Tight Morse  tightmorse = d0*pow((exp(-B2*(r[j]-re)*1e-8)-1),2);
  double const d0 = 29.40241869;  // this is not zero point corrected and is
                                 // a fitting paramter for extended morse

  double const B0 = 3.579538e08;
  double tightmorse = 0;

/* Extended Morse
    apart = alpha*pow((exp(-B1*(r[j]-re)*1e-8)-1),2);
    bpart = beta*pow((exp(-B1*(r[j]-re)*1e-8)-1),3);
    cpart = gamma*pow((exp(-B1*(r[j]-re)*1e-8)-1),4);
    dpart = delta*pow((exp(-B1*(r[j]-re)*1e-8)-1),5);
    extendmorse = d1*(apart+bpart+cpart+dpart);
*/
  double const B1 = 2.038438e8;  // the Beta paramter in the morse
  double const alpha = 3.369394;
  double const beta = 1.862433;
  double const gamma = -2.11206;
  double const delta = -1.578567;
  double const d1 = 29.40241869;  // this is not zero point corrected and is
                                 // a fitting paramter for extended morse
  double extendmorse = 0;
```

```
// Varshni
// constants for the varshni go here
  double varshni = 0;
  double B2 =  0.7636822;
  double d2 =  29.40241869;

// Lennard Jones 6-12
  double lj = 0;
  double eps = 29.38511;
  double ro =  1.583324;

// Lennard Jones (extended? from paper)
// constants for the Lennard Jones from paper go here
  double lj2 = 0;

    char* typeen;
    if (potential==1) typeen = "Tight Morse";
    if (potential==2) typeen = "Extended Morse";
    if (potential==3) typeen = "Varshni";
    if (potential==4) typeen = "Lennard-Jones 6-12";
    if (potential==5) typeen = "Other";

/* -----------------------------------------------------------------------
Read in all necessary files
------------------------------------------------------------------------- */
// switchfile contains exponential switching info for tst freqs
  char* switchfile="switchfile.dat";
```

```
// load in from switchfile
  ifstream infile(switchfile);
  if (!infile) {
  cout << "Error! Input file " << switchfile << " does not exist!" << endl;
  exit(-1);
  }
// freqfile contains freqs for equlibrium const calc
  char* freqfile="freqfile.dat";

// load in from freqfile
  ifstream infile2(freqfile);
  if (!infile2) {
  cout << "Error! Input file " << freqfile << " does not exist!" << endl;
  exit(-1);
  }

// output file
ofstream fileout("vtstout.txt", ios::out|ios::trunc);
fileout << "The type of potential is " << typeen << endl;
fileout << "The scaling factor for the frequencies is " << scalefact << endl;
fileout << "Temp" << '\t' << "rtst" << '\t' << "kf" << '\t'  << "1/Temp" << '\t' <<
"ln(kf)" << endl;
/* ---------------------------------------------------------------------
Reads in all arrays for the frequency calcs and the equilibrium const calcs
------------------------------------------------------------------------- */
 double n[numtstfreqs];
 double m[numtstfreqs];
 double A[numtstfreqs];
 double B[numtstfreqs];
```

```
 for (int i=0;i<numtstfreqs;i++) {
 infile >> n[i];
 infile >> m[i];
 infile >> A[i];
 infile >> B[i];
// cout << n[i] << '\t' << m[i] << '\t' << A[i] << '\t' << B[i] << endl;
 }

 double ohfreq[numohfreqs];
 double ethfreq[numethfreqs];
 double addfreq[numaddfreqs];
 double ohB[numohBs];
 double ethB[numethBs];
 double addB[numaddBs];

 for (int i=0;i<numaddfreqs;i++) {
 infile2 >> addfreq[i];
 addfreq[i] = scalefact*addfreq[i];
 }
 for (int i=0;i<numethfreqs;i++) {
 infile2 >> ethfreq[i];
 ethfreq[i] = scalefact*ethfreq[i];
 }
 for (int i=0;i<numohfreqs;i++) {
 infile2 >> ohfreq[i];
 ohfreq[i] = scalefact*ohfreq[i];
 }
 for (int i=0;i<numethBs;i++)  {
```

```
 infile2 >> ethB[i];
 }
 for (int i=0;i<numaddBs;i++)  {
 infile2 >> addB[i];
 }
 for (int i=0;i<numohBs;i++)  {
 infile2 >> ohB[i];
 }
 /* ---------------------------------------------------------------------
------------------------------------------------------------------------ */
/* ---------------------------------------------------------------------
Done with input
------------------------------------------------------------------------ */
/* ---------------------------------------------------------------------
No matter where we are on the reaction coordinate, the translational
partition function is fixed for a particular molecule of mass m
------------------------------------------------------------------------ */
double temp;
temp = inittemp-tempincs;
for (int t=0;t<numtempsteps;t++) {
temp=temp+tempincs;
  double qtadd = 0;
  double qteth = 0;
  double qtoh = 0;
  double qttst = 0;
  qtadd = (pow((2*pi*massadd*kb*temp),(1.5))*(1e-6))/h/h/h;  // 3-D translational
partition function
  qttst = (pow((2*pi*masstst*kb*temp),(1.5))*(1e-6))/h/h/h;
  qteth = (pow((2*pi*masseth*kb*temp),(1.5))*(1e-6))/h/h/h;
```

```
  qtoh = (pow((2*pi*massoh*kb*temp),(1.5))*(1e-6))/h/h/h;

/* ---------------------------------------------------------------------
---------------------------------------------------------------------- */
double qvoh = 1;
double qroh = 0;
double qeoh = 3.01;
// initialization loops
     for (int k=0;k<numohfreqs;k++) {
     qvoh = qvoh*(1/(1-exp(-ohfreq[k]/(207*(temp/300)))));
       }
      if (numohBs==1)
      qroh=kb*temp/h/ccm/ohB[0];
      else
      qroh =
(1/symmnumoh)*(pow((kb*temp/h/ccm),1.5))*(sqrt(pi/(ohB[0]*ohB[1]*ohB[2])));
/* ---------------------------------------------------------------------
---------------------------------------------------------------------- */
double qveth = 1;
double qreth = 0;
double qeeth = 1;
// initialization loops
     for (int k=0;k<numethfreqs;k++) {
     qveth = qveth*(1/(1-exp(-ethfreq[k]/(207*(temp/300)))));
     }
      if (numethBs==1)
      qreth=kb*temp/h/ccm/ethB[0];
      else
```

```
      qreth =
(1/symmnumeth)*(pow((kb*temp/h/ccm),1.5))*(sqrt(pi/(ethB[0]*ethB[1]*ethB[2])));
/* -----------------------------------------------------------------------*/
/* -----------------------------------------------------------------------*/
double qvadd = 1;
double qradd = 0;
double qeadd = 2;
// initialization loops
     for (int k=0;k<numaddfreqs;k++) {
     qvadd = qvadd*(1/(1-exp(-addfreq[k]/(207*(temp/300)))));
     }
      if (numaddBs==1)
      qradd=kb*temp/h/ccm/addB[0];
      else
      qradd =
(1/symmnumadd)*(pow((kb*temp/h/ccm),1.5))*(sqrt(pi/(addB[0]*addB[1]*addB[2]
)));
/* -----------------------------------------------------------------------*/

double QOH;
double QETH;
double QADD;
double K;
QOH=qtoh*qroh*qvoh*qeoh;
QETH=qteth*qreth*qveth*qeeth;
QADD=qtadd*qradd*qvadd*qeadd;
K=(QADD/(QOH*QETH))*exp(E/(Rkcal*temp));

/* -----------------------------------------------------------------------
```

```
---------------------------------------------------------------------------
Main loop of the program for a particular temperature
---------------------------------------------------------------------------
--------------------------------------------------------------------------- */
double minRate = 5e100;
double rtst = 0;
double zpeadduct=0;    // zero point energy of the adduct is zpe at r=re

 for (int j=0;j<numsteps;j++){
    double r[numsteps];
    double zpe = 0;
    double qvtst=1;
    double tstfreq[numtstfreqs];



    if (j==0)
      r[j] = re;
    else
       r[j] = r[j-1]+0.001;



// initialization loops
    for (int a=0;a<numtstfreqs;a++) {
    tstfreq[a] = 0;
    }

      // loops over all of the frequencies
      for (int k=0;k<numtstfreqs;k++) {
        tstfreq[k] = scalefact*(n[k]*exp(-A[k]*(r[j]-re))+m[k]*(1-exp(-B[k]*(r[j]-re))));
```

```
            if (tstfreq[k]<20) tstfreq[k] = 20;
            qvtst =qvtst*(1/(1-exp(-tstfreq[k]/(207*(temp/300)))));
            zpe = zpe+(0.5*h*ccm*tstfreq[k]*Av)/(4.184*1000);
            if (j==0) zpeadduct = zpe;
        }
// fileout << r[j] << '\t' << tstfreq[0] << '\t' << tstfreq[1] << '\t' << tstfreq[2] << '\t' <<
tstfreq[3] << '\t' << tstfreq[4] << '\t' << tstfreq[5] << '\t' << tstfreq[6] << '\t' <<
tstfreq[7] << '\t' << tstfreq[8] << '\t' << tstfreq[9] << '\t' << tstfreq[10] << '\t' <<
tstfreq[11] << '\t' << tstfreq[12] << '\t' << tstfreq[13] << '\t' << tstfreq[14] << '\t' <<
tstfreq[15] << '\t' << tstfreq[16] << '\t' << endl;
    double en = 0;
    double Eo = 0;
    double Atst = 0;
    double Btst = 0;
    double Ctst = 0;
    double qrtst = 0;
    double Rate = 0;

// at some point this should be re-written to include the possibility of a linear T.S.

    tightmorse = d0*pow((exp(-B0*(r[j]-re)*1e-8)-1),2);

    double apart = 0;
    double bpart = 0;
    double cpart = 0;
    double dpart = 0;
    apart = alpha*pow((exp(-B1*(r[j]-re)*1e-8)-1),2);
    bpart = beta*pow((exp(-B1*(r[j]-re)*1e-8)-1),3);
    cpart = gamma*pow((exp(-B1*(r[j]-re)*1e-8)-1),4);
```

```
   dpart = delta*pow((exp(-B1*(r[j]-re)*1e-8)-1),5);
   extendmorse = d1*(apart+bpart+cpart+dpart);

   double a2part = 0;
   double b2part = 0;
   a2part = pow(r[j],2)-pow(re,2);
   b2part = 1-(re/r[j])*exp(-B2*a2part);
   varshni = d2*pow(b2part,2);

   double a3part = 0;
   a3part = pow((ro/r[j]),12)-pow((ro/r[j]),6);
   lj = (4*eps*a3part)+eps;

   lj2 = 0;

   // Which potential?
   if (potential==1) en = tightmorse;
   if (potential==2) en = extendmorse;
   if (potential==3) en = varshni;
   if (potential==4) en = lj;
   if (potential==5) en = lj2;

   Eo = en+zpe-zpeadduct;
   Atst = 0.7478*exp(-0.5472*r[j]);
   Btst = 0.925*exp(-0.5905*r[j]);
   Ctst = 1.2131*exp(-0.0456*r[j]);
   qrtst =
(1/symmnumtst)*pow(((kb*temp)/(h*ccm)),1.5)*(sqrt(pi/(Atst*Btst*Ctst)));
   Rate = ((kb*temp)/(h*QADD))*(qttst*qvtst*qrtst)*exp(-Eo/(Rkcal*temp));
```

```
    if (Rate<minRate) rtst=r[j];
    if (Rate<minRate) minRate=Rate;

fileout  << r[j] << '\t' << Rate << '\t' << Eo << endl;
//fileout << r[j] << '\t' << zpe << endl;
}
 double kf = 0;
 kf=K*minRate;
 double invtemp = 0;
 invtemp = 1/temp;
 double logk = 0;
 logk = log(kf);     // this is actually natural log base e
//fileout << temp << '\t' << rtst << '\t' << kf << '\t' << invtemp << '\t' << logk <<
endl;
}
fileout.close();
infile.close();
      system("PAUSE");
      return 0;
}
```

VITA

Name: Erin Elizabeth Tullos

Address: 509 Holly Ave., Livingston, TX 77351-2651

Email: etullos@mail.chem.tamu.edu

Education: B.A. Chemistry, Texas A&M University

Ph.D. Chemistry, Texas A&M University